DISSERTATION

submitted to the
Combined Faculty of Mathematics, Engineering and Natural Sciences
of Heidelberg University, Germany
for the degree of
Doctor of Natural Sciences

Put forward by
Fabian Manuel Maier
born in Bad Säckingen, Germany

Oral examination: 12. July 2023

Estimating fossil fuel carbon dioxide (ffCO_2) emissions in the Rhine Valley metropolitan region from local atmospheric observations in Heidelberg

Referees:
apl. Prof. Dr. Ingeborg Levin
Prof. Dr. André Butz

Abstract

This cumulative dissertation investigates the potential of radiocarbon (^{14}C)-based and carbon monoxide (ΔCO)-based fossil fuel CO_2 (ΔffCO_2) estimates from the urban observation site Heidelberg to deduce the seasonal cycle of the ffCO_2 emissions in the Rhine Valley. For this, the CarboScope inversion system is used to investigate the benefit of few but accurate ^{14}C-based ΔffCO_2 estimates from about 100 hourly flask samples collected in 2019 and 2020, compared to a continuous ΔCO-based ΔffCO_2 record with about 4 times larger uncertainty. The urban observation site with large ffCO_2 point sources in the vicinity places special demands on the transport model. Therefore, a method is developed for the high-resolution Weather Research and Forecasting - Stochastic Time-Inverted Lagrangian Transport model (WRF-STILT) to represent the effective emission heights of point sources. This work shows that the ^{14}C-based ΔffCO_2 observations contain the seasonal cycle of the ffCO_2 emissions, but do not lead to robust inversion results. In contrast, the continuous ΔCO-based ΔffCO_2 estimates provide robust and data-driven seasonal cycles that show the distinct COVID-19 signal in 2020 and are suitable for validating the amplitude and phasing of the seasonal cycle of the emission inventories in the main footprint of Heidelberg.

Kurzfassung

Diese kumulative Dissertation untersucht das Potenzial von Radiokohlenstoff (^{14}C)-basierten und Kohlenmonoxid (ΔCO)-basierten fossilen CO_2 (ΔffCO_2) Abschätzungen von der urbanen Heidelberger Messstation, um damit den Jahresgang der ffCO_2 Emissionen im Rheintal abzuleiten. Hierzu soll mit dem CarboScope Inversionssystem der Nutzen von wenigen, aber genauen ^{14}C-basierten ΔffCO_2 Abschätzungen von etwa 100 stündlichen Luftproben, die in den Jahren 2019 und 2020 gesammelt wurden, im Vergleich zu einer kontinuierlichen ΔCO-basierten ΔffCO_2 Zeitreihe mit etwa 4-mal größerer Unsicherheit untersucht werden. Die urbane Messstation mit starken ffCO_2 Punktquellen im direkten Umfeld stellt besondere Anforderungen an das Transportmodell. Deshalb wurde für das hochaufgelöste Weather Research and Forecasting – Stochastic Time-Inverted Lagrangian Transport Modell (WRF-STILT) eine Methode entwickelt, um die effektive Emissionshöhe von Punktquellen zu repräsentieren. Diese Arbeit zeigt, dass die ^{14}C-basierten ΔffCO_2 Beobachtungen zwar den Jahresgang der ffCO_2 Emissionen enthalten, aber zu keinen robusten Inversionsergebnissen führen. Dagegen liefern die kontinuierlichen ΔCO-basierten ΔffCO_2 Abschätzungen robuste und datengetriebene Jahresgänge, die das ausgeprägte COVID-19 Signal im Jahr 2020 zeigen und für eine Validierung der Amplitude und der Phasenlage des Jahresgangs der Emissionsinventare im Haupteinzugsgebiet von Heidelberg geeignet sind.

TABLE OF CONTENTS

CHAPTER 1

Introduction

1.1 The global carbon cycle

1.1.1 Atmospheric carbon dioxide (CO_2) increase and global warming

As early as 1896, the Swedish scientist Svante Arrhenius found that the atmospheric CO_2 concentration affects the Earth's surface temperature through the absorption and re-emission of long-wave radiation from the ground (Arrhenius, 1896; Rodhe et al., 1997). In his pioneering work Arrhenius predicted a 5–6°C heating of the Earth's surface for a doubling of the atmospheric CO_2 concentration (Arrhenius, 1896). Today, well over 100 years later, there is no doubt that anthropogenic emissions of CO_2 by burning of fossil fuels (ff) and land use change have led to an increase in the atmospheric CO_2 concentration of about 50% compared to pre-industrial levels (Keeling et al., 1976; IPCC, 2021; Friedlingstein et al., 2022; Lan et al., 2023). Human induced CO_2 (and CH_4) emissions are thus the major driver for recent global warming, which is characterized by an about 1.1°C higher mean global surface temperature in 2011-2020 compared to 1850-1900 (IPCC, 2021).

The impact of global warming on weather extremes and climate change with its drastic implications for nature, society and economy are ubiquitously palpable. In particular, vulnerable communities who have historically least contributed to climate change are disproportionately affected by its consequences (IPCC, 2021; IPCC, 2023). Meanwhile, the urgency of mitigating climate change is reflected in politic actions such as the Paris Agreement to limit global temperature rise until 2100 to below 1.5°C compared to pre-industrial levels. This requires rapid and dramatic reductions of the anthropogenic CO_2 emissions with net zero CO_2 emissions by 2050, and even negative emissions thereafter (IPCC, 2021).

1.1.2 Natural CO_2 sources and sinks

The prediction of future warming requires a profound understanding of the global carbon cycle, i.e. how perturbing anthropogenic CO_2 emissions are redistributed "among atmosphere, ocean and terrestrial biosphere in a changing climate" (Friedlingstein et al., 2022). Fortunately, about 50% of the annual anthropogenic CO_2 emissions are taken up by the ocean and the terrestrial biosphere in roughly equal shares (see Fig. 1.1). This strongly weakens the CO_2 growth rate in the atmosphere, and thus global temperature rise.

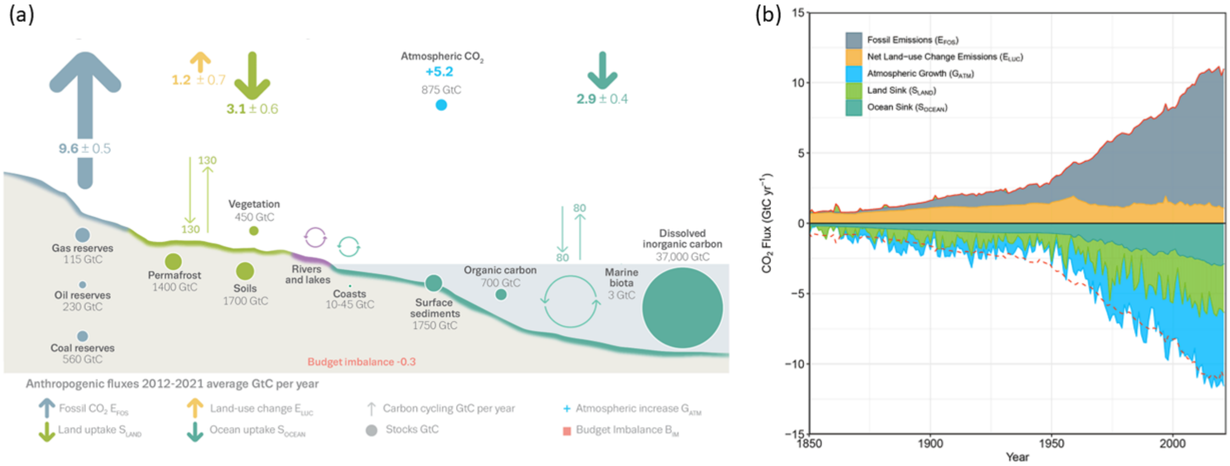

Figure 1.1 Global carbon cycle. Panel (a) shows the annual perturbation (thick arrows) of the global carbon cycle caused by anthropogenic ffCO$_2$ emissions and land-use change (averaged globally for the decade 2012-2021). The thin arrows show the annual gross land-atmosphere and ocean-atmosphere fluxes. Panel (b) illustrates the partitioning of the perturbing annual ffCO$_2$ and net land-use change emissions among the atmosphere, the ocean, and the terrestrial biosphere. The dashed red curve indicates the budget imbalance between the overall perturbing emissions and their partitioning into the three reservoirs. The figures are from Friedlingstein et al. (2022).

However, there are large uncertainties of roughly 15-20% in the annual CO$_2$ sinks of the ocean and the terrestrial biosphere (see Fig. 1.1). Moreover, the latter shows large interannual variabilities due to varying meteorological conditions (see Fig. 1.1b; Rödenbeck et al., 2018). While the fossil emissions in Fig. 1.1 are based on energy statistics, the ocean and land sinks are estimated with global ocean biogeochemistry models and dynamic global vegetation models, respectively (Friedlingstein et al., 2022). Apparently, the sum of the measured atmospheric CO$_2$ growth rate and the modelled natural CO$_2$ sinks from the ocean and the terrestrial biosphere is slightly larger than the sum of the CO$_2$ emissions due to fossil fuel burning and land-use change. This imbalance illustrates the current understanding of the global carbon cycle (Friedlingstein et al., 2022).

In the past, the natural CO$_2$ sinks have increased with the growing amount of CO$_2$ in the atmosphere (see Fig. 1.1b). However, the adaptation of these natural CO$_2$ sinks to increased future CO$_2$ levels is associated with large uncertainties (Walker et al., 2021). Furthermore, the fossil and natural CO$_2$ fluxes are associated with much larger uncertainties on a more regional or local and sub-annual scale, on which e.g. climate extremes take place. Therefore, a better understanding of the ocean-atmosphere and land-atmosphere CO$_2$ exchange fluxes and their driving processes is needed. For this, atmospheric CO_2 observations together with accurate estimates of the fossil emissions on the regional to local scale can help to constrain the natural CO_2 fluxes and their expected changes and enable a better understanding of the global carbon cycle (e.g., Monteil et al., 2020; Chandra et al., 2022).

Figure 1.2 (colored lines) shows the atmospheric CO_2 concentrations measured at 35 Integrated Carbon Observation System (ICOS) atmosphere stations between 2017 and 2021 in Europe (see Sect. 1.2 for a description of the ICOS network). They show a clear seasonal cycle with roughly 10-20 ppm larger concentrations during winter than during summer. This seasonal cycle is mainly caused by the seasonality in the fossil and the biospheric CO_2 fluxes. During the growing season, plant photosynthesis leads to a biospheric CO_2 uptake, and thus to the drawdown of the atmospheric CO_2 concentration in spring (see Kutsch et al., 2022). In contrast, the biosphere is a net CO_2 source during the dormant season. This leads to a CO_2 concentration maximum during winter. Furthermore, European ffCO_2 emissions are typically larger in winter than in summer because of heating emissions. The seasonal cycle in the ffCO_2 emissions must be accurately known, so that the ffCO_2 emissions can be used to separate the fossil from the biospheric contributions in the atmospheric CO_2 observations and therewith to constrain the biospheric CO_2 fluxes.

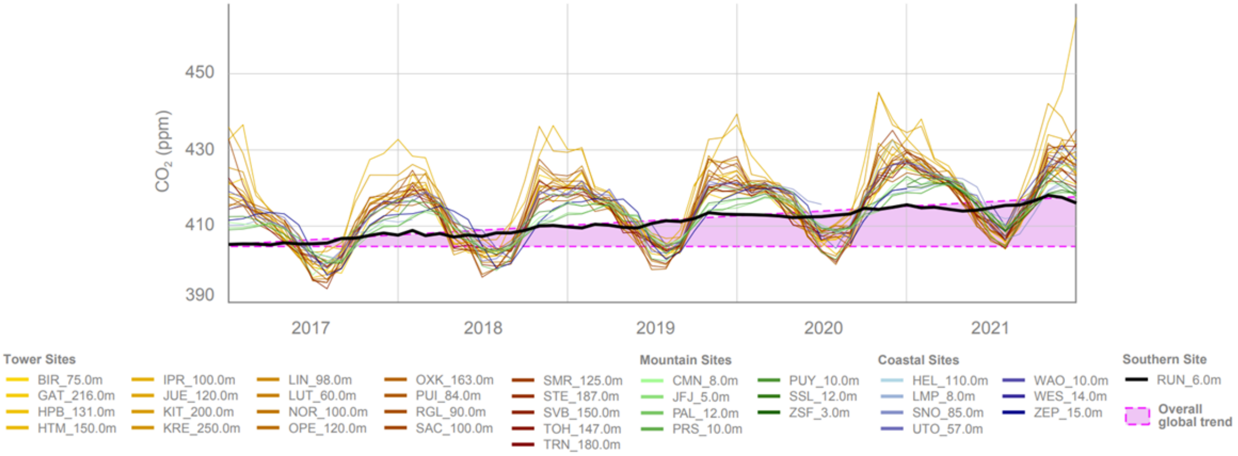

Figure 1.2 Monthly averaged atmospheric CO_2 concentration measurements from 35 European ICOS atmosphere stations for 2017-2021 (colored lines). The black line shows the measurements from the ICOS station of Réunion Island in the Indian Ocean, which is less influenced by biogenic or fossil CO_2 fluxes. Due to the very weak seasonal cycle, these observations can be used to illustrate the overall global CO_2 trend (highlighted in pink). This figure is from Kutsch et al. (2022).

1.2 ICOS Research Infrastructure & Heidelberg observation site

1.2.1 ICOS atmosphere station network

In Europe, the Integrated Carbon Observation System Research Infrastructure (ICOS RI) was set up to produce high-quality and long-term measurements from the different carbon reservoirs atmosphere, terrestrial ecosystems and oceans to provide the observational data for constraining surface-atmosphere CO_2 fluxes and thus improving the knowledge about the carbon cycle and possible climate feedbacks (ICOS RI, 2020; Heiskanen et al., 2022). Currently, the ICOS Atmosphere station network consists of 20 class-1 and 19 class-2 stations, which are distributed over the ICOS member countries. At ICOS class-1 and class-2 sites, ambient air CO_2, CH_4 and CO measurements are performed continuously. Furthermore, ICOS class-1 sites are equipped with an automated flask sampler, which is designed to regularly collecting hourly air samples, which are analyzed for additional tracers like radiocarbon (^{14}C) in CO_2 (see Ch. 4 for more details). Overall, these precise measurements are the basis for estimating fossil and natural CO_2 fluxes in Europe.

1.2.2 Heidelberg observation site

The urban Heidelberg observation site was selected as an ICOS pilot station to test and develop flask sampling and modelling strategies for estimating $ffCO_2$ emissions in the ICOS network. It is located in the highly populated and industrialized Upper Rhine Valley in Southwestern Germany. The large and variable CO_2 signals observed in Heidelberg are well suited to intensively test the performance of the ICOS flask sampler and to try out various flask sampling strategies (see Ch. 4). Moreover, there is a longtime experience with $^{14}CO_2$ observations in Heidelberg, dating back to the 1950s (Kromer et al., 2022).

The Heidelberg observation site is located in the northern part of the city on the campus of the university. Local emissions mainly originate from the traffic and heating sectors. About 500 m north of the observation site is a combined heat and power station, and a few kilometers south is a cement works. Moreover, there are the heavily industrialized cities Mannheim and Ludwigshafen, including a large coal-fired power plant and the BASF company, located about 15-20 km northwest of Heidelberg (see Fig. 1.3, blue dots). Due to the channeling effect of the Rhine Valley, Heidelberg is often influenced by southwesterly air masses, which transport polluted air from the southern part of the Rhine Valley to the station.

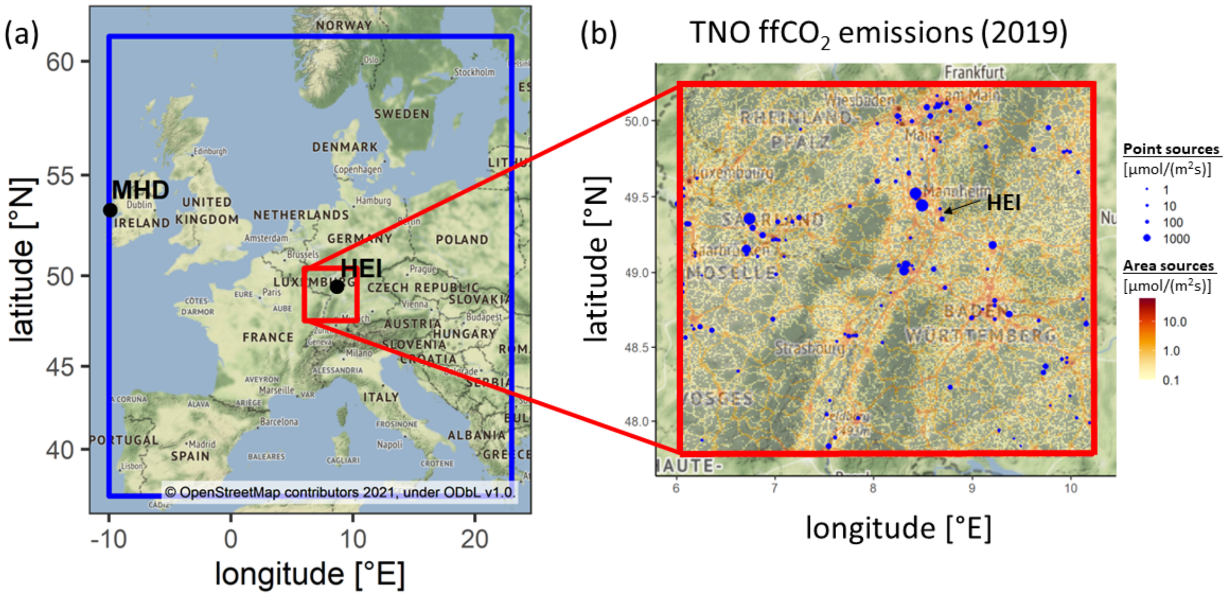

Figure 1.3 Map of the European STILT domain (a) and a zoom into the Rhine Valley domain (b). Panel (b) shows the TNO area and point source ffCO$_2$ emissions from 2019 in the Rhine Valley domain. The Heidelberg observation site (HEI) and the marine European background site Mace Head (MHD) are denoted.

The air intake of the Heidelberg observation site is at 30 m above ground on the roof of the building of the Institute of Environmental Physics. Ambient air CO$_2$ and CO measurements are performed with a Cavity Ring-Down Spectroscopy (CRDS) gas analyser. Furthermore, hourly integrated $^{14}CO_2$ flask samples are collected with the ICOS flask sampler. The flask air concentrations of several gases like CO$_2$, CH$_4$ and CO are measured at the ICOS Flask and Calibration Laboratory (FCL, `https://www.icos-cal.eu/fcl`) with a gas chromatographic analysis system. After that, the CO$_2$ in the flasks is extracted and graphitized at the Central Radiocarbon Laboratory (CRL, `https://www.icos-cal.eu/crl`; Lux, 2018), and analyzed for ^{14}C with an accelerator mass spectrometer (Kromer et al., 2013). The following sections describe how the CO$_2$, CO and $^{14}CO_2$ observations from Heidelberg can be used to estimate the ffCO$_2$ emissions in the Rhine Valley metropolitan region.

1.3 How to estimate ffCO$_2$ emissions

As mentioned above, reliable estimates of ffCO$_2$ emissions are essential for a better understanding of the natural CO$_2$ fluxes and their future development. However, they are also needed to assess the effectiveness of ffCO$_2$ emission reduction strategies and to verify compliance with emission reduction targets. There are two methods to estimate the major anthropogenic CO_2 emissions caused by burning of fossil fuels and cement production: the "bottom-up" and the "top-down" approach.

1.3.1 Bottom-up approach

In the bottom-up approach, national activity data like fuel consumption statistics are collected and combined with emission factors to derive national total ffCO_2 emissions for different emission sectors (Janssens-Maenhout et al., 2019). However, these national and annual totals are less suitable for estimating the more regional or local ffCO_2 emissions of, e.g., individual cities. Therefore, sector-specific annual and national total ffCO_2 emissions are typically redistributed on a grid with a higher spatiotemporal resolution by using spatial and temporal proxies like population density maps or traffic data and temporal activity profiles (Kuenen et al., 2014; Andres et al., 2016; Janssens-Maenhout et al., 2019).

The distribution of the emissions to individual regions or even grid cells with a horizontal resolution of only a few kilometers is associated with huge uncertainties (Andres et al., 2016). For example, Super et al. (2020) estimated for the ca. 1 km x 1 km resolved TNO emission inventory covering Central Europe a CO_2 emission uncertainty of 1% for the whole domain but of up to 40% for specific spatial grid cells. This uncertainty further increases for a sub-annual temporal resolution. The large uncertainties of bottom-up CO_2 emissions on sub-national and sub-annual scales can result from a poor representativeness of the spatial and temporal proxies used to disaggregate the country-level emissions as well as uncertainties in the proxy values themselves (Super et al., 2020). Overall, this strongly calls for an independent verification of the emission inventories from national to regional or local scales, so that wrong emission factors or disaggregation errors can be identified and corrected.

1.3.2 Top-down approach

In the top-down approach, observations of the atmospheric CO_2 concentration are used to independently deduce surface CO_2 fluxes with the so-called "atmospheric transport inversion" (Newsam and Enting, 1988). It exploits that the variations of atmospheric CO_2 concentrations are caused by the combination of spatially and temporally varying CO_2 sources and sinks and the effect of atmospheric transport and mixing processes (Enting, 2002). In a first step, an atmospheric transport model uses a-priori estimates of the surface CO_2 fluxes to simulate atmospheric CO_2 concentrations. Within the inversion framework, the difference between the modelled and observed CO_2 concentrations are minimized by adjusting the a-priori CO_2 sources and sinks.

Gridded bottom-up ffCO$_2$ emissions are used as "best-guess" estimates to describe the ffCO$_2$ emissions in the CO$_2$ inversion. Commonly, these ffCO$_2$ fluxes are prescribed and only the typically less known natural CO$_2$ fluxes from the ocean and the terrestrial biosphere are adjusted (e.g., Rödenbeck et al., 2003; Peylin et al., 2013; Monteil et al., 2020; Liu et al., 2021). Therefore, a reliable top-down estimation of natural CO$_2$ fluxes is based on accurate bottom-up ffCO$_2$ emissions. As mentioned above, estimating the seasonal (and diurnal) varying CO$_2$ fluxes from the land biosphere requires accurate temporal profiles in the bottom-up ffCO$_2$ emissions. Thus, it is important to also validate the bottom-up ffCO$_2$ emissions with top-down ffCO$_2$ emission estimates. However, for this, an additional observational tracer is needed, which allows to separate between the ffCO$_2$ fluxes and the natural CO$_2$ fluxes from the terrestrial biosphere or the ocean (Ciais et al., 2015; Bergamaschi et al., 2018).

Dual-tracer inversion

The absence of radiocarbon (^{14}C) in fossil fuels makes ^{14}CO$_2$ observations an ideal tracer to directly estimate ffCO$_2$ emissions (see Sect. 1.3 for a detailed description of ^{14}C). Basu et al. (2020) convincingly demonstrate the strong potential of ^{14}CO$_2$ observations to quantify the ffCO$_2$ emissions from the United States (US). They implemented the CO$_2$ and ^{14}CO$_2$ observations from the North American sites of the National Oceanic and Atmospheric Administration's Global Greenhouse Gas Reference Network in a (global) dual-tracer inversion system (Basu et al., 2016) and estimate the US national total ffCO$_2$ emissions for 2010 to be 1,653 ± 30 TgC/yr. Their top-down estimate is significantly larger ($>3\sigma$) than the bottom-up estimates of three widely used global inventories, but it agrees within 1σ with the US-specific high-resolution "Vulcan" emission inventory. However, such a dual-tracer inversion requires an a-priori representation of the ocean-atmosphere and land-atmosphere CO$_2$ fluxes as well as the isotopic ^{14}CO$_2$ signatures of surface ocean water and the terrestrial biosphere. Furthermore, as ^{14}CO$_2$ is formed in the upper atmosphere, its seasonal transport into the troposphere must also be described correctly in the inversion system.

Regional isotope budget approach

In this thesis I use an alternative – regional – inversion approach for estimating the ffCO$_2$ emissions in the Rhine Valley, which I call here the "regional isotope budget approach". In this approach, CO$_2$ and ^{14}CO$_2$ measurements from an observation and a background site are used to calculate the recently added ffCO$_2$ contribution (ΔffCO$_2$) in the CO$_2$ excess concentrations at the observation site compared to the background site (see Ch. 3 for a detailed derivation of this method). These ^{14}C-based ΔffCO$_2$ estimates can then be implemented in a ΔffCO$_2$ inversion to estimate the ffCO$_2$ emissions between the observation and the background site. The regional isotope budget approach assumes that the background observations adequately capture the CO$_2$ and ^{14}CO$_2$ boundary conditions. So, there is no need to explicitly describe e.g. the CO$_2$ flux and the ^{14}CO$_2$ signature of the ocean, or the ^{14}CO$_2$ transport from the stratosphere into the troposphere. However, the regional isotope budget approach is strongly dependent on the choice of the ^{14}CO$_2$ background.

Graven et al. (2018) applied this regional isotope budget approach to estimate the ffCO$_2$ emissions of California for three months in 2014-2015. Their inversion results are consistent with the officially reported ffCO$_2$ emissions. Therefore, continuing this inversion analysis could provide an independent validation of the reported ffCO$_2$ emissions and their reductions in California. Overall, the usage of ^{14}C-based ΔffCO$_2$ data in inverse models requires a careful estimation of their uncertainties (see Ch. 3). The following section describes the direct ΔffCO$_2$-tracer ^{14}C more in detail.

1.3.3 ^{14}C as tracer for ffCO$_2$ emissions

^{14}C is naturally produced in the upper atmosphere when thermalized neutrons react with nitrogen atoms. The ^{14}C isotopes quickly oxidize to ^{14}CO and ^{14}CO$_2$. In the latter form, it dissolves into the ocean or is taken up by plants via photosynthesis (Currie, 2004). The ^{14}C-decay with a half-life of 5700 years leads to a slow reduction of the ^{14}C isotopes in dead plant material or deep ocean waters without CO$_2$ exchange with the atmosphere. Consequently, million-year-old fossil fuels are devoid of ^{14}C and their combustion leads to an increase in CO$_2$ concentration and a depletion of the ambient air ^{14}C/C isotopic signature, which is known as the Suess effect (Suess, 1955). Therefore, the ^{14}C/C depletion in ambient air CO$_2$ compared to background air CO$_2$ is a direct tracer for the ΔffCO$_2$ excess at the observation site compared to the background site (Levin et al., 2003; Turnbull et al., 2006).

In this thesis, the Δ-notation introduced by Stuiver and Polach (1977) is used to report the ^{14}C/C isotopic signature as Δ^{14}CO$_2$ (see Eq. (1.1)):

$$\Delta^{14}\mathrm{C} = \left(\frac{\mathrm{A_{SN}} \cdot \mathrm{e}^{\lambda_c (y-x)}}{\mathrm{A_{abs}}} - 1 \right) \cdot 1000‰ \tag{1.1}$$

In this Δ-notation the (normalized) ^{14}C activity of the air sample $\mathrm{A_{SN}}$ is reported relative to a reference ^{14}C activity $\mathrm{A_{abs}}$. As fossil fuels are devoid of ^{14}C, the Δ^{14}CO$_2$ signature of fossil fuels is -1000‰. The advantage of this notation is that the $\Delta^{14}CO_2$ values are normalized with respect to $\delta^{13}C$, so that (mass-dependent) isotopic fractionation processes are accounted for. This makes $\Delta^{14}CO_2$ signatures from different compartments like atmosphere, plant material or ocean water directly comparable. Furthermore, the ^{14}C decay (with λ_c=1/8267 years^{-1}) between the year of sample collection (x) and the year of sample measurement (y) is considered.

Many studies have applied this approach to estimate the $\Delta ffCO_2$ concentrations for continental or urban sites (e.g., Levin et al., 2003; Turnbull et al., 2006; Levin and Rödenbeck, 2008; Zhou et al., 2020). However, this regional isotope budget approach is not always straightforward to apply as there are also anthropogenic $^{14}CO_2$ sources, which can mask a significant amount of $\Delta ffCO_2$ at the observation site. Nuclear installations like power plants or reprocessing plants emit pure $^{14}CO_2$, which can contaminate the $^{14}CO_2$ samples. Moreover, the nuclear weapons tests in the mid of the last century have led to a steep "bomb-peak" in the atmospheric $\Delta^{14}CO_2$ signature (see Fig. 1.4). By ongoing CO_2 exchange with the terrestrial biosphere and the ocean, this atmospheric $\Delta^{14}CO_2$ peak levelled off in the decades after the nuclear test ban treaty in 1963. Thus, CO_2 from decomposing organic material is associated with on average slightly higher $\Delta^{14}CO_2$ signatures compared to current atmospheric values. Consequently, heterotrophic respiration of the biosphere can also lead to a masking of $\Delta ffCO_2$ if this is not corrected for. Chapter 3 describes the challenges in estimating ^{14}C-based $\Delta ffCO_2$ concentrations in more detail and gives an estimate for the overall uncertainty of the $\Delta ffCO_2$ estimates, which is needed for their application in inverse models.

Unfortunately, $^{14}CO_2$ cannot be measured remotely nor continuously with the needed precision to estimate $\Delta ffCO_2$ concentrations. Therefore, air samples for $^{14}CO_2$ analyses must be collected in-situ. This makes $^{14}CO_2$ observations labor-intensive and expensive, so that they have a very low spatial and temporal resolution. That's why continuously measured trace gases like carbon monoxide (CO), which is co-emitted with CO_2 during incomplete combustion of fossil fuels, has been used as an alternative tracer for $ffCO_2$ emissions.

1.3.4 CO as tracer for ffCO$_2$ emissions

Many studies have used the continuously measured ΔCO excess at a polluted site compared to a background to determine ΔCO-based $\Delta ffCO_2$ estimates with a high temporal resolution (e.g., Gamnitzer et al., 2006; Turnbull et al., 2006; Levin and Karstens, 2007; Van Der Laan et al., 2010; Vogel et al., 2010). For this, the continuous ΔCO concentrations are divided by

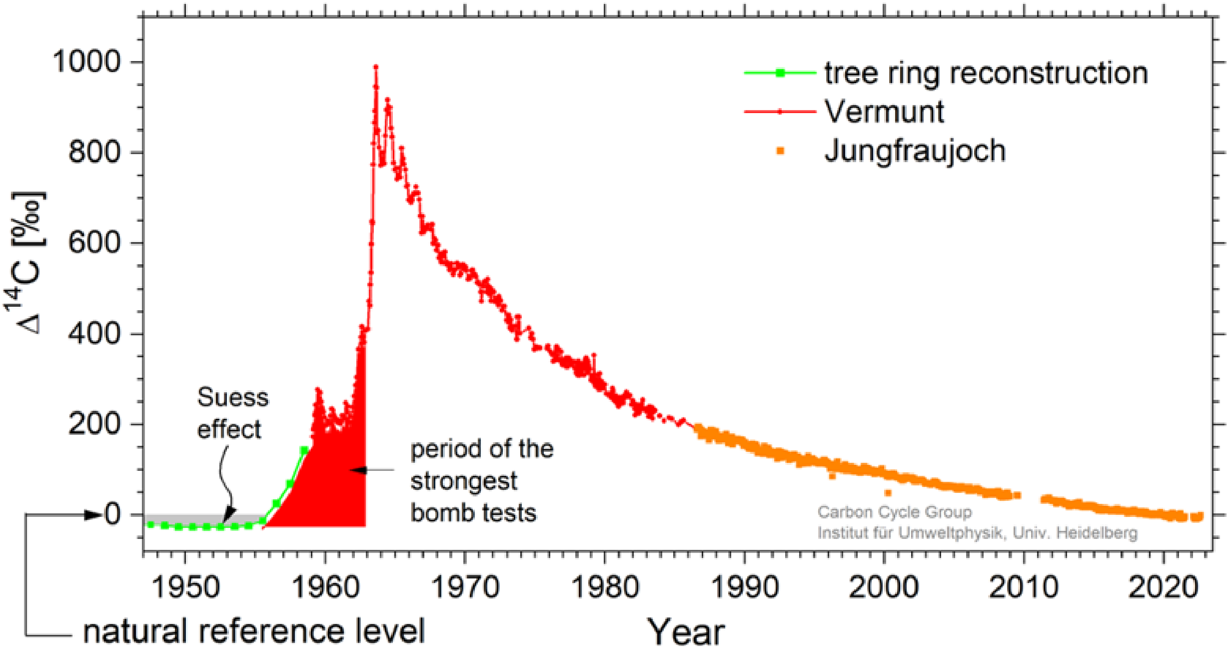

Figure 1.4 Development of the tropospheric $\Delta^{14}CO_2$ level. The figure is modified from Levin et al. (2022) and can be found online at `https://www.iup.uni-heidelberg.de/de/research/kk` (last access: 18. April, 2023).

mean ΔCO/ΔffCO$_2$ ratios, which are representative for the observation site and the averaging period. However, this requires an accurate determination of the ΔCO/ΔffCO$_2$ ratios. In fact, the CO/ffCO$_2$ emission ratios might differ between (and also within) the various emission sectors as they depend on the combustion efficiency and e.g., applied end-of-pipe treatments. Furthermore, these ratios might change with time due to technological progress (Rosendahl, 2022). This can lead to a high variability in the ΔCO/ΔffCO$_2$ ratios at the observation site, depending on its spatiotemporal footprint.

A fully observational approach to estimate the ΔCO/ΔffCO$_2$ ratios at the observation site is using ^{14}C-based ΔffCO$_2$ observations from air samples (e.g., Vogel et al., 2010). The advantage of this observational approach is that it intrinsically includes the non-fossil CO contributions from CO sources like biomass burning or oxidation of methane and volatile organic compounds and atmospheric CO sinks like the oxidation by OH (Folberth et al., 2006). However, as CO affects air pollution, and thus human health, there are many urban stations with CO – but without $^{14}CO_2$ – measurements (Pinty et al., 2019). For such sites, modelled ΔCO/ΔffCO$_2$ ratios based on bottom-up CO and ffCO$_2$ emissions could be used to determine continuous ΔCO-based ΔffCO$_2$ records. This would dramatically increase the number of sites, for which ΔCO-based ΔffCO_2 concentrations could be estimated. However, this approach urgently requires a reliable transport model and accurate bottom-up CO/ffCO_2 emission ratios, as a bias in the modelled ΔCO/ΔffCO_2 ratios would directly translate into a bias in the ΔCO-based ΔffCO_2 estimates, and thus in the top-down ffCO_2 emissions.

In this thesis, separate ΔffCO_2 inversion runs are performed with (1) discrete ^{14}C-based ΔffCO_2 observations from flask samples, and (2) a continuous ΔCO-based ΔffCO_2 record. Chapter 5 describes how this ΔCO-based ΔffCO_2 record has been constructed from flask-based ΔCO/ΔffCO_2 ratios. It further gives an estimate of its uncertainty, which is caused by the uncertainties of the ambient air and background measurements, as well as the spatiotemporal variability of the ratios at the observation site. Moreover, it compares the flask-based ΔCO/ΔffCO_2 ratios with modelled ratios to investigate the potential of using bottom-up emission ratios to deduce ΔCO-based ΔffCO_2 estimates.

1.4 Rhine Valley inversion

To my knowledge, ΔffCO_2 inversions have so far only been used to estimate national scale ffCO_2 emissions (see Graven et al., 2018). In this thesis, I use ^{14}C- and ΔCO-based ΔffCO_2 observations from the Heidelberg observation site to estimate the ffCO_2 emissions in this urban region. Thereby, the overarching goal is to investigate the potential of ^{14}C- vs. ΔCO-based ΔffCO_2 observations to estimate the amplitude and the phasing of the seasonal cycle of the ffCO_2 emissions in the main footprint of the Heidelberg observation site. For this, the Bayesian CarboScope inversion framework developed by Rödenbeck et al. (2003) is adapted for the urban Rhine Valley (see Ch. 6).

Before describing the CarboScope inversion system in more detail, I first want to give a few examples why it is important to independently estimate ffCO_2 emissions in urban regions.

1.4.1 Why to study ffCO_2 emissions in urban regions

First, about 70% of the global ffCO_2 emissions are released by cities (Duren and Miller, 2012). Consequently, emission reduction strategies would be most effective in urban areas. Indeed, there are already several urban networks like, e.g., the C40 cities, which advance in developing emission reduction strategies to mitigate global warming (see `https://www.c40.org/`). For this, high-resolution bottom-up statistics could help to identify the most important CO_2 emitters in a city and to take appropriate measures to reduce them. For such cities, top-down ffCO_2 emission estimates may provide an independent validation of the city-scale emissions. Moreover, continuing top-down estimates could be used to independently monitor the emission reductions in the cities.

Second, a verification of the bottom-up estimates on urban scales might also be helpful for identifying (and correcting) wrong emission factors or inappropriate spatial proxies, which are used to disaggregate the national total emissions to the urban grid cells. Moreover, since city emissions cause large ΔffCO_2 signals, they might be predestined for an observation-based evaluation of the temporal profiles used in the emission inventories. As mentioned before, accurate temporal profiles in the bottom-up ffCO_2 emissions are essential, e.g., when they are used in a CO_2 inversion, which evaluates the seasonal cycle of the CO_2 fluxes from the terrestrial biosphere.

Third, accurate bottom-up ffCO_2 emission estimates from urban regions are also needed for comparison with satellite retrievals. Satellite remote sensing is a powerful tool for getting (column) CO_2 observations with global coverage and high spatial resolution. Thereby, approaches have been developed to deduce the CO_2 emissions from intense industrial areas or individual power plants by monitoring their plumes with satellites (Reuter et al., 2019; Zheng et al., 2020; Chevallier et al., 2022). However, as these satellite observations cannot discriminate between fossil and non-fossil CO_2 contributions, the monitored CO_2 plumes must be of fossil origin so that the satellite-based CO_2 emission estimates can be compared with bottom-up ffCO_2 emissions. Therefore, Konovalov et al. (2016) used satellite column observations of NO_2 and CO, which are co-emitted with ffCO_2, to deduce top-down NO_x and CO emissions. By applying bottom-up NO_x/ffCO_2 and CO/ffCO_2 emission factors, they could derive ffCO_2 emission estimates for large industrial regions in Europe.

Overall, this illustrates the need for an independent top-down validation of bottom-up ffCO_2 emissions in urban regions. However, the complex emissions patterns in urban areas makes it challenging to estimate urban ffCO_2 emissions accurately. Indeed, the Rhine Valley inversion system must account for the very heterogeneously distributed ffCO_2 sources in the vicinity of the Heidelberg observation site. Therefore, a high-resolution transport model and a special treatment of the nearby point source emissions is needed.

1.4.2 Modelling of nearby point source emissions

In this thesis, I use the Stochastic Time-Inverted Lagrangian Transport model (STILT, Lin et al., 2003; Nehrkorn et al., 2010) driven with 2 km x 2 km resolved meteorological fields generated with the Weather Research and Forecasting model (WRF) to calculate hourly footprints, i.e. so-called surface source influences (SSI), for the Heidelberg observation site. These footprints are then mapped with 1 km x 1 km resolved ffCO$_2$ emissions from the Netherlands Organization for Applied Scientific Research (TNO) emission inventory (Dellaert et al., 2019; Denier van der Gon et al., 2019) to model ΔffCO$_2$ concentrations for Heidelberg.

Commonly, point source emissions are released from the surface in STILT. This means that their effective emission heights of a few hundred meters above the ground are fully ignored. In fact, this can lead to large overestimations in the near-surface ΔffCO$_2$ concentrations (Brunner et al., 2019). Consequently, the incorrect representation of nearby point sources in the inversion system will lead to biases in the top-down emissions. Therefore, I developed in this thesis an alternative STILT approach, the volume source influence (VSI) approach, which considers the effective emission heights of the point sources in the Rhine Valley domain (see Fig. 1.3). Both, the standard SSI and the new VSI approach are described in detail in Ch. 2, which also assesses the performance of the VSI approach.

1.4.3 CarboScope inversion framework

The special settings of the high-resolution Rhine Valley inversion system are detailed in Ch. 6. Therefore, the following section gives a more general description of the CarboScope inversion framework.

The ΔffCO$_2$ inversion tries to find the ffCO$_2$ flux realization that leads to the best agreement between the observed and the modelled ΔffCO$_2$ concentrations $\mathrm{C_{obs}}$ and $\mathrm{C_{mod}}$, respectively, and thus minimizes the model-data mismatch m=$\mathrm{C_{obs}}$-$\mathrm{C_{mod}}$. In case of linear regressions, the following least-squares cost function J_{LS} is minimized:

$$J_{\mathrm{LS}} = \frac{1}{2} m^T Q_m^{-1} m \tag{1.2}$$

The covariance matrix Q_m describes the uncertainties of the observations and the transport model. However, as atmospheric transport inversions are typically under-determined, additional Bayesian a-priori information is needed. In the CarboScope setup, a flux model is used to describe the added a-priori information. For this, the flux vector f is written in the form of a fixed "best-guess" a-priori estimate f_{fix} and a vector p with adjustable parameters:

$$f = f_{\mathrm{fix}} + Fp \tag{1.3}$$

The matrix F contains the information about the uncertainty of the a-priori fluxes and describes the spatiotemporal flux patterns. By construction of the a-priori parameters p_{pri}, i.e. $\langle p_{\mathrm{pri}} \rangle = 0$; $\langle p_{\mathrm{pri}} p_{\mathrm{pri}}^{\mathrm{T}} \rangle = 1/\mu$, this leads to the following cost function:

$$J = J_{\mathrm{LS}} + \frac{\mu}{2} p^{\mathrm{T}} p = \frac{1}{2} m^T Q_m^{-1} m + \frac{\mu}{2} p^{\mathrm{T}} p \tag{1.4}$$

The first term of J is the least-squares cost function and the second term of J is the Bayesian a-priori constraint. By definition, the parameter μ describes the ratio between a-priori and data constraint and can be used to scale the a-priori impact. For example, for $\mu = 0$ there is no a-priori constraint, since $J = J_{\mathrm{LS}}$. The Bayesian inversion algorithm then seeks those a-posteriori parameters p_{post} that minimize the cost function J. For this, it uses a conjugate gradient algorithm (see Rödenbeck, 2005).

1.5 Research questions and outline of this thesis

The main goal of this thesis is to answer the following question:

What is the potential of ^{14}C-based vs. ΔCO-based ΔffCO$_2$ observations to estimate the seasonal cycle of the ffCO$_2$ emissions in the Rhine Valley metropolitan region?

Thereby, I want to explore which observational information is more beneficial in this urban inversion system: discrete ^{14}C-based ΔffCO$_2$ observations with small uncertainties or continuous ΔCO-based ΔffCO$_2$ estimates with larger uncertainties. This main research question is addressed in Ch. 6. However, in order to be able to properly address this main research question, the following questions must first be answered:

1. How to represent elevated point source emissions in STILT?
2. How to calculate bias-free ^{14}C-based ΔffCO$_2$ estimates in Central Europe?
3. How to collect flask samples for ^{14}C analysis?
4. How to determine continuous ΔCO-based ΔffCO$_2$ estimates and their uncertainties?

These leading questions are discussed in the chapters Ch. 2 to Ch. 5. The following Sect. 1.5.1 gives a detailed overview of this thesis.

1.5.1 Overview of the manuscripts

This thesis is written in a cumulative form. This means that each of the result chapters Ch. 2 to Ch. 6 is based on a manuscript. The manuscripts in Ch. 2 and Ch. 4 are already published, and the manuscript in Ch. 3 is accepted for publication. The manuscripts in Ch. 5 and Ch. 6 are still being submitted. The appendix of this thesis shows a description of my contribution to the individual manuscripts. Chapter 7 provides an overall discussion of the results of this thesis, and a conclusion can be found in Ch. 8. Table 1.1 summarizes the research questions of the individual manuscripts. They are explained in more detail in the following.

Chapter 2: Effects of point source emission heights in WRF–STILT: a step towards exploiting nocturnal observations in models

As mentioned above, the Heidelberg observation site's proximity to large point sources requires the development of an alternative so-called volume source influence (VSI) approach, which considers the effective emission heights of point sources in STILT. This is needed to avoid large overestimations in the modelled ΔffCO_2 concentrations in Heidelberg during situations with suppressed atmospheric mixing, and thus to prevent biases in the top-down ffCO_2 emission estimates. Chapter 2 introduces this new STILT-VSI approach and describes its performance by comparing the modelled ΔffCO_2 concentrations with ^{14}C-based ΔffCO_2 observations. Moreover, it investigates up to which distance from the observation site the point sources should be represented with this VSI approach.

Chapter 3: Estimating regional fossil-fuel CO_2 concentrations from $^{14}CO_2$ observations: Challenges and uncertainties

The methodological Ch. 3 re-visits the challenges in estimating ^{14}C-based ΔffCO_2 observations. It carefully examines the potential biases and uncertainties of ^{14}C-based ΔffCO_2 estimates, so that they can be used in a ΔffCO_2 model inversion. In particular, Ch. 3 assesses the ΔffCO_2 masking effects of nuclear contaminations and biosphere respiration, and evaluates the suitability of a marine $\Delta^{14}CO_2$ background (see Fig. 1.3) for observation sites in Central Europe. It further compares the mean ΔffCO_2 signals at remote ICOS sites with their uncertainties.

Chapter 4: A dedicated flask sampling strategy developed for Integrated Carbon Observation System (ICOS) stations based on CO_2 and CO measurements and Stochastic Time-Inverted Lagrangian Transport (STILT) footprint modelling

After the two methodological manuscripts on the representation of point sources in STILT and the estimation of ^{14}C-based $\Delta ffCO_2$ observations, Ch. 4 shows the performance of the ICOS flask sampler. This sampler was constructed at the ICOS FCL and has been installed at the ICOS class-1 stations. The sampler is programmed to collect flask samples whose concentration corresponds to the hourly mean value of the ambient air concentration. The advantage of sampling hourly means is that they are less influenced by sub-hourly variabilities in the ambient air concentrations, which cannot be represented by atmospheric transport models. Moreover, the flask data are easier to compare with in-situ measurements. I have tested the sampler intensively at the ICOS pilot site Heidelberg from 2018 onwards. That's why there are many ^{14}C flask analyses from Heidelberg between 2019 and 2020. Those ^{14}C flasks form the observational basis for this thesis.

Chapter 4 also describes a dedicated flask sampling strategy for the ICOS sites, which provides routinely flasks for quality control of the continuously measured in-situ data and additional flask samples for ^{14}C analyses. The results of the previous Ch. 3 illustrate that ^{14}C flasks should be collected during situations with pronounced $\Delta ffCO_2$ signals to reduce their relative uncertainty. Therefore, Ch. 4 also shows how CO can help to sample $\Delta ffCO_2$ signals at remote ICOS sites.

Chapter 5: Uncertainty of continuous ΔCO-based $\Delta ffCO_2$ estimates derived from ^{14}C flask and bottom-up $\Delta CO/\Delta ffCO_2$ ratios

In Ch. 5 the large pool of ^{14}C flasks from Heidelberg is used to calculate $\Delta CO/\Delta ffCO_2$ ratios from which a continuous ΔCO-based $\Delta ffCO_2$ record is constructed. By comparing the ΔCO-based $\Delta ffCO_2$ with the ^{14}C-based $\Delta ffCO_2$ of the flask samples, a reliable estimate for the uncertainty of the ΔCO-based $\Delta ffCO_2$ is determined. This is needed for an application of the ΔCO-based $\Delta ffCO_2$ estimates in an inversion framework. Furthermore, Ch. 5 investigates whether inventory-based $\Delta CO/\Delta ffCO_2$ ratios could be used instead of ^{14}C-based ratios to calculate the ΔCO-based $\Delta ffCO_2$ record.

Chapter 6: Potential of ^{14}C-based versus ΔCO-based ΔffCO_2 observations to estimate urban fossil fuel CO_2 (ffCO_2) emissions

The various findings from Ch. 2 to Ch. 5 form the basis for Ch. 6, which finally shows the results of the Rhine Valley inversion and addresses the main research question of this thesis. It investigates whether the ^{14}C- and ΔCO-based ΔffCO_2 observations from Heidelberg can be used to estimate the seasonal cycle of the ffCO_2 emissions in the Upper Rhine Valley. Furthermore, it analyses whether these observational data are suitable for validating the seasonal cycle of the bottom-up ffCO_2 emissions in the main footprint of Heidelberg. As mentioned above, this is crucial for using bottom-up ffCO_2 emissions in CO_2 inversions to estimate natural CO_2 fluxes, and thus improving the understanding of the carbon cycle.

Table 1.1 Specific research questions of this work and where they are addressed.

Specific research questions	**Manuscript/publication**
1. How can elevated point source emissions be represented in STILT? 2. What is the performance of the volume source influence (VSI) approach, which considers the effective emission heights of point sources in STILT? 3. Up to which distance from the observation site should the point source emissions be treated with the VSI approach?	**Chapter 2**: Effects of point source emission heights in WRF–STILT: a step towards exploiting nocturnal observations in models (DOI: 10.5194/gmd-15-5391-2022)
1. What are the challenges in estimating ΔffCO_2 concentrations from $^{14}CO_2$ observations? 2. What is an appropriate marine $\Delta 14CO_2$ background for observation sites in Central Europe? 3. What are potential ΔffCO_2 biases and uncertainties induced by nuclear contamination and biosphere respiration? 4. What are the ΔffCO_2 signals at the ICOS sites and how large are their uncertainties?	**Chapter 3**: Estimating regional fossil-fuel CO_2 concentrations from $^{14}CO_2$ observations: Challenges and uncertainties (DOI: 10.1098/rsta.2022.0203)
1. What is a dedicated flask sampling strategy for ICOS sites? 2. How suitable is the ICOS flask sampler for detecting CO_2 biases between flask and in-situ data? 3. How can in-situ CO observations help to select flasks for $^{14}CO_2$ analysis?	**Chapter 4**: A dedicated flask sampling strategy developed for Integrated Carbon Observation System (ICOS) stations based on CO_2 and CO measurements and Stochastic Time-Inverted Lagrangian Transport (STILT) footprint modelling (DOI: 10.5194/acp-20-11161-2020)

1. How can flask ΔCO/ΔffCO$_2$ ratios be used to construct a continuous, bias-free ΔCO-based ΔffCO$_2$ record? 2. How large is the uncertainty of this ΔCO-based ΔffCO$_2$ record at an urban and at a remote site? 3. Can inventory-based ΔCO/ΔffCO$_2$ ratios be used to estimate the continuous ΔCO-based ΔffCO$_2$ record?	**Chapter 5**: Uncertainty of continuous ΔCO-based ΔffCO$_2$ estimates derived from ^{14}C flask and bottom-up ΔCO/ΔffCO$_2$ ratios
1. What is the potential of discrete ^{14}C-based ΔffCO$_2$ estimates from flasks vs. continuous ΔCO-based ΔffCO$_2$ observations to estimate the seasonal cycle of ffCO$_2$ emissions in the urban Rhine Valley? 2. Can the ^{14}C- and ΔCO-based ΔffCO$_2$ observations from Heidelberg be used to detect the COVID-19 signal in 2020 and to validate the seasonal cycle of the bottom-up ffCO$_2$ emissions in the main footprint of Heidelberg? 3. How can the impact of an inadequate point source modelling on the inversion results be reduced?	**Chapter 6**: Potential of ^{14}C-based versus ΔCO-based ΔffCO$_2$ observations to estimate urban fossil fuel CO$_2$ (ffCO$_2$) emissions

CHAPTER 2

Effects of point source emission heights in WRF–STILT: a step towards exploiting nocturnal observations in models

This chapter is based on:

Maier, F., Gerbig, C., Levin, I., Super, I., Marshall, J., and Hammer, S.: Effects of point source emission heights in WRF–STILT: a step towards exploiting nocturnal observations in models, Geosci. Model Dev., 15, 5391–5406, https://doi.org/10.5194/gmd-15-5391-2022, 2022.

Geosci. Model Dev., 15, 5391–5406, 2022
https://doi.org/10.5194/gmd-15-5391-2022

Geoscientific
Model Development
Open Access

Effects of point source emission heights in WRF–STILT: a step towards exploiting nocturnal observations in models

Fabian Maier[1,2], **Christoph Gerbig**[3], **Ingeborg Levin**[1], **Ingrid Super**[4], **Julia Marshall**[5], **and Samuel Hammer**[1,2]

[1]Institut für Umweltphysik, Heidelberg University, INF 229, 69120 Heidelberg, Germany
[2]ICOS Central Radiocarbon Laboratory, Heidelberg University, Berliner Straße 53, 69120 Heidelberg, Germany
[3]Department Biogeochemical Systems, Max Planck Institute for Biogeochemistry,
Hans-Knöll-Straße 10, 07745 Jena, Germany
[4]Department of Climate, Air and Sustainability, TNO, P.O. Box 80015, 3508 TA Utrecht, the Netherlands
[5]Deutsches Zentrum für Luft- und Raumfahrt (DLR), Institut für Physik der Atmosphäre, 82234 Oberpfaffenhofen, Germany

Correspondence: Fabian Maier (fabian.maier@iup.uni-heidelberg.de)

Received: 19 November 2021 – Discussion started: 10 December 2021
Revised: 25 May 2022 – Accepted: 20 June 2022 – Published: 14 July 2022

Abstract. An appropriate representation of point source emissions in atmospheric transport models is very challenging. In the Stochastic Time-Inverted Lagrangian Transport model (STILT), all point source emissions are typically released from the surface, meaning that the actual emission stack height plus subsequent plume rise is not considered. This can lead to erroneous predictions of trace gas concentrations, especially during nighttime when vertical atmospheric mixing is minimal. In this study we use two Weather Research and Forecasting (WRF)–STILT model approaches to simulate fossil fuel CO_2 (ffCO_2) concentrations: (1) the standard "surface source influence (SSI)" approach and (2) an alternative "volume source influence (VSI)" approach where nearby point sources release CO_2 according to their effective emission height profiles. The comparison with ^{14}C-based measured ffCO_2 data from 2-week integrated afternoon and nighttime samples collected at Heidelberg, 30 m above ground level shows that the root-mean-square deviation (RMSD) between modelled and measured ffCO_2 is indeed almost twice as high during the night (RMSD = 6.3 ppm) compared to the afternoon (RMSD = 3.7 ppm) when using the standard SSI approach. In contrast, the VSI approach leads to a much better performance at nighttime (RMSD = 3.4 ppm), which is similar to its performance during afternoon (RMSD = 3.7 ppm). Representing nearby point source emissions with the VSI approach could thus be a first step towards exploiting nocturnal observations in STILT. The ability to use nighttime observations in atmospheric inversions would dramatically increase the observational data and allow for the investigation of different source mixtures or diurnal cycles. To further investigate the differences between these two approaches, we conducted a model experiment in which we simulated the ffCO_2 contributions from 12 artificial power plants with typical annual emissions of 1 million tonnes of CO_2 and with distances between 5 and 200 km from the Heidelberg observation site. We find that such a power plant must be more than 50 km away from the observation site in order for the mean modelled ffCO_2 concentration difference between the SSI and VSI approach to fall below 0.1 ppm during situations with low mixing heights smaller than 500 m.

1 Introduction

The Integrated Carbon Observation System (ICOS) research infrastructure was established to set up a dense European monitoring network of high-precision greenhouse gas measurements of concentrations and fluxes, therewith providing the observational basis to better understand the European carbon budget (Heiskanen et al., 2022). In Europe, one major challenge is the quantification of anthropogenic fossil fuel CO_2 (ffCO_2) emissions, but it is similarly important to understand "their redistribution among the atmosphere, ocean and terrestrial biosphere in a changing climate" (Friedlingstein et al., 2020). If the share of ffCO_2 in the total conti-

Published by Copernicus Publications on behalf of the European Geosciences Union.

nental signal is modelled correctly, the remaining biogenic share can be used as a top-down constraint on the continental biospheric CO_2 fluxes (Basu et al., 2016). In this study, we use the term $ffCO_2$ to refer to not only CO_2 emissions resulting from the combustion of fossil fuels but also fossil CO_2 emissions that occur during cement production. A well-established approach to determine the regional $ffCO_2$ component in the observed atmospheric CO_2 concentration is via $\Delta^{14}CO_2$ measurements (e.g. Levin et al., 2003). Since CO_2 emissions from fossil fuel combustion are devoid of ^{14}C (the half-life of ^{14}C is 5700 years; Currie, 2004), the atmospheric $\Delta^{14}CO_2$ depletion measured in polluted areas relative to clean background air allows the regional (or "recently added") $ffCO_2$ surplus to be determined. Many studies have used this approach at various urban and rural sites (e.g. Levin et al., 2008; Turnbull et al., 2015; Wenger et al., 2019). Some 2-week integrated air samples and hourly flask samples are collected at ICOS class-1 stations for ^{14}C analysis to estimate regional $ffCO_2$ concentrations (Levin et al., 2020), thus helping to separate biospheric from fossil CO_2 fluxes, e.g. in an inverse modelling framework (Wang et al., 2018; Basu et al., 2020).

Estimating $ffCO_2$ fluxes from atmospheric CO_2 and ^{14}C measurements within an inverse modelling framework requires a correct representation of the atmospheric transport and mixing processes. Geels et al. (2007) evaluated five different Eulerian atmospheric transport models with continuous CO_2 observations from various European sites, as well as aircraft flask samples, and showed that the model predictions are much better in the afternoon hours during well-mixed atmospheric conditions than during stable nocturnal conditions. That is why they recommend to only use afternoon observations from low-altitude sites to constrain CO_2 sources or sinks. In addition, Lagrangian transport models like the Stochastic Time-Inverted Lagrangian Transport model (STILT) are very sensitive to the representation of the planetary boundary layer height (PBLH). STILT determines the sensitivity of atmospheric trace gas mixing ratios at an observation site to upwind surface fluxes (Lin et al., 2003). This so-called footprint defines the catchment area of the observation site, and in STILT it is by default sensitive to emissions from the bottom half of the planetary boundary layer (PBL). In STILT it is assumed that surface emissions are instantaneously mixed by turbulence in the bottom half of the PBL within one model time step. Gerbig et al. (2008) compared radiosonde-derived mixing heights with mixing heights derived from the European Centre for Medium-Range Weather Forecasts (ECMWF) meteorological data for 2 European summer months in 2005 and used STILT to assess the propagated uncertainty in the CO_2 mole fraction. During daytime, they found no significant relative bias between radiosonde and ECMWF-derived mixing heights, but they found a relative standard deviation of about 40 % for the difference between both estimates. However, nighttime situations showed a relative bias of more than 50 % with a relative standard deviation of almost 100 %, meaning that the ECMWF-derived nocturnal mixing heights are on average larger compared to the radiosonde estimates. The authors showed that the 40 % uncertainty in daytime mixing heights already resulted in CO_2 mole fraction uncertainties of 3 ppm on average during the 2 summer months studied, which corresponds to about 30 % of the simulated biogenic signals.

There is an additional problem in a time-reversed Lagrangian particle dispersion model (LPDM) like STILT, namely the incorrect representation of point source emissions. First, the calculated footprints are usually stored on a horizontal grid with limited resolution, which may lead to false attribution of point source emissions in cases where a higher-resolution footprint may actually have missed the point source. Since STILT dynamically coarsens the footprint resolution with distance to the receptor location, this problem may be more important for distant point sources. However, false attribution may also happen for nearby point sources due to a limited and inappropriate near-field footprint resolution. Second, point source emissions are often released from chimneys, whose stack height can be above the bottom half of the PBL during the night depending on the meteorological situation. However, in STILT the default is that all emissions, including point sources, are released from the ground and mixed into the bottom half of the PBL. Under stable conditions this can result in large overestimations of concentrations near the surface and large underestimations of concentrations above the PBL.

In central Europe, about 45 % of the $ffCO_2$ emissions are released from point sources (Super et al., 2020), underlining the potential impact of these elevated emissions on downwind measurement sites. Figure 1 shows the distributions of $ffCO_2$ point sources in Europe and illustrates how close some of the ICOS stations are located to these big $ffCO_2$ point source emitters. An attempt was made to avoid station locations with strong emissions in the vicinity when designing the ICOS atmosphere station network. Nevertheless, there are eight ICOS class-1 or class-2 stations for which the emissions of the energy and industrial $ffCO_2$ point sources within a 50 km × 50 km box around the station sum up to more than 1 million tonnes of CO_2 per year. This calls for an appropriate representation of point source emissions when modelling $ffCO_2$ concentrations at these ICOS stations.

Together, the inadequate representation of atmospheric transport processes during stable (nighttime) conditions and the incorrect release of point source emissions at ground level restrict the use of observational data in STILT inversions to daytime situations only. Atmospheric transport processes are more reliably modelled for daytime situations and the exact representation of the point source emission heights is less important when atmospheric mixing is strong (Brunner et al., 2019). However, using nighttime observations would have several advantages. First, they contain more data. Usually (e.g. at ICOS stations) continuous greenhouse gas mea-

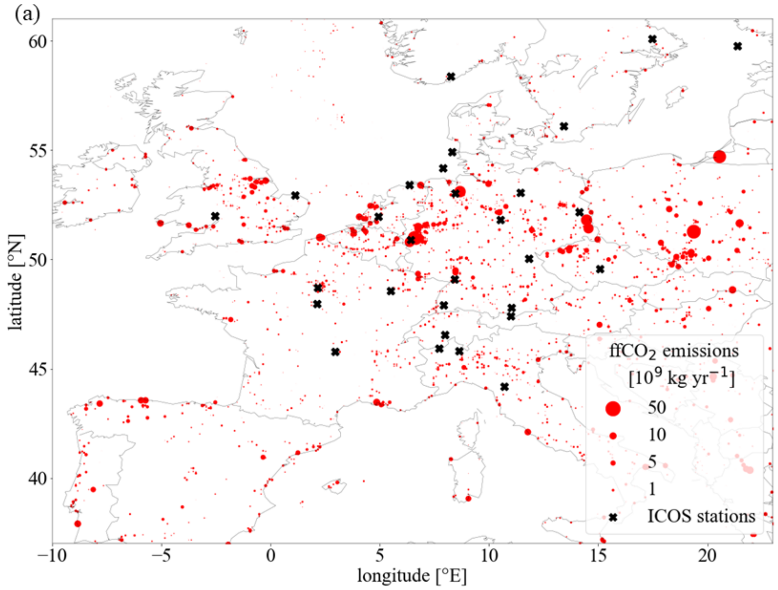

(b)

ICOS atmosphere station	point source ffCO$_2$ emissions [10^9 kg yr^{-1}]
Jülich	92.8
Steinkimmen	34.8
Karlsruhe	7.9
Saclay	5.6
Schauinsland	1.4
Ispra	1.2
Cabauw	1.2
Torfhaus	1.2

Figure 1. (a) European ffCO$_2$ point source emissions according to Super et al. (2020, red dots) and the locations of ICOS atmosphere class-1 and class-2 stations (black crosses). **(b)** ICOS atmosphere stations with a total of more than 1 million tonnes of ffCO$_2$ emissions from point sources within a 50 km × 50 km box around the station.

surements are available at all hours of the day and night. A restriction to the afternoon hours means that about 75 % of the available observations are not used. Second, they provide a different field of view. The average daytime footprint differs significantly from the average nighttime footprint. For tall towers (above the nocturnal PBL), the nighttime footprint is usually larger and more sensitive to distant sources, whereas the daytime (convective) footprint is often dominated by more local sources. For observation sites with sampling heights within the nocturnal PBL this may be reversed. Third, they provide different source mixtures. Nighttime (morning and evening) measurements sample different source mixtures than afternoon measurements. As an example, diffuse sources such as heating or traffic are more dominant during nighttime and the morning or evening rush hours, respectively. Finally, they allow for the analysis of diurnal cycles. Including nighttime observations could help to constrain diurnal emission patterns. For instance, Super et al. (2021) showed that a correct representation of temporal emission profiles is essential for inverse modelling in urban areas. An important goal for the future should therefore be to also exploit nighttime observations in modelling frameworks. However, the important prerequisite for this is that atmospheric transport models are able to realistically reproduce nighttime stable boundary layers and their erosion in the morning hours.

In this study, we want to focus on point source emissions and show the improvement in the agreement between model and observations when using a more realistic representation of point source emission heights. Instead of using the classical approach in STILT, where footprints describe the surface influence on the bottom half of the PBL (hereafter called "surface source influence" approach), we introduce the so-called "volume source influence" approach that allows point source emissions to be better represented in STILT. In the volume source influence (VSI) approach, point source emissions are distributed to pre-defined height intervals in the catchment area of the observation site. If the height profile of a point source emission is known, its contribution at the observation site can then be estimated with this VSI approach. In the following, we first evaluate the VSI approach against the standard surface source influence (SSI) approach (Sect. 3.1). For this, we model the ffCO$_2$ concentrations for our study site, Heidelberg, from July 2018 to June 2020 by applying (a) the SSI approach and (b) the VSI approach to the point source emissions in the surroundings of Heidelberg. We then compare modelled ffCO$_2$ concentrations to ffCO$_2$ estimates based on 2-week integrated daytime and nighttime $\Delta^{14}CO_2$ data from samples collected in Heidelberg during these 2 years. In a second step, we investigate how the surface and volume source influence approaches behave for point sources at increasing distances from the observation site during different atmospheric conditions (Sect. 3.2). For this, we placed 12 artificial ("pseudo") power plants at distances of 5 to 200 km from our study site and modelled their mean contribution during different atmospheric conditions.

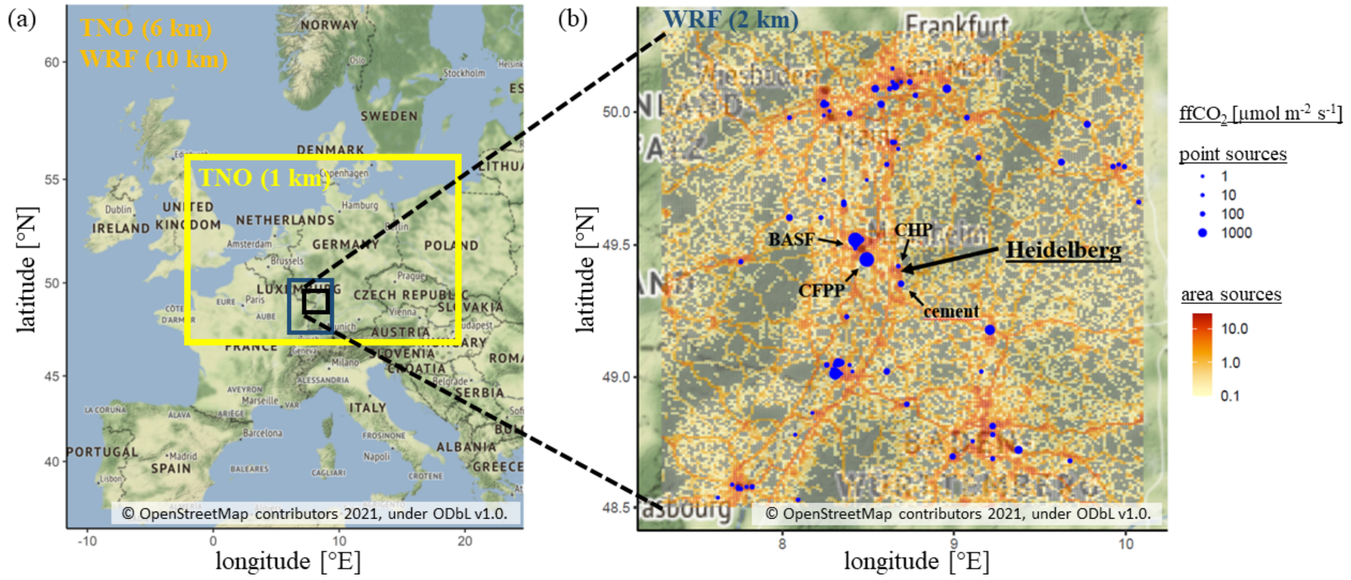

Figure 2. (a) Model domain and spatial resolution (in brackets) of nested WRF meteorological fields and TNO emission inventories. In the blue-grey box, TNO has a resolution of about 1 km × 1 km and WRF has a resolution of 2 km × 2 km. Outside the blue-grey box, the WRF resolution is decreased to 10 km × 10 km. Outside the yellow box the TNO inventory has a horizontal resolution of ca. 6 km × 6 km. Panel **(b)** shows a closer view of the Rhine Valley with the TNO area (orange) and point (in blue) source emissions shown (from Super et al., 2020). The observation site Heidelberg and the four closest point sources, i.e. a combined heat and power station (CHP), a cement production facility (cement), a coal-fired power plant (CFPP) and the BASF company in Ludwigshafen, are labelled. The Map tiles are by Stamen Design and used here under CC BY 3.0 (http://maps.stamen.com/terrain/, last access: 4 May 2022). The data are © OpenStreetMap contributors 2021 and distributed under the Open Data Commons Open Database License (ODbL) v1.0.

2 Methods

2.1 Site description

Heidelberg is a medium-sized city with about 160 000 inhabitants located in the Upper Rhine valley in southwestern Germany. It is part of the Rhine–Neckar metropolitan area and includes the heavily industrialised cities of Mannheim (310 000 inhabitants) and Ludwigshafen (170 000 inhabitants) about 15–20 km northwest of Heidelberg. The measurement site is in the northern outskirts of Heidelberg at the Institute of Environmental Physics, which is located on the university campus. There, continuous greenhouse gas measurements and $^{14}CO_2$ sampling are performed with the sample air intake on the roof of the Institute's building about 30 m above the ground. A more detailed description of the Heidelberg measurement site can be found in Hammer (2008). Figure 2 shows the main $ffCO_2$ point sources in the surroundings of Heidelberg. The largest nearby $ffCO_2$ emitters are the coal-fired power plant in Mannheim, the BASF company in Ludwigshafen, a cement production facility (Heidelberg Zement) south of Heidelberg, and a combined heat and power station about 500 m north of the measurement site.

2.2 Model configuration

We use the coupled Weather Research and Forecasting–Stochastic Time-Inverted Lagrangian Transport model (WRF–STILT) to simulate hourly $ffCO_2$ concentrations for our measurement site in Heidelberg. STILT is a well-established particle dispersion model that uses the mean advection scheme from the Hybrid Single-Particle Lagrangian Integrated Trajectory (HYSPLIT) model (Stein et al., 2015) but with a different representation of turbulence. A detailed description of the WRF–STILT model can be found in Nehrkorn et al. (2010). Hourly ERA5 (European ReAnalysis 5) model estimates at 0.25° resolution from the European Centre for Medium-Range Weather Forecasts (ECMWF) are used as input for the WRF model to generate two nested WRF domains. The inner domain covers the Upper Rhine valley with a horizontal resolution of 2 km. The outer domain with a 10 km horizontal resolution includes most of Europe. STILT is driven by these nested WRF fields to calculate hourly back-trajectories for 100 released particles with a maximum backward runtime of 72 h for the Heidelberg observation site. Sensitivity studies with 500 released particles and a maximum backward runtime of 10 d, respectively, showed only minor differences. Thus, we used the mentioned configuration to save computational power for the high-resolution simulations.

Highly resolved $ffCO_2$ emission inventories from the Netherlands Organisation for Applied Scientific Research (TNO) are used to describe the European $ffCO_2$ area and point source emissions separately (Super et al., 2020). The area and point source $ffCO_2$ emissions are again divided into 15 different emission source sectors, each with its own temporal (diurnal, weekly and seasonal) profiles. There are two inventories with different horizontal resolutions available, which we nested for this study. The $ffCO_2$ emissions from Germany and its surroundings are resolved on a horizontal grid of about $1\,\mathrm{km}^2$ ($1/60° \times 1/120°$ longitude × latitude). Emissions from the rest of Europe have a horizontal resolution of $0.1° \times 0.05°$. Moreover, TNO provides source sector-specific vertical height profiles for the point source emissions, which we will use for the VSI approach. In the following we explain the mapping of the $ffCO_2$ emissions to the back-trajectories calculated with WRF–STILT.

2.2.1 Surface source influence (SSI) approach

According to Lin et al. (2003) concentration changes $\Delta C(\mathbf{x}_r, t_r)$ at the observation site at $\mathbf{x}_r$ and at time t_r can be described by

$$\Delta C\left(\mathbf{x}_r, t_r\right) = \int_{t_0}^{t_r} \mathrm{d}t \int_V \mathrm{d}x\,\mathrm{d}y\,\mathrm{d}z\, I\left(\mathbf{x}_r, t_r | \mathbf{x}, t\right) \cdot S(\mathbf{x}, t), \qquad (1)$$

where $S(\mathbf{x}, t)$ describes volume $ffCO_2$ sources (in $\mathrm{ppm\,h^{-1}}$) and $I\left(\mathbf{x}_r, t_r | \mathbf{x}, t\right)$ is the influence function for the observation site (with units of $\mathrm{m^{-3}}$), which links the sources to concentration enhancements. The time and volume integration of the influence function can be realised by tallying the total length of time $\Delta t_{p,m,i,j,k}$ each released particle p spends in a volume element (i, j, k) over time step m (see Lin et al., 2003) and then normalising to the number of released particles N_{tot}:

$$\int_{t_m}^{t_m+\tau} \int_{x_i}^{x_i+\Delta x} \mathrm{d}x \int_{y_j}^{y_j+\Delta y} \mathrm{d}y \int_{z_k}^{z_k+\Delta z} \mathrm{d}z\, I\left(\mathbf{x}_r, t_r | \mathbf{x}, t\right) = \frac{1}{N_{\mathrm{tot}}} \sum_{p=1}^{N_{\mathrm{tot}}} \Delta t_{p,m,i,j,k}. \qquad (2)$$

Moreover, the volume source $S(\mathbf{x}, t)$ can be linked to surface fluxes $F(x, y, t)$ (in units of $\mathrm{mol\,m^{-2}\,s^{-1}}$) by assuming that turbulent mixing is strong enough to completely mix the surface emissions from the ground into an air column with height h within one model time step m. In STILT, this height h is usually set to half of the planetary boundary layer height h_{PBL}: $h = \frac{1}{2} h_{\mathrm{PBL}}$. Using this method, one receives the following equation:

$$S(\mathbf{x}, t) = \begin{cases} \frac{m_{\mathrm{air}}}{h\,\overline{\rho}(x,y,t)} F(x, y, t) & \text{for } z \le h \\ 0 & \text{for } z > h \end{cases}, \qquad (3)$$

with the molar mass of air m_{air} and the average air density $\overline{\rho}(x, y, t)$ below h. Inserting Eqs. (2) and (3) into Eq. (1) yields the contribution from each surface grid cell (i, j) and time step m to the total $ffCO_2$ concentration enhancement $\Delta C\left(\mathbf{x}_r, t_r\right)$ at the observation site:

$$\begin{aligned}\Delta C_{m,i,j}\left(\mathbf{x}_r, t_r\right) &= \frac{m_{\mathrm{air}}}{h\,\overline{\rho}\left(x_i, y_j, t_m\right)} \cdot \frac{1}{N_{\mathrm{tot}}} \sum_{p=1}^{N_{\mathrm{tot}}} \Delta t_{p,m,i,j,k} \cdot F\left(x_i, y_j, t_m\right) \\ &\equiv f\left(\mathbf{x}_r, t_r | x_i, y_j, t_m\right) \cdot F\left(x_i, y_j, t_m\right). \end{aligned} \qquad (4)$$

Here, we call $f\left(\mathbf{x}_r, t_r | x_i, y_j, t_m\right)$ the footprint or surface source influence element, which connects the surface fluxes from grid cell (x_i, y_j) at time t_m to a surface source contribution $\Delta C_{m,i,j}\left(\mathbf{x}_r, t_r\right)$ to the concentration enhancement at the observation site. The sum over all grid cells and times then yields the total concentration enhancement $\Delta C\left(\mathbf{x}_r, t_r\right)$ at the observation site at $\mathbf{x}_r$ and time t_r.

Fasoli et al. (2018) showed that nearby area sources in the so-called hyper near field (i.e. typically within a distance of less than 10 km) of the observation site are often diluted to only a fraction of the PBLH due to insufficient mixing. Since STILT assumes a complete dilution below $\frac{1}{2} h_{\mathrm{PBL}}$ this leads to an underestimation of the contribution of the nearby surface fluxes at the observation site. A solution for this is to calculate an effective mixing depth h' in the hyper near field based on homogeneous turbulence theory (Fasoli et al., 2018; Taylor, 1922), which grows with the distance from the receptor site until it reaches $h' = \frac{1}{2} h_{\mathrm{PBL}}$ outside the hyper near field. The growth of this effective emission height h' depends on the meteorological conditions.

2.2.2 Volume source influence (VSI) approach

Here, we focus on nearby point source emissions, which are released from stack heights of up to several hundred metres. Handling these nearby point source emissions as surface fluxes will cause errors in the concentration estimates. Consider, for example, a sample collection at 30 m a.g.l. and a 200 m coal power plant exhaust at a distance of about 10 km, which is the situation at our measurement site in Heidelberg (see sketch in Fig. 3a). During typical summer nights with nocturnal inversions, the emissions of the power plant can be above the planetary boundary layer and its influence on the Heidelberg measurements would be very small. But in the surface source influence (SSI) approach, where all emissions from this power plant are mixed into the bottom half of the boundary layer, this will result in large $ffCO_2$ overestimations at the measurement site. To tackle this problem and improve the representation of nearby point source emissions in STILT, we use sector-specific height profiles of the point source emissions from TNO and calculate the so-called volume source influence (VSI) for each height interval. Figure 3b shows the discrete TNO emission height profiles for the relevant point source sectors, i.e. those which are present in the 200 km × 200 km area around Heidelberg.

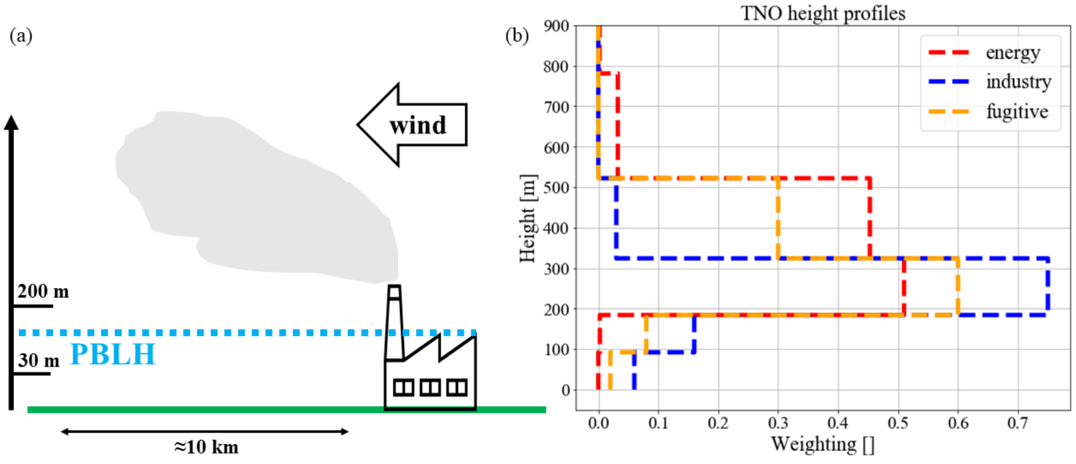

Figure 3. (a) Sketch of a possible nocturnal situation when the planetary boundary layer height (PBLH) lies above the measurement height at 30 m a.g.l. but below the exhaust of a nearby power plant stack. **(b)** TNO height profiles for the public power (energy), industry and fugitive sectors, which were used to calculate the volume influences for the associated point sources. These height profiles are source sector-specific averages, which are representative for Europe.

These effective emission heights take the stack heights of the point sources as well as subsequent plume rise into account (Kuenen et al., 2022); however, these profiles are source-sector-specific averages, which are representative for Europe. We also used the sector-specific diurnal, weekly and seasonal temporal emission profiles from TNO to consider time-varying area and point source emissions.

The point source fluxes $F(x,y,t)$ can be distributed into these individual height intervals κ with the TNO sector-specific and height-dependent weighting factors g_κ so that the volume source $S(\mathbf{x},t)$ can be expressed for each height interval κ by

$$S_\kappa(\mathbf{x},t)=V_{\mathrm{mol}}(\mathbf{x},t)\cdot\frac{F(x,y,t)}{(z_{\kappa+1}-z_\kappa)}\cdot g_\kappa,\quad \text{for } z_\kappa\leq z<z_{\kappa+1}. \qquad (5)$$

For this, we simply assume the molar volume to be constant throughout the different TNO height intervals (from 0 to 1106 m), i.e. $V_{\mathrm{mol}}(x_i,y_j,z_k,t_m)=V_{\mathrm{mol}}(x_i,y_j,t_m)=\frac{m_{\mathrm{air}}}{\tilde\rho(x_i,y_j,t_m)}$, with $\tilde\rho(x_i,y_j,t_m)$ being the average of the air densities at the particle positions in the air column above (i,j) at time step m. We now can calculate the contribution $\Delta C_{\kappa,m,i,j}(\mathbf{x}_r,t_r)$ to the total concentration enhancement at the observation site for each height interval κ by tallying the total length of time $\Delta t_{p,m,i,j,\kappa}$ each released particle p spends in the volume element (i,j,κ) over time step m:

$$\begin{aligned}\Delta C_{\kappa,m,i,j}(\mathbf{x}_r,t_r)=&\frac{m_{\mathrm{air}}}{\tilde\rho(x_i,y_j,t_m)}\\&\cdot\frac{1}{N_{\mathrm{tot}}}\sum_{p=1}^{N_{\mathrm{tot}}}\Delta t_{p,m,i,j,\kappa}\cdot F(x_i,y_j,t_m)\\&\cdot\frac{g_\kappa}{(z_{\kappa+1}-z_\kappa)}\equiv v(\mathbf{x}_r,t_r|x_i,y_j,z_\kappa,t_m)\\&\cdot F(x_i,y_j,t_m)\cdot\frac{g_\kappa}{(z_{\kappa+1}-z_\kappa)}.\end{aligned} \qquad (6)$$

In analogy to the surface source influence, we here call $v(\mathbf{x}_r,t_r|x_i,y_j,z_\kappa,t_m)$ the volume source influence and $\Delta C_{\kappa,m,i,j}(\mathbf{x}_r,t_r)$ the volume source contribution to the total concentration enhancement at the observation site.

In this study we used the volume source influence approach to model the contributions from the TNO point sources within a 200 km × 200 km box around Heidelberg. All point sources that were further away and the area sources were treated with the surface source approach.

2.3 CO_2 sampling for ^{14}C analysis

Since in Heidelberg separate nighttime (from 18:00 to 06:00 UTC) and daytime (from 11:00 to 16:00 UTC) 2-week integrated CO_2 samples for ^{14}C analysis are available, the model performance can be investigated separately for night and day. The CO_2 sampling technique is described in detail by Levin et al. (1980), and the analysis technique is described by Kromer and Münnich (1992). To estimate regional $ffCO_2$ concentration enhancements from the measured $\Delta^{14}CO_2$, the $\Delta^{14}CO_2$ signature of background air must be known. Here we use a harmonic fit curve calculated through the $\Delta^{14}CO_2$ observations from Mace Head on the western coast of Ireland (MHD, 53°20′ N, 9°54′ W, 25 m a.s.l.) and Izaña on Tenerife (IZO, 28°18′ N, 16°29′ W, 2400 m a.s.l.), which are both presumably mainly influenced by clean Atlantic air masses (at Mace Head only clean Atlantic air masses are collected for $\Delta^{14}CO_2$ analysis). We assume this marine background to be most comparable to the model ffCO$_2$ background, which is set to zero at the border of the model domain (Fig. 2a). Footprint analyses also confirmed that Heidelberg is predominantly influenced by westerly winds and air masses with Atlantic origin. However, for situations with easterly winds and continental air masses from Russia, neither the chosen observational background nor the model background may be fully appropriate. The ffCO$_2$ enhancement c_{ff} based on the Heidelberg $\Delta^{14}CO_2$ measurements can then be calculated according to

$$c_{\mathrm{ff}} = c_{\mathrm{CO_2}} \cdot \frac{\Delta^{14}\mathrm{CO}_{2,\mathrm{BG}} - \left(\Delta^{14}\mathrm{CO}_2 - \Delta^{14}\mathrm{CO}_{2,\mathrm{NUC}}\right)}{\Delta^{14}\mathrm{CO}_{2,\mathrm{BG}} + 1000\,‰}, \quad (7)$$

with $c_{\mathrm{CO_2}}$ being the average CO$_2$ concentration in Heidelberg during the 2-week integrated sampling period and $\Delta^{14}\mathrm{CO}_{2,\mathrm{BG}}$ being the $\Delta^{14}CO_2$ signature of background air. The $\Delta^{14}\mathrm{CO}_{2,\mathrm{NUC}}$ term describes the contributions from $^{14}CO_2$ emissions from nuclear facilities and is modelled with the volume source influence approach by assuming that all nuclear $^{14}CO_2$ emissions are released within a 20 m height interval above a typical stack height of 120 m. In order to avoid interference with our results, we used the VSI approach to calculate the nuclear corrections regardless of whether we later use the VSI or SSI approach for the comparison between modelled and observed ffCO$_2$. To calculate the nuclear corrections, we used the annual mean $^{14}CO_2$ emissions from the European Commission RAdioactive Discharges Database (RADD, 2021) for the year 2019. We calculated a mean nuclear contribution of $\Delta^{14}\mathrm{CO}_{2,\mathrm{NUC}} = 1.3 \pm 0.7\,‰$ and $1.4 \pm 0.7\,‰$ for the daytime and nighttime samples, respectively. This corresponds to about 7 % of the mean $\Delta^{14}\mathrm{CO}_{2,\mathrm{BG}} - \Delta^{14}\mathrm{CO}_2$ difference between the background and measurement sites for both the daytime and nighttime samples. A detailed derivation of Eq. (7) can be found, e.g. in Levin et al. (2003).

3 Results

3.1 Comparison of observed and modelled ffCO$_2$ in Heidelberg

In the following section we present the ffCO$_2$ concentrations estimated based on the Heidelberg afternoon and nighttime 2-week integrated samples and compare them to two different WRF–STILT model runs, i.e. the SSI and the VSI approach. Figure 4 shows the measured and modelled 2-week integrated afternoon (left column) and nighttime (right column) ffCO$_2$ enhancements for Heidelberg from July 2018 to June 2020. The black lines show the $\Delta^{14}CO_2$ observation-based ffCO$_2$ concentrations calculated using Eq. (7). They represent the ffCO$_2$ enhancement compared to a maritime background introduced in Sect. 2.3. During these 2 years, the 2-week integrated regional ffCO$_2$ concentrations of the afternoon and nighttime samples range from 0.8 to 26.9 and from 2.3 to 23.7 ppm, respectively, with quite similar mean concentrations of 8.2 ppm in the afternoon and 9.0 ppm during the night. Both the afternoon and the nighttime samples show a clear seasonal cycle, with about 3 to 4 times larger ffCO$_2$ concentrations during winter than during summer.

For the afternoon situations, the SSI and the VSI model runs lead to similar root-mean-square deviation (RMSD) between modelled and measured ffCO$_2$ concentrations of 3.7 ppm considered over the whole 2-year period. Whereas the SSI approach leads on average to a small (10 %) overestimation of the ffCO$_2$ concentrations by 0.8 ppm, the VSI approach tends to underestimate ffCO$_2$ by 0.7 ppm (9 %). To put the observed ffCO$_2$ variability and the variability that cannot be explained by the model into perspective, we calculated the coefficient of determination (R^2) of linear regression. Both model approaches show similar R^2 values of 0.67 (SSI) and 0.63 (VSI) during the afternoon. However, there are seasonal differences in the performance of the two approaches. Whereas both model runs lead to an RMSD between modelled and measured ffCO$_2$ concentrations of 2.0 ppm during the summer half year (from April to September), the RMSD during the winter half year (between October and March) is more than twice as high (4.6 and 4.7 ppm with the SSI approach and the VSI approach, respectively). The worse model performance during winter could be caused by synoptic events with suppressed atmospheric mixing, which frequently occur in winter and are not well represented by transport models. There are, however, differences between the two modelled winters: whereas the VSI approach leads to an improvement compared to the SSI approach during the winter 2018/2019 (RMSD of 2.9 ppm vs. 4.3 ppm), the subsequent winter 2019/2020 shows poorer performance by both modelling approaches (RMSD of 5.9 ppm for the VSI approach and RMSD of 4.9 ppm for the SSI approach).

During nighttime situations we observe large differences between the SSI and VSI approaches. The VSI approach leads to a model–data mismatch comparable to the afternoon situations, with a mean offset between model and observations of −0.7 ppm (8 %) and an RMSD of 3.4 ppm (the RMSD is 3.3 ppm during summertime and 3.6 ppm during wintertime). In contrast, the nighttime SSI run shows by far the largest ffCO$_2$ overestimations throughout the 2 years, with the largest model–observations deviations seen during summer (the RMSD is 6.7 ppm during summertime and 5.8 ppm during wintertime). Over the whole 2 years the average offset is −4.6 ppm (51 %), and the RMSD of 6.3 ppm is almost twice as high as the RMSD of the VSI approach and that of the SSI approach in the afternoon. The poorer SSI performance during the night can also be seen in the R^2 values. The VSI approach leads to a R^2 of 0.62, which is comparable to the afternoon performance, but the SSI approach shows a

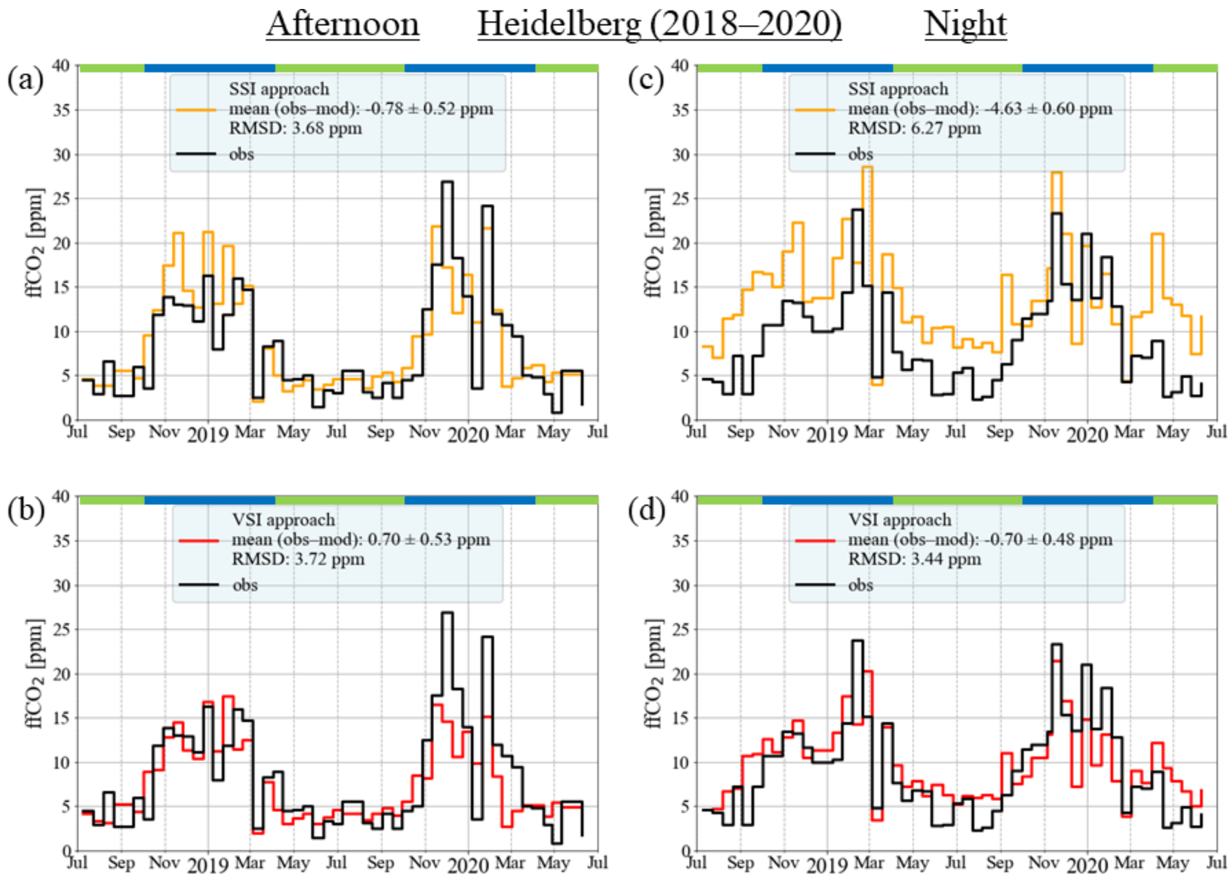

Figure 4. Comparison of 2-week integrated ^{14}C-based measured (black) and modelled (coloured) ffCO$_2$ concentration enhancements during afternoon hours (between 11:00 and 16:00 UTC; **a** and **b**) and during nighttime (between 18:00 and 06:00 UTC; **c** and **d**) for the time period of July 2018 until June 2020 in Heidelberg. The follow two modelling approaches were tested: the standard surface source influence (SSI) approach (orange; **a** and **c**) and the volume source influence (VSI) approach (red; **b** and **d**); see the text for further details. For each of the comparisons, the root-mean-square deviation (RMSD) between the model and observations, as well as the mean difference (observation minus model) and the standard error of the mean, are given. At the top of each panel the winter and summer periods are marked in blue and green, respectively.

lower R^2 of 0.48 during the night. To check if the representation of the variability beyond the bias has been improved in the case of the VSI approach, we calculated the bias-corrected (centred) RMSD (CRMSD). It turns out that during the night the SSI approach leads to a CRMSD of 4.2 ppm and the VSI approach leads to a CRMSD of 3.4 ppm. Thus, there is also a slight improvement of the VSI approach in the CRMSD during the night. However, whereas the RMSD is reduced by 46 % in the VSI approach compared to the SSI approach during nighttime, the CRMSD is only reduced by 19 %. This indicates that the VSI approach mainly improves the mean bias between observed and modelled ffCO$_2$ concentrations.

We further investigated why the VSI approach is better than the SSI approach during nighttime, whereas both approaches are comparable during afternoon situations. For this we extracted the modelled planetary boundary layer height for Heidelberg from the simulations and averaged it over the nighttime or afternoon times for the full 2 weeks. Figure 5 shows the ffCO$_2$ concentration difference between the SSI and VSI approaches plotted vs. the planetary boundary layer height for all 2-week integrated afternoon (in blue) and nighttime (in red) situations over the 2 years of measurements. During most of the afternoon situations the PBLHs are large, indicating strong convective mixing. The SSI approach with emissions into the bottom half of the PBL then yields similar concentrations at the measurement point as the VSI approach because the VSI height profiles do not (or only slightly) exceed the bottom half of the PBL. On the other hand, low PBLHs result in large concentration differences between the SSI and VSI approaches, which is the case in most of the nighttime and in some afternoon situations between mid-October and February with suppressed convective mixing. During these situations, the SSI approach releases all point source emissions into a shallow layer below the bottom half of the PBL, thus overestimating concentrations at

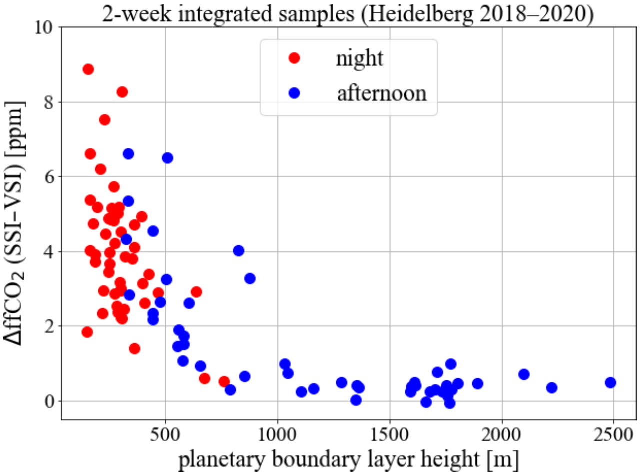

Figure 5. Modelled $ffCO_2$ differences between the SSI and VSI approaches for Heidelberg afternoon (blue) and nighttime (red) samples plotted against the modelled mean height of the planetary boundary layer (PBL) during sampling.

30 m a.g.l. In contrast, the VSI approach releases emissions at the actual plume height; however, due to the shallow PBL and suppressed convective mixing this leads to only small contributions for an observation site inside the PBL (as is the case for low sampling heights such as at the measurement site in Heidelberg).

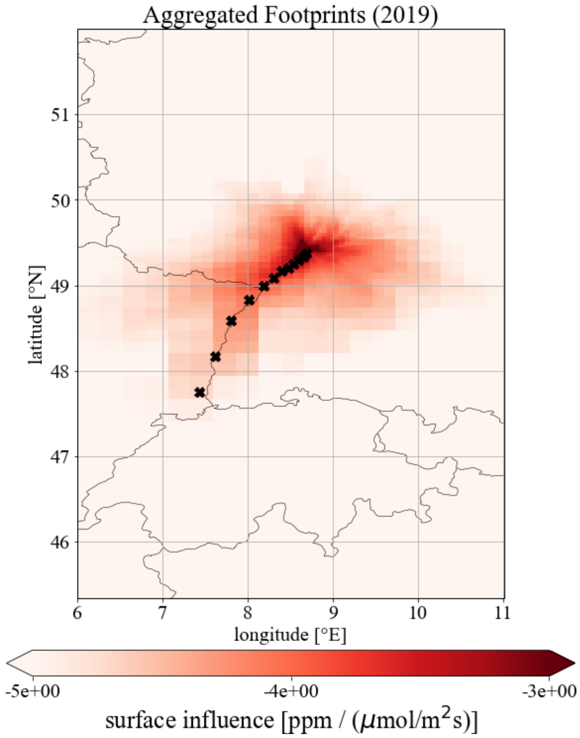

Figure 6. Aggregated hourly footprints in 2019, calculated with the SSI approach for the observation site Heidelberg at 30 m height a.g.l. The black crosses indicate the locations of the 12 pseudo power plants, which are located at distances of 5, 10, 15, 20, 25, 30, 40, 50, 70, 100, 150 and 200 km from the Heidelberg observation site.

3.2 Surface and volume source contributions from nearby point sources in a “pseudo power plant experiment”

Next, we wanted to evaluate if the VSI approach is also relevant for typical continental tall tower stations with elevated sampling heights of, e.g. 200 m a.g.l. For this we conducted a so-called “pseudo power plant experiment”. This experiment should also help determine up to which distance from the measurement site point source emissions should be modelled with the VSI approach to avoid strong overestimations in modelled concentrations during nighttime. Figure 6 shows the aggregated footprints for Heidelberg in 2019, calculated with the SSI approach and our WRF–STILT configuration presented in Sect. 2.2. This mean footprint shows a tail towards the southwestern direction, which can be explained by the channelling effect of the Rhine valley. In our experiment we placed 12 artificial (pseudo) power plants along this footprint tail at distances of 5 to 200 km from Heidelberg, as indicated by the black crosses, so that many situations with contributions from these locations reaching the measurement site in Heidelberg could be expected. All power plants were assigned a CO_2 emission rate of 10^6 t yr^{-1}, which corresponds to typical emissions of small hard coal power plants in Germany (Fraunhofer, 2021). For every hour in 2019, the $ffCO_2$ contribution from each pseudo power plant was modelled with the SSI and VSI approach. In the case of the VSI approach, we used the TNO emission height profile for the public power (energy) sector (see Fig. 3b). We then selected only those hours for which the volume source influence matrix of Heidelberg for a height range between 0 and 1106 m a.g.l. has nonzero entries in each of the 12 pseudo power plant grid cells. By doing so, we have for each pseudo power plant the identical number of selected events (with nonzero contributions) for which we can compare the SSI and the VSI approach. This yields 2060 selected hours in 2019. We then extracted the PBLH at Heidelberg from the WRF–STILT simulation and divided these events into two PBLH regimes (PBLH $<$ 500 and PBLH $>$ 500 m). The PBLH $<$ 500 m situations are predominantly nighttime situations, and those at PBLH $>$ 500 m are mainly daytime situations (in 2019, 84 % of the nighttime hours have a PBLH $<$ 500 m and 75 % of the daytime situations have a PBLH $>$ 500 m).

Figure 7a (7b) shows the mean $ffCO_2$ contributions from the individual pseudo power plants vs. their distances from Heidelberg when the SSI (VSI) approach is used. Events were separated into situations when the PBLH in Heidelberg was smaller than 500 m (red dots) or larger than 500 m (blue dots). The mean $ffCO_2$ contribution differences between the SSI and VSI approach (SSI minus VSI) for the individual pseudo power plants are shown in Fig. 7c. It is obvious that

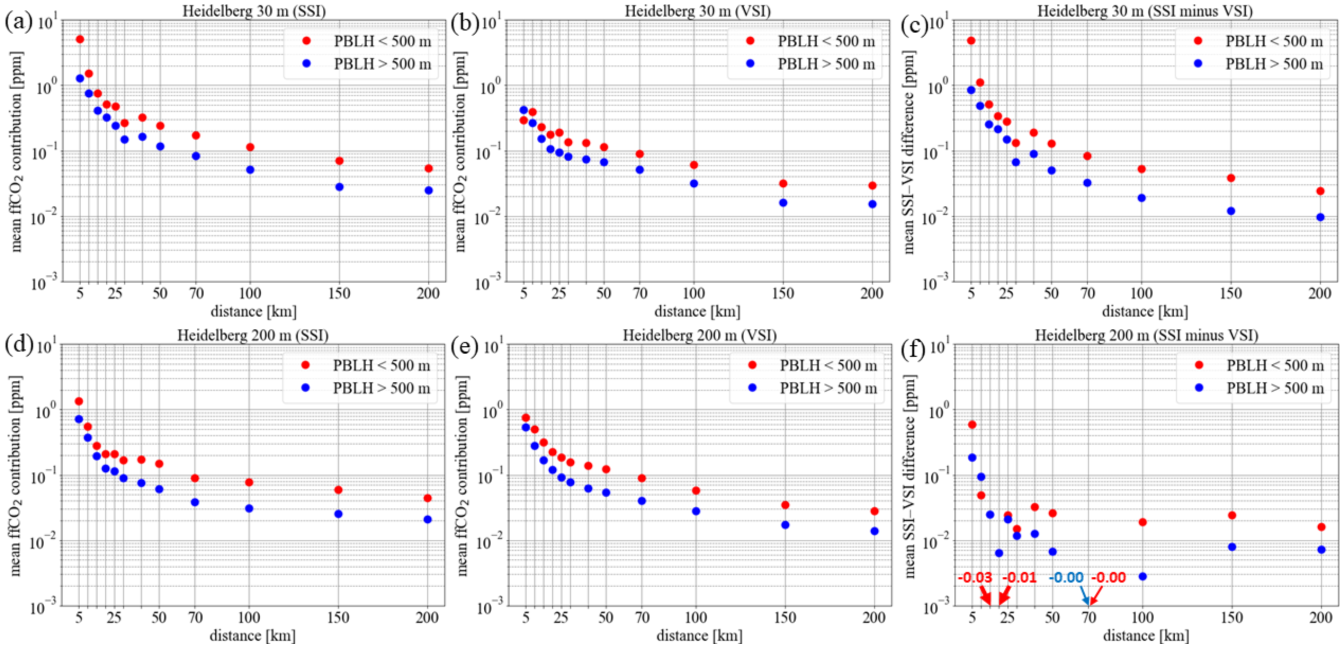

Figure 7. Mean $ffCO_2$ contributions from pseudo power plants, which were placed at distances between 5 and 200 km from the observation site Heidelberg at 30 m (**a–c**) and at a virtual 200 m height (**d–f**). Shown are the results from the SSI (**a** and **d**) and VSI approach when using the TNO public power (energy) profile (**b** and **e**), as well as the mean difference between the SSI and VSI $ffCO_2$ contributions (**c** and **f**). From all hours in 2019, only those situations were selected for which each pseudo power plant grid cell is hit by at least 1 of the 100 back-trajectories, which were calculated for each hour. These selected hours are then divided into two planetary boundary layer height (PBLH) regimes (blue and red) and averaged. For this, we always used the PBLH at the Heidelberg measurement site at the time when the air parcels from the power plants arrived in Heidelberg. In **(f)**, negative values are indicated with red (PBLH < 500 m) and blue (PBLH > 500 m) arrows.

the mean $ffCO_2$ contributions from the power plants decrease with increasing distance from the observation site in both modelling approaches. This can be explained by the dispersion of the power plant plumes and the associated dilution. To restrict the mean $ffCO_2$ contribution from these power plants to below 0.1 ppm, the observation site should be more than 100 km (SSI) or 50 km (VSI) away from this power plant. This is in line with the ICOS recommendations that suggest a distance of at least 40 km from strong anthropogenic sources (ICOS RI, 2020). Figure 7a shows that the SSI approach yields larger contributions for stable PBLH < 500 m situations compared to (daytime) situations with PBLH > 500 m. Since in the SSI approach the emissions are homogeneously mixed into the bottom half of the PBL, the smaller mixing volume during PBLH < 500 m situations leads to larger $ffCO_2$ concentrations. This is what we have already seen from our daytime and nighttime simulations of real-world $ffCO_2$ (see Fig. 5). The reduction of the $ffCO_2$ contributions with increasing PBLH could be seen as an increased vertical dispersion of the power plant plumes. In the "pseudo power plant experiment" the VSI approach shows the same behaviour as the SSI approach with larger $ffCO_2$ contributions during stable PBLH < 500 m situations for most power plants, which can also be explained by less dispersion of the power plant plumes. However, there is one exception in the VSI approach. The power plant with a 5 km distance yields lower $ffCO_2$ contributions during stable PBLH < 500 m conditions than during PBLH > 500 m situations (in contrast to the SSI approach). A possible explanation is that during stable PBL conditions the mixing is too weak to transport the emissions from the power plant stack down to the sampling height at 30 m within the time the air mass needs to travel the 5 km from the power plant to the observation site (see Fasoli et al., 2018).

Looking at the mean $ffCO_2$ contribution differences (Fig. 7c) between the two model approaches reveals that for the 30 m high observation site the SSI approach simulates almost 5 ppm larger $ffCO_2$ contributions on average than the VSI approach for the closest (5 km distance) power plant during stable conditions. This can be explained by (i) the large SSI contributions due to the shallow boundary layer and (ii) the low VSI contributions due to suppressed downward mixing of the power plant plume to the 30 m high observation site. During PBLH > 500 m situations and for more distant power plants the mean difference between the SSI and VSI contributions decreases due to stronger mixing or more time for mixing over the longer air mass travel time between the power plant and observation site. In both cases, the assumption in the SSI approach, i.e. an instantaneous and homogeneous dilution of all power plant emissions in the bottom half of the PBL, seems to be more justified than during PBLH < 500 m situations and for power plants very close to the measurement site. Further, the difference between PBLH < 500 m and PBLH > 500 m situations decreases with distance to the power plants. One reason for this could be that, due to the longer travel time (e.g. > 12 h for the furthest power plant during wind velocities of $< 5\,\mathrm{m\,s^{-1}}$), a power plant plume arriving at nighttime in Heidelberg was still well mixed over a large boundary layer during the previous day.

Since ICOS tower stations have most of their air inlets above 30 m a.g.l. (typically between 30 and 250 m), we also investigated the behaviour of the SSI and VSI approach for a virtual Heidelberg sampling height at 200 m a.g.l. The results are shown in Fig. 7d–f. In contrast to the 30 m air inlet, for the 200 m air inlet the SSI approach shows less enhancements compared to the VSI approach during stable conditions and for power plants very close by. Whereas for example the closest 5 km distant power plant leads to an SSI minus VSI ffCO_2 difference of 4.9 ppm in the case of the 30 m air inlet, this difference is reduced to 0.6 ppm in the case of the 200 m air inlet. This means that the SSI contribution in the case of the 30 m air inlet is 17.4 times larger than the VSI contribution. In the case of the 200 m air inlet, the SSI contribution from the closest power plant is only 1.8 times larger during PBLH < 500 m situations. This could be explained by situations with very stable conditions (with for PBLH < 200 m), when the sampling height at 200 m a.g.l. is above the PBL and hardly sensitive to emissions that are mixed within the bottom half of the PBL (in the SSI approach). In contrast, the VSI approach yields larger ffCO_2 contributions from nearby power plants compared to the case with the 30 m sampling height, since the sampling height (200 m a.g.l.) is now closer to the effective emission height. Consequently, the 200 m sampling height shows (in contrast to the 30 m sampling height) on average lower ffCO_2 contribution differences between SSI and VSI approach, especially for contributions from very close power plants and during stable PBL situations.

4 Discussion

4.1 Effects of emission uncertainties on the comparison between observed and modelled ffCO_2 in Heidelberg

The model–data mismatch presented in Fig. 4 depends not only on the representation of atmospheric transport and the handling of point source emissions but also on uncertainties in the emission inventory. Since we interpret the model–data mismatch difference for the evaluation of the SSI and VSI approach, we need to ensure that it is not caused by incorrect area or point source distribution or temporal profiles in the emission inventory. If, for example, the nocturnal point source emissions were overestimated in the inventory, we would consider the VSI approach to yield better agreement with observations for the wrong reason. Therefore, we first want to discuss uncertainties in the inventory and assess which theoretical overestimation in the inventory would be needed to generate the apparent improvement of the model–data mismatch going from SSI to the VSI approach. Super et al. (2020) identified four sources of uncertainties in the high-resolution TNO inventory: (1) uncertainties in the national activity data, (2) uncertainties in the emission factors, which quantify the ffCO_2 emissions that are released per unit of activity and are related to the carbon content of the fuels, (3) uncertainties in the spatial distribution of the national emissions, which rely on spatial proxies like population or traffic density and finally (4) uncertainties in the temporal profiles of emissions. Super et al. (2020) used a Monte Carlo approach to produce 10 high-resolution TNO inventory ensembles for the annual emissions in 2015 by incorporating uncertainties (1) to (3) for the area sources. They regard the point source emission uncertainties as quite low and thus excluded them from the Monte Carlo simulations. For a 200 km × 200 km area around Heidelberg, the annual total ffCO_2 area source emission calculated from the 10 emission grid realisations spreads by about $\pm 3\,\%$. Based on the results of Super et al. (2020), we may thus assume a very low uncertainty for the area and point sources, which could not explain the observed differences in the model–data mismatch between SSI and VSI.

In a thought experiment we tested how much we would have to change the actual point source emissions so that SSI and VSI approach lead to a similarly good agreement with observations during nighttime. In Fig. 8 we show that the point source emissions would have to be reduced by as much as 70 % during nighttime to show a similar model–data mismatch for the SSI approach to that of the VSI approach. Such large point source emission uncertainties are unrealistic and unexpected. Based on these considerations, we conclude that it is highly unlikely that the improved model–data mismatch of the nocturnal VSI approach is due to biases in the temporal profile of the emissions. The improvement in the VSI approach can therefore be attributed to the different vertical representation of the point sources.

4.2 Representation of nearby point source emissions in models

Typically, flask samples for model–observation comparisons or inversions are collected in the afternoon during well-mixed conditions when the atmospheric transport and mixing processes can be best simulated (Geels et al., 2007). However, the inclusion of nighttime observations into inversion modelling frameworks would drastically increase the number of observational data that could be used to optimise emissions and could help draw conclusions about the mixture and the diurnal emission profiles of source sectors that are more

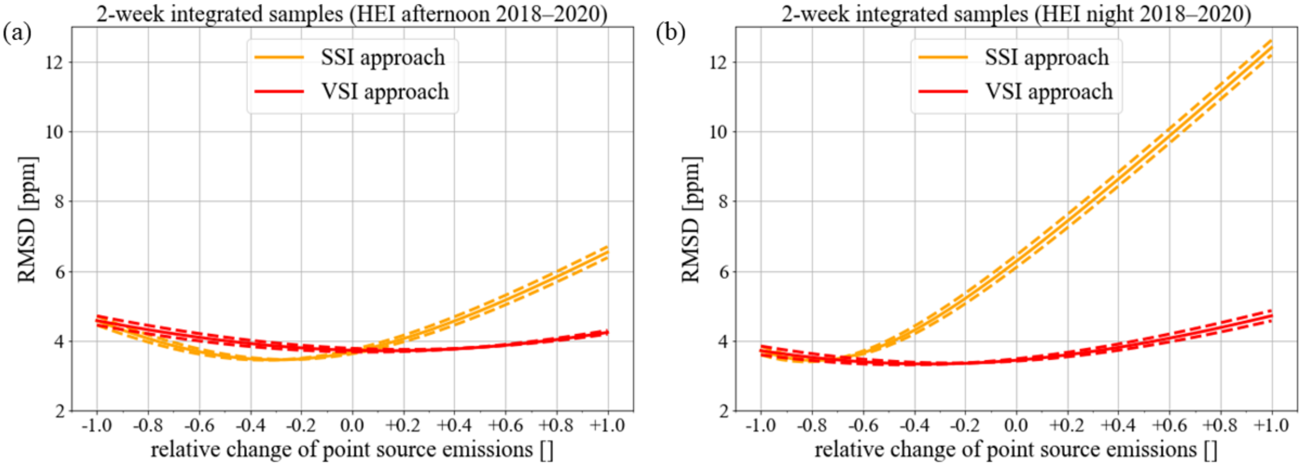

Figure 8. Root-mean-square deviation (RMSD) between measured and modelled $ffCO_2$ concentrations of 2-week integrated afternoon (**a**) and nighttime (**b**) $\Delta^{14}CO_2$ samples collected during July 2018 and June 2020 in Heidelberg (HEI) at 30 m a.g.l. for the surface (SSI, in orange) and volume source influence (VSI, in red) approaches for different relative changes in the TNO point source emissions. A relative change of -1 means that all point source emissions are switched off, and a relative change of $+1$ means that the actual emissions of all point sources are doubled. For instance, the actual point source emissions would have to be decreased by about 70 % (corresponds to -0.7 on the x axis), and thus SSI and VSI approach lead to a similar RMSD for nighttime situations. The dashed lines show the additional impact of a TNO area source emission uncertainty of ±3 % (see Super et al., 2020) on the RMSD between measured and modelled $ffCO_2$ concentrations.

active during night or in the morning and evening hours. The exploitation of nighttime observations in inverse modelling studies relies on the model's ability to realistically reproduce stable nocturnal boundary layers. Here, we discuss the effect of point source emission heights on the model–data mismatch, especially during nighttime, and assess when and where the volume source influence approach should be applied.

The pseudo power plant experiment yields a mean SSI minus VSI contribution difference between about 0.5 ppm (for a 15 km distant power plant) and 4.9 ppm (for a 5 km distant power plant) during stable conditions with low PBLHs. Since the Heidelberg measurement site is surrounded by several point sources, some of them emitting more than 10^6 t CO_2 yr^{-1} (see Fig. 2), we decided to apply the VSI approach to all point sources within a 200 km × 200 km area around Heidelberg and use the SSI approach for the point sources further away, where we expect only small differences between the VSI and SSI approach. The $ffCO_2$ results for the 2-week integrated nighttime samples showed that the model–data mismatch could already be reduced by about 3 ppm (RMSD = 3.4 ppm) when using this VSI approach for nearby point sources instead of the standard SSI approach (RMSD = 6.3 ppm). During well-mixed conditions the pseudo power plant experiment showed smaller differences between the VSI and SSI approach, which can also be seen in the $ffCO_2$ results for the 2-week integrated afternoon samples, where the VSI approach and the SSI approach differ by merely ca. 1 % (both approaches lead to an RMSD of about 3.7 ppm). Thus, we strongly recommend the application of the VSI approach for measurement sites with sampling heights typically within the nocturnal boundary layer and with nearby point sources so that also nighttime observations could be used, e.g. for a model–observation comparison. However, the VSI approach is accompanied by larger computational costs since the volume influence field v must be calculated for each height interval. In contrast, in the SSI approach only one surface influence field f must be calculated (see Sect. 2.2). To save computational power we therefore suggest that the VSI approach only be used for nearby point sources and to use the SSI approach for more distant point sources where both model approaches lead to similar results. Depending on the distribution and the emission strength of the point sources around the measurement site and the intake height of the measurement site, the results from the pseudo power plant experiment can help to decide for which point sources the VSI approach should be applied. From this experiment it follows that the SSI minus VSI differences are substantial for low intake heights (e.g. 30 m) and power plants within a radius of 5 to 15 km. When averaged over the two PBLH regimes (< 500 and > 500 m), these differences come to 3.9 and 0.5 ppm respectively, equivalent to a 12- or 2-fold increase in the absolute VSI contribution for a point source emitting 1 $MtCO_2$ yr^{-1}. Such a station and point source configuration is realistic for urban observations. For ICOS-like background stations, which should typically be located 50 km from point sources, the SSI minus VSI difference is less than 0.1 ppm and thus even less than the World Meteorological Organization (WMO) compatibility goal for CO_2 (WMO, 2018).

Since the $^{14}CO_2$ samples are collected at many ICOS stations from a higher intake, we performed the pseudo power plant experiment also for a (virtual) Heidelberg observation site at 200 m a.g.l. (where we do not have real measurements). The results show that for nearby power plants the mean SSI minus VSI contribution differences are roughly an order of magnitude smaller than in the case of the observation site at 30 m a.g.l. However, one has to keep in mind that although the SSI minus VSI contribution differences are smaller in the case of the 200 m high observation site, the SSI approach does not represent the atmospheric transport processes any better than in the case of the observation site at 30 m a.g.l. It simply means that the 200 m intake height is less sensitive to the bottom half of the PBL during stable conditions, which leads to less overestimations for the SSI compared to the VSI approach. The randomness of the SSI contributions becomes immediately clear if one considers the 15 and 20 km distant power plant. Here, the SSI approach yields even smaller contributions than the VSI approach during stable conditions. Moreover, the 200 m intake height is vertically closer to the effective emission height of the power plants, which leads to larger VSI contributions compared to the 30 m level. These two circumstances cause the smaller mean SSI minus VSI contribution differences for nearby point sources in the case of the 200 m level. The mean SSI minus VSI contribution difference for a 10^6 t CO_2 yr^{-1} emitting point source is below 0.1 ppm if the point source is at least 10 km away from the measurement site. However, one has to keep in mind that this absolute difference in SSI minus VSI contribution increases linearly with the emission strength of the point sources. Thus, for ICOS-like stations and point sources at least 10 km away, the SSI approach again seems to be well suited when there is enough time for mixing throughout the PBL and the SSI assumptions are justified.

Inaccurate representation of point source emissions from stacks is not limited to Lagrangian models but is found in many Eulerian modelling setups as well. Super et al. (2017) investigated how well a Eulerian model (WRF–Chem) alone, as well as in combination with a Gaussian plume model, agrees with CO_2 and CO mixing ratios at an urban site in the Netherlands. In the case of the Eulerian model, the point source emissions are distributed over the different vertical model levels according to the emission height profiles shown in Fig. 3, which is rather similar to the VSI approach we used in WRF–STILT. The Gaussian plume model is able to represent the exact emission stack heights and improves the description of the transport and dispersion of the point source plumes, which in the case of Eulerian models are instantly mixed within individual grid boxes (Super et al., 2017). The authors could show that both the exact representation of the stack heights and the more appropriate description of the plume dispersion will lead to a better agreement to the observations in the case of the WRF–Chem model in combination with the Gaussian plume model. Therefore, they recommend to treat all large point source emissions within a 10 km radius around the observation site with such a plume model.

5 Conclusions

In this study we used a 2-year record of afternoon and nighttime 2-week integrated ^{14}C-based $ffCO_2$ measurements conducted in Heidelberg at 30 m a.g.l. to examine the performance of the standard STILT surface source influence (SSI) approach. We find that it is almost twice as good for afternoon situations (RMSD = 3.7 ppm) than for the nighttime situations (RMSD = 6.3 ppm) when comparing modelled and observed $ffCO_2$ concentrations. The lower performance during the night could be explained by the large overestimation of the contributions from nearby point sources. We therefore introduced an alternative modelling approach – the volume source influence (VSI) approach – which is able to represent the emission height and the plume rise of the point source emissions more correctly. With this approach, the performance of STILT is similar for the afternoon (RMSD = 3.7 ppm) and nighttime samples (RMSD = 3.4 ppm).

We further investigated the behaviour of the SSI and VSI approach for point sources at different distances to the measurement site and under different atmospheric conditions. For this we performed a pseudo power plant experiment by modelling the $ffCO_2$ contributions from 12 virtual power plants with distances between 5 and 200 km from the observation site and annual emissions of one million tonnes of CO_2. This model experiment could confirm what we already observed in the model–observation comparison of the 2-week integrated samples, namely that the standard SSI approach leads to strong overestimations compared to the VSI approach given stable atmospheric conditions with low planetary boundary layer heights, especially for point sources close to the observation site. For instance, point sources with a distance between 5 and 15 km from the observation site lead to a mean SSI minus VSI difference of 3.9 to 0.5 ppm $ffCO_2$, which is 12 to 2 times larger than the mean VSI $ffCO_2$ contribution from these point sources. Thus, we strongly recommend the use of the VSI approach for these close-by point sources when modelling their $ffCO_2$ contribution at low-altitude measurement sites. For ICOS-like background stations, which should typically be located more than 50 km away from point sources, the mean SSI minus VSI difference reduces to below 0.1 ppm. We also performed this model experiment for a virtual observation site with a 200 m sampling height, which is more comparable to the uppermost measurement height of typical ICOS stations. Here, the mean contribution differences between the SSI and VSI approaches for nearby point sources are smaller compared to those at the 30 m sampling height because the 200 m height is less sensitive to the bottom half of the PBL during very stable situations (leading to smaller SSI contributions) and is vertically closer to the effective power plant emission height (leading to larger VSI contributions). Whereas for low sampling heights the VSI approach is strongly recommended to model contributions from nearby point sources in order to avoid large overestimations (on the order of several parts per million for $ffCO_2$) during stable conditions, we also suggest the use of the VSI approach in the case of sampling heights well above the nocturnal boundary layer since it is the physically more correct approach for these situations with suppressed mixing. The contributions from more distant point sources are generally smaller and also the assumptions in the SSI approach seem to be more justified for longer air mass travel times between the point source and observation site and during unstable atmospheric conditions. This explains the smaller differences between the SSI and VSI approach for these situations. Depending on the atmospheric conditions, the sampling height, the distance to the point source and the emission strength of the point source, the results of our pseudo power plant experiment can be used to assess the contribution of the point source in both modelling approaches. Then one can decide if the SSI approach is sufficient (e.g. for distant point sources with lower emissions or during unstable conditions) or if the VSI approach is the better alternative.

Whereas the modelling of transport and mixing processes is still challenging during nighttime, we showed with this study that using the VSI approach for nearby point sources will greatly reduce the overestimations of contributions from nearby point source emissions during periods with low PBLH, especially for low-altitude measurement sites. Therefore, this approach could possibly be a first step towards the usage of nighttime observations for modelling purposes in STILT. A further inevitable step towards the exploitation of nighttime observations in models is the realistic representation of stable nocturnal boundary layers and their erosion in the morning hours. Moreover, we want to underline the importance of having an inventory containing the effective point source emission heights for the whole globe, which is a prerequisite for applying this VSI approach also outside Europe.

Code and data availability. The measurement and model results for the 2-week integrated samples collected at Heidelberg and the outcome of the pseudo power plant experiment are available at the Heidelberg University data depository (https://doi.org/10.11588/data/CK3ZTX, Maier et al., 2021). The R script ("volume.infl.ffco2.timeres.r") to calculate $ffCO_2$ contributions from point sources and the used trajectory information calculated with WRF–STILT and the TNO point source emissions around Heidelberg can be found at https://doi.org/10.5281/zenodo.5911518 (Maier et al., 2022). To calculate the trajectories for other locations or times, one has to download the full STILT model, which is available at http://stilt-model.org/ (last access: 7 July 2022, Lin et al., 2003) after registration. We used revision number 747 of the STILT repository.

Author contributions. FM designed the study together with CG, IL and SH. FM performed the STILT modelling and evaluated the data. CG helped with the implementation of STILT. SH compiled the measurement results of the 2-week integrated $^{14}CO_2$ samples. IS was responsible for the TNO emission inventories. JM generated the highly resolved meteorological fields with WRF. FM wrote the manuscript with help of all co-authors.

Competing interests. The contact author has declared that none of the authors has any competing interests.

Acknowledgements. We would like to thank Sharon Gourdji and the anonymous reviewer for their inspiring comments and suggestions, which helped to improve the paper. We gratefully acknowledge Thomas Koch and Michał Gałkowski for their help with running STILT. We wish to thank the staff of TNO at the Department of Climate, Air and Sustainability in Utrecht for the emission inventories and height profiles. A special thank goes to Sabine Kühr and the whole staff of the ICOS-CRL Karl Otto Münnich Laboratory for their careful $^{14}CO_2$ sampling and analysis and to Julian Della Coletta and the ICOS Atmospheric Thematic Centre for conducting and evaluating the continuous CO_2 measurements in Heidelberg. We further would like to thank Ida Storm and the members of the ICOS Carbon Portal for their cooperation in developing tools for estimating nuclear $^{14}CO_2$ contamination at European ICOS stations.

Financial support. This research has been supported by the German Weather Service (DWD), the ICOS Research Infrastructure and VERIFY (grant no. 776810, Horizon 2020 Framework). The ICOS Central Radiocarbon Laboratory is funded by the German Federal Ministry of Transport and Digital Infrastructure. Fabian Maier was paid by the DWD.

Review statement. This paper was edited by Christoph Knote and reviewed by Sharon Gourdji and one anonymous referee.

References

Basu, S., Miller, J. B., and Lehman, S.: Separation of biospheric and fossil fuel fluxes of CO_2 by atmospheric inversion of CO_2 and $^{14}CO_2$ measurements: Observation System Simulations, Atmos. Chem. Phys., 16, 5665–5683, https://doi.org/10.5194/acp-16-5665-2016, 2016.

Basu, S., Lehman, S. J., Miller, J. B., Andrews, A. E., Sweeney, C., Gurney, K. R., Xue, X., Southon, J., and Tans, P. P.: Estimating US fossil fuel CO_2 emissions from measurements of ^{14}C in atmospheric CO_2, P. Natl. Acad. Sci. USA, 117, 13300–13307, https://doi.org/10.1073/pnas.1919032117, 2020.

Brunner, D., Kuhlmann, G., Marshall, J., Clément, V., Fuhrer, O., Broquet, G., Löscher, A., and Meijer, Y.: Accounting for the vertical distribution of emissions in atmospheric CO_2 simulations, Atmos. Chem. Phys., 19, 4541–4559, https://doi.org/10.5194/acp-19-4541-2019, 2019.

Currie, L. A.: The remarkable metrological history of radiocarbon dating [II], J. Res. Natl. Inst. Stan., 109, 185–217, https://doi.org/10.6028/jres.109.013, 2004.

Fasoli, B., Lin, J. C., Bowling, D. R., Mitchell, L., and Mendoza, D.: Simulating atmospheric tracer concentrations for spatially distributed receptors: updates to the Stochastic Time-Inverted Lagrangian Transport model's R interface (STILT-R version 2), Geosci. Model Dev., 11, 2813–2824, https://doi.org/10.5194/gmd-11-2813-2018, 2018.

Fraunhofer: Fraunhofer-Institut für Solare Energiesysteme ISE, Energy-Charts, https://energy-charts.info/charts/emissions/chart.htm?l=de&c=DE&source=hard_coal, last access: 6 August 2021.

Friedlingstein, P., O'Sullivan, M., Jones, M. W., Andrew, R. M., Hauck, J., Olsen, A., Peters, G. P., Peters, W., Pongratz, J., Sitch, S., Le Quéré, C., Canadell, J. G., Ciais, P., Jackson, R. B., Alin, S., Aragão, L. E. O. C., Arneth, A., Arora, V., Bates, N. R., Becker, M., Benoit-Cattin, A., Bittig, H. C., Bopp, L., Bultan, S., Chandra, N., Chevallier, F., Chini, L. P., Evans, W., Florentie, L., Forster, P. M., Gasser, T., Gehlen, M., Gilfillan, D., Gkritzalis, T., Gregor, L., Gruber, N., Harris, I., Hartung, K., Haverd, V., Houghton, R. A., Ilyina, T., Jain, A. K., Joetzjer, E., Kadono, K., Kato, E., Kitidis, V., Korsbakken, J. I., Landschützer, P., Lefèvre, N., Lenton, A., Lienert, S., Liu, Z., Lombardozzi, D., Marland, G., Metzl, N., Munro, D. R., Nabel, J. E. M. S., Nakaoka, S.-I., Niwa, Y., O'Brien, K., Ono, T., Palmer, P. I., Pierrot, D., Poulter, B., Resplandy, L., Robertson, E., Rödenbeck, C., Schwinger, J., Séférian, R., Skjelvan, I., Smith, A. J. P., Sutton, A. J., Tanhua, T., Tans, P. P., Tian, H., Tilbrook, B., van der Werf, G., Vuichard, N., Walker, A. P., Wanninkhof, R., Watson, A. J., Willis, D., Wiltshire, A. J., Yuan, W., Yue, X., and Zaehle, S.: Global Carbon Budget 2020, Earth Syst. Sci. Data, 12, 3269–3340, https://doi.org/10.5194/essd-12-3269-2020, 2020.

Geels, C., Gloor, M., Ciais, P., Bousquet, P., Peylin, P., Vermeulen, A. T., Dargaville, R., Aalto, T., Brandt, J., Christensen, J. H., Frohn, L. M., Haszpra, L., Karstens, U., Rödenbeck, C., Ramonet, M., Carboni, G., and Santaguida, R.: Comparing atmospheric transport models for future regional inversions over Europe – Part 1: mapping the atmospheric CO_2 signals, Atmos. Chem. Phys., 7, 3461–3479, https://doi.org/10.5194/acp-7-3461-2007, 2007.

Gerbig, C., Körner, S., and Lin, J. C.: Vertical mixing in atmospheric tracer transport models: error characterization and propagation, Atmos. Chem. Phys., 8, 591–602, https://doi.org/10.5194/acp-8-591-2008, 2008.

Hammer, S.: Quantification of the regional H_2 sources and sinks inferred from atmospheric trace gas variability, PhD Thesis, University of Heidelberg, 2008.

Heiskanen, J., Brümmer, C., Buchmann, N., Calfapietra, C., Chen, H., Gielen, B., Gkritzalis, T., Hammer, S., Hartman, S., Herbst, M., Janssens, I. A., Jordan, A., Juurola, E., Karstens, U., Kasurinen, V., Kruijt, B., Lankreijer, H., Levin, I., Linderson, M., Loustau, D., Merbold, L., Myhre, C. L., Papale, D., Pavelka, M., Pilegaard, K., Ramonet, M., Rebmann, C., Rinne, J., Rivier, L., Saltikoff, E., Sanders, R., Steinbacher, M., Steinhoff, T., Watson, A., Vermeulen, A. T., Vesala, T., Vítková, G., and Kutsch, W.: The Integrated Carbon Observation System in Europe, B. Am. Meteorol. Soc., 103, E855–E872, https://doi.org/10.1175/BAMS-D-19-0364.1, 2022.

ICOS RI: ICOS Atmosphere Station Specifications V2.0, edited by: Laurent, O., ICOS ERIC, https://doi.org/10.18160/GK28-2188, 2020.

Kromer, B. and Münnich, K. O.: CO_2 gas proportional counting in radiocarbon dating – review and perspective, in: Radiocarbon after four decades, edited by: Taylor, R. E., Long, A., and Kra, R. S., Springer, New York, 184–197, https://doi.org/10.1007/978-1-4757-4249-7_13, 1992.

Kuenen, J., Dellaert, S., Visschedijk, A., Jalkanen, J.-P., Super, I., and Denier van der Gon, H.: CAMS-REG-v4: a state-of-the-art high-resolution European emission inventory for air quality modelling, Earth Syst. Sci. Data, 14, 491–515, https://doi.org/10.5194/essd-14-491-2022, 2022.

Levin, I., Münnich, K. O., and Weiss, W.: The Effect of Anthropogenic CO_2 and ^{14}C Sources on the Distribution of ^{14}C in the Atmosphere, Radiocarbon, 22, 379–391, https://doi.org/10.1017/S003382220000967X, 1980.

Levin, I., Kromer, B., Schmidt, M., and Sartorius, H.: A novel approach for independent budgeting of fossil fuel CO_2 over Europe by $^{14}CO_2$ observations, Geophys. Res. Lett., 30, 2194, https://doi.org/10.1029/2003GL018477, 2003.

Levin, I., Hammer, S., Kromer, B., and Meinhardt, F.: Radiocarbon observations in atmospheric CO_2: determining fossil fuel CO_2 over Europe using Jungfraujoch observations as background, Sci. Total Environ., 391, 211–216, https://doi.org/10.1016/j.scitotenv.2007.10.019, 2008.

Levin, I., Karstens, U., Eritt, M., Maier, F., Arnold, S., Rzesanke, D., Hammer, S., Ramonet, M., Vítková, G., Conil, S., Heliasz, M., Kubistin, D., and Lindauer, M.: A dedicated flask sampling strategy developed for Integrated Carbon Observation System (ICOS) stations based on CO_2 and CO measurements and Stochastic Time-Inverted Lagrangian Transport (STILT) footprint modelling, Atmos. Chem. Phys., 20, 11161–11180, https://doi.org/10.5194/acp-20-11161-2020, 2020.

Lin, J. C., Gerbig, C., Wofsy, S. C., Andrews, A. E., Daube, B. C., Davis, K. J., and Grainger, C. A.: A near-field tool for simulating the upstream influence of atmospheric observations: The Stochastic Time-Inverted Lagrangian Transport (STILT) model, J. Geophys. Res., 108, 4493, https://doi.org/10.1029/2002JD003161, 2003 (data available at: http://stilt-model.org/, last access: 7/ July 2022).

Maier, F., Gerbig, C., Levin, I., Super, I., Marshall, J., and Hammer, S.: Heidelberg integrated samples 2018–2020 and pseudo power plant experiment results, Heidelberg University – Institute of Environmental Physics, heiData [data set], https://doi.org/10.11588/data/CK3ZTX, 2021.

Maier, F., Gerbig, C., and Koch, T. F.: Calculating ffCO2 contributions from nearby point sources with STILT surface source and volume source influence approach, Zenodo, https://doi.org/10.5281/zenodo.5911518, 2022.

Nehrkorn, T., Eluszkiewicz, J., Wofsy, S. C., Lin, J. C., Gerbig, C., Longo, M., and Freitas, S.: Coupled weather research and forecasting–stochastic time-inverted lagrangian transport (WRF–STILT) model, Meteorol. Atmos. Phys., 107, 51–64, https://doi.org/10.1007/s00703-010-0068-x, 2010.

RADD: European Commission RAdioactive Discharges Database, https://europa.eu/radd/query.dox?pageID=Query, last access: 8 June 2021.

Stein, A. F., Draxler, R. R., Rolph, G. D., Stunder, B. J. B., Cohen, M. D., and Ngan, F.: NOAA's HYSPLIT Atmospheric Transport and Dispersion Modeling System, B. Am. Meteorol. Soc., 96, 2059–2077, https://doi.org/10.1175/BAMS-D-14-00110.1, 2015.

Super, I., Denier van der Gon, H. A. C., van der Molen, M. K., Sterk, H. A. M., Hensen, A., and Peters, W.: A multi-model approach to monitor emissions of CO_2 and CO from an urban–industrial complex, Atmos. Chem. Phys., 17, 13297–13316, https://doi.org/10.5194/acp-17-13297-2017, 2017.

Super, I., Dellaert, S. N. C., Visschedijk, A. J. H., and Denier van der Gon, H. A. C.: Uncertainty analysis of a European high-resolution emission inventory of CO_2 and CO to support inverse modelling and network design, Atmos. Chem. Phys., 20, 1795–1816, https://doi.org/10.5194/acp-20-1795-2020, 2020.

Super, I., Dellaert, S. N. C., Tokaya, J. P., and Schaap, M.: The impact of temporal variability in prior emissions on the optimization of urban anthropogenic emissions of CO_2, CH_4 and CO using in-situ observations, Atmos. Environ., 11, 100119, https://doi.org/10.1016/j.aeaoa.2021.100119, 2021.

Taylor, G. I.: Diffusion by continuous movements, P. Lond. Mathe. Soc., s2–20, 196–212, https://doi.org/10.1112/plms/s2-20.1.196, 1922.

Turnbull, J. C., Sweeney, C., Karion, A., Newberger, T., Lehman, S. J., Tans, P. P., Davis, K. J., Lauvaux, T., Miles, N. L., Richardson, S. J., Cambaliza, M. O., Shepson, P. B., Gurney, K., Patarasuk, R., and Razlivanov, I.: Toward quantification and source sector identification of fossil fuel CO_2 emissions from an urban area: Results from the INFLUX experiment, J. Geophys. Res.-Atmos., 120, 292–312, https://doi.org/10.1002/2014JD022555, 2015.

Wang, Y., Broquet, G., Ciais, P., Chevallier, F., Vogel, F., Wu, L., Yin, Y., Wang, R., and Tao, S.: Potential of European $^{14}CO_2$ observation network to estimate the fossil fuel CO_2 emissions via atmospheric inversions, Atmos. Chem. Phys., 18, 4229–4250, https://doi.org/10.5194/acp-18-4229-2018, 2018.

Wenger, A., Pugsley, K., O'Doherty, S., Rigby, M., Manning, A. J., Lunt, M. F., and White, E. D.: Atmospheric radiocarbon measurements to quantify CO_2 emissions in the UK from 2014 to 2015, Atmos. Chem. Phys., 19, 14057–14070, https://doi.org/10.5194/acp-19-14057-2019, 2019.

WMO: GAW Report No. 242, 19th WMO/IAEA Meeting on Carbon Dioxide, Other Greenhouse Gases and Related Tracers Measurement Techniques (GGMT-2017), edited by: Crotwell, A. and Steinbacher, M., World Meteorological Organization, Geneva, Dübendorf, Switzerland, 27–31 August 2017, https://library.wmo.int/doc_num.php?explnum_id=5456 (last access: 7 July 2022), 2018.

CHAPTER 3

Estimating regional fossil-fuel CO_2 concentrations from $^{14}CO_2$ observations: Challenges and uncertainties

This chapter is based on:

Maier, F., Levin, I., Gachkivskyi, M., Rödenbeck, C., and Hammer, S.: Estimating regional fossil-fuel CO_2 concentrations from $^{14}CO_2$ observations: Challenges and uncertainties, Phil. Trans. R. Soc. A, https://doi.org/10.1098/rsta.2022.0203 [link not yet available], 2023 [approved for publication].

PHILOSOPHICAL
TRANSACTIONS A

Phil. Trans. R. Soc. A.

doi:10.1098/rsta.2022.0203

Estimating regional fossil-fuel CO_2 concentrations from $^{14}CO_2$ observations: Challenges and uncertainties

Fabian Maier[1], Ingeborg Levin[1], Maksym Gachkivskyi[1,2], Christian Rödenbeck[3] and Samuel Hammer[1,2]

[1]*Institut für Umweltphysik, Heidelberg University, INF 229, 69120 Heidelberg, Germany*
[2]*ICOS Central Radiocarbon Laboratory, Heidelberg University, Berliner Straße 53, 69120 Heidelberg, Germany*
[3]*Department Biogeochemical Systems, Max Planck Institute for Biogeochemistry, Hans-Knöll-Straße 10, 07745 Jena, Germany*

Keywords: fossil fuel CO_2, radiocarbon, $\Delta^{14}CO_2$ background, nuclear $^{14}CO_2$ contamination

Summary

The direct way to estimate the regional fossil fuel CO_2 surplus ($\Delta ffCO_2$) at a station is by measuring the $\Delta^{14}CO_2$ depletion compared to a respective background. However, this approach has several challenges, which are (1) the choice of an appropriate $\Delta^{14}CO_2$ background, (2) potential contaminations through nuclear $^{14}CO_2$ emissions and (3) masking of $\Delta ffCO_2$ by ^{14}C-enriched biosphere respiration. Here we evaluate these challenges and estimate potential biases and typical uncertainties of ^{14}C-based $\Delta ffCO_2$ estimates in Europe. We show that Mace Head (MHD), Ireland, is a representative background station for the ICOS (Integrated Carbon Observation System) atmosphere station network. The mean $\Delta ffCO_2$ representativeness bias when using the MHD $\Delta^{14}CO_2$ background for the whole observation network is of order 0.1 ± 0.3 ppm. At ICOS sites, the median nuclear contamination leads to 25% low-biased $\Delta ffCO_2$ estimates if not corrected for. The $\Delta ffCO_2$ masking due to ^{14}C-enriched heterotrophic CO_2 respiration can lead to similar $\Delta ffCO_2$ biases as the nuclear contaminations, especially in summer. Our evaluation of all components contributing to the uncertainty of $\Delta ffCO_2$ estimates reveals that, due to the small $ffCO_2$ signals at ICOS stations, almost half of the ^{14}C-based $\Delta ffCO_2$ estimates from integrated samples have an uncertainty that is larger than 50%.

*Author for correspondence (Fabian.Maier@iup.uni-heidelberg.de).

†Present address: Institut für Umweltphysik, Heidelberg University, INF 229, 69120 Heidelberg, Germany

1 Introduction

Large uncertainties still exist in greenhouse gases (GHG) budgets to fully understand the causes of their recent atmospheric changes (Friedlingstein et al., 2022). The atmospheric boundary layer is the natural integrator of ground-level emissions. In conjunction with atmospheric transport models, trace gas observations in the boundary layer can, therefore, be used to estimate emissions or uptake rates of these gases (e.g. Bergamaschi et al., 2018; Petrescu et al., 2021). Including process-based emission models and inventories further helps to disentangle natural e.g. climate-driven changes from anthropogenic emissions. However, there still exist large uncertainties in source attribution. Therefore, supplementary measurements, such as isotopic observations, have been added to the monitoring programs to help distinguish different sources or constrain sink processes. In the case of CO_2, the radioactive isotope radiocarbon (^{14}C) has a prominent role, e.g. in separating fossil (radiocarbon-free) CO_2 emissions from natural carbon fluxes between atmosphere, ocean and continental biosphere.

^{14}C is a particularly useful tracer on regional and continental scales, where anthropogenic emissions from the burning of fossil fuels play an important role in the carbon budget (Levin et al., 1980; Levin et al., 2003; Turnbull et al., 2006; Miller et al., 2012; Basu et al., 2016; Wang et al., 2018; Basu et al. 2020; Potier et al. 2022). Disentangling the influence of fossil emissions from ecosystem fluxes on the observed CO_2 concentrations over densely populated areas would, on one hand, provide a means to follow the effectiveness of fossil CO_2 emission reduction strategies (e.g. Levin and Rödenbeck, 2008), on the other hand, allows observing e.g. climate-driven variations and long-term changes in ecosystem functioning directly from the atmosphere (Basu et al., 2020). Co-located observations of CO_2 and $\Delta^{14}CO_2$ (for a definition of the $\Delta^{14}CO_2$-notation that is generally used to report atmospheric $^{14}CO_2$ observations, see Sec. 2.1) over continents and in polluted areas can be exploited in two ways. One possibility is to derive $\Delta ffCO_2$ estimates from the atmospheric $\Delta^{14}CO_2$ differences between a background site and the (polluted) monitoring station in what we call here the regional isotope budget approach. Alternatively, the CO_2 and $\Delta^{14}CO_2$ observations can be used in a dual-tracer atmospheric inverse modelling framework to estimate the $ffCO_2$ emissions directly (Basu et al., 2016; Basu et al., 2020).

The regional isotope budget approach is frequently used to estimate the share of the so-called recently added CO_2 from fossil fuel burning and cement production (e.g. Levin et al., 2003; Turnbull et al., 2006; Levin et al., 2011; Turnbull et al., 2015; Berhanu et al., 2017; Major et al., 2018; Zhou et al., 2020). These studies determined the regional fossil CO_2 excess at an observational station with respect to a non-polluted reference site. This reference or background site could be a high mountain station, which is sampling air from the free troposphere, or a marine site located at the boundary of a continent. The regional isotope budget approach provides the fossil CO_2 excess concentration ($\Delta ffCO_2$, which for clarity we will name C_{ff} in all equations and figures) directly, without the need to model the complete CO_2 and $^{14}CO_2$ cycles. For sites with a long-term $\Delta^{14}CO_2$ record, this approach can also be used to investigate $ffCO_2$ emission trends under the assumption that the atmospheric transport had no significant trend during the considered time period (Levin and Rödenbeck, 2008).

Typically, however, the $\Delta ffCO_2$ estimates at an observation station show large variations not only on long but also on sub-seasonal time scales, which are mainly driven by atmospheric transport and mixing processes. If this variability can be represented by atmospheric transport models, the $\Delta ffCO_2$ observations can be used in inverse modelling frameworks to estimate the $ffCO_2$ emissions in the footprint of the station (Graven et al., 2018). In contrast, the dual-tracer inversion framework (Basu et al. 2016; Basu et al. 2020; Potier et al. 2022) allows for direct usage of the CO_2 and $\Delta^{14}CO_2$ observations to estimate the $ffCO_2$ emissions. But in this alternative approach a priori information is needed to represent the CO_2 fluxes from the ocean and the terrestrial biosphere as well as their respective isotopic $^{14}CO_2$ signatures. Furthermore, a representation of the atmospheric $\delta^{13}CO_2$ signature is required and the cosmogenic production of $^{14}CO_2$ in the upper atmosphere and its (seasonal) transport into the troposphere must be implemented correctly.

Both, the regional isotope budget, and the dual-tracer inversion approach have, thus, advantages and disadvantages. While the dual-tracer inversion requires an a priori representation of the CO_2 and $^{14}CO_2$ fluxes and the related atmospheric gradients to directly estimate $ffCO_2$ emissions, the regional isotope budget approach effectively assumes that these can be adequately captured by the appropriate selection of a representative background. Still, both approaches are not always straight-forward to apply. In populated areas, we need to consider $^{14}CO_2$ emissions e.g. from nuclear installations, that contaminate the $\Delta^{14}CO_2$ observations if such emitters are located in the footprints of the sites. Also, CO_2 respired from decomposing organic material e.g. in soils can mask part of the fossil signal. The biosphere had incorporated bomb ^{14}C in the decades following the atmospheric nuclear bomb testing during the last century, and this $^{14}CO_2$ is today released by heterotrophic respiration (Caldeira et al., 1998; Randerson et al., 2002; Naegler and Levin, 2009a). While these contaminating $^{14}CO_2$ fluxes must be implemented in the dual-tracer inversion, the regional isotope budget approach uses estimates of correction terms to adjust the observed $\Delta^{14}CO_2$ gradients regarding these masking effects. These correction terms are either based on expert judgement or estimated by simulating the $\Delta^{14}CO_2$ contaminations with a priori fluxes and transport models.

Over the years, different assumptions have been made when applying the regional isotope budget approach to e.g. account for the masking effects mentioned above. The aim of the present study is to in-depth re-visit the regional isotope budget approach, its underlying assumptions and investigate potential biases introduced in the respective results. We make sensitivity analyses to estimate the error contributions from all relevant components in this approach, including effects related to the choice of the background station. To obtain typical estimates of these potential biases and errors, we use the highly populated European continent as target region as this area has established a dense network of $\Delta^{14}CO_2$ observations to validate fossil CO_2 emissions and follow its potential changes (Levin et al., 2020; Heiskanen et al., 2022).

2 Methods

2.1 The regional isotope budget approach to calculate recently added ffCO$_2$

In the regional isotope budget approach, the CO$_2$ concentration C$_{meas}$ observed at a measurement station can be written as the sum of the background CO$_2$ concentration C$_{bg}$ and the recently added or removed CO$_2$ contributions from different sources and sinks (e.g. Levin et al., 2003; Turnbull et al., 2006):

$$C_{meas} = C_{bg} + C_{ff} + C_{resp} + C_{photo}\ (+C_{ocean} + C_{strato}) \qquad (1)$$

The contribution from the background C$_{bg}$ accounts for the by far largest share and is globally increasing due to global anthropogenic emissions and land use change. The regionally added or removed CO$_2$ contributions originate from the combustion of fossil fuels and cement production (C$_{ff}$), the biosphere respiration (C$_{resp}$) and photosynthesis uptake (C$_{photo}$) in the target area. It may also contain a component from coastal ocean areas (C$_{ocean}$) and may be influenced by air mass intrusions from the stratosphere (C$_{strato}$). Each CO$_2$ component in Eq. 1 is associated with a characteristic ^{14}CO$_2$ signature. When expressing these ^{14}CO$_2$ signatures in the so-called Δ-notation, i.e. the relative deviation of the ^{14}C/C isotopic ratios from a standard material in permil (as introduced by Stuiver and Pollach (1977)) the Δ^{14}C signatures of the different components are directly comparable, since the Δ-notation accounts for mass-dependent isotopic fractionation during the different exchange processes between the corresponding reservoirs and the atmosphere and also corrects for radioactive decay between sampling and analysis times. Note that, in the following, we replace Δ^{14}C by Δ^{14} to improve the readability of the equations below.

Since the sum over the products of the individual CO$_2$ contributions and the associated isotopic signatures $\sum_i C_i \cdot \Delta_i^{14}$ is a conserved quantity (Tans et al., 1993), it follows that (see Turnbull et al., 2006):

$$C_{meas} \cdot \Delta_{meas}^{14} = C_{bg} \cdot \Delta_{bg}^{14} + C_{ff} \cdot \Delta_{ff}^{14} + C_{resp} \cdot \Delta_{resp}^{14} + C_{photo} \cdot \Delta_{photo}^{14} (+C_{ocean} \cdot \Delta_{ocean}^{14} + C_{strato} \cdot \Delta_{strato}^{14}) + C_{meas} \cdot \Delta_{nuc}^{14} \qquad (2)$$

The last term in Eq. 2 considers the potential contamination of the Δ_{meas}^{14} signature at the measurement site by ^{14}CO$_2$ emissions from nuclear facilities. These pure ^{14}CO$_2$ emissions cause a change in the measured Δ^{14}CO$_2$ (Δ_{nuc}^{14}) at the station but no change in the observed CO$_2$ concentration. For European stations the ICOS Carbon Portal (CP) provides a dedicated Jupyter notebook to calculate the contamination from nuclear facilities in Europe (freely available after registration at: https://www.icos-cp.eu/data-services/tools/jupyter-notebook, last access: October 05, 2022). With this

Jupyter notebook the 3-hourly footprints from each ICOS station can be mapped with the annual mean $^{14}CO_2$ emissions of the European nuclear facilities taken from the Radioactive Discharges Database (RADD). Hence, we use this Jupyter notebook to model for each $\Delta^{14}CO_2$ sample an individual Δ^{14}_{nuc} contribution. The used footprints were calculated with the Stochastic Time-Inverted Lagrangian Transport (STILT, Lin et al., 2003) model. Note that the influence from these (elevated) point sources requires an additional modelling effort if the nuclear installation is located at a distance smaller than ca. 50 km from the measurement site as shown by Maier et al. (2022). This modification has, however, not yet been implemented in the ICOS CP tool. We assume for the modelled Δ^{14}_{nuc} contributions an uncertainty of 100% to account for possible time dependent (sub-annual) variations in the nuclear $^{14}CO_2$ emissions as well as transport uncertainties. A brief description of how the nuclear $^{14}CO_2$ contributions Δ^{14}_{nuc} are calculated and a more detailed explanation of their assumed uncertainty is given in appendix A.1. The regional isotope budget approach assumes that the background station contains all nuclear contributions from outside the target area and that contaminations from nuclear facilities inside the target area are negligibly small at the background station. This assumption should be appropriate if we use a background site at which only marine air is sampled.

In the further evaluations, we neglect the contributions from (1) the ocean and (2) the stratosphere, because of the following reasons: (1) In Europe we mainly focus on continental measurement stations without direct oceanic influence. Therefore, we assume that the oceanic CO_2 contribution and its Δ^{14} signature are integrated in the background measurements. This assumption should be appropriate if we use a marine background station. (2) We further assume that the latitudinal and vertical differences between the measurement site and the background station are small enough, so that both stations are similarly influenced by ^{14}C-enriched stratospheric air; therefore, we assumed that also the stratospheric component is already integrated in the background measurements. Note that longitudinal differences in the stratospheric ^{14}C production and corresponding influence on tropospheric $\Delta^{14}C$ can be neglected (e.g. Lingenfelter, 1963).

As the $^{14}C/C$ ratio of fossil CO_2 is zero, the Δ^{14}_{ff} signature of fossil fuel combustion CO_2 is -1000‰. Therefore, Eq. 2 can directly be used to calculate the regionally added $ffCO_2$ contribution C_{ff} if all other CO_2 contributions and Δ^{14} signatures are known. However, as the two biospheric CO_2 components, C_{photo} and C_{resp}, are typically not known separately, it is convenient to use Eq. 1 for eliminating the (potentially poorest known) CO_2 contribution from photosynthesis C_{photo} in Eq. 2. As the Δ-notation accounts for mass-dependent isotopic fractionation, we can directly use the Δ^{14} signature of the photosynthesized atmospheric CO_2 to substitute the Δ^{14}_{photo} in Eq. 2. However, the Δ^{14} signature of an air mass changes on its path from the background station to the measurement site and therewith also the Δ^{14} signature taken up by photosynthesis (Δ^{14}_{photo}). Previous studies have either approximated the Δ^{14}_{photo}signature of the photosynthetically absorbed CO_2 with Δ^{14}_{bg} or with Δ^{14}_{meas}. If Δ^{14}_{photo} is approximated by the Δ^{14}_{meas} value of the ambient CO_2, the $ffCO_2$ excess can be calculated according to:

$$C_{ff} = C_{bg} \cdot \frac{\Delta^{14}_{bg} - \Delta^{14}_{meas}}{\Delta^{14}_{meas} + 1000\,‰} + C_{meas} \cdot \frac{\Delta^{14}_{nuc}}{\Delta^{14}_{meas} + 1000\,‰} + C_{resp} \cdot \frac{\Delta^{14}_{resp} - \Delta^{14}_{meas}}{\Delta^{14}_{meas} + 1000\,‰} \quad . \tag{3}$$

Otherwise, if Δ^{14}_{photo} is approximated with the background Δ^{14}_{bg} signature, one gets:

$$C_{ff} = C_{meas} \cdot \frac{\Delta^{14}_{bg} - \Delta^{14}_{meas}}{\Delta^{14}_{bg} + 1000\,‰} + C_{meas} \cdot \frac{\Delta^{14}_{nuc}}{\Delta^{14}_{bg} + 1000\,‰} + C_{resp} \cdot \frac{\Delta^{14}_{resp} - \Delta^{14}_{bg}}{\Delta^{14}_{bg} + 1000\,‰} \quad . \tag{4}$$

Which of the approximations, Eq. 3 or 4, better estimates regional ΔffCO$_2$ depends on how representative the respective Δ^{14}_{photo} approximation is for the biosphere affecting the measurement site. Eq. 3, for example, is suitable for remote stations that are significantly influenced by the local biosphere. Therefore, the Δ^{14}_{photo} signature of the (mainly contributing) local biosphere is best approximated by the measured Δ^{14}_{meas} signature of the ambient air CO$_2$ at the measurement site. In contrast, Eq. 4 might be applicable for stations with very little influence of the local biosphere and supposedly large local fossil emissions. Thus, it might be less appropriate to approximate the Δ^{14}_{photo} signature of the photosynthetically absorbed air with the strongly depleted ambient air Δ^{14}_{meas} signature. Indeed, for such cases the Δ^{14}_{bg} signature might more accurately describe the Δ^{14}_{photo} signature of the (mainly contributing) far field biosphere. The difference between using the two alternative equations will be evaluated in Sect. 3.1.1.

2.2 Importance of the components and correction terms in the regional isotope budget approach for estimating ΔffCO$_2$

The choice of the background station is crucial for the ΔffCO$_2$ estimate, since the first term in Eq. 3 and 4 is proportional to the Δ^{14} difference between the measurement station and the background station and usually contributes the most. Ideally, a single site can be used to provide a physically representative background for all other observation sites within a Δ^{14}CO$_2$ monitoring network. This will be the case when all observation sites within the sampling domain are influenced by the same weather systems, generally flowing from the background to the observation sites. In the modelling world, this would mean that the unique background should be valid for all boundaries of the targeted domain, for which the ffCO$_2$ flux shall be estimated. This assumption of representativeness is examined further in Sect. 3.1.2.

The second term in Eq. 3 and 4 describes the corrections for nuclear contaminations at the measurement site. Particularly in Europe with many nuclear power plants and two large nuclear fuel reprocessing plants (cf. Fig. A1), disregarding these nuclear contaminations would result in significant under-estimation of ΔffCO$_2$ estimates (Levin et al., 2003; Graven and Gruber, 2011; Kuderer et al., 2018).

The third term in Eq. 3 and 4 accounts for the correction for biosphere respiration, which, if not accounted for, may also mask part of the ΔffCO$_2$. The Δ^{14}_{resp} signature differs for autotrophic and heterotrophic respiration. In earlier studies (e.g. Levin et al., 2011), we approximated the autotrophic Δ^{14}_{resp} signature with that of background air, while for the heterotrophic component, we used the Δ^{14}C signature modelled by Naegler and Levin (2009b). Turnbull et al. (2006) assumed a mean terrestrial carbon residence time of 10±10 years and used the ^{14}C history of the Northern Hemisphere to calculate the Δ^{14} signature of heterotrophic respiration. Δ^{14}_{soil} of soil respiration was measured in summer 2012 at a boreal forest site in Finland by Palonen et al. (2018) to lie between (48.2 – 56.7) ‰, values about 20‰ higher than background air in that year. Chanca (2022) reported a mean Δ^{14}_{resp} of 32.0±7.4‰ for a tropical rainforest site in Brazil. This latter value was on average 29‰ higher than atmospheric CO$_2$ in that year. From these studies, we conclude that Δ^{14}_{resp} in the last decade was a few tens of ‰ higher than the contemporary atmospheric CO$_2$. We used the Vegetation Photosynthesis and Respiration Model (VPRM, Mahadevan et al., 2008) in combination with STILT to simulate the respiration CO$_2$ signal C_{resp} for the two ICOS sites Observatoire Pérenne de l'Environnement (OPE) in France and Křešín (KRE) in the Czech Republic. These results show on average about twice as high C_{resp} signals in summer than in winter. Overall, we would expect the typical range of C_{resp} to be between 2 and 8 ppm at ICOS sites in Central Europe.

3 Results

The aim of the present study is to quantify potential biases and estimate individual error contributions to the total uncertainty of ΔffCO$_2$ resulting from the uncertainties of the measured and estimated parameters and corrections in Eq. 3 and 4. In Sect. 3.1. we first evaluate the difference of results when approximating Δ^{14}_{photo} by Δ^{14}_{meas} or Δ^{14}_{bg}, respectively. Then, as a typical example for a populated region, we evaluate biases introduced in the ΔffCO$_2$ result when selecting only a single background station for Europe that is located on the western coast of Ireland. We will further quantify the biases in the ΔffCO$_2$ estimates, which would be induced when ignoring nuclear contaminations, and finally, we investigate the bias related to Δ^{14}C-enriched respiration CO$_2$. Sect. 3.2 investigates the relative uncertainty contributions introduced through (1) the uncertainty of the CO$_2$ and Δ^{14}CO$_2$ observations at the measurement station, (2) the uncertainty of the background Δ^{14}CO$_2$ curve, which incorporates the uncertainty of its construction (smooth curve fitted through observational data at that background station) as well as the uncertainty due to the representativeness of the background curve. We will (3) estimate the uncertainty of the correction for nuclear ^{14}CO$_2$ contamination and (4) the error contribution of the correction for heterotrophic respiration. Finally, we assess the total uncertainty of typical (bias-corrected) ΔffCO$_2$ estimates at European ICOS stations by identifying those components/parameters with the largest impact.

3.1 Potential bias components in the ΔffCO$_2$ estimates

3.1.1 Bias due to the approximation of Δ^{14}_{photo}(choice of Eq. 3 or 4)

To investigate the impact of the approximation of Δ^{14}_{photo} on the ΔffCO$_2$ estimates, i.e. the difference between Eq. 3 and 4, Fig. 1 shows the ratio of the ΔffCO$_2$ results from Eq. 3 and 4 plotted versus the $(\Delta^{14}_{bg} - \Delta^{14}_{meas})$ difference for typical current Δ^{14}CO$_2$ and CO$_2$ values (cf. Tab. 1) and a large range of possible ratios of C_{photo} to C_{ff}. As can be seen from Fig. 1, the differences in the final ΔffCO$_2$ results when using Eq. 4 vs. 3 can be large at stations where the (negative) photosynthetic component is much larger than the (positive) ΔffCO$_2$ component *and* if the Δ^{14}CO$_2$ difference between station and background is large. Typical $(\Delta^{14}_{bg} - \Delta^{14}_{meas})$ differences at ICOS stations go up to 10‰ (cf. Fig. 6 below), and in cases with high differences (large ΔffCO$_2$), i.e. in winter, the photosynthetic uptake is generally small, so that we expect $|C_{photo}/C_{ff}|$ ratios < 2 (see Fig. A2). Therefore, we expect biases between using Eq. 3 relative to Eq. 4 to be restricted to a few percent only. In summer, the $|C_{photo}/C_{ff}|$ ratio is larger but the Δ^{14}CO$_2$ difference to the background tends to be smaller, again pushing the difference between the equations into the range of few percent. As we are evaluating here typical biases and uncertainties of ^{14}C-based ΔffCO$_2$ at ICOS stations that are typically located more than 40 km away from large ffCO$_2$ emitting regions (ICOS RI, 2020), the photosynthetic uptake signals will most probably be larger than those from fossil emissions (see Fig. A2). Therefore, we restrict our further analysis on ΔffCO$_2$ estimates applying Eq. 3.

3.1.2 Biases due to the choice of one background station

Representation of background air with respect to individual ICOS stations:

The regional isotope budget approach estimates ΔffCO$_2$ with respect to a (measured) background. It implicitly assumes that the air masses arriving at the stations started with this background value. In order to use the ΔffCO$_2$ estimates to obtain information on fossil emissions in a given target area, it is necessary to assess the implicit assumption that the selected background is representative of all boundaries of this target area. We examine the representativeness problem using Europe and the ICOS observation network as an example target area. We base our evaluation on the standard STILT domain over Europe, which extends from 33°N to 73°N and from 15°W to 35°E (Fig. 2). The distribution of the typical air mass origins entering the STILT domain is constructed by the endpoints of hourly 10-days STILT back-trajectories for the year 2018 for nine ICOS stations, where regular Δ^{14}CO$_2$ observations are conducted. The abundance distributions of those trajectory endpoints at the four boundaries (Fig. 2) clearly indicate that these central European stations are predominantly influenced by westerly winds, which transport Atlantic air masses to the European continent. On average, 67% of the back-trajectories from the ICOS sites end at (or go beyond) the western boundary of the model domain, with an accumulation between roughly 45° and 60°N. This is a good argument to select Mace Head (MHD, 53.33°N, 9.90°W, 5 m a.s.l.), located close to the western boundary of the STILT domain, as a background site to calculate the ffCO$_2$ excess at European (ICOS) stations. Mace Head is located on the west coast of Ireland and atmospheric ^{14}CO$_2$ samples are only collected during situations when the air comes from the marine sector. These Δ^{14}CO$_2$ (together with CO$_2$) background measurements can thus be assumed as representative for the Atlantic boundary of the European continent. However, they may be less suitable as background reference in situations when the measurement stations are influenced by easterly (or southerly) air masses, which transport potentially polluted continental air to our domain. Also northerly Arctic air masses may have a different $\Delta^{14}CO_2$ level. Figure 2 shows that for on average 33% of the time in 2018 the air masses originated from non-western boundaries (or from within the target area) with on average 13% of all situations in 2018 entering via the eastern boundary.

Background variability at boundaries of the target area:

Currently, no background $\Delta^{14}CO_2$ observations exist in eastern Europe or close to the eastern boundary of our target domain. This makes it impossible to construct a purely observation-based $\Delta^{14}CO_2$ reference for the eastern air masses entering our target region and to deduce the bias of the representativeness problem from this. Therefore, we used the global atmospheric tracer transport model TM3 (Heimann and Körner, 2003; spatial resolution of 4° x 5°) to estimate $ffCO_2$ concentrations of air masses entering the eastern boundary of our domain. For this simulation, $ffCO_2$ emissions within the European target domain have been set to zero, while we used the Global Carbon Budget Gridded Fossil Emissions Dataset (GCP-GridFED; version 2022.2) emissions (Jones et al., 2022) elsewhere. The upper panels of Fig. 3 show the simulated $ffCO_2$ concentration difference of hourly data (purple dots) between a virtual station located at the eastern boundary of the STILT domain at mid-latitudes (55°N, 34°E, 150m a.g.l.) and Mace Head for the years 2016 – 2020. As expected, this difference is generally positive. It varies between a few tenths of a ppm up to more than 8 ppm in one event in 2020. A significant seasonal variation is observed, with higher concentration differences compared to MHD during winter and lower differences in summer. This seasonality is mainly due to seasonal variations of emissions, but also due to seasonal variations in atmospheric transport. As emissions within the target domain were set to zero in this TM3 model run, the concentration differences in Fig. 3 (upper panels) provide a good approximation of the $ffCO_2$ concentration offset (relative to MHD) of air masses entering the domain from the east. The upper left panel shows the biases for all hours in 2016 – 2020 and for averages of two-week integrated samples (black solid line). The upper right panel shows the difference for potential flask samples collected at midday. For any potential station located close to this border, this difference would represent the approximate positive bias of the calculated $\Delta ffCO_2$ for those situations when the station is *not* influenced by westerly air masses but by air from the east. The mean bias is about 20% larger for all hours and two-week integrated samples than for flask samples collected at midday. For flask samples, however, the standard deviation of that bias is about 30% higher than for two-week integrated samples since flask samples depend stronger on individual weather situations. The station in the ICOS network located closest to the eastern border of the target domain is Křešín (KRE). This station typically experiences about 16% of situations with easterly trajectories (Fig. 2). On average over *all* situations of potential flasks sampled at Křešín at midday, the $\Delta ffCO_2$ bias would thus be only 0.56 x 0.16 = 0.09 ppm. However, Křešín station is located about 20° west of the eastern boundary. Therefore, any contribution from domain-external $ffCO_2$ emissions coming from the east will be diluted during transport of the air mass to the station.

We can use similar arguments and the TM3 model results to estimate the influence on ICOS stations due to emissions from outside our domain from the west, e.g. from North America. The concentration from such sources as observed at Mace Head would also be (further) diluted when the air mass travels over Europe and reaches e.g. the Křešín station. This is why in the lower panel of Fig. 3, where we plot the difference of the TM3 concentrations simulated for KRE minus those at MHD, often turn out to be negative. Note that the positive values in this plot are the signals from the easterly trajectories, but here diluted during the transport from the eastern boundary to the Křešín site. As the majority of trajectories reaching Křešín comes from the west, the average difference is negative. In summary, we expect typical mean representativeness biases of order 0.1±0.3 ppm $\Delta ffCO_2$ when applying the regional isotope budget approach for the investigated example of the ICOS station network with MHD as a background in the STILT domain. A $ffCO_2$ inversion using our $\Delta ffCO_2$ estimates would incorrectly locate this 0.1±0.3 ppm representativeness bias within the STILT domain.

Influence of a latitudinal $\Delta^{14}CO_2$ *gradient:*

The Mace Head background station is located at about 55°N, a latitude where global fossil CO_2 emissions are large. We would, thus, expect lower fossil CO_2 concentrations at lower latitudes of the Northern Hemisphere, corresponding to slightly higher $\Delta^{14}CO_2$ in background air further south. Levin et al. (2021) published mean $\Delta^{14}CO_2$ data from Izaña station on Tenerife Island (28.3°N, 16.48°W, 2373 m a.s.l.) in the Atlantic Ocean, which indeed showed slightly higher values in the 1990s. However, in the last decade, the $\Delta^{14}CO_2$ difference to Mace Head is smaller than 1‰. As air masses only occasionally arrive from latitudes south of 40°N, the potential bias due to a latitudinal $\Delta^{14}CO_2$ gradient is assumed negligible and thus not taken into account here as a potential bias.

3.1.3 Biases due to nuclear $^{14}CO_2$ emissions

As mentioned before, $^{14}CO_2$ contaminations by emissions from nuclear installations are a potentially serious problem for ^{14}C-based $\Delta ffCO_2$ estimates in Europe (Graven and Gruber, 2011; Kuderer et al., 2018; see Fig. A1 for a distribution of the nuclear $^{14}CO_2$ emissions in Europe). This may be particularly true at stations with small $\Delta ffCO_2$ signals, i.e. small $\Delta^{14}CO_2$ depletion at the measurement station compared to the background ($\Delta^{14}_{bg} - \Delta^{14}_{meas}$). We, therefore, estimated the masking of $\Delta ffCO_2$ ($C_{ff}^{uncorrected}/C_{ff}^{nuc-corrected}$) with respect to the ratio between Δ^{14}_{nuc} and ($\Delta^{14}_{bg} - \Delta^{14}_{meas}$). As this masking effect (second term in Eq. 3) also depends on the CO_2 concentration at the measurement station, we estimated the masking for two typical concentrations, C_{meas} = 430 ppm and 450 ppm, respectively, as displayed in Fig. 4.

A relative Δ^{14}_{nuc} contamination from nuclear emissions of about 25% of the ($\Delta^{14}_{bg} - \Delta^{14}_{meas}$) signal would mask about 20% of the $\Delta ffCO_2$ signal. The nuclear correction is, thus, especially important for stations with small $\Delta^{14}C$-depletions compared to the background site, as indeed expected at ICOS atmosphere stations (see below, Fig. 6). Sampling during times with potential influence from nuclear installations should, therefore, be avoided, e.g. for flask sampling, or the bias must be calculated precisely (see Sec. 3.2.4).

3.1.4 Biases due to ^{14}C-enriched biosphere respiration

Also soil respiration can mask part of the fossil fuel-related Δ^{14}C difference between the stations and the background site. In this case, however, the contaminating source does not emit pure $^{14}CO_2$, as is the case for nuclear installations. The respired CO_2 today, if at all, is only slightly enriched in Δ^{14}C compared to contemporary ambient CO_2. Unfortunately, only very few measured data are available on Δ^{14}_{resp} in different ecosystems. These data suggest enrichments of a few tens of ‰ compared to atmospheric CO_2 (Palonen et al., 2018; Chanca, 2022). Figure 5 shows the masking of $\Delta ffCO_2$ ($C_{ff}^{uncorrected}/C_{ff}^{bio-corrected}$) in relation to the Δ^{14} difference between respired and measured CO_2 $\left(\Delta^{14}_{resp} - \Delta^{14}_{meas}\right)$ for a range of C_{resp}/C_{ff} ratios between 0.1 and 6.

If the C_{resp} signal has a similar magnitude as $\Delta ffCO_2$ (i.e. $C_{resp}/C_{ff} = 1$), which is a typical ratio in winter (see Fig. A2), the uncorrected $\Delta ffCO_2$ is underestimated by less than 5%, under the assumption that the Δ^{14} difference between respiration CO_2 and measured CO_2 is smaller than 40‰. Apparently, this bias increases with an increasing relative C_{resp} signal. Thus, the biosphere correction is potentially important at stations with low $\Delta ffCO_2$ and a high respiration component C_{resp}, which is the case for a number of ICOS stations in summer and in Northern Europe, i.e. far away from high $ffCO_2$ emission areas. Here we can find C_{resp}/C_{ff} ratios as large as 6 (see Fig. A2). In such situations, the $\Delta ffCO_2$ masking due to ignoring the biosphere correction (3rd term in Eq. 3) could become as large as 20%, if the Δ^{14} difference between respiration CO_2 and ambient air CO_2 is larger than 40‰.

3.1.5 Typical $\Delta^{14}CO_2$ signals at ICOS stations

The relevance of the two bias correction terms for nuclear and respiration contamination at ICOS stations discussed above depends on their individual influence areas with respect to fossil emitters and $^{14}CO_2$-emitting nuclear installations. It also depends on the type of samples collected (two-week integrated vs. midday flasks). Figure 6 shows in its upper left panel the distribution of $(\Delta^{14}_{bg} - \Delta^{14}_{meas})$ of two-week integrated samples collected in the years 2017-2020 at the nine ICOS stations shown in Fig. 1. The upper right panel in Fig. 6 gives the distribution of the mean Δ^{14}_{nuc} contaminations for the same stations and sample type. The median measured $\Delta^{14}CO_2$ difference between station and background (MHD) is only 3.8‰ while the median nuclear contamination amounts to about 30% of that value. If not corrected, this would correspond to an almost 25% masking of $\Delta ffCO_2$. This illustrates the importance of the nuclear contamination problem in Europe and the need to correctly model Δ^{14}_{nuc}. Such a correction could best be done with high-resolution emissions data and a reliable transport modelling system. Currently, however, only annual mean $^{14}CO_2$ emission data are available.

The lower panels of Fig. 6 show similar distributions as the upper panels, but for hourly flask samples collected at 13h local time. The median $(\Delta^{14}_{bg} - \Delta^{14}_{meas})$ difference for the currently available flask samples - yet collected only at seven ICOS class-1 stations - is 4.4‰, slightly larger than for two-week integrated samples, while the nuclear correction term is, on average, only half of that for the integrated samples. Still the average masking of about 15% is significant and should be corrected.

3.2 Uncertainty of the ΔffCO$_2$ estimates

After having quantified potential biases when using (1) Eq. 4 instead of Eq. 3 to estimate recently added ffCO$_2$, (2) the potential bias due to the use of a single background station for all European ICOS sites, (3) neglecting corrections for nuclear ^{14}CO$_2$ emissions and (4) for ΔffCO$_2$ masking due to ^{14}C-elevated biosphere respiration, in the following we evaluate the contributions to the total uncertainty of the bias-corrected ΔffCO$_2$, including the uncertainty due to these bias corrections.

3.2.1 Typical measurement uncertainty

One important uncertainty contribution to estimate recently added fossil CO$_2$ is the Δ^{14}CO$_2$ measurement uncertainty. This uncertainty is relevant for the measurements at the ICOS sites but also for estimating the background reference, here from MHD data. Both determine the uncertainty of the main term in Eq. 3 and 4. Typical high-precision radiocarbon laboratories measure single atmospheric ^{14}CO$_2$ samples with a precision between $\Delta^{14}C = (1.7 – 2.3)$ ‰ (e.g. Hammer et al., 2017). This range also covers the average precision and long-term repeatability in the ICOS Radiocarbon Laboratory for integrated and flask samples. For simplicity we assume here a measurement precision of 2‰ for all Δ^{14}CO$_2$ analyses.

3.2.2 Uncertainty of the ^{14}CO$_2$ background estimate

The uncertainty of the ^{14}CO$_2$ background estimate comprises two components. On the one hand, the uncertainties resulting from the construction of the ^{14}CO$_2$ background curve from the measurements at the background station, and on the other hand, the uncertainties resulting from the representativeness assumption. As illustrated in Sect. 3.1.2, using MHD as single background for all ICOS stations in western and central Europe could lead to a mean ΔffCO$_2$ bias of order 0.1 ppm for two-week integrated samples and also for flask samples collected over one hour at midday at the most easterly located station KRE. The standard deviation of this bias was estimated to 0.12 ppm for integrated and to 0.28 ppm for flask samples, with individual biases of up to 2 ppm in exceptional cases. The variability of the bias can be seen as the representativeness uncertainty of the ^{14}CO$_2$ background.

To construct a continuous Δ^{14}CO$_2$ background curve for MHD that is applicable for flask and integrated samples, we calculated a smooth curve through these data by using a curve fitting routine developed by the National Oceanic and Atmospheric Administration NOAA (Thoning et al., 1989). A detailed description how the background curve has been calculated is given in Appendix A.2. Two different uncertainty estimates have been made for the background reference, one based on the standard NOAA routine and a second one using a Monte Carlo approach. From these estimates we derived a mean uncertainty for Δ^{14}_{bg} of ±0.86‰. Adding the (independent) background representativeness uncertainty mentioned above, we obtain a total background reference uncertainty for integrated samples of 0.9‰ and for flask samples of 1.0‰. The uncertainty of the background CO_2 reference concentration curve is negligible for the overall $\Delta ffCO_2$ uncertainty, even if an assumed upper-limit CO_2 background representativeness uncertainty of 5 ppm is added.

3.2.3 Uncertainty of the nuclear and respiration masking corrections

In order to estimate the error contributions of the two correction terms in Eq. 3 (masking by nuclear $^{14}CO_2$ emissions, 2nd term, and contribution from respiration of ^{14}C-enriched CO_2, 3rd term), we made the following assumptions: We assume 100% uncertainty for the nuclear contamination estimates; this is justified with a significant transport model error to correctly simulate the dispersion and location of power plant plumes and by the fact that the significant temporal variability of the nuclear emissions (e.g. Kuderer et al., 2018) is totally ignored when using the currently reported annual mean emissions from RADD for estimating Δ^{14}_{nuc} (see Appendix A.1). The $\Delta ffCO_2$ masking contribution from CO_2 respiration, C_{resp}, has also a significant uncertainty because for daytime situations it has to be estimated using e.g. a vegetation model that is coupled to an atmospheric transport model. For nighttime situations when photosynthetic uptake of CO_2 is negligible, C_{resp} or C_{resp}/C_{ff}, the latter being the relevant parameter that determines the masking (cf. Fig. 5), could be estimated in an iterative way as the difference between $C_{meas,}$ C_{bg} and C_{ff}. Finally, we estimate the uncertainty of Δ^{14}_{resp} to be 50% of the difference between Δ^{14}_{resp} and Δ^{14}_{meas}. This means, if we measure a Δ^{14}_{meas} of 1‰ and assume a Δ^{14}_{resp} signature of 25‰, the applied uncertainty for Δ^{14}_{resp} would be 12‰. The dependence of the Δ^{14}_{resp} uncertainty on the ($\Delta^{14}_{resp} - \Delta^{14}_{meas}$) difference seems appropriate as the biosphere correction (3rd term in Eq. 3) is also dependent on the ($\Delta^{14}_{resp} - \Delta^{14}_{meas}$) difference (see Fig. 5).

3.2.4 Overall uncertainty of $\Delta ffCO_2$ for typical ICOS stations

The assumed concrete values and parameters that were used in the following overall error estimate of $\Delta ffCO_2$ derived from $\Delta^{14}CO_2$ measurements of two-week integrated and flask samples at typical ICOS stations and their assumed uncertainties are listed in Tab. 1. Figure 7 (left panel) shows the relative uncertainty of bias-corrected $\Delta ffCO_2$ in relation to the difference of Δ^{14} between background and station ($\Delta^{14}_{bg} - \Delta^{14}_{meas}$), while the right panel shows the absolute uncertainty in ppm. The different colors show different combinations of individual uncertainty contributions. It is obvious that the largest contribution to the overall uncertainty of bias-corrected $\Delta ffCO_2$ is due to the analytical error of the ^{14}C measurements, Δ^{14}_{meas}. When adding an uncertainty of the background reference Δ^{14}_{bg} of 1‰ and a typical nuclear contamination of Δ^{14}_{nuc} = (1 ± 1) ‰, the overall uncertainty of (bias-corrected) $\Delta ffCO_2$ is larger than 50% at an observed ($\Delta^{14}_{bg} - \Delta^{14}_{meas}$) difference smaller than 3.5‰. (Note that the uncertainty of C_{meas} and C_{bg} have not been added in Fig. 7 as both error contributions are negligible.) Considering the median ($\Delta^{14}_{bg} - \Delta^{14}_{meas}$) value (Fig. 6, upper panel), this means that, when ignoring the uncertainty due to respiration masking (yellow curve in Fig. 7), almost half of the ^{14}C-based $\Delta ffCO_2$ estimates from integrated samples at ICOS stations have an uncertainty > 50%. Only at observed

$(\Delta^{14}_{bg} - \Delta^{14}_{meas})$ differences larger than 8‰ the uncertainty of the ΔffCO$_2$ estimate becomes smaller than 25%. This illustrates the importance of precise Δ^{14}CO$_2$ measurements. If the Δ^{14}CO$_2$ measurement uncertainty can be reduced to 1‰, only about 1/3 of the integrated samples at ICOS stations would have an ΔffCO$_2$ uncertainty > 50%.

The right panel in Fig. 7 shows the absolute uncertainty of bias-corrected ΔffCO$_2$ in ppm. The absolute error is only slightly increasing to 1.1 ppm (for an assumed 2‰ Δ^{14}_{meas} uncertainty) with larger differences between background reference and station $(\Delta^{14}_{bg} - \Delta^{14}_{meas})$. The yellow curves in both panels of Fig. 7 show the uncertainty contribution from C_{resp}, when assuming that the respiration CO$_2$ (C_{resp}) signal is 3 times higher than C_{ff}. During summer, when the $(\Delta^{14}_{bg} - \Delta^{14}_{meas})$ difference is small, the C_{resp}/C_{ff} is often larger than 3 (see Fig. A2); however, in connection with low $(\Delta^{14}_{bg} - \Delta^{14}_{meas})$ differences the error contribution from respiration masking will still be small. Contrary, for situations with high fossil components, i.e. during winter, we expect a ratio of less than 3; therefore, we conclude that an uncertainty contribution of 0.5 ppm due to respiration masking correction, as shown in the right panel of Fig. 7, probably represents an upper limit. All-in-all, however, the potential uncertainty of ffCO$_2$ masking by ^{14}C-enriched soil respiration is non-negligible and potentially of similar magnitude as the uncertainty of the contamination from nuclear installations, if the respiration CO$_2$ is significantly ^{14}C-enriched compared to that of the ambient atmosphere.

4 Discussion and Conclusion

The property of fossil emissions being free from ^{14}C makes Δ^{14}CO$_2$ a unique and direct tracer for the fossil share in regional CO$_2$ excess compared to a (clean air) background. However, this method, called the regional isotope budget approach here, also has its challenges and uncertainties. In this study, we revisited the assumptions made to address these various challenges and gave an overall uncertainty of the ^{14}C-based ΔffCO$_2$ estimates so that those could be used in atmospheric inversion modelling to verify or evaluate fossil fuel emissions. In the following, we will summarise and discuss our main findings.

The first and most important decision is the choice of the background site, as the Δ^{14}CO$_2$ difference between observation and background site directly determines the ΔffCO$_2$ concentrations. In general, the background site should be chosen to suit the target area of the ffCO$_2$ emission estimates. For example, if the emissions of a city are to be sampled, it might be convenient to measure the signals from the city downwind and to use a regional or local background station upwind of the city (e.g. Turnbull et al., 2015). In our study, we wanted to select a background site for a station network like ICOS that covers wide parts of the European continent. If the ΔffCO$_2$ estimates derived with the regional isotope budget approach shall be used as a constraint in an inversion modelling framework to evaluate the fossil fuel emissions, the used background site has to be representative for all boundaries of the targeted domain. Otherwise, ΔffCO$_2$ signals originating from outside the domain would be distributed within the domain. For the European example, STILT back-trajectories suggest that the entire European domain is dominated by westerly winds in about 2/3 of all situations. Therefore, we chose Mace Head (MHD), located on the west coast of Ireland, as our background station. To construct a background $\Delta^{14}CO_2$ curve, we calculated a smooth fit through the integrated $\Delta^{14}CO_2$ observations of MHD and estimated its construction uncertainty to be less than 1‰. However, the clean Atlantic air background from MHD might be less representative for potentially slightly polluted continental air masses with non-western origin, which are expected to occur in about 1/3 of all situations. The lack of representativeness of the MHD reference for these situations induces a bias and an additional uncertainty to the $\Delta ffCO_2$ estimates. We used the global TM3 model (Heimann and Körner, 2003) and switched off the emissions from the European target area to estimate this representativeness bias and additional uncertainty. The bias depends on the distance between the observation site and the boundaries of the target area, as it affects the dilution of the background signal from the boundaries to the observation site. This means that potential observation sites close to the e.g. eastern boundary of the target domain can show substantial biases for situations when they are affected by CO_2 plumes from outside the target region. Therefore, the $\Delta ffCO_2$ estimates from such sites should be corrected for those biases if the $\Delta ffCO_2$ observations are to be used in inverse models to evaluate $ffCO_2$ emissions. Concerning the current ICOS atmosphere stations, these plumes from outside the European domain are typically well mixed when they arrive at the observation site; here we expect mean biases of order 0.1ppm. Therefore, we think that it is appropriate to use MHD as a single background site for the observation sites in Central Europe and for all wind conditions. Furthermore, we recommend to not exclude data under easterly wind conditions as this could lead to sampling biases if the $\Delta ffCO_2$ estimates are used in an atmospheric transport inversion to optimize $ffCO_2$ emissions. However, the variability in the bias induces a representativeness uncertainty of the MHD reference, which must be added quadratically to the MHD background fit uncertainty. This representativeness uncertainty depends also on the sample type. For Křešín (KRE), which is an eastern ICOS site in Central Europe and therefore expected to be most influenced by a false representation of the eastern boundary, the standard deviation of the bias amounts to 0.12 ppm for two-week integrated samples and 0.28 ppm for potential midday flasks; these could have a bias of up to 2 ppm. The overall background $\Delta^{14}CO_2$ uncertainty (0.9‰ for two-week integrated samples and 1.0‰ for flasks), i.e. the combination of the MHD fit and representativeness uncertainties, together with the measurement uncertainty of the $\Delta^{14}CO_2$ signals at the monitoring sites (ca. 2‰) account for ca. 0.9-1.0 ppm uncertainty of the $\Delta ffCO_2$ estimates for typical signals observed at ICOS sites (see Tab. 2).

In Europe, with more than 170 in-operation reactors and two reprocessing plants (IAEA-PRIS, 2022), the nuclear contamination of the $\Delta^{14}CO_2$ samples is a serious problem. The median nuclear contamination at the ICOS sites accounts for about 30% (for day-and-night integrated samples) and almost 15% (for flasks that are collected during midday integrated over one hour) of the median $\Delta^{14}CO_2$ depletion compared to the MHD reference. This would roughly result in a 25% and 15%, respectively, underestimation of the $\Delta ffCO_2$ estimates if no correction is applied. Therefore, we strongly recommend correcting the $\Delta ffCO_2$ estimates for nuclear contaminations, especially for sites with small signals or substantial influence from nuclear facilities. The uncertainty for the nuclear contaminations originates from the transport model uncertainty as well as the uncertainty of the nuclear $^{14}CO_2$ emissions. The transport model uncertainty depends on the sample type and the distance to the nuclear facilities. On the one hand, the nuclear corrections might be more reliable for integrated samples than for flasks as it is less relevant when exactly the plume of a nuclear point source hits the observation site. On the other hand, integrated samples include also nighttime situations when transport models show typically poorer performance. The uncertainty of the nuclear emissions is mainly based on the strong temporal variability of the emissions (Kuderer et al., 2018; Varga et al., 2021), which we could not consider as we only had access to the officially reported annual mean $^{14}CO_2$ emissions. Therefore, we assumed an uncertainty of 100% for the nuclear corrections. This increases the overall uncertainty of the nuclear corrected $\Delta ffCO_2$ estimates by about 0.1 ppm for a typical nuclear contamination of 1‰. Overall, and particularly for flask sampling, we suggest calculating near-real time (or even better forecast) back-trajectories or footprints so that sampling during situations with potentially large nuclear influences can be avoided.

Soil respiration CO_2 is expected to be a few tens of ‰ enriched in $\Delta^{14}CO_2$ compared to atmospheric CO_2, since it was initially fixed by plants during higher atmospheric $\Delta^{14}CO_2$ levels after the atmospheric nuclear bomb testing. Therefore, also respiration CO_2 may lead to masking part of the $\Delta ffCO_2$ signal, depending on the $\Delta^{14}CO_2$ difference between respired and atmospheric CO_2 and the relative amount of respired CO_2. For typical winter C_{resp}/C_{ff} ratios of 1 (see Fig. A2), the $\Delta ffCO_2$ masking is less than 5% if the respiration $\Delta^{14}CO_2$ signature is enriched by less than 40‰ compared to the ambient $\Delta^{14}CO_2$. However, this masking effect can easily increase for a larger relative share of respiration CO_2, e.g. during summer, and with higher soil respiration $\Delta^{14}CO_2$ signatures. For a typical summer C_{resp}/C_{ff} ratio of 6 at ICOS sites, the $\Delta ffCO_2$ masking reaches already almost 20% for a 40‰ $\Delta^{14}CO_2$ enrichment in the respired CO_2. Therefore, the correction for soil respiration is especially important for sites with low $ffCO_2$ signals and strong biosphere influence, which might be the case for many ICOS sites. The respiration CO_2 component in the ambient CO_2 concentration is hard to estimate, particularly during the day when photosynthesis is active. In these situations, a vegetation model in combination with an atmospheric transport model is needed. Therefore, we assume an uncertainty of 100% for the respiration CO_2. Moreover, we estimated the uncertainty of the respiration $\Delta^{14}CO_2$ signature to 50% of the $\Delta^{14}CO_2$ enrichment compared to the ambient $\Delta^{14}CO_2$. With those uncertainty assumptions, we expect the contribution of the uncertainty of the biosphere correction to the overall $\Delta ffCO_2$ uncertainty to be smaller than 0.5 ppm for typical ICOS sites.

In this study, we also investigated the effect, if the $\Delta^{14}CO_2$ signature of the photosynthetically absorbed CO_2 is approximated with the ambient air $\Delta^{14}CO_2$ at the measurement site (see Eq. 3) or, alternatively, with the background $\Delta^{14}CO_2$ observations (see Eq. 4). It turns out that the relative bias in the $\Delta ffCO_2$ estimates caused by these two different approximations is typically restricted to a few percent only. The choice between Eq. 3 or Eq. 4 to calculate the $\Delta ffCO_2$ concentrations may also depend on the availability of the required measurements. For example, Eq. 4 requires CO_2 concentration data at the observation site. However, in some cases, the CO_2 concentration at the observation site is not known, e.g. if the $\Delta ffCO_2$ is based on $\Delta^{14}C$ from plant material. For such cases, Eq. 3 might be more useful, as its major term depends on the background CO_2 concentration C_{bg} instead of C_{meas}. However, C_{meas} is also needed in the nuclear correction term (2nd term of Eq. 3). We, therefore, investigated the bias if C_{meas} is replaced by C_{bg} in Eq. 3. Obviously, it depends on the CO_2 concentration difference between C_{meas} and C_{bg} and the magnitude of the nuclear contamination. Even if the nuclear contamination is of the order of the Δ^{14} difference between measurement and background site, this bias will still be below 5% for CO_2 differences ($C_{meas} - C_{bg}$) of up to 40 ppm. Thus, this effect is much smaller compared to the bias introduced by neglecting the nuclear correction itself.

Overall, this study shows that the largest single uncertainty contribution to $\Delta ffCO_2$ estimates still comes from the limited precision in $\Delta^{14}CO_2$ analyses if the potential biases due to nuclear contamination or biosphere respiration are corrected for. Even a $\Delta^{14}CO_2$ measurement uncertainty of 1‰ would still make up a substantial contribution to the overall $\Delta ffCO_2$ uncertainty for typical ($\Delta_{bg}^{14} - \Delta_{meas}^{14}$) gradients at ICOS sites and assumed nuclear Δ_{nuc}^{14} contributions of 1‰. This means that about every second (or third) integrated sample from the ICOS network would yield a $\Delta ffCO_2$ uncertainty larger than 50% for an assumed 2‰ (or 1‰) $\Delta^{14}CO_2$ measurement uncertainty. These large relative $\Delta ffCO_2$ uncertainties can be explained by the small ($\Delta_{bg}^{14} - \Delta_{meas}^{14}$) gradients at the remote ICOS sites. Therefore, the regional isotope budget approach is best suited in polluted areas with large Δ_{meas}^{14} depletions due to fossil CO_2 emissions. In such cases, the regional isotope budget approach is also relatively less sensitive to possible representativeness biases in Δ_{bg}^{14}. If the transport-driven variability in the $\Delta ffCO_2$ estimates can be reproduced by an atmospheric transport model, the $\Delta ffCO_2$ observations can be used in inversion frameworks to estimate $ffCO_2$ emissions. Graven et al. (2018) used ^{14}C-based $\Delta ffCO_2$ observations from nine urban and non-urban sites in California to investigate the $ffCO_2$ surface fluxes with a Bayesian inversion framework based on Fischer et al. (2017). They could show that their estimates for the total in-state emissions are consistent with bottom-up estimates. Thus, it would also be interesting to investigate if the $\Delta ffCO_2$ observations from the ICOS sites can be used to estimate the $ffCO_2$ emissions in Europe. Indeed, the signal-to-noise constraints that limit the $\Delta ffCO_2$ detection at remote sites might not limit the inverse problem in the same way. Thus, the large and growing number of samples from distributed ICOS sites with small but persistent $\Delta ffCO_2$ signals may provide meaningful adjustments of the $ffCO_2$ surface fluxes in Central Europe. An alternative approach to investigate $ffCO_2$ emissions is the dual-tracer inversion, which uses the CO_2 and $\Delta^{14}CO_2$ observations directly. This approach has already successfully been applied in the US by Basu et al. (2020). The authors used the CO_2 and $\Delta^{14}CO_2$ observations from the NOAA station network in Northern America and showed that the estimated US national total $ffCO_2$ emissions for 2010 are significantly larger than reported by bottom-up inventories. Undoubtedly, this dual-tracer inversion approach should also be implemented in Europe to take advantage of the ICOS observation network. Ideally, the results of the $ffCO_2$ inversion and the dual-tracer inversion would then converge within their individual uncertainty margins.

Certainly, a big challenge in Europe is the large number of nuclear power plants (Graven and Gruber, 2011), which affect both, the regional isotope budget approach, and the dual-tracer inversion approach. Thus, there is an urgent need for temporally highly resolved (i.e. at least monthly or weekly) $^{14}CO_2$ emissions data from nuclear facilities in Europe, so that reliable and un-biased $ffCO_2$ emission estimates can be deduced. In other parts of the world with a much lower spatial density of nuclear installations this "nuclear problem" seems to be less prominent than in Europe. However, we showed that the biosphere respiration could lead to similar biases as the nuclear contaminations if not properly taken into account. In other rural regions of the world the respiration Δ^{14}_{resp} might be different, depending on climate and vegetation types. This must be considered, so that $\Delta ffCO_2$ concentrations can be estimated bias-free. But also, the dual-tracer inversion requires a reliable a priori representation of the Δ^{14}_{resp} signature.

Finally, we showed that a marine site located at the western edge of the European target region is an appropriate background site for calculating $\Delta ffCO_2$ estimates for sites in Central Europe. Similarly, Graven et al. (2018) used measurements from three coastal sites in California to construct a $\Delta^{14}CO_2$ background for observation sites in California. Zhou et al. (2020) defined the Qixianling Mountain, which is located on the Hainan Island in the south of China as a background to estimate $\Delta ffCO_2$ concentrations for 15 Chinese cities. To conclude, if the $\Delta^{14}C$ observations of a single site are used to estimate $\Delta ffCO_2$ concentrations for an observation network, a potential background representativeness bias and uncertainty should be investigated by either comparing the Δ^{14}_{bg} values with observations from other potential background sites or estimating the representativeness bias via model simulations as in the present study.

Acknowledgements

We are grateful to Sabine Kühr, Eva Gier, Julian Della Coletta and the whole staff of the ICOS Central Radiocarbon Laboratory (CRL) as well as the ICOS Atmosphere stations for collecting and analysing the integrated and flask samples. Moreover, we like to thank Ida Storm and the members of the ICOS Carbon Portal for developing and providing a Jupyter notebook for the estimation of nuclear $^{14}CO_2$ contaminations at the ICOS stations. The ICOS-CRL is funded by the German Federal Ministry for Digital and Transport. FM was funded by the VERIFY Project (EC grant no. 776810).

References

Basu, S., Miller, J. B., and Lehman, S.: Separation of biospheric and fossil fuel fluxes of CO_2 by atmospheric inversion of CO_2 and $^{14}CO_2$ measurements: Observation System Simulations, Atmos. Chem. Phys., 16, 5665–5683, https://doi.org/10.5194/acp-16-5665-2016, 2016.

Basu, S., Lehman, S. J., Miller, J. B., Andrews, A. E., Sweeney, C., Gurney, K. R., Xue, X., Southon, J., and Tans, P. P.: Estimating US fossil fuel CO_2 emissions from measurements of ^{14}C in atmospheric CO_2, PNAS 117(24): 13300–13307, https://doi.org/10.1073/pnas.1919032117, 2020.

Bergamaschi, P., Danila, A., Weiss, R. F., Ciais, P., Thompson, R. L., Brunner, D., Levin, I., Meijer, Y., Chevallier, F., Janssens-Maenhout, G., Bovensmann, H., Crisp, D., Basu, S., Dlugokencky, E., Engelen, R., Gerbig, C., Günther, D., Hammer, S., Henne, S., Houweling, S., Karstens, U., Kort, E., Maione, M., Manning, A. J., Miller, J., Montzka, S., Pandey, S., Peters, W., Peylin, P., Pinty, B., Ramonet, M., Reimann, S., Röckmann, T., Schmidt, M., Strogies, M., Sussams, J., Tarasova, O., van Aardenne, J., Vermeulen, A. T., and Vogel, F.: Atmospheric monitoring and inverse modelling for verification of greenhouse gas inventories, JRC111789, EUR 29276 EN, Publications Office of the European Union, Luxembourg, ISBN 978-92-79-88938-7, doi:10.2760/759928, 2018.

Berhanu, T. A., Szidat, S., Brunner, D., Satar, E., Schanda, R., Nyfeler, P., Battaglia, M., Steinbacher, M., Hammer, S., and Leuenberger, M.: Estimation of the fossil fuel component in atmospheric CO_2 based on radiocarbon measurements at the Beromünster tall tower, Switzerland, Atmos. Chem. Phys., 17, 10753–10766, https://doi.org/10.5194/acp-17-10753-2017, 2017.

Caldeira, K., Rau, G. H., Duffy, P. B.: Predicted net efflux of radiocarbon from the ocean and increase in atmospheric radiocarbon content, Geophys. Res. Lett., 25(20), 3811-3814, https://doi.org/10.1029/1998GL900010, 1998.

Chanca, Ingrid: Theoretical and experimental approaches using $\Delta^{14}C$ for estimating system diagnostic times in the central Amazon rainforest, PhD Thesis, Instituto de Física, Universidade Federal Fluminense, 2022.

Fischer, M. L., Parazoo, N., Brophy, K., Cui, X., Jeong, S., Liu, J., Keeling, R., Taylor, T. E., Gurney, K., Oda, T., Graven, H.: Simulating estimation of California fossil fuel and biosphere carbon dioxide exchanges combining in situ tower and satellite column observations, J. Geophys. Res. Atmos., 122, 3653– 3671, doi:10.1002/2016JD025617, 2017.

Friedlingstein, P., Jones, M. W., O'Sullivan, M., Andrew, R. M., Bakker, D. C. E., Hauck, J., Le Quéré, C., Peters, G. P., Peters, W., Pongratz, J., Sitch, S., Canadell, J. G., Ciais, P., Jackson, R. B., Alin, S. R., Anthoni, P., Bates, N. R., Becker, M., Bellouin, N., Bopp, L., Chau, T. T. T., Chevallier, F., Chini, L. P., Cronin, M., Currie, K. I., Decharme, B., Djeutchouang, L. M., Dou, X., Evans, W., Feely, R. A., Feng, L., Gasser, T., Gilfillan, D., Gkritzalis, T., Grassi, G., Gregor, L., Gruber, N., Gürses, Ö., Harris, I., Houghton, R. A., Hurtt, G. C., Iida, Y., Ilyina, T., Luijkx, I. T., Jain, A., Jones, S. D., Kato, E., Kennedy, D., Klein Goldewijk, K., Knauer, J., Korsbakken, J. I., Körtzinger, A., Landschützer, P., Lauvset, S. K., Lefèvre, N., Lienert, S., Liu, J., Marland, G., McGuire, P. C., Melton, J. R., Munro, D. R., Nabel, J. E. M. S., Nakaoka, S.-I., Niwa, Y., Ono, T., Pierrot, D., Poulter, B., Rehder, G., Resplandy, L., Robertson, E., Rödenbeck, C., Rosan, T. M., Schwinger, J., Schwingshackl, C., Séférian, R., Sutton, A. J., Sweeney, C., Tanhua, T., Tans, P. P., Tian, H., Tilbrook, B., Tubiello, F., van der Werf, G. R., Vuichard, N., Wada, C., Wanninkhof, R., Watson, A. J., Willis, D., Wiltshire, A. J., Yuan, W., Yue, C., Yue, X., Zaehle, S., and Zeng, J.: Global Carbon Budget 2021, Earth Syst. Sci. Data, 14, 1917–2005, https://doi.org/10.5194/essd-14-1917-2022, 2022.

Graven, H. D. and Gruber, N.: Continental-scale enrichment of atmospheric $^{14}CO_2$ from the nuclear power industry: potential impact on the estimation of fossil fuel-derived CO_2, Atmos. Chem. Phys., 11, 12339–12349, https://doi.org/10.5194/acp-11-12339-2011, 2011.

Graven, H., Fischer, M. L., Lueker, T., Jeong, S., Guilderson, T. P., Keeling, R. F., Bambha, R., Brophy, K., Callahan, W., Cui, X., Frankenberg, C., Gurney, K. R., LaFranchi, B. W., Lehman, S. J., Michelsen, H., Miller, J. B., Newman, S., Paplawsky, W., Parazoo, N. C., Sloop, C., Walker, S. J.: Assessing fossil fuel CO2 emissions in California using atmospheric observations and models, Environ. Res. Lett., 13, 065007, https://doi.org/10.1088/1748-9326/aabd43, 2018.

Hammer, S., Friedrich, R., Kromer, B., Cherkinsky, A., Lehman, S., Meijer, H., Nakamura, T., Palonen, V., Reimer, R. W., Smith, A. M., Southon, J. R., Szidat, S., Turnbull, J., and Uchida, M.: Compatibility of Atmospheric $^{14}CO_2$ Measurements: Comparing the Heidelberg Low-Level Counting Facility to International Accelerator Mass Spectrometry (AMS) Laboratories, Radiocarbon, 59(3), 875-883, doi:10.1017/RDC.2016.62, 2017.

Heimann, M. and Körner, S.: The Global Atmospheric Tracer Model TM3, Model Description and User's Manual Release 3.8a, Tech. Rep. 5, Max Planck Institute for Biogeochemistry (MPI-BGC), Jena, Germany, 2003.

Heiskanen, J., Brümmer, C., Buchmann, N., Calfapietra, C., Chen, H., Gielen, B., Gkritzalis, T., Hammer, S., Hartman, S., Herbst, M., Janssens, I. A., Jordan, A., Juurola, E., Karstens, U., Kasurinen, V., Kruijt, B., Lankreijer, H., Levin, I., Linderson, M., Loustau, D., Merbold, L., Myhre, C. L., Papale, D., Pavelka, M., Pilegaard, K., Ramonet, M., Rebmann, C., Rinne, J., Rivier, L., Saltikoff, E., Sanders, R., Steinbacher, M., Steinhoff, T., Watson, A., Vermeulen, A. T., Vesala, T., Vítková, G., and Kutsch, W.: The Integrated Carbon Observation System in Europe, Bulletin of the American Meteorological Society, 103(3), E855-E872, https://doi.org/10.1175/BAMS-D-19-0364.1, 2022.

ICOS RI: ICOS Atmosphere Station Specifications V2.0 edited by: Laurent, O., ICOS ERIC, https://doi.org/10.18160/GK28-2188, 2020.

IAEA-PRIS: International Atomic Energy Agency - Power Reactor Information System, https://pris.iaea.org/pris/home.aspx, last access: October 05, 2022.

Janssens-Maenhout, G., Crippa, M., Guizzardi, D., Muntean, M., Schaaf, E., Dentener, F., Bergamaschi, P., Pagliari, V., Olivier, J. G. J., Peters, J. A. H. W., van Aardenne, J. A., Monni, S., Doering, U., Petrescu, A. M. R., Solazzo, E., and Oreggioni, G. D.: EDGAR v4.3.2 Global Atlas of the three major greenhouse gas emissions for the period 1970–2012, Earth Syst. Sci. Data, 11, 959–1002, https://doi.org/10.5194/essd-11-959-2019, 2019.

Jones, M. W., Andrew, R. M., Peters, G. P., Janssens-Maenhout, G., De-Gol, A. J., Dou, X., Liu, Z., Pickers, P., Ciais, P., Patra, P. K., Chevallier, F., and Le Quéré, C.: Gridded fossil CO_2 emissions and related O_2 combustion consistent with national inventories 1959-2021 (GCP-GridFEDv2022.2) [Data set], Zenodo, https://doi.org/10.5281/zenodo.7016360, 2022.

Kuderer, M., Hammer, S., and Levin, I.: The influence of $^{14}CO_2$ releases from regional nuclear facilities at the Heidelberg $^{14}CO_2$ sampling site (1986–2014), Atmos. Chem. Phys., 18, 7951–7959, https://doi.org/10.5194/acp-18-7951-2018, 2018.

Levin, I., Münnich, K. O., and Weiss, W.: The Effect of Anthropogenic CO_2 and ^{14}C Sources on the Distribution of ^{14}C in the Atmosphere, Radiocarbon, 22(2), 379-391, https://doi.org/10.1017/S003382220000967X, 1980.

Levin, I., Kromer, B., Schmidt, M., and Sartorius, H.: A novel approach for independent budgeting of fossil fuel CO_2 over Europe by $^{14}CO_2$ observations, Geophys. Res. Lett., 30, 2194, https://doi.org/10.1029/2003GL018477, 2003.

Levin, I. and Rödenbeck, C.: Can the envisaged reductions of fossil fuel CO_2 emissions be detected by atmospheric observations?, Naturwissenschaften, 95(3), 203-208, DOI. 10.1007/s00114-007-0313-4, 2008.

Levin, I., Hammer, S., Eichelmann, E., and Vogel, F.: Verification of greenhouse gas emission reductions: The prospect of atmospheric monitoring in polluted areas, Philosophical Transactions A, 369, 1906-1924, doi:10.1098/rsta.2010.0249, 2011.

Levin, I., Karstens, U., Eritt, M., Maier, F., Arnold, S., Rzesanke, D., Hammer, S., Ramonet, M., Vítková, G., Conil, S., Heliasz, M., Kubistin, D., and Lindauer, M.: A dedicated flask sampling strategy developed for Integrated Carbon Observation System (ICOS) stations based on CO_2 and CO measurements and Stochastic Time-Inverted Lagrangian Transport (STILT) footprint modelling, Atmos. Chem. Phys., 20, 11161–11180, https://doi.org/10.5194/acp-20-11161-2020, 2020.

Levin, I., Hammer, S., Kromer, B., Preunkert, S., Weller, R., and Worthy, D.: Radiocarbon in global tropospheric carbon dioxide, Radiocarbon, 1-11. doi:10.1017/RDC.2021.102, 2021.

Lin, J. C., Gerbig, C., Wofsy, S. C., Andrews, A. E., Daube, B. C., Davis, K. J., and Grainger, C. A.: A near-field tool for simulating the upstream influence of atmospheric observations: The Stochastic Time-Inverted Lagrangian Transport (STILT) model, J. Geophys. Res., 108, 4493, https://doi.org/10.1029/2002JD003161, 2003.

Lingenfelter, R. E.: Production of carbon 14 by cosmic-ray neutrons, Rev. Geophys., 1(1), 35–55, doi:10.1029/RG001i001p00035, 1963.

Mahadevan, P., Wofsy, S. C., Matross, D. M., Xiao, X., Dunn, A. L., Lin, J. C., Gerbig, C., Munger, J. W., Chow, V. Y., and Gottlieb, E. W.: A satellite-based biosphere parameterization for net ecosystem CO_2 exchange: Vegetation Photosynthesis and Respiration Model (VPRM), Global Biogeochem. Cycles, 22, GB2005, doi:10.1029/2006GB002735, 2008.

Maier, F., Gerbig, C., Levin, I., Super, I., Marshall, J., and Hammer, S.: Effects of point source emission heights in WRF–STILT: a step towards exploiting nocturnal observations in models, Geosci. Model Dev., 15, 5391–5406, https://doi.org/10.5194/gmd-15-5391-2022, 2022.

Major, I., Haszpra, L., Rinyu, L., Futó, I., Bihari, Á, Hammer, S., Jull, A. J. T., and Molnár, M.: Temporal variation of atmospheric fossil and modern CO_2 excess at a Central European rural tower station between 2008 and 2014, Radiocarbon, 60(5), 1285-1299, 2018.

Miller, J. B., Lehman, S. J., Montzka, S. A., Sweeney, C., Miller, B. R., Karion, A., Wolak, C., Dlugokencky, E. J., Southon, J., Turnbull, J. C., and Tans, P. P.: Linking emissions of fossil fuel CO_2 and other anthropogenic trace gases using atmospheric $^{14}CO_2$, Journal of Geophysical Research, 117, D08302, 10.1029/2011JD017048, 2012.

Naegler, T. and Levin, I.: Observation-based global biospheric excess radiocarbon inventory 1963-2005, J. Geophys. Res. 114, D17302, doi:10.1029/2008JD011100, 2009a.

Naegler, T. and Levin, I.: Biosphere-atmosphere gross carbon exchange flux and the $\delta^{13}CO_2$ and $\Delta14CO_2$ disequilibria constrained by the biospheric excess radiocarbon inventory, J. Geophys. Res., 114, D17303, doi:10.1029/2008JD011116, 2009b.

Palonen, V., Pumpanen, J., Kulmala, L., Levin, I., Heinonsalo, J., and Vesala, T.: Seasonal and Diurnal Variations in Atmospheric and Soil Air $^{14}CO_2$ in a Boreal Scots Pine Forest, Radiocarbon, 60(1), 283-297, doi:10.1017/RDC.2017.95, 2018.

Petrescu, A. M. R., Qiu, C., Ciais, P., Thompson, R. L., Peylin, P., McGrath, M. J., Solazzo, E., Janssens-Maenhout, G., Tubiello, F. N., Bergamaschi, P., Brunner, D., Peters, G. P., Höglund-Isaksson, L., Regnier, P., Lauerwald, R., Bastviken, D., Tsuruta, A., Winiwarter, W., Patra, P. K., Kuhnert, M., Oreggioni, G. D., Crippa, M., Saunois, M., Perugini, L., Markkanen, T., Aalto, T., Groot Zwaaftink, C. D., Tian, H., Yao, Y.,Wilson, C., Conchedda, G., Günther, D., Leip, A., Smith, P., Haussaire, J.-M., Leppänen, A., Manning, A. J., McNorton, J., Brockmann, P., and Dolman, A. J.: The consolidated European synthesis of CH_4 and N_2O emissions for the European Union and United Kingdom: 1990–2017, Earth Syst. Sci. Data, 13, 2307– 2362, https://doi.org/10.5194/essd-13-2307-2021, 2021.

Potier, E., Broquet, G., Wang, Y., Santaren, D., Berchet, A., Pison, I., Marshall, J., Ciais, P., Bréon, F.-M., and Chevallier, F.: Complementing XCO_2 imagery with ground-based CO_2 and $^{14}CO_2$ measurements to monitor CO_2 emissions from fossil fuels on a regional to local scale, Atmos. Meas. Tech., 15, 5261–5288, https://doi.org/10.5194/amt-15-5261-2022, 2022.

RADD: European Commission RAdioactive Discharges Database, https://europa.eu/radd/query.dox?pageID=Query, last access: March 11, 2022.

Randerson, J. T., Enting, I. G., Schuur, E. A. G., Caldeira, K., and Fung, I. Y.: Seasonal and latitudinal variability of troposphere $\Delta^{14}CO_2$: Post bomb contributions from fossil fuels, oceans, the stratosphere, and the terrestrial biosphere, Global Biogeochem. Cycles, 16(4), 1112, doi:10.1029/2002GB001876, 2002.

Stuiver, M. and Polach, H.: Discussion Reporting of ^{14}C Data, Radiocarbon, 19(3), 355-363, doi:10.1017/S0033822200003672, 1977.

Tans, P. P., Berry, J. A., and Keeling, R. F.: Ocean $^{13}C/^{12}C$ observations: A new window on ocean CO_2 uptake, Global Biogeochem. Cycles, 7(2), 353– 368, 1993.

Thoning, K. W., Tans, P. P., and Komhyr, W. D.: Atmospheric carbon dioxide at Mauna Loa Observatory: 2. Analysis of the NOAA GMCC data, 1974–1985, J. Geophys. Res., 94(D6), 8549–8565, doi:10.1029/JD094iD06p08549, 1989.

Turnbull, J. C., Miller, J. B., Lehman, S. J., Tans, P. P., Sparks, R. J., and Southon, J.: Comparison of $^{14}CO_2$, CO, and SF_6 as tracers for recently added fossil fuel CO_2 in the atmosphere and implications for biological CO_2 exchange, Geophys. Res. Lett., 33, L01817, https://doi.org/10.1029/2005GL024213, 2006.

Turnbull, J., Sweeney, C., Karion, A., Newberger, T., Lehman, S., Tans, P., Davis, K., Lauvaux, T., Miles, N., Richardson, S., Cambaliza, M., Shepson, P., Gurney, K., Patarasuk, R., and Razlivanov, I.: Toward quantification and source sector identification of fossil fuel CO_2 emissions from an urban area: Results from the INFLUX experiment, J. Geophys. Res. Atmos., 120, 292– 312, doi:10.1002/2014JD022555, 2015.

Varga, T., Major, I., Gergely, V., Lencsés, A., Bujtás, T., Jull, A. J. T., Veres, M., and Molnár, M.: Radiocarbon in the atmospheric gases and PM10 aerosol around the Paks Nuclear Power Plant, Hungary, Journal of Environmental Radioactivity, Volume 237, 106670, ISSN 0265-931X, https://doi.org/10.1016/j.jenvrad.2021.106670, 2021.

Wang, Y., Broquet, G., Ciais, P., Chevallier, F., Vogel, F., Wu, L., Yin, Y., Wang, R., and Tao, S.: Potential of European $^{14}CO_2$ observation network to estimate the fossil fuel CO_2 emissions via atmospheric inversions, Atmos. Chem. Phys., 18, 4229–4250, https://doi.org/10.5194/acp-18-4229-2018, 2018.

Zazzeri, G., Acuña Yeomans, E., and Graven, H.: Global and Regional Emissions of Radiocarbon from Nuclear Power Plants from 1972 to 2016, Radiocarbon, 60(4), 1067-1081, doi:10.1017/RDC.2018.42, 2018.

Zhou, W., Niu, Z., Wu, S., Xiong, X., Hou, Y., Wang, P., Feng, T., Cheng, P., Du, H., Lu, X., An, Z., Burr, G. S., Zhu, Y.: Fossil fuel CO_2 traced by radiocarbon in fifteen Chinese cities, Science of The Total Environment, Volume 729, 138639, ISSN 0048-9697, https://doi.org/10.1016/j.scitotenv.2020.138639, 2020.

Tables

Table 1: Assumed values and parameters for our standard uncertainty evaluation.

Parameter	Value ± uncertainty	Description
C_{meas}	420 ± 0.1 ppm	CO_2 concentration at station
Δ^{14}_{meas}	± 2 ‰	typical $\Delta^{14}CO_2$ measurement uncertainty
C_{bg}	(410 ± 1) ppm	background CO_2 concentration
Δ^{14}_{bg}	(3 ± 1) ‰	taken from fitted background curve of MHD data
Δ^{14}_{nuc}	(1 ± 1) ‰	typical nuclear $\Delta^{14}CO_2$ contamination at ICOS stations
C_{resp}/C_{ff}	3 ± 3	respiration CO_2 component relative to $\Delta ffCO_2$
Δ^{14}_{resp}	(25 ± 12) ‰	respiration $\Delta^{14}CO_2$ signature

Table 2: Contributions to the overall ΔffCO₂ uncertainty. The shown uncertainties are representative of a range of ($\Delta^{14}_{bg} - \Delta^{14}_{meas}$) differences from -2 to 20‰, which covers most of the observed range in Fig. 6. The uncertainty contribution of a certain parameter is the increase in the ΔffCO₂ uncertainty if the uncertainty of this parameter is (quadratically) added to the ΔffCO₂ uncertainty, which was caused by the previous parameters (in the rows above this certain parameter).

Parameter	Contribution to overall ΔffCO₂ uncertainty	Parameter value ± uncertainty
Δ^{14}_{meas}	0.8 – 0.9 ppm	± 2 ‰
Δ^{14}_{bg}	0.1 ppm	(3 ± 1) ‰
Δ^{14}_{nuc}	0.1 ppm [0.3 ppm]	(1 ± 1) ‰ [(2 ± 2) ‰]
Δ^{14}_{resp}	0 – 0.05 ppm	(25 ± 12) ‰
C_{resp}/C_{ff}	0 – 0.5 ppm	3 ± 3
C_{bg}	$\sim 10^{-4}$ ppm	(410 ± 1) ppm
C_{meas}	$\sim 10^{-9}$ ppm	(420 ± 0.1) ppm

Figures

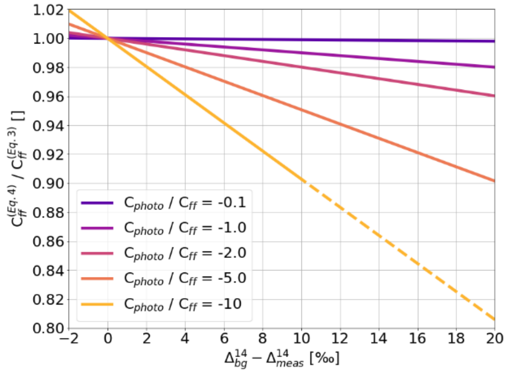

Figure 1: Ratio of ΔffCO₂ when estimated with Eq. 4 vs. Eq. 3 for C_{photo}/C_{ff} ratios ranging from -0.1 to -10.

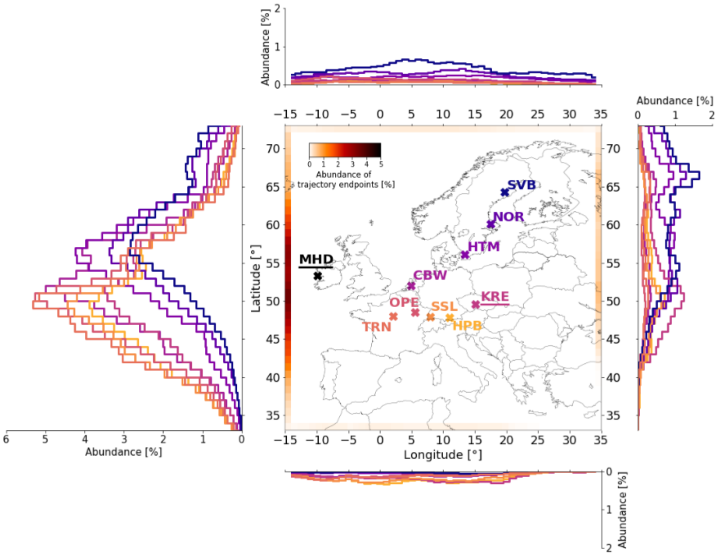

Figure 2: Abundance distribution for the endpoints of the STILT back-trajectories from nine ICOS sites (colored crosses) in 2018. At each hour and each station, 100 particles were released in STILT, and their back-trajectories were calculated for 10 days backward in time. If the trajectory leaves the shown domain, its endpoint is defined as the grid cell where the trajectory leaves the domain the first time. STILT was driven with the 0.25° resolved ERA5 (European ReAnalysis 5) meteorology from the European Center for Medium-Range Weather Forecasts (ECMWF). The black cross indicates the position of the Mace Head (MHD) background site (back-trajectories were not calculated for MHD).

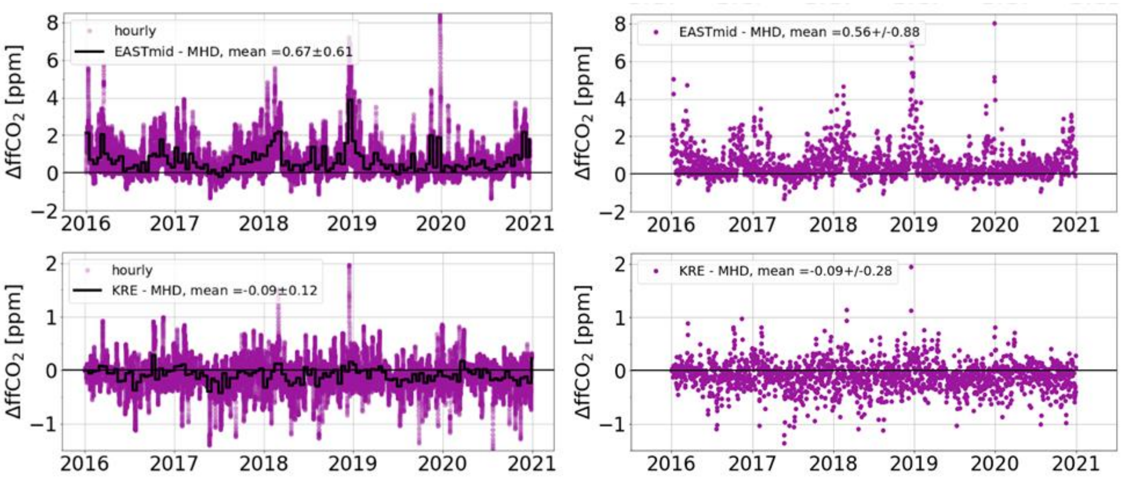

Figure 3: TM3-simulated fossil fuel CO₂ concentration offsets relative to Mace Head caused by emissions outside of our target region (Fig. 2). The upper panels show the offsets at a location at mid-latitudes of the eastern boundary, for all hours (left panel) and for 13h UTC only (right panel). The lower panels show corresponding data for the ICOS station Křešín (KRE). Note the different scales in upper and lower panels.

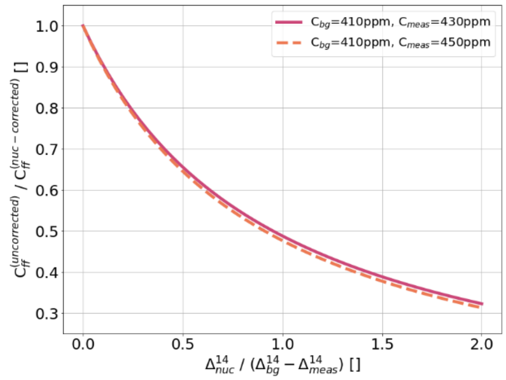

Figure 4: ΔffCO₂ masking by $^{14}CO_2$ *emissions from nuclear installations in relation to the ratio between* Δ_{nuc}^{14} *and* $(\Delta_{bg}^{14} - \Delta_{meas}^{14})$*.*

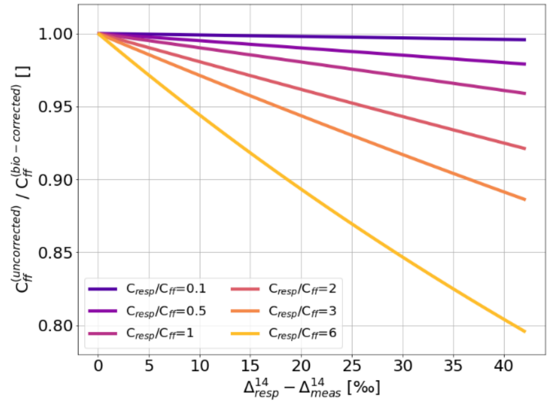

Figure 5: ΔffCO₂ masking by ^{14}C*-enriched respiration CO₂ plotted vs. the difference between* $(\Delta_{resp}^{14} - \Delta_{meas}^{14})$ *for* C_{resp}/C_{ff} *ratios between 0.1 and 6.*

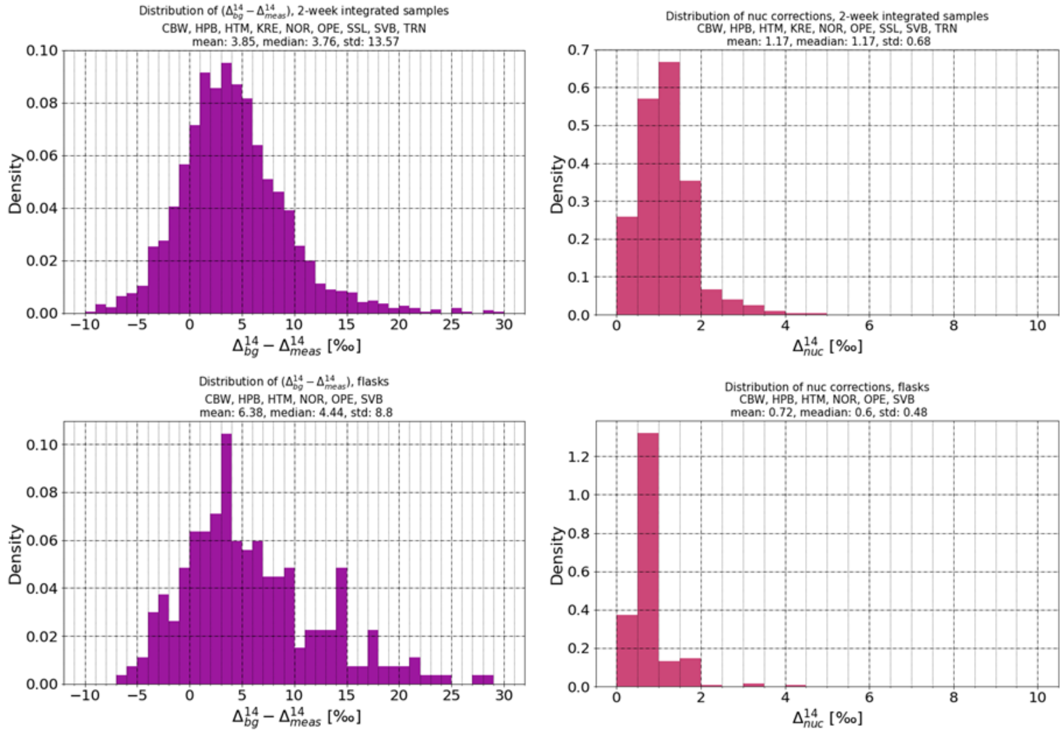

Figure 6: Distribution of observed Δ^{14} signals between reference station (MHD) and ICOS stations (in the left panels, the upper graph shows the data for two-week integrated samples, the lower graph those for the currently available flask samples). The right panels show the distributions of the estimated nuclear corrections of the samples.

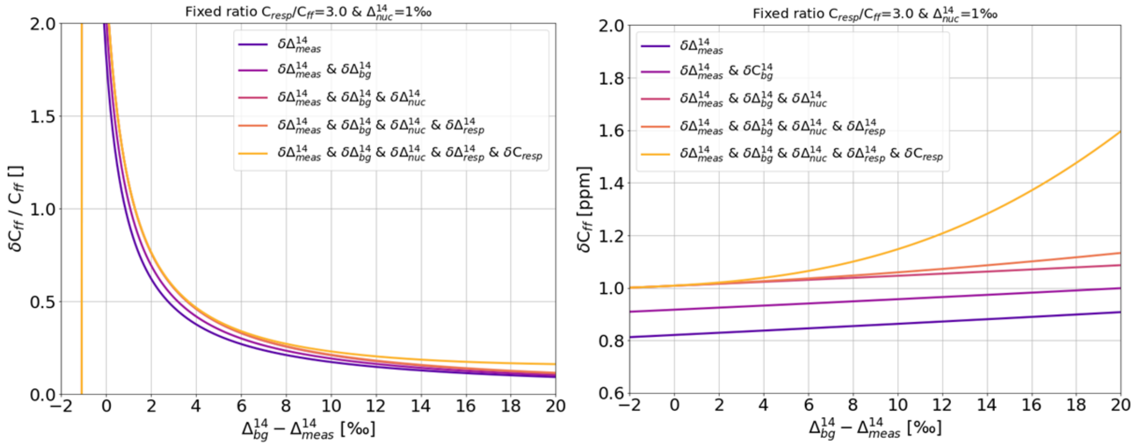

Figure 7: Left panel: relative uncertainty of $\Delta ffCO_2$ in relation to the observed difference of Δ^{14} between background and station ($\Delta^{14}_{bg} - \Delta^{14}_{meas}$). The right panel shows the absolute uncertainty in ppm. Note, the x axis starts at -2 to account for masking effects.

Appendixes

A.1 Nuclear contaminations and their uncertainties

We used the $^{14}CO_2$ emissions from the European Commission RAdioactive Discharges Database (RADD) where the member states of the European Union report their annual nuclear emissions (RADD, 2022). For some facilities, only the total ^{14}C emission but not the $^{14}CO_2$ emission is reported. In these cases, we assume that Pressurised Water Reactors (PWR) emit 28% of the ^{14}C as $^{14}CO_2$ and that all other reactor types emit all ^{14}C as $^{14}CO_2$ according to Zazzeri et al. (2018) and Graven and Gruber (2011). Since the Belgian facilities are missing in the RADD database, we used the energy consumption data from the International Atomic Energy Agency – Power Reactor Information System (IAEA-PRIS, available at: https://pris.iaea.org/PRIS/CountryStatistics/CountryDetails.aspx?current=BE, last access: October 05, 2022) and multiplying a factor of 0.24 TBq/a per GWa for PWRs and 0.51 TBq/a per GWa for BWRs (Boiling Water Reactors) to get the annual ^{14}C emissions (as Zazzeri et al., 2018). For the nuclear facilities in Switzerland the $^{14}CO_2$ emissions were taken from the annual Radiological Protection Reports (available at: https://www.ensi.ch/en/documents/document-category/strahlenschutzberichte/, last access: October 05, 2022) authored by the Swiss Federal Nuclear Safety Inspectorate (ENSI). This nuclear $^{14}CO_2$ emission map (see Fig. A1) has been implemented at the ICOS CP.

To calculate the $\Delta^{14}CO_2$ contaminations from nuclear facilities at the observation site (Δ^{14}_{nuc}), we transport the $^{14}CO_2$ emissions with the STILT model (Lin et al., 2003). In STILT, the surface source influence f with units (μmol/mol_{air})/(μmol/m^2s) describes the sensitivity to emissions from surface grid cells (x_i, y_j) in the footprint of the station. As the nuclear $^{14}CO_2$ emissions Q are given in units Bq/(m^2s), the mapping of those emissions with the surface source influence f yields a nuclear activity A_S = (Q o f) in units Bq/mol_{air} ("o" indicates the element-wise multiplication of each surface influence grid cell (x_i, y_j) with its corresponding flux Q(x_i, y_j) and the subsequent sum over all grid cells). Eq. A1 gives the definition of the Δ-notation according to Stuiver and Pollach (1977) and Eq. A2 the Δ^{14}_{nuc}:

$$\Delta^{14}CO_2 = \left(\frac{A_{SN}}{A_{abs}} - 1\right)\cdot 1000\text{‰} \approx \left(\frac{0.968\cdot A_S}{A_{abs}} - 1\right)\cdot 1000\text{‰} \qquad \text{(A1)}$$

$$\Delta^{14}_{nuc} = \frac{0.968\,(Q\circ f)}{C_{meas}\cdot M_C\cdot A_{abs}}\cdot 1000\text{‰} \qquad \text{(A2)}$$

Here, we assume a constant atmospheric $\delta^{13}C$-CO_2 value of -9‰ and use the standard activity A_{abs} of 0.226 Bq/gC ("gC" means gram carbon). To get the sample activity in the same units as the standard activity, we have to divide the sample activity by the product of the CO_2 concentration at the measurement site C_{meas} and the molar mass of carbon M_C. Since the RADD nuclear emissions are reported only on an annual basis, we assume constant emissions throughout the year. This procedure of mapping the RADD $^{14}CO_2$ emissions with modelled surface source influences has been implemented in the radiocarbon Jupyter notebook offered by the ICOS Carbon Portal. The surface source influence fields are available for all ICOS sites on a three-hourly resolution and were generated with 0.25° resolution meteorological data from the European Center for Medium-Range Weather Forecasts (ECMWF). Since the nuclear emissions are released from stacks with a height of typically above 100 m, using the standard STILT approach that can transport only surface emissions, may over-estimate $^{14}CO_2$ activity concentrations during stable (night-time) conditions if the nuclear installations are located closer than ca. 50 km from the measurement site. For these stations a more sophisticated approach introduced by Maier et al. (2022) should be applied. In the current study we did, however, only use the standard surface influence approach and the distribution of Δ^{14}_{nuc} for integrated samples shown in Fig. 6 (upper right panel) may, thus, be slightly biased high for some of the stations (i.e. NOR).

The uncertainty of the transport model is mainly due to the uncertainty of the meteorological input fields and their resolution as well as on the correct representation of the effective emission heights. Kuderer et al. (2018) showed with the Hybrid Single-Particle Lagrangian Integrated Trajectory (HYSPLIT) model that the mean nuclear contamination from nearby power plants can be more than doubled if the horizontal resolution of the meteorological fields is increased from 0.5° to 2.5°. Therefore, we used high resolution meteorological fields from ECMWF. Considering these various and difficult-to-quantify sources of uncertainty to calculate Δ^{14}_{nuc}, we choose a simple but justified approach and applied an uncertainty of 100% for all sample types. This allows on the one hand to cover situations with the dominant nuclear $^{14}CO_2$ emissions during the two-week period being twice as high as expected (i.e., the annual average). On the other hand, it considers situations when the model erroneously predicts nuclear influences at the observation site.

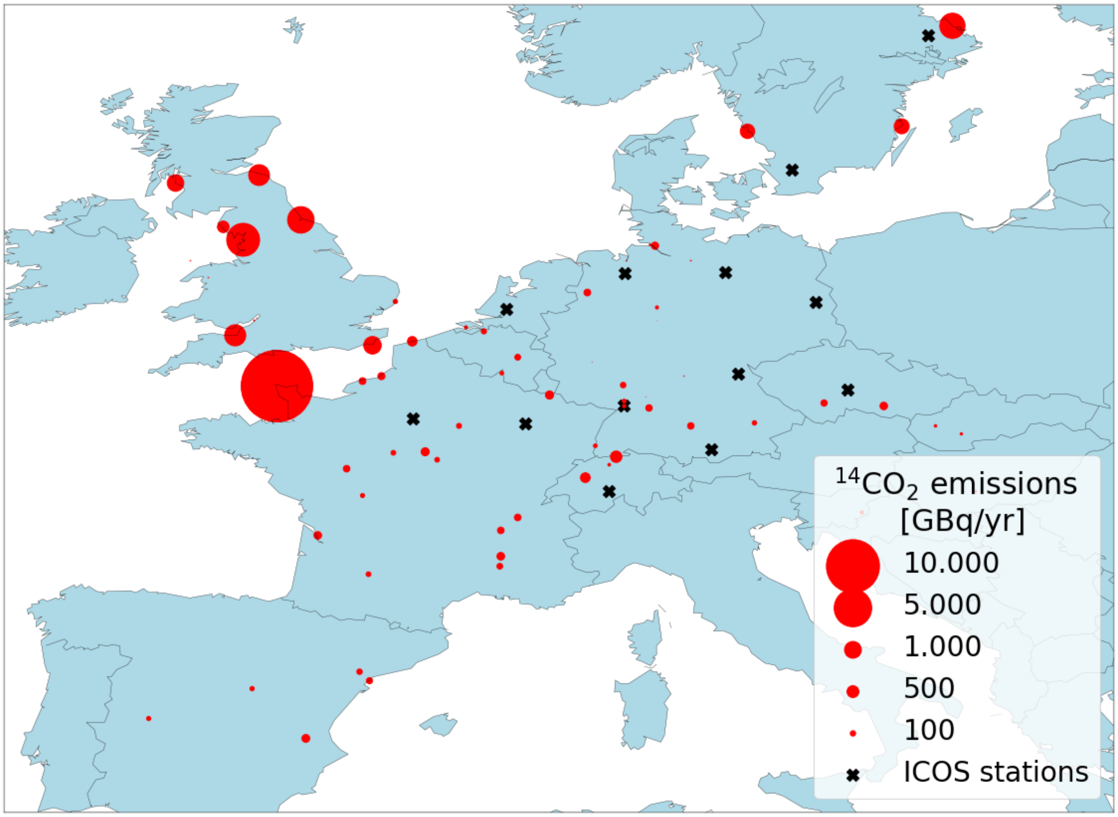

Figure A1: Nuclear $^{14}CO_2$ emissions in Europe (annual means for 2018). The black crosses show the locations of the ICOS class-1 stations. See the text for a description of how this map was created.

A.2 Construction of the MHD Δ^{14}_{bg} background curve

In this study, we use the two-week integrated $\Delta^{14}CO_2$ data from the maritime site Mace Head (MHD, 53.33°N, 9.90°W, 5 m a.s.l.) located at the west coast of Ireland to calculate marine background reference curves for all ICOS stations. We applied the curve fitting algorithm from the National Oceanic and Atmospheric Administration (NOAA) to the two-week integrated $\Delta^{14}CO_2$ measurements. A description of the fitting routine can be found at: https://gml.noaa.gov/ccgg/mbl/crvfit/crvfit.html and a Python script is freely available at: https://gml.noaa.gov/aftp/user/thoning/ccgcrv/ (last access: March 11, 2022). We used the following three components of the NOAA curve fitting routine: (1) a polynomial function with three terms (i.e., a quadratic function) to account for the long-term $\Delta^{14}CO_2$ decline, (2) two harmonics to simulate the annual $\Delta^{14}CO_2$ cycle, and (3) a low-pass filter to the residuals with a long-term cut-off value of five years to consider interannual variations. This NOAA fitting routine also provides variances σ^2_{func} and σ^2_{filt} for the function, which is set up by the polynomial terms and the harmonics, and for the low-pass filtering of the residuals, respectively. The total variance σ_{fit}^2 of the NOAA fit is then given by the combination of both variances (see https://gml.noaa.gov/ccgg/mbl/crvfit/crvfit.html, Eq. A3):

$$\sigma_{fit}^2 = \sigma_{func}^2 + \sigma_{filt}^2 \tag{A3}$$

The NOAA fitting routine was originally developed for CO_2 concentrations, which can be measured very accurately with uncertainties of typically below 0.1 ppm. So, the ratio between measurement uncertainty and a typical seasonal variation of 20 ppm is only 5‰. That's why the measurement uncertainties of the individual observations are not considered by the NOAA fit. However, in case of $\Delta^{14}CO_2$ the measurement uncertainty is ca. 2‰, which is 40% of a typical 5‰ peak-to-peak seasonal $\Delta^{14}CO_2$ variation at background sites. Therefore, we also performed a Monte-Carlo approach, to take into account the measurement uncertainties of the individual two-week integrated $\Delta^{14}CO_2$ samples. We draw for each $\Delta^{14}CO_2$ sample a random number from a Gaussian distribution with zero mean and the one-sigma standard deviation given by the respective measurement uncertainty. The initial $\Delta^{14}CO_2$ measurements were then shifted by those random numbers. Afterwards, we calculated the NOAA fitting curve for this configuration. After repeating this procedure 1000 times, we could calculate the standard deviation over all 1000 background curves to get an additional estimate of the average background curve uncertainty.

The NOAA fitting routine yields a standard deviation for Δ_{bg}^{14} of 0.86‰ for the points relative to the background curve, while the standard deviation over the 1000 Monte-Carlo realisations was on average only 0.43‰, i.e. half the standard deviation calculated with the NOAA fitting algorithm. This small standard deviation of the Monte-Carlo realisations shows that the chosen parameters (i.e., the long-term cut-off value of five years) leads to a background curve, which is robust to variations within the one-sigma range of the individual $\Delta^{14}CO_2$ measurements. If we vary the individual $\Delta^{14}CO_2$ measurements within their two-sigma uncertainty range, we get a standard deviation of 0.86‰ over the 1000 Monte-Carlo realisations, i.e. the same value as the standard deviation computed with the NOAA algorithm. We also investigated the influence of a different number of polynomials (2 or 4 polynomials instead of 3), harmonics (3 or 4 harmonics instead of 2) and years for the long-term cut-off value (1 or 3 years instead of 5). These parameter-varied background curves lie all well within the 0.86‰ uncertainty band of the MHD background curve. On average, the deviations are even less than 0.1‰. That's why we will use in the following the 0.86‰ standard deviation as an estimate for the uncertainty of the MHD background $\Delta^{14}CO_2$ curve.

A.3 Modelled C_{resp}/C_{ff} and C_{photo}/C_{ff} ratios for two ICOS sites

Figure A2 shows the modelled C_{photo}/C_{ff} and C_{resp}/C_{ff} ratios for the integrated samples collected at the two ICOS sites Křešín (KRE) in the Czech Republic and Observatoire Pérenne de l'Environnement (OPE) in France between 2016 and 2021. We used VPRM-STILT to simulate the biospheric CO_2 signals and the Emissions Database for Global Atmospheric Research (EDGAR, Janssens-Maenhout et al.,

2019) and STILT to calculate the C_{ff} contributions. The model results illustrate the expected range of the ratios at typical ICOS sites in Central Europe as well as their seasonal cycle with lower (absolute) ratios in winter compared to summer.

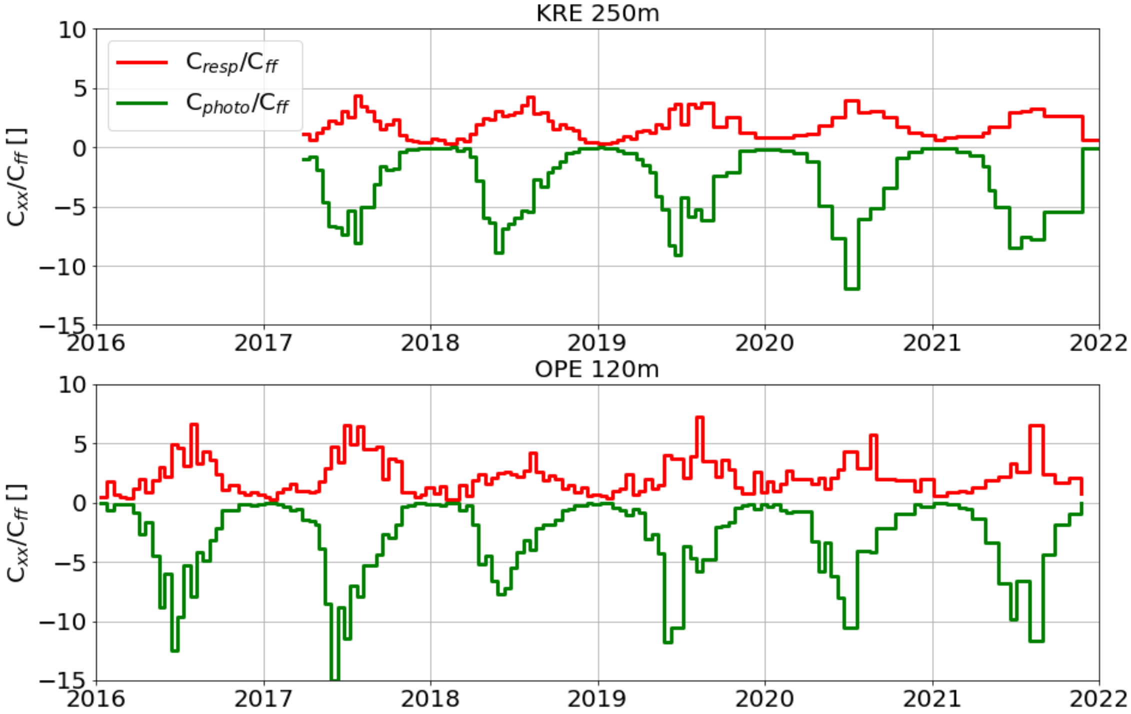

Figure A2: Simulated C_{photo}/C_{ff} (green) and C_{resp}/C_{ff} (red) ratios for the integrated samples collected at the two ICOS sites KRE (upper panel) and OPE (lower panel).

CHAPTER 4

A dedicated flask sampling strategy developed for Integrated Carbon Observation System (ICOS) stations based on CO_2 and CO measurements and Stochastic Time-Inverted Lagrangian Transport (STILT) footprint modelling

This chapter is based on:

Levin, I., Karstens, U., Eritt, M., Maier, F., Arnold, S., Rzesanke, D., Hammer, S., Ramonet, M., Vítková, G., Conil, S., Heliasz, M., Kubistin, D., and Lindauer, M.: A dedicated flask sampling strategy developed for Integrated Carbon Observation System (ICOS) stations based on CO_2 and CO measurements and Stochastic Time-Inverted Lagrangian Transport (STILT) footprint modelling, Atmos. Chem. Phys., 20, 11161–11180, https://doi.org/10.5194/acp-20-11161-2020, 2020.

Atmos. Chem. Phys., 20, 11161–11180, 2020
https://doi.org/10.5194/acp-20-11161-2020

Atmospheric Chemistry and Physics
Open Access

A dedicated flask sampling strategy developed for Integrated Carbon Observation System (ICOS) stations based on CO_2 and CO measurements and Stochastic Time-Inverted Lagrangian Transport (STILT) footprint modelling

Ingeborg Levin[1], Ute Karstens[2], Markus Eritt[3], Fabian Maier[1], Sabrina Arnold[4], Daniel Rzesanke[3], Samuel Hammer[1], Michel Ramonet[5], Gabriela Vítková[6], Sebastien Conil[7], Michal Heliasz[8], Dagmar Kubistin[4], and Matthias Lindauer[4]

[1]Institut für Umweltphysik, Heidelberg University, 69120 Heidelberg, Germany
[2]ICOS Carbon Portal, Lund University, 22362 Lund, Sweden
[3]Max Planck Institute for Biogeochemistry, ICOS Flask- und Kalibrierlabor, 07745 Jena, Germany
[4]Meteorologisches Observatorium Hohenpeißenberg, Deutscher Wetterdienst,
82383 Hohenpeißenberg, Germany
[5]Laboratoire des Sciences du Climat et de l'Environnement (LSCE), IPSL, CEA-CNRS-UVSQ, Université Paris-Saclay,
91191 Gif-sur-Yvette, France
[6]Global Change Research Institute of the Czech Academy of Sciences, 603 00 Brno, Czech Republic
[7]DRD/OPE, Andra, 55290 Bure, France
[8]Centre for Environmental and Climate Research, Lund University, 22362 Lund, Sweden

Correspondence: Ingeborg Levin (ingeborg.levin@iup.uni-heidelberg.de)

Received: 27 February 2020 – Discussion started: 17 March 2020
Revised: 2 June 2020 – Accepted: 8 August 2020 – Published: 29 September 2020

Abstract. In situ CO_2 and CO measurements from five Integrated Carbon Observation System (ICOS) atmosphere stations have been analysed together with footprint model runs from the regional Stochastic Time-Inverted Lagrangian Transport (STILT) model to develop a dedicated strategy for flask sampling with an automated sampler. Flask sampling in ICOS has three different purposes, namely (1) to provide an independent quality control for in situ observations, (2) to provide representative information on atmospheric components currently not monitored in situ at the stations, and (3) to collect samples for $^{14}CO_2$ analysis that are significantly influenced by fossil fuel CO_2 ($ffCO_2$) emission areas. Based on the existing data and experimental results obtained at the Heidelberg pilot station with a prototype flask sampler, we suggest that single flask samples are collected regularly every third day around noon or in the afternoon from the highest level of a tower station. Air samples shall be collected over 1 h, with equal temporal weighting, to obtain a true hourly mean. At all stations studied, more than 50 % of flasks collected around midday will likely be sampled during low ambient variability (<0.5 parts per million (ppm) standard deviation of 1 min values). Based on a first application at the Hohenpeißenberg ICOS site, such flask data are principally suitable for detecting CO_2 concentration biases larger than 0.1 ppm with a 1σ confidence level between flask and in situ observations from only five flask comparisons. In order to have a maximum chance to also sample $ffCO_2$ emission areas, additional flasks are collected on all other days in the afternoon. To check if the $ffCO_2$ component will indeed be large in these samples, we use the continuous in situ CO observations. The CO deviation from an estimated background value is determined the day after each flask sampling, and depending on this offset, an automated decision is made as to whether a flask shall be retained for $^{14}CO_2$ analysis. It turned out that, based on existing data, $ffCO_2$ events of more than 4–5 ppm that would allow $ffCO_2$ estimates with an uncertainty below 30 % were very rare at all stations studied, particularly in summer (only zero to five events per month from May to August). During the other seasons, events could be collected more frequently. The strategy developed in this project is currently being implemented at the ICOS stations.

---

1 Introduction

Since the pioneering work by Charles David Keeling who, already in the 1950s, started continuous monitoring of atmospheric carbon dioxide concentrations at the South Pole and Mauna Loa (Brown and Keeling, 1965), global coverage of continuous greenhouse gas (GHG) observations has considerably improved (https://gaw.kishou.go.jp, last access: 20 September 2020). However, there still exist large observational gaps in remote marine and continental regions of the globe, which have partly been filled by regular flask sampling and analysis in central laboratories. If frequently conducted, data from flask sampling in the marine realm are often representative of the large-scale distribution of GHGs in the atmosphere and, thus, suitable for estimating large-scale flux distributions by inverse modelling. The situation is more difficult when it comes to representative flask sampling at continental sites because there the distribution of sources and sinks is much more heterogeneous and variable than over the oceans.

In the last few decades, observational networks have been extended to the continents in order to closely monitor GHG concentrations and quantify terrestrial GHG sources and sinks. These heterogeneous terrestrial fluxes are often less well implemented in models compared to ocean fluxes (Friedlingstein et al., 2019). As biogenic sources and sinks are strongly influenced by regional climatic variability, only continental observations can provide insight into the associated ecosystem processes (Ciais et al., 2005; Ramonet et al., 2020). Besides monitoring the terrestrial biosphere, measurements over continents are also conducted to observe anthropogenic emissions, in particular from fossil fuel burning and agriculture. Due to their proximity to these highly variable sources and sinks, measurements over continents are best conducted continuously with in situ instrumentation at a high temporal resolution. Only continuous observations can resolve the variability and fully represent the entire footprint of a station (e.g. Andrews et al., 2014). However, not all atmospheric trace components we are interested in can be precisely measured in situ at remote stations yet. The most prominent example is radiocarbon (^{14}C) in atmospheric CO_2, a quantitative tracer that separates the fossil fuel from the biospheric component in recently emitted CO_2 from continental sources (e.g. Levin et al., 2003). Note that in industrialised and highly populated areas of midlatitudes in the Northern Hemisphere, i.e. in North America, eastern Asia, or Europe, atmospheric signals from the biosphere and from fossil fuel sources are of same order (see Sect. 4.3.1). To correctly interpret absolute CO_2 concentration variations in terms of source and/or sink attribution, separation of the fossil fuel from the biogenic CO_2 signal is, therefore, mandatory. Precise $^{14}CO_2$ measurements are, however, currently only possible in dedicated laboratories and on discrete samples.

In Europe the Integrated Carbon Observation System research infrastructure (ICOS RI; https://www.icos-cp.eu/, last access: 20 September 2020) has been established to monitor GHG concentrations and fluxes in the atmosphere, in various ecosystems, and over the neighbouring ocean basins. ICOS atmosphere has set up a pan-European network of preferentially tall tower stations located at least 50 km away from industrialised and highly populated areas. The primary purpose is to monitor biogenic sources and sinks in Europe and monitor their behaviour under changing climatic conditions. In addition to continuous CO_2, CH_4, and CO observations, a subset of stations (Class 1 stations) perform 2-week integrated sampling of CO_2 for ^{14}C analysis. Class 1 stations are additionally equipped with an automated flask sampler dedicated to three major objectives. First, the collected flasks shall provide an independent quality control (QC) for the continuous in situ measurements of CO_2, CH_4, CO, and further species mole fractions. Second, flasks shall be collected for the analysis of additional trace components not measured in situ at the stations; finally, flasks with a potentially elevated fossil fuel CO_2 component originating from anthropogenic sources in the footprint of the stations shall be analysed for $^{14}CO_2$.

Dedicated sampling strategies had to be developed for ICOS which best meet these three objectives and which can be accomplished in the framework of the infrastructure and its available capabilities and resources. This includes technical constraints at the stations but also analysis capacity at the ICOS Central Analytical Laboratories, which are analysing all flask samples in ICOS. The ICOS flask sampling strategy might change in the future, e.g. when real-time GHGs or footprint prediction tools become available.

In the current paper, we first give an introduction to the current ICOS atmosphere station network and then present a strategy for how to collect the flask samples for ICOS in a simple and cost-effective way. The sampling strategies have been developed based on footprint model simulations with a regional transport model, the Stochastic Time-Inverted Lagrangian Transport (STILT) model (Lin et al., 2003), that was implemented at the ICOS Carbon Portal (https://www.icos-cp.eu/about-stilt, last access: 20 September 2020) for ICOS station principal investigators (PIs) and data users. The first tests to develop a strategy for the quality control objective were performed at the ICOS pilot station in Heidelberg, where ICOS instrumentation and a prototype of the ICOS flask sampler have been installed, and at the Hohenpeißenberg station. The strategy was further tested for its feasibility based on the first years of continuous ICOS CO_2 and CO observations available at the ICOS Carbon Portal (ICOS RI, 2019).

2 The atmosphere component of the ICOS research infrastructure

2.1 The atmosphere station network and its Central Facilities

The ICOS atmosphere station network currently consists of 25 officially labelled stations (with 12 stations still to come), located in 12 countries, and covering Europe from Scandinavia to Italy and from Great Britain to the Czech Republic (see Fig. 1). The preferred station types are tall tower sites, allowing vertical profile sampling at a minimum of three height levels up to at least 100 m above ground level (a.g.l.). Tall tower stations cover footprints of several tens to hundreds of kilometres of distance from the sites (Gloor et al., 2001; Gerbig et al., 2006). Although their representation in state-of-the-art regional atmospheric transport models is more difficult than in the case of tower observations, due to their often long history of GHG measurements, a number of mountain and coastal stations are also part of the ICOS network. However, the flask sampling strategy developed here was designed specifically for the standard ICOS tall tower stations.

All ICOS atmosphere stations are equipped with commercially available instruments measuring CO_2, CH_4, and CO continuously at high temporal resolutions. Instruments are tested at the Atmosphere Thematic Centre (ATC), an ICOS Central Facility hosted by the Laboratoire des sciences du climat et de l'environnement (LSCE) in Gif-sur-Yvette, France, before they are installed at the sites (Yver Kwok et al., 2015). The calibration gases for the in situ measurements are prepared and calibrated at the Flask and Calibration Laboratory (FCL), which has been established at the Max Planck Institute for Biogeochemistry in Jena, Germany, as part of the ICOS Central Analytical Laboratories (CAL). This procedure guarantees the best possible compatibility of observations within the ICOS atmosphere network and maintains the link to the internationally accepted World Meteorological Organization (WMO) calibration scales. In addition, the FCL analyses the flasks with a focus on QC and additional species. Precise $^{14}CO_2$ analysis of integrated samples and selected flasks is conducted in the second part of ICOS CAL at the Heidelberg University Institute of Environmental Physics in the Karl Otto Münnich Central Radiocarbon Laboratory (CRL).

All raw data (level 0) are automatically transferred, on a daily basis, from the measurement sites to the ATC, where they are converted to calibrated (level 1) concentration values (Hazan et al., 2016) based on regular on-site calibrations and FCL-assigned calibration values. For ongoing automatic data quality assurance of all measurements, the ATC has developed automatic procedures. Further software tools are made available by the ATC for mandatory validation of all raw data by the station PIs. These quality-assessed data form the basis of the hourly mean concentrations, which are finally released as level 2 data and made available to the user community on the ICOS Carbon Portal hosted by Lund University, Sweden. For the latest data release, see ICOS RI (2020a).

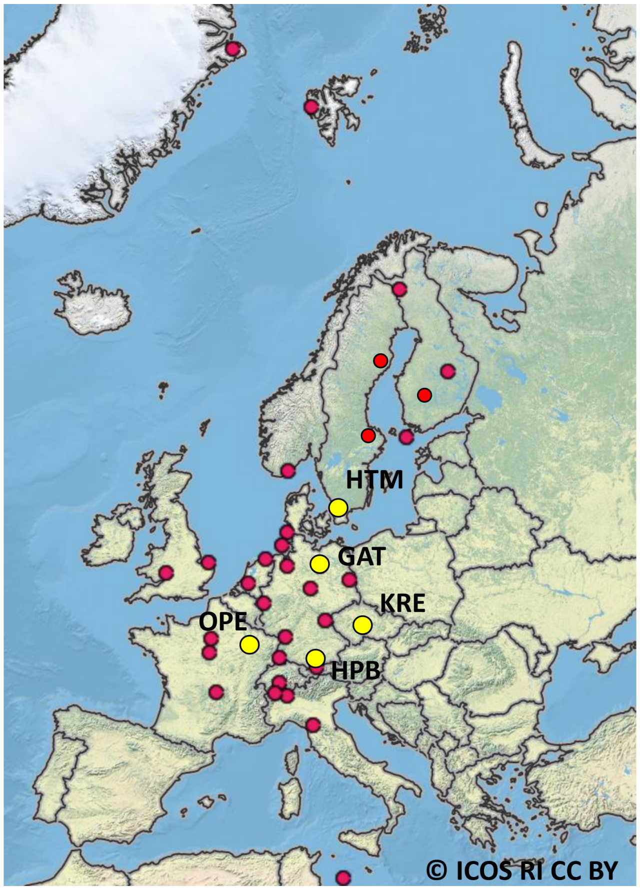

Figure 1. Map of ICOS atmosphere stations. The five stations included in this study are marked with big yellow dots: HTM – Hyltemossa, GAT – Gartow, KRE – Křešín, OPE – Observatoire Pérenne de l'Environnement, and HPB – Hohenpeißenberg. Sources: ESRI, US National Park Service and ICOS Carbon Portal.

Two station types are currently implemented in the ICOS atmosphere station network, namely Class 1 and Class 2. Class 1 stations are equipped with the complete instrumentation, including integrated $^{14}CO_2$ and flask sampling. Class 2 stations perform only in situ continuous measurements of CO_2, CH_4, and CO (currently not mandatory) but with the same instrumentation and demand for data quality as Class 1 stations. A detailed description of the specifications of the instrumentation is given in the ICOS Atmosphere Station Specification document (ICOS RI, 2020b), which is regularly updated. To become an official part of the ICOS atmosphere station network, stations have to undergo a two-step labelling process, which warrants their conformance with the ICOS station specifications, including smooth data transfer to the ATC and meeting ICOS data quality requirements.

2.2 Description of selected ICOS stations

To develop and test our flask sampling strategy, we selected five ICOS Class 1 tall tower stations in four different countries. A short description of these stations is given in the following.

Hyltemossa (HTM) is located a few kilometres south of Perstorp in northwestern Skåne, Sweden (56.098° N, 13.418° E; 115 m above sea level – a.s.l.). It hosts a combined atmosphere and ecosystem station labelled, respectively, as Class 1 and Class 2 sites in its respective networks. The site was established in 2014 in a 30-year-old managed Norwegian spruce forest. More than 600 m away from the tower there is a mosaic consisting of forests, clear-cuts, and farm fields. Within a radius of 100 km, the elevation changes from 0 to 200 m a.s.l., while in the near vicinity of the tower the elevation gently changes by only 35 m. In the larger footprint, the site is surrounded by cities; i.e. Halmstad to the north (70 km; 58 000 inhabitants), Kristianstad to the east (45 km; 36 000 inhabitants), Lund (45 km; 111 000 inhabitants), Malmö (60 km; 318 000 inhabitants), and Copenhagen (in Denmark; 70 km; 1 990 000 inhabitants) to the southwest, and Helsingborg (45 km; 124 000 inhabitants) and Helsingør (in Denmark; 55 km; 61 000 inhabitants) to the west. The station is equipped with a Picarro, Inc. G2401 cavity ring-down spectroscopy (CRDS) gas analyser that measures CO_2, CH_4, and CO. Air inlets are located at 30, 70, and 150 m a.g.l. Air is sampled for 5 min from each level, where the data for the first minute after switching to the new level are discarded. Subsampling lines have installed 8 L mixing volumes that are continuously flushed with a flow rate of 2.1 $\mathrm{L\,min^{-1}}$, resulting in a residence time of 270 s in each line. In addition, at the height of each air inlet, air temperature, relative humidity, and wind speed and direction are being measured.

The ICOS tall tower station Gartow (GAT; 53.066° N, 11.443° E; 70 m a.s.l.) is situated in the easternmost region of Lower Saxony, Germany, close to the river Elbe, approximately at the midpoint between Hamburg and Berlin. The surrounding area is very flat, with elevations ranging from less than 9 m a.s.l. (Elbe Valley) up to 124 m a.s.l. (at the Hoher Mechtin hill 35 km west of GAT). The land use in this area is dominated by forests and agricultural fields. The station hosts a lattice television tower operated and managed by the Deutsche Funkturm GmbH (DFMG). The closest cities are Schwerin (65 km north of the station; ca. 100 000 inhabitants), Wolfsburg (80 km south of the station; ca. 120 000 inhabitants), and Lüneburg (70 km northwest of the station; ca. 70 000 inhabitants). Air inlets are at 30, 60, 132, 216, and 341 m. A Picarro, Inc. G2301 cavity ring-down spectroscopy (CRDS) gas analyser, measuring CO_2, CH_4, and CO, and, since the beginning of 2019, a Los Gatos Research, Inc. (part no. 913-0015; Enhanced Performance – EP) off-axis integrated cavity output spectroscopy (OA-ICOS) analyser, measuring CO and N_2O, have been installed in a container next to the tower. Air is sampled for 5 min from each level, where data for the first minute after switching to the new level are discarded. All inlet lines are continuously flushed with approximately 5 $\mathrm{L\,min^{-1}}$. Meteorological sensors for air temperature, relative humidity, and wind speed and direction have been installed at every sampling height. For historical reasons, Gartow modelling was conducted for 344 m a.g.l. (and not for the highest sampling level at 341 m); this difference between the measured and modelled level is, however, not relevant for the comparisons presented in the context of this study.

Station Křešín u Pacova (KRE; 49.572° N, 15.080° E; 534 m a.s.l.) is located in the central Czech Republic, about 100 km southeast of Prague. The site was established in 2013 close to the Košetice Observatory, a station of the Czech Hydrometeorological Institute with 30 years of practice in meteorology and air quality monitoring. Today, these two stations form the National Atmospheric Observatory in the Czech Republic. Since the site is designed as a background station, the area is not significantly influenced by human activity. The tower is surrounded by fields and, at a greater distance, forests and small villages (the closest is 1 km away). There is a highway running northeast of the tower at an approximate distance of 6 km; however, the wind frequencies from the north and east are 9 % and 5 %, respectively. The closest towns, namely Pelhřimov, Vlašim, and Humpolec, with 10 000 to 17 000 inhabitants, are located approximately 20 km away from the station. As for industrial activity, a small wood-processing company is located 20 km to the west (which is the prevailing wind direction). The town of Havlíčkův Brod, with ca. 20 000 inhabitants, is located about 30 km from the site; larger towns (up to 50 000 inhabitants) are about 40 km away (i.e. Jihlava and Tábor). Further still, there are only towns with populations of, at most, 35 000 inhabitants, except for Prague (80 km; 1 million inhabitants), Pardubice (80 km; 90 000 inhabitants), and České Budějovice (90 km; 90 000 inhabitants). The terrain around the tower is relatively flat within a few kilometres' distance, with only small hills around. The Bohemian-Moravian Highlands, where the site is located, have an average altitude of 500–600 m a.s.l., with rare spots of 800 m a.s.l. The highest hills, namely Javořice (837 m a.s.l.) and Devět skal (836 m a.s.l.), are located 43 m and 69 km away. The station is equipped with the ICOS atmosphere-recommended instrumentation for CO_2 and CH_4 (Picarro, Inc. G2301 CRDS) and for N_2O and CO (Los Gatos Research, Inc.; part no. 913-0015; EP). The air is sampled at 10, 50, 125, and 250 m levels of the tower. Sampling period is 10 min per height, where the highest level is sampled in between all other levels. This results in a complete vertical profile measured within 1 h, with a preference for the 250 m level. After switching to a new height, 3 min measurements are always excluded (known as the stabilisation period). All sampling heights of the tower are equipped with meteorological sensors (wind speed and direction, air pressure and temperature, and relative humidity).

The Observatoire Pérenne de l'Environnement (OPE; 48.563° N, 5.506° E; 395 m a.s.l.) is located on the eastern edge of the Paris basin in the northeastern part of France. The station is located in a rural area with large crop fields, some pastures, and forest patches. A local village and small roads are about 1 km away. The closest large towns are between 30 and 40 km away, and a major road is found at a distance of about 15 km. The station hosts a complete set of in situ measurements of meteorological parameters, trace gases (CO_2, CH_4, N_2O, CO, O_3, NO_x, and SO_2), and particle characteristics. The station is part of the French aerosol in situ network, contributing to Aerosol, Clouds and Trace Gases Research Infrastructure (ACTRIS; https://www.actris.eu/, last access: 20 September 2020) and the Institut de Radioprotection et de Sûreté Nucléaire (IRSN) network for ambient air radioactivity monitoring. It also contributes to the French air quality monitoring network and to the European Monitoring and Evaluation Programme (EMEP). The infrastructure, including a 120 m tall tower, was built in 2009–2010, and the various measurements started between 2011 and 2013. Ambient air is sampled at three levels, namely 10, 50 and 120 m a.g.l., of the tower and is analysed by Picarro, Inc. cavity ring-down spectrometers (CRDSs; series G1000 and G2000) for CO_2, CH_4, H_2O, and CO as well as Los Gatos Research, Inc. off-axis-ICOS spectrometers for N_2O and CO (Conil et al., 2019). The sampling period for each level is 20 min, including an automatic rejection of the first 5 min. Meteorological parameters are measured at all air sampling levels.

The ICOS station Hohenpeißenberg (HPB; 47.801° N, 11.010° E; 934 m a.s.l.) is located on top of a solitary hill that rises approximately 300 m above the almost flat to rolling landscape, 30 km north of the Alps and approximately 60 km southwest of Munich. The main land uses are forests and meadows. The station hosts a concrete television tower operated and managed by the DFMG. Cities closest to the station are Weilheim (10 km east of the station; 20 000 inhabitants), Landsberg (30 km north of the station; 30 000 inhabitants), Augsburg (60 km north of the station; 270 000 inhabitants), Munich (60 km northeast of the station; 1 million inhabitants), and Innsbruck (in Austria; 65 km south of the station; 127 000 inhabitants). Air inlets are at 50, 93, and 131 m. A Picarro, Inc. G2401 CRDS analyser, measuring CO_2, CH_4, and CO, and a Los Gatos Research, Inc. (part no. 913-0015; EP) OA-ICOS analyser, measuring CO and N_2O, are installed in the basement of the tower. Air is sampled for 5 min from each level, where data for the first minute after switching to the new level are discarded. All inlet lines are continuously flushed with approximately 5 L min^{-1}. Meteorological sensors (air temperature, relative humidity, and wind speed and direction) are installed at every sampling height.

2.3 Atmospheric transport modelling for ICOS stations

A footprint simulation tool based on the regional atmospheric transport model, STILT (Lin et al., 2003; Gerbig et al., 2006), was implemented at the ICOS Carbon Portal (https://www.icos-cp.eu/about-stilt, last access: 20 September 2020) as a service for ICOS station PIs and data users. The STILT model simulates atmospheric transport by following a particle ensemble, released at the measurement site, backwards in time and calculating footprints that represent the sensitivity of tracer concentrations at this site to surface fluxes upstream. The footprints are mapped on a $1/12°$ latitude $\times 1/8°$ longitude grid and are coupled to the Emission Database for Global Atmospheric Research (EDGAR) version 4.3.2 emission inventory (Janssens-Meanhout et al., 2019) and the biosphere model, Vegetation Photosynthesis and Respiration Model (VPRM; Mahadevan et al., 2008), to simulate atmospheric CO_2 and CO concentrations. These regional concentration components represent the influence from surface fluxes inside the model domain (covering the greater part of Europe). For CO_2, the contributions from global fluxes are accounted for by using initial and lateral boundary conditions from the Jena CarboScope globally analysed CO_2 concentration fields (http://www.bgc-jena.mpg.de/CarboScope/s/s04oc_v4.3.3D.html, last access: 20 September 2020), while for CO only regional contributions are evaluated in our study. Note that STILT does not account for the stack emission height of point sources. This may cause biases when estimating $ffCO_2$ contributions from close-by emissions of, for example, power plants. However, as this model deficiency becomes less important with increasing distance from the source, it seems of minor relevance for the ICOS stations studied here as they are located far away from major emitters.

2.4 The automated ICOS flask sampler

The automated ICOS flask sampler was designed and constructed at the Max Planck Institute for Biogeochemistry (MPI-BGC), Jena, Germany, by the Flask and Calibration Laboratory (FCL) of the CAL to allow automated air sampling under highly standardised conditions. The sampler can hold up to 24 individual glass flasks (four drawers with six flasks each) for separate air sampling events (Fig. 2, upper panel). The glass flasks can be individually replaced and sent to the CAL for analysis. The glass flasks used within ICOS (3 L volume; product no. ICOS3000; Pfaudler Normag Systems GmbH, Germany) were developed according to ICOS' specific requirements based on well-proven designs (Sturm et al., 2004). Each flask has two valves, one at each end, that allow air exchange by flushing sample air through the flask. The flasks are attached with 1/2 in. clamp ring connectors to the flask sampler. The flask valves, with polychlorotrifluoroethylene (PCTFE) sealed end caps, can be opened and closed by a motor.

A sample is taken by flushing air through a flask at a constant overpressure of 1.6 bar (absolute). Sampling at overpressure increases the amount of available sample air for analysis and allows for the detection of flasks with leak prob-

Figure 2. Photograph of the ICOS flask sampler with a schematic flow diagram.

lems. Flasks are prefilled with 1.6 bar of dry ambient air with a well-known composition at the FCL to avoid concentration changes due to wall adsorption effects. The schematic sampler layout is depicted in the flow diagram in Fig. 2. Incoming air is dried to a dew point of approximately −40 °C by passing through a cooled glass vessel where the exceeding humidity is frozen out. The glass vessel is placed in a silicon oil heat bath that is cooled for drying and heated for flushing out the collected water to regenerate the trap. The drying unit is automated and consists of two independent inter-switchable drying branches that complement each other and allow a near interruption-free drying. The dryer design is inspired by an already existing system from Neubert et al. (2004). The incoming sample air is compressed with a pump (J161-AF-HJ0; Air Dimensions, Inc.). A mass flow controller (MFC; F-201CV; Bronkhorst) between the compressor and flasks allows one to sample preset flow rates; i.e. with a decreasing flow rate over time so that the sample represents a real average, for example, over 1 h (Turnbull et al., 2012). The flask pressure during sampling (1.6 bar) is kept constant through a pressure regulator at the outlet of the flasks. An overpressure valve set at 2.0 bar behind the pump assures a constant flow rate through the intake line, independent of the flow rate through the mass flow controller.

In ICOS we strive to sample real 1 h mean concentrations in 3 L flasks. The $1/t$ filling approach requires, for this specific case, a theoretical dynamic flow rate between $80\,\mathrm{mL\,min^{-1}}$ and infinity. In reality, the maximum flow rate of the selected flow controller is limited to $2\,\mathrm{L\,min^{-1}}$. An almost constant weighting of the sample concentration over the 1 h sampling time is achieved by the temporal modulation of the sample flow $f(t)$ (standard litre per minute – SLPM) passing a flask, which acts at the same time as mixing volume V given in litre standard temperature and pressure (STP). The flow rate f is changed over time t according to $f(t) = V/(t - t_0)$. Since the flow rate at the start time t_0 in a $1/t$ function would be infinite, a 30 min flushing phase at maximum flow rate precedes the averaging period to ensure a complete air exchange in the flask with ambient air before the sampling starts.

The concentration $c_\mathrm{F}(t)$ in the flask is determined by the ambient air concentration $c_\mathrm{A}(t)$ and can be described as a time series using sufficiently small time steps Δt as follows:

$$c_\mathrm{F}(t+\Delta t) = \frac{c_\mathrm{F}(t) \cdot (V - f(t) \cdot \Delta t) + c_\mathrm{A}(t) \cdot (f(t) \cdot \Delta t)}{V}. \quad (1)$$

The resulting weight of the ambient air concentration w_{c_A} at time step t_n in the flask depends on the following two factors:

$$w_{c_\mathrm{A}}(t_n) \sim c_\mathrm{A}(t_n) \cdot \frac{f(t_n) \cdot \Delta t}{V} \cdot \prod_{i=n+1}^{\mathrm{E}} \left(1 - \frac{f(t_i) \cdot \Delta t}{V}\right), \quad (2)$$

namely the weight at the moment when the ambient air portion enters the flask, and a weight-reduction factor caused by dilution with sampled air entering the flask at later times. The reduction is calculated by multiplication of the respective dilution steps from t_n to the sampling end time t_E. This weighting function has to be applied to the ambient air measurements so that the flask concentrations can be compared with the in situ data. Average in situ minus flask concentration differences with the aimed uncertainty can only be reached under sufficiently stable concentration conditions during sampling.

With the current design of the flask sampler, technical restrictions do not allow parallel sampling of flask duplicates or triplicates as a means for quality control, for example, based on flask pair agreement. The technical effort for allowing exact parallel hourly averaged sampling is very high;

it would, for example, require flow controllers for all individual flasks sampled in parallel. Therefore, the ICOS Atmosphere Monitoring Station Assembly (MSA) decided to sample only single flasks. This seems appropriate because in the ICOS network the flask sampler is always collecting flasks in parallel to continuous measurements, and erroneously collected flasks, or errors due to flask leakages, can be detected when comparing results with the continuous data. Therefore, in contrast to the general practice of duplicate flask sampling, in our network single flask sampling seems to be sufficient for meeting ICOS objectives. This has the additional advantage that single flask sampling allows more frequent sampling and, thus, a more representative coverage of the footprint of the stations. If true duplicate samples are required in the future, the flask sampler is designed to accommodate an additional mass flow controller to fulfil this task. The sampler is controlled by an embedded PC offering a broad range of interaction possibilities satisfying the emerging needs within ICOS. Sampling event time schemes can be preprogrammed, and communication with external devices (i.e. data loggers) is possible with analogue or digital signals. Flask-to-port attributions are completely barcode controlled. Sampling and sensor data are automatically stored, and all necessary sampling-related data can be automatically transferred to the CAL. Various automated internet-assisted approaches, like remote programming of sampling times and preselection of samples, are possible.

3 Aims and technical constraints of ICOS flask sampling

As briefly outlined above, there are three main aims for regular flask sampling at ICOS stations:

1. Flask results are used for comparison with in situ observations (i.e. CO_2, CH_4, CO, and N_2O). This comparison provides an ongoing quality control (QC) of the in situ measurement system, including the intake lines. It is of the utmost importance that ICOS measurements meet the WMO compatibility goals (WMO, 2020) for all GHG components. Already very small biases between station data lead to erroneous source and/or sink distributions if used in model inversions (e.g. Corazza et al., 2011). Therefore, a comparison of continuous in situ data with flask data provides a very efficient QC and a basis for determining reliable uncertainties of data.

2. Flasks are analysed for components not measured continuously at the station, such as SF_6 or H_2, but also stable isotopes of CO_2 or the $O_2 : N_2$ ratio. The aim here is to monitor large-scale representative concentration levels of these components, allowing estimations of their continental fluxes with the help of inverse modelling. Selecting, for example, only situations of low ambient variability may cause a significant bias when these data are used in inverse models for source and/or sink budgeting.

3. A subset of flasks is analysed for ^{14}C in CO_2, allowing the determination of the atmospheric fossil fuel CO_2 component ($ffCO_2$) and, with help of these data and inverse modelling, estimating the continental fossil fuel CO_2 source strength of the sampled areas.

To meet aims 1 and 2, flask sampling during well-mixed meteorological conditions is required, and the sampled footprints should not be dominated by particular hotspot source areas. Particularly for aim 2, we further strive to cover the entire daytime footprint of the station. In contrast, aim 3, due to the generally small fossil fuel signals at ICOS stations, requires targeted sampling of "hotspot emission areas" in the footprint to maximise the fossil fuel CO_2 signal in the samples. Note that the detection limit (or measurement uncertainty) of the fossil fuel CO_2 ($ffCO_2$) component with $^{14}CO_2$ measurements is of order 1–1.5 parts per million (ppm; e.g. Levin et al., 2011).

There are a number of technical and/or logistical constraints concerning flask sampling, shipment, and analysis in ICOS which need to be taken into account when designing an operational sampling strategy that best meets the three aims listed above. The most important limitations are listed in the following:

1. Timing. In order that all flask sample results are useful for flux estimates with current regional inversion models, flasks should be collected during midday or in the early afternoon at the standard ICOS tall tower stations. During this time of the day, atmospheric mixing is strong, and model transport errors are smaller than during night (Geels et al., 2007). For all samplings, wind speeds should be larger than about $2\,m\,s^{-1}$ so that the sampled footprint is well defined. The strategy outlined below has been developed for tall tower sites that are located not directly at the coast (i.e. that are of a predominantly continental character).

2. Intake height. There is only one intake line from the highest level of the tower running to the flask sampler; therefore, only the continuous observations from this height can be quality controlled with parallel sampled flasks (aim 1). As modellers prefer using data (aim 2) from the highest level of the tower (largest footprint, most representative, etc.), all flasks will be sampled from that highest level (as specified in the ICOS Atmosphere Station Specification Document; ICOS RI, 2020b).

3. Integration period. Flasks should be sampled as integrals; i.e. the collected sample should represent a real mean of ambient air (e.g. 1 h mean, comparable to the current model resolution). Also, synchronising in situ continuous observations and integrated flask sampling

is important for the quality control aim (aim 1). This latter requirement is easier to achieve with longer integration times in flask sampling. This means, however, that for comparison reasons, the continuous in situ observations must be kept at the flask sampling height during the entire flask sampling period (i.e. no calibration gas measurement, no switching of in situ intake heights during flask sampling, and no profile information available). This also means that flow rates, delay volumes, and residence times in the tubing, as well as the time of both flask and in situ sampling systems must be properly monitored.

4. Flask handling. Flasks need to be installed and removed manually from the sampler. Remote stations are regularly visited, about once per month, by a technician. The flasks sampled to meet aim 1 should be shipped to the FCL within 1 month after sampling so that a potential bias between in situ and flask analyses is detected without major delay. $^{14}CO_2$ analysis of flasks in the CRL is less urgent; therefore, a few months' delay in the shipment of flasks collected for aim 3 are acceptable.

5. CAL measurement capacity. While the capacity for flask analysis at the FCL has been designed for a total of about 100 flask analyses per station per year, the capacity for $^{14}CO_2$ analyses in the Central Radiocarbon Laboratory (CRL), which are performed *after* the analysis of all other components at the FCL, are only about one-quarter, i.e., on average, 25 samples per station per year. Consequently, all flasks will be shipped from the station to the FCL, and after analysis, a subset will be shipped to the CRL for further analysis. After all analyses have been finished, all flasks, including those which were analysed at the CRL, are leak-tested and conditioned at the FCL before being dispatched to the stations.

4 Results

4.1 Solutions and testing to meet aim 1: ongoing quality control

The ICOS atmosphere station network, supported by the ICOS Central Facilities (ATC and CAL), has been designed and implemented to achieve the highest possible accuracy, precision, and compatibility of atmospheric GHG measurements. For ICOS CO_2 observations, a compatibility goal of 0.1 ppm or better is compulsory. Similarly, ICOS needs to meet the WMO compatibility goals for CH_4 and CO, which are 2 parts per billion (ppb) for both gases (WMO, 2020). First evaluations of ICOS CO_2 measurements indeed yield monthly mean afternoon differences between stations in the free troposphere above 100 m of typically very few parts per million (Ramonet et al., 2020), underlining the importance of the excellent precision and compatibility of these observations.

With regular and frequent comparisons of flask and in situ measurements, ICOS aims to independently monitor their compatibility and provide respective alerts if, for example, the average difference of CO_2 exceeds 0.1 ppm over a few weeks of comparisons. Using flasks sampled from a dedicated intake line to crosscheck the in situ measurements is an important part of the ICOS quality management. It allows an independent end-to-end QC of the entire in situ measurement system consisting of inlet system, drier, analyser, and calibration. As mentioned above, for logistical reasons, about once per month, or every 5 weeks, a box with 12 flasks is scheduled to be shipped from a remote station to the FCL. After analysis, the flask results covering about 1 month of time will be compared with the corresponding in situ data. In the following paragraph, we elaborate on the minimum number of comparison flasks and the corresponding time delay for detecting a significant CO_2 bias between flask and in situ measurements larger than 0.1 ppm. Therefore, we tested the envisaged flask sampling procedure experimentally at the ICOS pilot station in Heidelberg and present here its first application at an ICOS field station.

4.1.1 Flask and in situ CO_2 comparisons in Heidelberg

Similar to the official ICOS atmosphere stations, Heidelberg is equipped with an ICOS-conforming CRDS instrument continuously measuring CO_2, CH_4, and CO in ambient air. In addition, the Heidelberg instrument is calibrated with standard gases provided by the FCL, and its continuous data are automatically evaluated at the ATC. All flasks have been analysed at the FCL. However, since the site does not have a high tower and is located in an urban environment, the variability of the signal can complicate the flask versus in situ comparison.

In order to collect a real hourly integrated air sample in the flask, the flow rate through the flask has to be adjusted during the filling process (Turnbull et al., 2012; see Sect. 2.4). First tests with a $1/t$ decreasing flow rate through the flasks were conducted in Heidelberg during the period from September 2018 to February 2019 and with a better-suited flow controller for the $1/t$ decreasing flow rate from May to October 2019. Ambient air, for continuous measurements and for flask sampling, was collected via a bypass from a permanently flushed intake line from the roof of the institute's building, about 30 m above local ground. These flasks were collected not only at low ambient air variability during afternoon hours but also during other times of the day when within-hour concentration variations for CO_2 at this urban site were higher than 10 ppm. The results of the concentration differences between in situ and flask measurements for CO_2 are shown in Fig. 3a and b. During the first experimental period we obtained three outliers for which the flask CO_2 results were up to more than 3 ppm higher than the in situ measurements. CH_4 and CO in the flasks (not shown) did, however, compare very well and were within a few parts per billion of the continuous in situ data. Although one of the mass flow controllers had some problems with regulating the flow over the large range of flow rates exactly, we did not find obvious reasons for the malfunction of the sampling system. The only explanation for the outliers may, thus, be the contamination of these flasks with room air, which is elevated in CO_2, but not in CH_4 or CO, compared to outside air.

If we disregard the three outliers in the first testing period (one at a low variability situation; see Fig. 3a) and consider only the observations with ambient air CO_2 variability <0.5 ppm, the limited results from the (polluted) Heidelberg site give us the confidence that the flask samples collected over 1 h at low ambient CO_2 variability are well suited for meeting our first aim (i.e. ongoing quality control at Class 1 stations). It is important, though, that the different air residence times in the intake systems of the flask sampler and in situ instrument are properly adjusted; they may significantly differ, for example, if a mixing volume system is installed in the intake lines (as at Hyltemossa). The mean differences between in situ and flask measurements for CO_2 in Heidelberg have been -0.01 ppm at an ambient CO_2 variability of less than 0.5 ppm, with a standard deviation of ± 0.04 ppm ($n = 18$); also see Fig. 3b, which shows that all 18 low variability comparisons lie within the ± 0.1 ppm compatibility range indicated by the dashed red lines. For CH_4 we observed, for ambient variability smaller than ± 10 ppb, a mean difference of 0.20 ppb, with a standard deviation of ± 0.81 ppb ($n = 111$). CO comparison data have not been evaluated here as the CRDS in situ data were not finally calibrated and, thus, not fully compatible with the flask results.

The test measurements in Heidelberg clearly showed that meaningful QC results can best be obtained during situations of low ambient concentration variability. Individual concentration differences increase with increasing ambient variability within the 1 h comparison period. The reason for this increase may be uncertainties in the synchronisation of the measurements (note that a few minutes of shifts in the timing of the integration already introduces a significant bias) or due to incorrect flow rates through the flasks in the $1/t$ sampling scheme. For the QC aim, flask samples should preferentially be collected during low variability situations. We therefore evaluated how frequent afternoon events with less than 0.5 ppm variability occur at typical ICOS stations. In the years 2016 to 2019, except for a few stations and a few summer months, we found, at all five stations, at least 10 h per month at midday (13:00 h local time – LT) with hourly CO_2 standard deviations smaller than 0.5 ppm. On average over the year, more than half of all midday hours had CO_2 standard deviations below 0.5 ppm. Based on this evaluation, we decided that we would not need to preselect sampling days with low ambient variability but could pursue a very simple sampling scheme, e.g. sampling every 3 or 4 d, to be able to detect a mean bias larger than 0.1 ppm between flask and continuous measurements within a period of 4–5 weeks. On average, we can expect that every second flask we sample is suitable for precise intercomparison with in situ measurements. This simple methodology will help us meet aim 2 (see below).

4.1.2 Flask and in situ CO_2 comparisons at the ICOS station Hohenpeißenberg

The very first field test of our flask sampling scheme for QC was conducted at the ICOS station of Hohenpeißenberg (HPB). From the highest level of the tall tower (131 m), ambient air, for continuous measurements and for flask sampling, was collected via two separate lines. Collecting flasks at HPB started in July 2019. The flasks were always sampled with a decreasing $1/t$ flow rate and sampled between 12:30 and 14:00 Coordinated Universal Time (UTC) as we aimed for conditions with low ambient variability, which occurs more frequently in well-mixed conditions during the afternoon. Up to now, 48 flasks have been collected, which could be used for the QC of this ICOS Class 1 station. The overall results of the concentration differences for CO_2 for the complete test period are shown in Fig. 3c.

Our first results of the comparison between continuous measurements and flasks were available in October 2019 and showed larger differences between in situ and flask measurements than expected. A mean difference of 0.34 ppm, with a standard deviation of ± 0.13 ppm ($n = 4$), was determined for situations with an ambient variability of less than 0.5 ppm. Based on these results, the intake system and the entire CO_2 instrumentation were carefully checked. Whilst the last regular leak test on 10 April 2019 passed the ICOS specifications, an unscheduled leak test was performed at the end of October 2019, following the unexpected flasks results. During this test, a leak in the 131 m sampling line to the instruments for the continuous measurements was detected in the shelter. The leak was eliminated on 30 October 2019, and leak tightness was confirmed by a second leak test on 19 November 2019.

For the period after the leak elimination, the calculated differences between in situ and flask measurements for an ambient variability of less than 0.5 ppm all lay within the compatibility goal for CO_2 (0.1 ppm); see blue dots in Fig. 3d. The mean difference between flasks and in situ measurements is -0.02 ppm, with a standard deviation of ± 0.04 ppm ($n = 5$). These results of the first field test of the flask sampling scheme for QC are promising, for example, for enabling the detection of potential leaks at the stations. Once the flask QC procedures have been set up operationally, potential system malfunctions can be detected within a month, complementing the half-yearly compulsory ICOS leak tests.

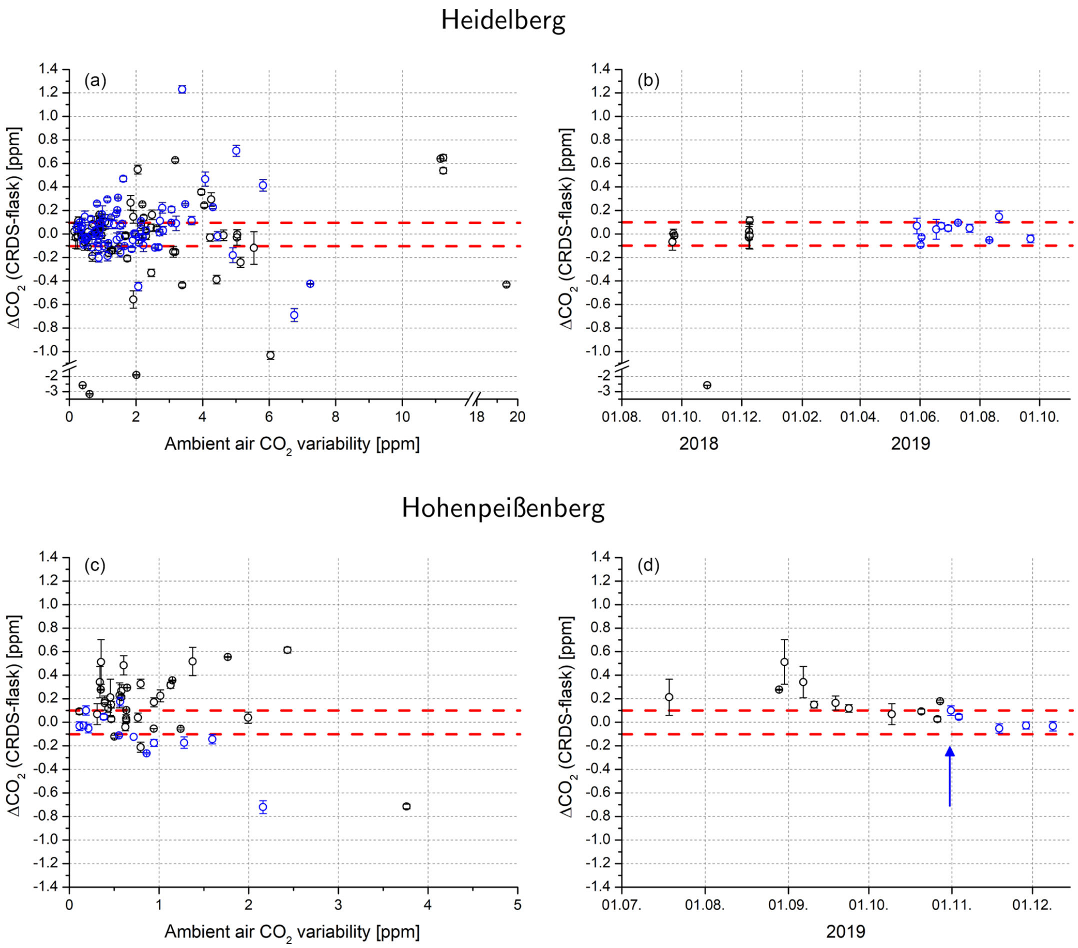

Figure 3. In situ minus flask CO_2 results obtained with the $1/t$ flask flushing method to obtain a real hourly mean sample. **(a–b)** Results from Heidelberg; flasks from the second comparison period are marked in blue. **(a)** Results for all comparison flasks plotted versus ambient variability. **(b)** Temporal development of the in situ minus flask measurements for ambient air CO_2 variability <0.5 parts per million – ppm. All differences in the second comparison period lie within the required ±0.1 ppm compatibility range. No sampling was performed between February and May 2019. **(c–d)** Same as **(a)** and **(b)** but for results from Hohenpeißenberg. Flasks from the comparison period after 30 October 2019 (the date when the leak was sealed) are plotted in blue. **(d)** Temporal development of the in situ minus flask measurement for ambient CO_2 variability <0.5 ppm. All five differences, after sealing the leak on 30 October 2019 (blue arrow; blue dots), lie within the required ±0.1 ppm compatibility range.

4.2 Solutions and testing to meet aim 2: representative flask sampling

In the preceding section we showed that low ambient variability situations would be best suited for meeting aim 1 as synchronisation and exact weighting of flask filling and in situ measurements are not so important at low ambient variability. Moreover, a potential bias between flask and in situ measurements could be detected with better confidence and with an increased number of comparisons. However, to meet aim 2, a scheme for collecting flasks only during low variability situations may cause a significant bias in the sampled footprint. We have tested if such a sampling bias would be visible in the European ICOS network and calculated, with STILT, all midday (13:00 LT) footprints of the five selected stations for the year 2017, using the Jupyter Notebook package of Karstens (2020). Figure 4 shows the respective aggregated footprints for October 2017. A time of 13:00 LT was chosen as an example throughout the paper, but other afternoon hours could also have been chosen, leading to similar results. The left column in Fig. 4 shows the aggregations if every afternoon hour (13:00 LT) was sampled, the middle column shows the aggregated footprints for every third day, and the right column shows the 10 footprints with the lowest variability during October 2017. As expected, the regional coverage of the entire station footprint is generally better when sampling randomly, every third day, than when sampling on the 10 d with the lowest variability.

In addition to the footprint analysis, which gives a visual, qualitative idea of the effect of different flask sampling

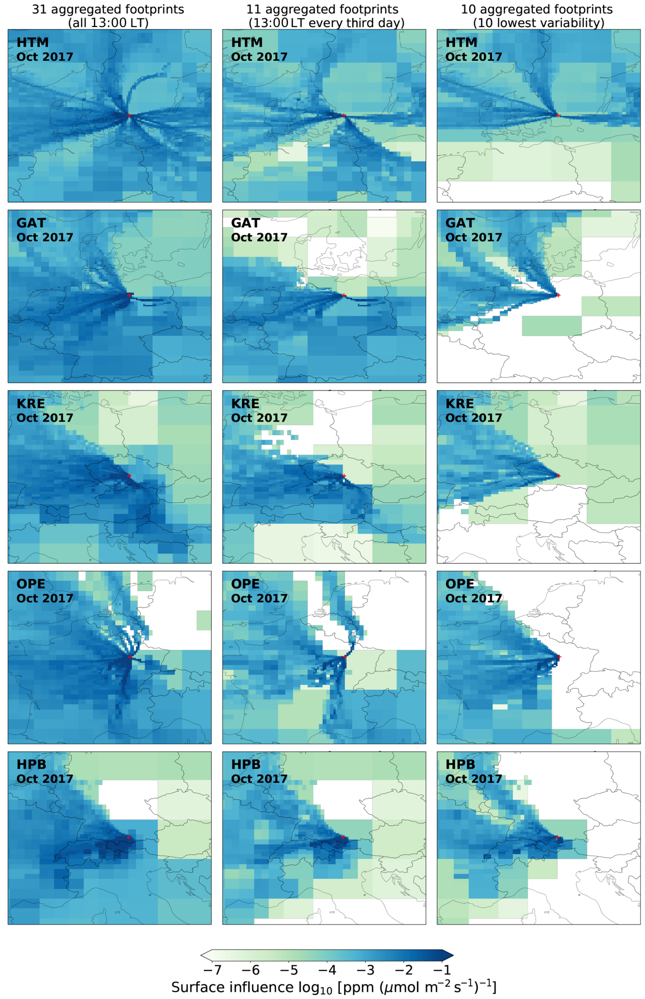

Figure 4. Aggregated footprints calculated for the five ICOS stations from top to bottom: Hyltemossa (HTM), Gartow (GAR), Křešín (KRE), Observatoire Pérenne de l'Environnement (OPE), and Hohenpeißenberg (HPB) for October 2017. The left column shows the footprints for all 31 d at 13:00 local time (LT), the middle column shows the same footprints, but sampled only every third day, and the right column shows those of the 10 d with the lowest variability. Note the logarithmic colour scale.

schemes, we evaluated the first 3 years of continuous CO_2 measurements from the five ICOS stations to quantify the effect of random sampling every 3 d versus only sampling low variability situations. Figure 5a–e show, in the upper panels, for each station, all available hourly atmospheric CO_2 data as grey dots, while the blue lines, each shifted by 1 d, connect the 13:00 LT data every 3 d. The red dots in the upper panels highlight the 10 lowest variability afternoon values in each month. As expected, all summer afternoon concentrations generally fall into the lower concentration range of the bulk of data. At all stations, the variability changes from a diurnal shape during the summer months to a more synoptic variability in the winter (for more details, also see Figs. 7 and 8). This synoptic variability is also represented in the afternoon sampling. In the middle panels of Fig. 5a–e we have plotted, as black dots, monthly means calculated from all afternoon hours between 11:00 and 15:00 LT and their standard deviations. The blue dots show the monthly mean values obtained from sampling every third day (the three different 3 d patterns are shown in individual shifted blue dots), while the red dots represent the monthly means calculated from the 10 samples with the lowest variability (the coloured dots were shifted by 1 d each for better visibility). It is obvious that regular sampling provides better representative monthly means, deviating in only a few cases from the all-afternoon means in CO_2 by more than 2 ppm (Fig. 5a–e, bottom panels). If samples were collected at low variability only, they would often underestimate monthly mean values, in some cases by more than 4 ppm (red lines in Fig. 5a–e, bottom panels). Although regular sampling every third day also introduces some variable deviations from the correct afternoon means, sampling only at low variability may introduce rather large biases – mainly towards lower CO_2 concentrations. Note that inversion models also select measured data for their inversion runs only for the time of the day, and not for low variability data, to estimate fluxes (Rödenbeck, 2005).

We have investigated only potential sampling effects on CO_2 concentrations here; however, other tracer concentrations are also expected to be affected in a similar way. For the ICOS atmosphere network we, therefore, choose the simpler sampling scheme of one flask every third day. This sampling scheme is expected to serve aims 1 and 2, where those flasks with low within-hour variability (on average one flask per week; see Sect. 4.1) could be used for the quality control aim, while all flask samples would deliver as much representative data as possible for all additional trace components analysed in the FCL solely based on flasks.

4.3 Solutions and testing to meet aim 3: catching potentially high fossil fuel CO_2 events

The first ^{14}C analyses on integrated CO_2 samples at ICOS stations showed rather low average fossil fuel CO_2 ($ffCO_2$) concentrations, therewith confirming that ICOS stations primarily monitor the terrestrial biospheric signals. Figure 6a–d (upper panels of the graphs for the individual stations) shows our first $^{14}CO_2$ results from the 2-week integrated CO_2 sampling at Hohenpeißenberg, Observatoire Pérenne de l'Environnement, Hyltemossa, and Křešín. Particularly during summer, the monthly mean regional fossil fuel CO_2 offsets, if compared to a background level calculated from the composite of 2-week integrated $^{14}CO_2$ measurements at Jungfraujoch in the Swiss Alps and Mace Head on the Irish coast, are often lower than a few parts per million (Fig. 6a–d, lower panels). Only during winter can regional $ffCO_2$ offsets reach 2-week mean concentrations of more than 5 ppm. These signals, although providing good mean $ffCO_2$ results for the average footprints of the stations, are often too small

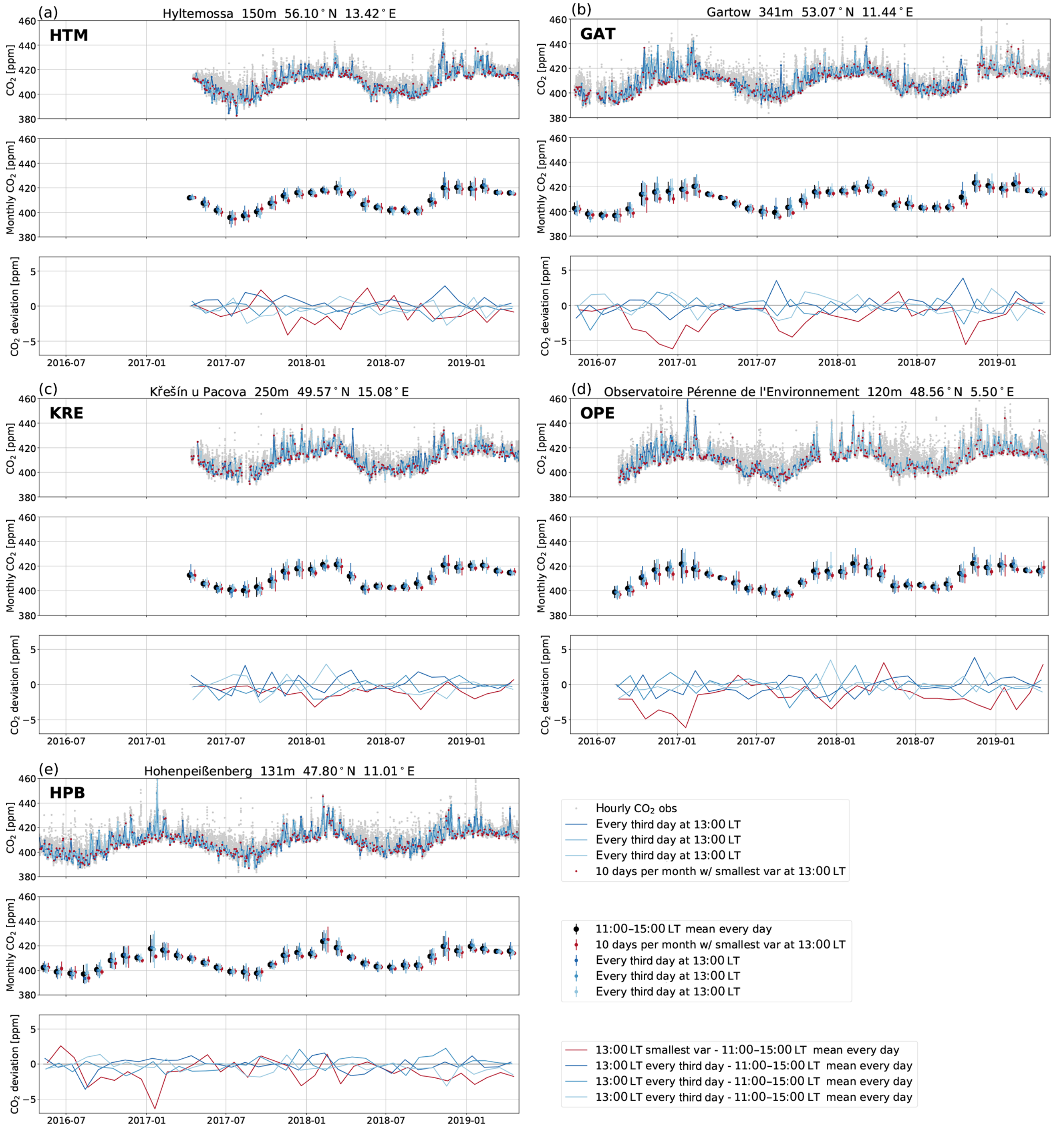

Figure 5. CO_2 concentration data measured at Hyltemossa **(a)**, Gartow **(b)**, Křešín **(c)**, Observatoire Pérenne de l'Environnement **(d)**, and Hohenpeißenberg **(e)**. For each station the upper panel shows all hourly data as grey dots, while afternoon data (13:00 LT) from every third day are displayed as three blue lines shifted by 1 d each. Red dots highlight the 10 afternoon values with the lowest variability for each month. The middle panels show monthly means and standard deviations of all afternoon hours (11:00–15:00 LT) as black dots, respective means from afternoon data collected every third day are shown in blue, and means of the 10 afternoon values with the lowest variability are shown in red (for better visibility the coloured dots were shifted by 1 d each). The lower panels present the differences in the selected afternoon means from the respective mean calculated from all afternoon data.

to provide a solid top-down constraint of regional fossil fuel CO_2 emission inventories and its changes when evaluated in regional model inversions (Levin and Rödenbeck, 2008; Wang et al., 2018). One of the aims of flask sampling in ICOS is, therefore, to explicitly sample air which has passed over fossil fuel CO_2 emission areas. Ideally we would like to obtain signals and analyse flasks for $^{14}CO_2$ only in cases when the expected fossil fuel CO_2 component is larger than 4–5 ppm. This would allow us to obtain an uncertainty of the estimated $ffCO_2$ component below 30 % (Levin et al., 2003; Turnbull et al., 2006). Furthermore, as sample preparation for ^{14}C analysis is very laborious and the capacity of the CRL is limited to about 25 flask samples per station per year, one should know beforehand if a sample potentially contains a significant regional fossil fuel CO_2 component. This could either be found out with near real-time transport model simulations or directly using the in situ observations at the station.

A good indicator of the potential regional fossil fuel CO_2 concentration at a station is the ambient CO concentration (Levin and Karstens, 2007), a trace gas that is monitored continuously at all ICOS Class 1 sites. It would then depend on the average CO : $ffCO_2$ ratio of fossil fuel emissions in the footprint of the stations to estimate, from the measured CO, the expected $ffCO_2$ concentration. Mean CO : $ffCO_2$ emission ratios can be very different in different countries; they mainly depend on the energy production processes and on domestic heating systems (Gamnitzer et al., 2006; Turnbull et al., 2006, 2011; Levin and Karstens, 2007; Vogel et al., 2010). In this respect, the share of biofuel use may also be relevant. In our study we first analysed our selected ICOS stations for regional fossil fuel CO_2 signals larger than 4 ppm and determined the frequencies of those events. Note that in order for the flask results to be used in transport model investigations, similar to all other flask samples, $^{14}CO_2$ flasks should also be collected during early afternoon when atmospheric mixing can be modelled with good confidence. During these situations, however, any $ffCO_2$ signals will be highly diluted. Similar to the approach in the previous section, we investigated the potential $ffCO_2$ levels for the five stations of Hyltemossa, Gartow, Křešín, Observatoire Pérenne de l'Environnement, and Hohenpeißenberg; this was first done theoretically with STILT model simulations transporting EDGAR version 4.3.2 emissions to the five measurement sites. As a second step, we evaluated the real continuous CO_2 and CO observations from 2017 and 2018 (see Table 1).

4.3.1 Investigation of afternoon fossil fuel CO_2 events in 2017 at Gartow

Figure 7a–b show ambient STILT-simulated CO_2 and CO mole fractions at Gartow 341 m in July 2017 (13:00 LT values highlighted by coloured symbols), while Fig. 7c compares STILT-simulated total CO_2 (blue line) to observations (black line). The agreement between model and observations turned out to be reasonable, particularly during afternoon hours. In July 2017, deviations of the model simulations from observations are larger during night when the model seems to underestimate the measured concentration pile up. This model deficiency is the reason why we decided to collect the flask samples at midday or in the afternoon, making sure the data can be used in inversion estimates of fluxes. In Fig. 7d the simulated regional CO_2 components ($ffCO_2$ offset and biospheric CO_2 offset) originating from fluxes in the model domain covering the greater part of Europe are displayed, underlining the generally moderate fossil fuel CO_2 signal at Gartow in July. Indeed, summer situations with potentially high $ffCO_2$ concentrations are rare (one to five cases) at all ICOS stations and, at Gartow, only during 3 d; i.e. on 1, 7, and 27 July the modelled afternoon $ffCO_2$ was larger than 4 ppm (highlighted by red crosses in Fig. 7a). At the same time, the modelled CO offset was elevated but did not reach 0.04 ppm (Fig. 7b). CO offsets were estimated relative to the minimum modelled CO concentration of the last 3 d (grey line in Fig. 7b). In October 2017, the modelled (Fig. 8b) and measured CO (Fig. 8f) offsets do, however, rather frequently exceed 0.04 ppm. The generally good correlation between simulated $ffCO_2$ and CO offset can therefore be used as a criterion for $ffCO_2$ in collected flasks, and 0.04 ppm may be a good threshold for Gartow to predict a $ffCO_2$ signal of more than 4 ppm in sampled ambient air. This is supported by real observations displayed in Figs. 7f and 8f, where observed CO offsets >0.04 ppm (marked by magenta crosses) coincide with high total CO_2 and also with STILT-simulated $ffCO_2$ (see, for example, the synoptic event on 19–20 October 2017).

The aggregated footprints of the three afternoon situations with STILT-simulated $ffCO_2$ >4 ppm in July 2017 are displayed in Fig. 9a. They show southwesterly trajectories and a dominating surface influence from the highly populated German Ruhr area but also some influences from large emitters (e.g. power plants) in northwestern Germany and at the Netherlands' North Sea coast (see Fig. 9b). The main influence area with high $ffCO_2$ emissions in October 2017 (Fig. 9d) also shows Berlin as a significant emitter and some "hotspots" close to the German–Polish border in the southeast.

4.3.2 Investigation of afternoon fossil fuel CO_2 events in 2017 and 2018 at Hyltemossa, Křešín, Observatoire Pérenne de l'Environnement, and Hohenpeißenberg

Overlapping measurements and STILT model runs are also available for the other four ICOS stations (Karstens, 2020). The general picture is similar here as in Gartow, but the number of elevated $ffCO_2$ events is often even smaller at these stations than at Gartow. For example, we find no $ffCO_2$ events at Hyltemossa, Gartow, Křešín, and Hohenpeißenberg and only three at Observatoire Pérenne de l'Environnement in July 2018 (Table 1). Simultaneously observed CO eleva-

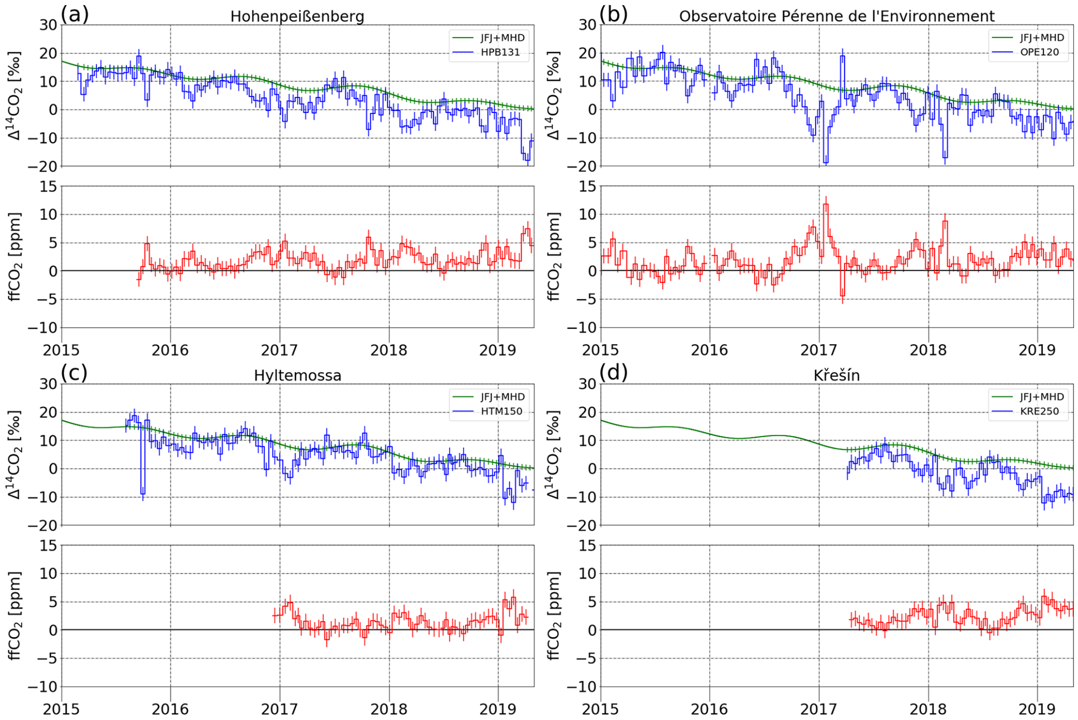

Figure 6. $^{14}CO_2$ observations and estimated fossil fuel CO_2 concentrations relative to European background at the ICOS stations **(a–d)** Hohenpeißenberg, Observatoire Pérenne de l'Environnement, Hyltemossa, and Křešín. The top panel for each station shows the $\Delta^{14}CO_2$ results in permil deviation from the National Bureau of Standards (NBS) oxalic acid standard (Stuiver and Polach, 1977) for the respective station (blue histogram) together with the European background, which is estimated as the fit curve to measured data from Jungfraujoch (JFJ) and Mace Head (MHD). The bottom panel for each station gives the regional fossil fuel CO_2 offset calculated from the $^{14}CO_2$ and CO_2 data, according to Levin et al. (2011). For Hohenpeißenberg and Hyltemossa, the $ffCO_2$ calculation starts later than the $^{14}CO_2$ data since no ICOS CO_2 data are available in the early periods for these stations.

Table 1. Number of midday (13:00 LT) $ffCO_2$ events >4 ppm estimated by the Stochastic Time-Inverted Lagrangian Transport (STILT) model for 2017 and 2018 and potential fossil fuel CO_2 events in both years, based on modelled (M) and observed (O) ΔCO elevations of more than 0.04 ppm compared to background (entries are empty if fewer than 20 afternoon CO observations are available in the respective month).

	Hyltemossa			Gartow			Křešín			Observatoire Pérenne de l'Environnement			Hohenpeißenberg		
	$ffCO_2$	ΔCO		$ffCO_2$	ΔCO		$ffCO_2$	ΔCO		$ffCO_2$	ΔCO		$ffCO_2$	ΔCO	
2017/ 2018	M	M	O	M	M	O	M	M	O	M	M	O	M	M	O
Jan	9/4	2/3	/7	15/8	7/3	/8	6/5	8/5		11/4	10/4	10/8	10/10	15/11	/6
Feb	7/5	4/1	/7	10/7	6/4	/11	7/4	7/2	/16	6/10	3/7	10/13	4/9	9/6	/17
Mar	2/3	0/4	/8	5/6	4/4	/11	4/1	3/3	/16	5/4	5/4	4/7	3/4	3/5	6/9
Apr	1/2	0/2	/3	0/4	0/1	/2	2/1	0/0	/3	1/2	0/2	0/1	6/2	0/1	3/0
May	0/0	0/0	/0	1/0	0/0	3/1	4/3	1/0	2/0	2/2	1/2	1/3	2/3	2/2	1/1
Jun	0/0	0/0	/0	2/4	0/0	1/1	0/2	0/0	/0	0/4	0/2	2/1	1/3	0/0	0/0
Jul	0/0	0/0	/0	3/0	0/0	2/2	0/0	0/0	/0	0/3	0/2	1/0	0/0	0/0	0/0
Aug	0/1	0/0	2/1	2/2	1/0	2/5	0/0	0/0	/3	0/1	0/1	0/6	0/1	0/0	3/3
Sep	2/0	0/0	0/0	6/4	2/1	10/1	3/4	0/1	/3	3/6	1/3	2/5	1/5	0/2	0/2
Oct	1/7	0/2	2/6	8/8	4/3	7/6	4/6	3/1	/10	1/12	1/7	0/8	1/5	0/3	2/8
Nov	5/9	4/5	5/12	13/12	10/7	11/	5/3	2/4	/18	5/9	5/6	5/12	9/15	8/15	14/12
Dec	3/5	1/4	5/8	8/8	3/2	2/	10/9	2/6	/12	2/7	1/7	/8	9/5	8/9	10/5

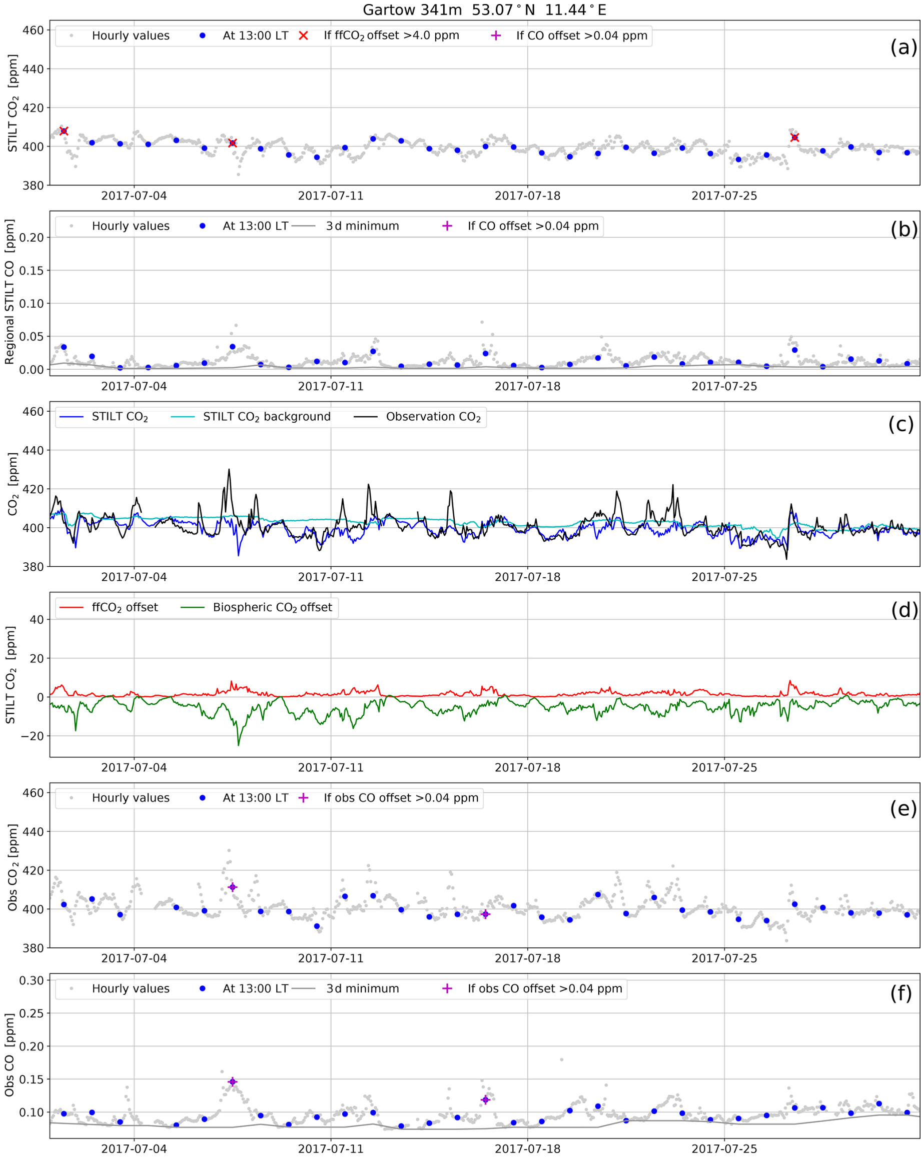

Figure 7. Variability of STILT-simulated **(a–d)** and measured **(c, e, f)** CO_2 and CO concentrations at Gartow at the 344 or 341 m level in July 2017. Afternoon values are highlighted with coloured symbols (blue dots) and situations with elevated $ffCO_2$, based on modelled or measured CO (CO offset >0.04 ppm), are marked with a magenta cross in the CO and also in the CO_2 records (clearer in Fig. 8 for October 2017 when such situations occur more often). CO offsets in STILT model simulations **(b)** and observations **(f)** were estimated relative to the minimum CO concentration of the last 3 d (grey lines).

tions relative to background are often only small in summer and do not reach the (preliminary) threshold of 0.04 ppm. Starting in October or November, $ffCO_2$ elevations become more frequent, coupled to the more synoptic variability of GHGs in the winter half-year (see Fig. 5a–e, upper panels). The number of modelled fossil fuel CO_2 events larger than 4 ppm for all months in 2017 and 2018, or based on observed CO offsets larger than 0.04 ppm using the same estimate for the CO background as for the model results displayed in Figs. 7b and 8b, are listed in Table 1. Only in the winter half-year can we potentially sample measurable fossil fuel CO_2 signals well. Lower ΔCO thresholds could be used for summer, which means accepting larger uncertainties of the $ffCO_2$ component. Although it would be most desirable to have a good $ffCO_2$ estimate in summer when the biospheric signal is large, our present measurement precision does not allow us to determine very small $ffCO_2$ contributions with good confidence. Therefore, we will currently have to restrict ^{14}C analysis to flasks mainly collected in autumn, winter, and spring to constrain $ffCO_2$ emission inventories, with the additional advantage that the variability of biospheric signals is smaller during these seasons (see Fig. 8d).

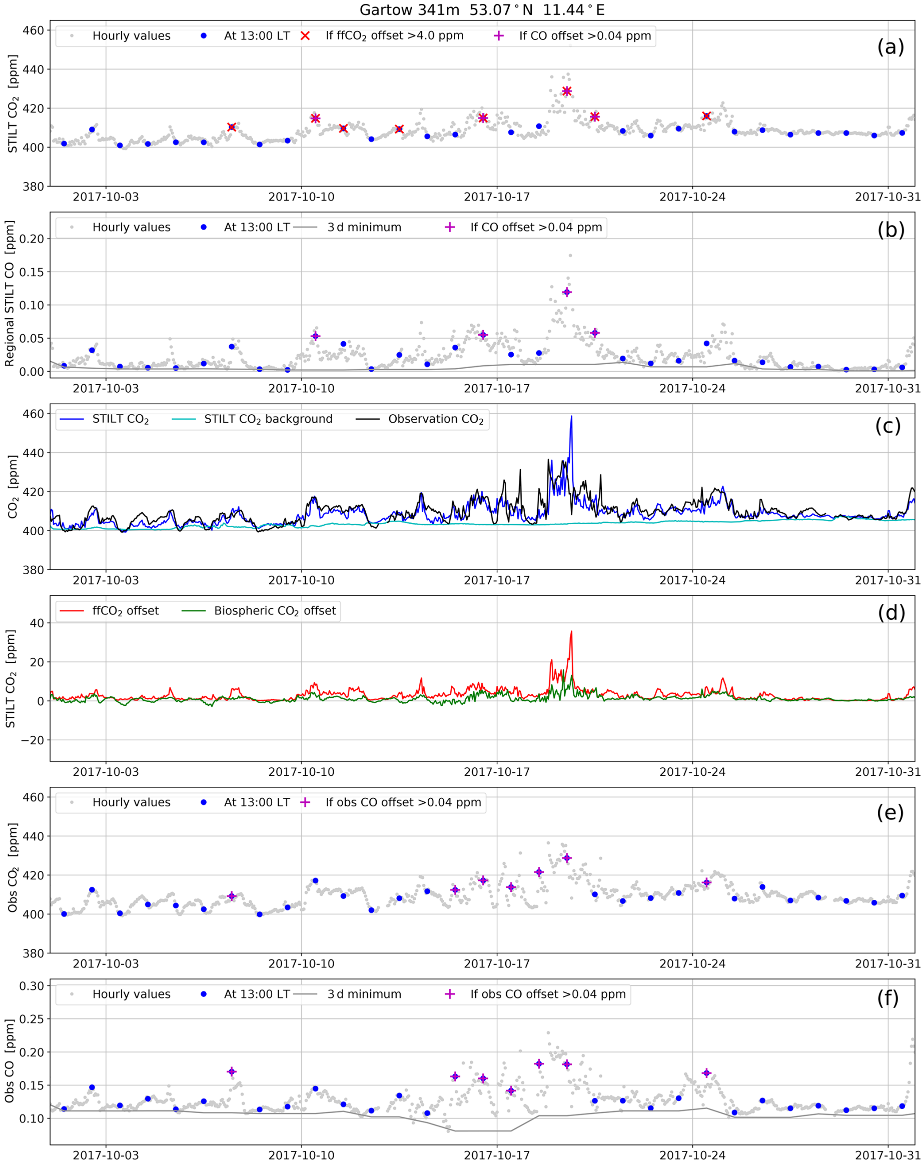

Figure 8. Same as Fig. 7 but for October 2017.

To give some indication of the main ffCO$_2$ emission areas influencing the four stations, Fig. 10 shows aggregated footprints and the respective surface influence areas contributing to modelled ffCO$_2$ concentrations larger than 4 ppm in October 2017. At all four stations, and also at Gartow (Fig. 9), the areas potentially contributing significantly to the fossil fuel signals are located rather far away, and many of them are associated with large coal-fired power plants or other point sources. But a few big cities, such as Prague at Křešín, also occasionally contribute.

5 Implementation of the flask sampling scheme at ICOS stations

Sampling one flask every third day, independent of ambient CO$_2$ variability, can easily be implemented at ICOS stations, since sampling of all 24 flasks in the sampler can individually be programmed in advance. Assuming that flasks can be exchanged about once per month, during this time span 12 flasks would have been collected and could then be shipped in one box to the FCL for analysis. The remaining 12 flasks in the sampler would be reserved for ffCO$_2$ event sampling. In order to have a realistic chance to catch all possible events at a station, the sampler would be set to fill one of these flasks on each day in between the regular sampling every third day. As continuous trace gas measurement data are transferred

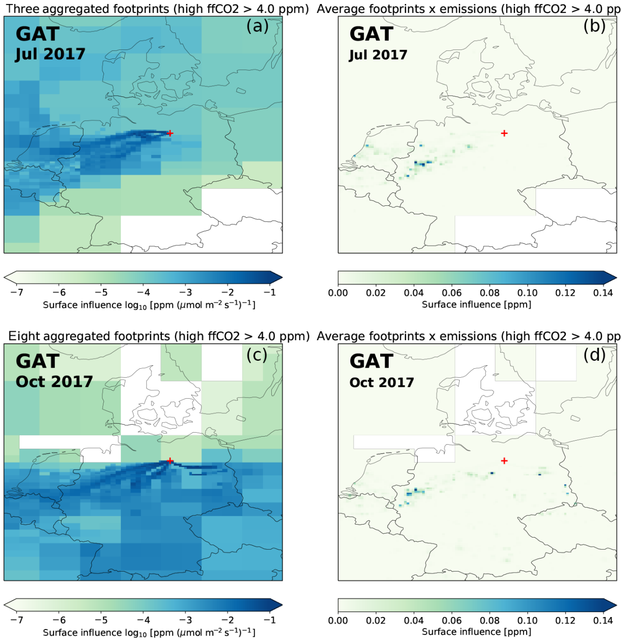

Figure 9. Aggregated footprints with elevated $ffCO_2$, and the corresponding surface influences for Gartow in July 2017 **(a–b)** and October 2017 **(c–d)**, based on the EDGAR version 4.3.2 emission inventory. Note the logarithmic colour scale in the aggregated footprint maps.

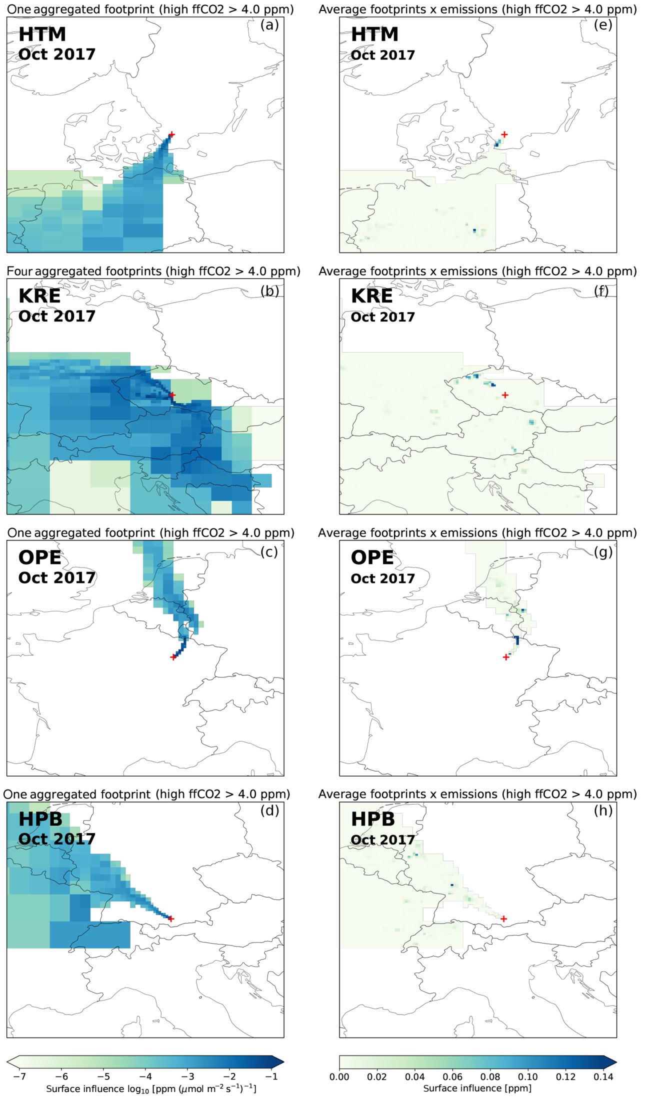

Figure 10. Aggregated footprints with elevated $ffCO_2$ and the corresponding surface influences for Hyltemossa **(a, e)**, Křešín **(b, f)**, Observatoire Pérenne de l'Environnement **(c, g)**, and Hohenpeißenberg **(d, h)** in October 2017.

from the station to the ATC every night, level 1 CO data are available on the morning after flask sampling the day before. These data will then be automatically evaluated at the ATC for potentially elevated CO to decide if the flask that had been collected on the day before potentially has an elevated $ffCO_2$ concentration and should be retained for $^{14}CO_2$ analysis. If yes, the flask sampler will receive a respective message from the ATC. If not, the flask can be resampled. Based on our analysis of modelled $ffCO_2$ for the years 2017 and 2018, the likelihood is small that more than 12 $ffCO_2$ events are sampled within 1 month. Also, some of the events may already have been sampled in one of the "regular"flasks sampled every third day. If this is the case, these flasks will be marked so that they are passed on to the CRL after analysis of all other components in the FCL. In the future, the flask sampling strategy, in particular, for $ffCO_2$ events might change once real-time GHG prediction systems or prognostic footprint products are available, which would allow more accurate targeting of certain emission areas. The first tests, using prognostic trajectories to automatically trigger $^{14}CO_2$ flask sampling, are made at the ICOS CRL pilot station and at selected ICOS Class 1 stations but are not yet mature enough to be implemented in the entire ICOS network. It is, however, also worth mentioning that sampling flasks during nighttime could largely increase the significance of ^{14}C-based $ffCO_2$ estimates. Currently, we optimise our sampling strategy to meet the inability of transport models that are not digesting nighttime data. This situation is unfortunate and must urgently be improved in order to increase our ability to monitor, in a top-down way, long-term changes of the envisaged $ffCO_2$ emissions in Europe.

6 Conclusions

Although other flask sampling programmes from continental tall tower stations have similar aims, as presented here for ICOS, developing a dedicated sampling strategy to maximise the information from a minimum number of flasks is a new approach which, to our knowledge, has not yet been taken in any other sampling network. It may contribute to optimising efforts at the (remote) ICOS stations and the analytical capacities and capabilities of the ICOS Central Analytical Laboratories. Our strategy was designed to meet, on one hand, the requirements for quality control, making sure, by comparison of flask results with the parallel in situ measurements, that ICOS data are of highest precision and accuracy. Our first results showed that this strategy of independent quality control is working successfully. However, it requires fast turnaround of flasks in order to quickly detect errors in the in situ and also in the flask sampling systems. Besides ongoing QC, our sampling scheme will provide flask results that can be optimally used in current inverse modelling tasks to estimate continental fluxes, not only of core ICOS components, such as CO_2 and CH_4, but also of trace substances, which are not yet measured continuously. Trying to also monitor fossil fuel CO_2 emission hotspots at ICOS stations during well-mixed afternoon hours will be a particular challenge because the $ffCO_2$ influence at that time of the day is often very small, particularly in summer. There is thus an urgent need for transport model improvement so that nighttime data can also be used for the inversion of fluxes. Experience in the coming years will show if our current strategy is successful in meeting all the aims or if it needs further adaption.

Code availability. The Jupyter Notebook package for performing the analysis of STILT model results and ICOS in situ measurements is available at https://doi.org/10.18160/FSS2-SH26 (Karstens, 2020).

Data availability. Data are available at https://doi.org/10.18160/CE2R-CC91 (ICOS RI, 2019).

Author contributions. IL and UK designed the study, UK developed the Jupyter Notebook package and conducted the STILT model runs, and ME built the flask sampler and developed its software. FM and SA conducted the flask sampling and evaluated the comparison data. DR was responsible for flask and SH for $^{14}CO_2$ analysis. MR was responsible for the ICOS data evaluation, and GV, SC, MH, DK, and ML were responsible for the measurements at the ICOS stations. IL and UK prepared the paper, with contributions from all other coauthors.

Competing interests. The authors declare that they have no conflict of interest.

Acknowledgements. All measurements and model estimates were conducted within the ICOS RI consortium by technicians and scientists contributing to the different components (National Networks, Central Facilities, and Carbon Portal). We wish to thank all members of the ICOS Atmosphere Monitoring Station Assembly for their contributions to the discussion of the ICOS flask sampling strategy. Jocelyn Turnbull and Auke van der Woude are acknowledged for their helpful comments and suggestions that improved the paper.

Financial support. This research has been supported by the European Commission (RINGO; grant no. 730944). Operation of the Křešín u Pacova station was supported by the Ministry of Education, Youth and Sports of the Czech Republic as part of the CzeCOS project (grant no. LM2015061). ICOS RI is jointly funded by national funding agencies from all ICOS partner countries.

Review statement. This paper was edited by Astrid Kiendler-Scharr and reviewed by Jocelyn Turnbull and Auke van der Woude.

References

Andrews, A. E., Kofler, J. D., Trudeau, M. E., Williams, J. C., Neff, D. H., Masarie, K. A., Chao, D. Y., Kitzis, D. R., Novelli, P. C., Zhao, C. L., Dlugokencky, E. J., Lang, P. M., Crotwell, M. J., Fischer, M. L., Parker, M. J., Lee, J. T., Baumann, D. D., Desai, A. R., Stanier, C. O., De Wekker, S. F. J., Wolfe, D. E., Munger, J. W., and Tans, P. P.: CO_2, CO, and CH_4 measurements from tall towers in the NOAA Earth System Research Laboratory's Global Greenhouse Gas Reference Network: instrumentation, uncertainty analysis, and recommendations for future high-accuracy greenhouse gas monitoring efforts, Atmos. Meas. Tech., 7, 647–687, https://doi.org/10.5194/amt-7-647-2014, 2014.

Brown, C. W. and Keeling, C. D.: The concentration of atmospheric carbon dioxide in Antarctica, J. Geophys. Res., 70, 6077–6085, https://doi.org/10.1029/JZ070i024p06077, 1965.

Ciais, P., Reichstein, M., Viovy, N., Granier, A., Ogee, J., Allard, V., Aubinet, M., Buchmann, N., Bernhofer, C., Carrara, A., Chevallier, F., De Noblet, N., Friend, A. D., Friedlingstein, P. T., Grünwald, T., Heinesch, B., Keronen, P., Knohl, A., Krinner, G., Loustau, D., Manca, G., Matteucci, G., Miglietta, F., Ourcival, J. M., Papale, D., Pilegaard, K., Rambal, S., Seufert, G., Soussana, J. F., Sanz, M. J., Schulze, E. D., Vesala, T., and Valentini, R.: Europe-wide reduction in primary productivity caused by the heat and drought in 2003, Nature, 437, 529–533, 2005.

Conil, S., Helle, J., Langrene, L., Laurent, O., Delmotte, M., and Ramonet, M.: Continuous atmospheric CO_2, CH_4 and CO measurements at the Observatoire Pérenne de l'Environnement (OPE) station in France from 2011 to 2018, Atmos. Meas. Tech., 12, 6361–6383, https://doi.org/10.5194/amt-12-6361-2019, 2019.

Corazza, M., Bergamaschi, P., Vermeulen, A. T., Aalto, T., Haszpra, L., Meinhardt, F., O'Doherty, S., Thompson, R., Moncrieff, J., Popa, E., Steinbacher, M., Jordan, A., Dlugokencky, E., Brühl, C., Krol, M., and Dentener, F.: Inverse modelling of European N_2O emissions: assimilating observations from different networks, Atmos. Chem. Phys., 11, 2381–2398, https://doi.org/10.5194/acp-11-2381-2011, 2011.

Friedlingstein, P., Jones, M. W., O'Sullivan, M., Andrew, R. M., Hauck, J., Peters, G. P., Peters, W., Pongratz, J., Sitch, S., Le Quéré, C., Bakker, D. C. E., Canadell, J. G., Ciais, P., Jackson, R. B., Anthoni, P., Barbero, L., Bastos, A., Bastrikov, V., Becker, M., Bopp, L., Buitenhuis, E., Chandra, N., Chevallier, F., Chini, L. P., Currie, K. I., Feely, R. A., Gehlen, M., Gilfillan, D., Gkritzalis, T., Goll, D. S., Gruber, N., Gutekunst, S., Harris, I., Haverd, V., Houghton, R. A., Hurtt, G., Ilyina, T., Jain, A. K., Joetzjer, E., Kaplan, J. O., Kato, E., Klein Goldewijk, K., Korsbakken, J. I., Landschützer, P., Lauvset, S. K., Lefèvre, N., Lenton, A., Lienert, S., Lombardozzi, D., Marland, G., McGuire, P. C., Melton, J. R., Metzl, N., Munro, D. R., Nabel, J. E. M. S., Nakaoka, S.-I., Neill, C., Omar, A. M., Ono, T., Peregon, A., Pierrot, D., Poulter, B., Rehder, G., Resplandy, L., Robertson, E., Rödenbeck, C., Séférian, R., Schwinger, J., Smith, N., Tans, P. P., Tian, H., Tilbrook, B., Tubiello, F. N., van der Werf, G. R., Wiltshire, A. J., and Zaehle, S.: Global Carbon Budget 2019, Earth Syst. Sci. Data, 11, 1783–1838, https://doi.org/10.5194/essd-11-1783-2019, 2019.

Gamnitzer, U., Karstens, U., Kromer, B., Neubert, R. E. M., Meijer, H. A. J., Schroeder, H., and Levin, I.: Carbon monoxide: A quantitative tracer for fossil fuel CO_2?, J. Geophys. Res., 111, D22302, https://doi.org/10.1029/2005JD006966, 2006.

Geels, C., Gloor, M., Ciais, P., Bousquet, P., Peylin, P., Vermeulen, A. T., Dargaville, R., Aalto, T., Brandt, J., Christensen, J. H., Frohn, L. M., Haszpra, L., Karstens, U., Rödenbeck, C., Ramonet, M., Carboni, G., and Santaguida, R.: Comparing atmospheric transport models for future regional inversions over Europe – Part 1: mapping the atmospheric CO_2 signals, Atmos. Chem. Phys., 7, 3461–3479, https://doi.org/10.5194/acp-7-3461-2007, 2007.

Gerbig, C., Lin, J. C., Munger, J. W., and Wofsy, S. C.: What can tracer observations in the continental boundary layer tell us about surface-atmosphere fluxes?, Atmos. Chem. Phys., 6, 539–554, https://doi.org/10.5194/acp-6-539-2006, 2006.

Gloor, M., Bakwin, P., Hurst, D., Lock, L., Draxler, R., and Tans, P.: What is the concentration footprint of a tall tower?, J. Geophys. Res., 106, 17831–17840, 2001.

Hazan, L., Tarniewicz, J., Ramonet, M., Laurent, O., and Abbaris, A.: Automatic processing of atmospheric CO_2 and CH_4 mole fractions at the ICOS Atmosphere Thematic Centre, Atmos. Meas. Tech., 9, 4719–4736, https://doi.org/10.5194/amt-9-4719-2016, 2016.

ICOS RI: Atmospheric Greenhouse Gas Mole Fractions of CO_2, CH_4, CO, $^{14}CO_2$ and Meteorological Observations September 2015–April 2019 for 19 stations (49 vertical levels), final quality controlled Level 2 data (Version 1.0), ICOS ERIC – Carbon Portal, https://doi.org/10.18160/CE2R-CC91, 2019.

ICOS RI: ICOS Atmosphere Release 2020-1 of Level 2 Greenhouse Gas Mole Fractions of CO_2, CH_4, CO, meteorology and $^{14}CO_2$ (Version 1.0), ICOS ERIC – Carbon Portal, https://doi.org/10.18160/H522-A9S0, 2020a.

ICOS RI: ICOS Atmosphere Station Specification V2.0, edited by: Laurent, O., ICOS ERIC, https://doi.org/10.18160/GK28-2188, 2020b.

Janssens-Maenhout, G., Crippa, M., Guizzardi, D., Muntean, M., Schaaf, E., Dentener, F., Bergamaschi, P., Pagliari, V., Olivier, J. G. J., Peters, J. A. H. W., van Aardenne, J. A., Monni, S., Doering, U., Petrescu, A. M. R., Solazzo, E., and Oreggioni, G. D.: EDGAR v4.3.2 Global Atlas of the three major greenhouse gas emissions for the period 1970–2012, Earth Syst. Sci. Data, 11, 959–1002, https://doi.org/10.5194/essd-11-959-2019, 2019.

Karstens, U.: Jupyter Notebook for ICOS Flask Sampling Strategy (Version 1.0), ICOS-ERIC – Carbon Portal, https://doi.org/10.18160/FSS2-SH26, 2020.

Levin, I. and Karstens, U.: Inferring high-resolution fossil fuel CO_2 records at continental sites from combined (CO_2)-C-14 and CO observations, Tellus B, 59, 245–250, 2007.

Levin, I. and Rödenbeck, C.: Can the envisaged reductions of fossil fuel CO_2 emissions be detected by atmospheric observations? Naturwissenschaften, 95, 203–208, https://doi.org/10.1007/s00114-007-0313-4, 2008.

Levin, I., Kromer, B., Schmidt, M., and Sartorius, H.: A novel approach for independent budgeting of fossil fuels CO_2 over Europe by $^{14}CO_2$ observations, Geophys. Res. Lett., 30, 2194, https://doi.org/10.1029/2003GL018477, 2003.

Levin, I., Hammer, S., Eichelmann, E., and Vogel, F.: Verification of greenhouse gas emission reductions: The prospect of atmospheric monitoring in polluted areas, Philos. T. R. Soc. A, 369, 1906–1924, https://doi.org/10.1098/rsta.2010.0249, 2011.

Lin, J. C., Gerbig, C., Wofsy, S. C., Andrews, A. E., Daube, B. C., Davis, K. J., and Grainger, C. A.: A near-field tool for simulating the upstream influence of atmospheric observations: The Stochastic Time-Inverted Lagrangian Transport (STILT) model, J. Geophys. Res., 108, 4493, https://doi.org/10.1029/2002JD003161, 2003.

Mahadevan, P., Wofsy, S. C., Matross, D. M., Xiao, X., Dunn, A. L., Lin, J. C., Gerbig, C., Munger, J. W., Chow, V. Y., and Gottlieb, E. W.: A satellite-based biosphere parameterization for net ecosystem CO_2 exchange: Vegetation Photosynthesis and Respiration Model (VPRM), Global Biogeochem. Cy., 22, GB2005, https://doi.org/10.1029/2006GB002735, 2008.

Neubert, R. E. M., Spijkervet, L. L., Schut, J. K., Been, H. A., and Meijer, H. A. J.: A computer-controlled continuous air drying and flask sampling system, J. Atmos. Oceanic Technol. 21, 4, 651–659, https://doi.org/10.1175/1520-0426(2004)021<0651:ACCADA>2.0.CO;2, 2004.

Ramonet, M., Ciais, P., Apadula, F., Bartyzel, J., Bastos, A., Bergamaschi, P., Blanc, P. E., Brunner, D., Caracciolo di Torchiarolo, L., Calzolari, F., Chen, H., Chmura, L., Colomb, A., Conil, S., Cristofanelli, P., Cuevas, E., Curcoll, R., Delmotte, M., di Sarra, A., Emmenegger, L., Forster, G., Frumau, A., Gerbig, C., Gheusi, F., Hammer, S., Haszpra, L., Hatakka, J., Hazan, L., Heliasz, M., Henne, S., Hensen, A., Hermansen, O., Keronen, P., Kivi, R., Komínková, K., Kubistin, D., Laurent, O., Laurila, T., Lavric, J. V., Lehner, I., Lehtinen, K. E. J., Leskinen, A., Leuenberger, M., Levin, I., Lindauer, M., Lopez, M., Lund Myhre, C., Mammarella, I., Manca, G., Manning, A., Marek, M. V., Marklund, P., Martin, D., Meinhardt, F., Mihalopoulos, N., Mölder, M., Morgui, J. A., Necki, J., O'Doherty, S., O'Dowd, C., Ottosson, M., Philippon, C., Piacentino, S., Pichon, J. M., Plass-Duelmer, C., Resovsky, A., Rivier, L., Rodó, X., Sha, M. K., Scheeren, H. A., Sferlazzo, D., Spain, T. G., Stanley, K. M., Steinbacher, M., Trisolino, P., Vermeulen, A., Vítková, G., Weyrauch, D., Xueref-Remy, I., Yala, K., and Yver Kwok, C.: The fingerprint of the summer 2018 drought in Europe on ground-based tmospheric CO_2 measurements, Philos. T. R. Soc. B, 375, 20190513, https://doi.org/10.1098/rstb.2019.0513, 2020.

Rödenbeck, C.: Estimating CO_2 sources and sinks from atmospheric mixing ratio measurements using a global inversion of atmospheric transport, Technical Report 6, available at: https:

//www.bgc-jena.mpg.de/CarboScope/s/tech_report6.pdf (last access: 10 February 2020), Max Planck Institute for Biogeochemistry, Jena, 2005.

Stuiver, M. and Polach, H. A.: Discussion: Reporting of ^{14}C data, Radiocarbon, 19, 355–363, 1977.

Sturm, P., Leuenberger, M., Neubert, R. E. M., Meijer, H. A. J., Langenfelds, R., Brand, W. A., and Tohjima, Y.: Permeation of atmospheric gases through polymer O-rings used in flasks for air sampling, J. Geophys. Res., 109, D04309, https://doi.org/10.1029/2003JD004073, 2004.

Turnbull, J., Guenther, D., Karion, A., Sweeney, C., Anderson, E., Andrews, A., Kofler, J., Miles, N., Newberger, T., Richardson, S., and Tans, P.: An integrated flask sample collection system for greenhouse gas measurements, Atmos. Meas. Tech., 5, 2321–2327, https://doi.org/10.5194/amt-5-2321-2012, 2012.

Turnbull, J. C., Miller, B., Lehman, S. J., Tans, P. P., Sparks, R. J., and Southon, J.: Comparison of $^{14}CO_2$, CO, and SF_6 as tracers for recently added fossil fuel CO_2 in the atmosphere and implications for biological CO_2 exchange, Geophys. Res. Lett., 33, L01817, https://doi.org/10.1029/2005GL024213, 2006.

Turnbull, J. C., Tans, P. P., Lehman, S. J., Baker, D., Conway, T. J., Chung, Y. S., Gregg, J., Miller, J. B., Southon, J. R., and Zhou, L.-X.: Atmospheric observations of carbon monoxide and fossil fuel CO_2 emissions from East Asia, J. Geophys. Res., 116, D24306, https://doi.org/10.1029/2011JD016691, 2011.

Vogel, F. R., Hammer, S., Steinhof, A., Kromer, B., and Levin, I.: Implication of weekly and diurnal ^{14}C calibration on hourly estimates of CO-based fossil fuel CO_2 at a moderately polluted site in south-western Germany, Tellus, 62B, 512–520, https://doi.org/10.1111/j.1600-0889.2010.00477.x, 2010.

Wang, Y., Broquet, G., Ciais, P., Chevallier, F., Vogel, F., Wu, L., Yin, Y., Wang, R., and Tao, S.: Potential of European $^{14}CO_2$ observation network to estimate the fossil fuel CO_2 emissions via atmospheric inversions, Atmos. Chem. Phys., 18, 4229–4250, https://doi.org/10.5194/acp-18-4229-2018, 2018.

WMO (World Meteorological Organization): 20th WMO/IAEA Meeting on Carbon Dioxide, Other Greenhouse Gases and Related Measurement Techniques (GGMT-2019), GAW-Report No. 255, Geneva, Switzerland, 2020.

Yver Kwok, C., Laurent, O., Guemri, A., Philippon, C., Wastine, B., Rella, C. W., Vuillemin, C., Truong, F., Delmotte, M., Kazan, V., Darding, M., Lebègue, B., Kaiser, C., Xueref-Rémy, I., and Ramonet, M.: Comprehensive laboratory and field testing of cavity ring-down spectroscopy analyzers measuring H_2O, CO_2, CH_4 and CO, Atmos. Meas. Tech., 8, 3867–3892, https://doi.org/10.5194/amt-8-3867-2015, 2015.

CHAPTER 5

Uncertainty of continuous ΔCO-based ΔffCO$_2$ estimates derived from ^{14}C flask and bottom-up ΔCO/ΔffCO$_2$ ratios

This chapter will be submitted to *Atmospheric Chemistry and Physics*: Maier, F., and co-authors: Uncertainty of continuous ΔCO-based ΔffCO$_2$ estimates derived from ^{14}C flask and bottom-up ΔCO/ΔffCO$_2$ ratios, 2023.

Abstract

Measuring the ^{14}C/C depletion in atmospheric CO_2 compared to a clean-air reference is the most direct way to estimate the recently added CO_2 contribution from fossil fuel (ff) combustion (ΔffCO_2) in ambient air CO_2 excess with respect to a clean air background. However, since $^{14}CO_2$ measurements cannot be conducted continuously nor remotely, there are only very sparse ^{14}C-based ΔffCO_2 estimates available. Therefore, continuously measured tracers like carbon monoxide (CO), which are co-emitted with ffCO_2 can be used as additional proxies for ΔffCO_2, provided that the ΔCO/ΔffCO_2 ratios can be determined correctly. Here, we use almost 350 $^{14}CO_2$ measurements from flask samples collected between 2019 and 2020 at the urban site Heidelberg in Germany, and corresponding analyses from more than 50 afternoon flasks collected between September 2020 and March 2021 at the remote ICOS site Observatoire pérenne de l'environnement (OPE) in France, to calculate average ΔCO/ΔffCO_2 ratios for those sites. By dividing the hourly ΔCO excess observations by the averaged flask ratios, we construct continuous and bias-free ΔCO-based ΔffCO_2 records. The comparison between ΔCO-based ΔffCO_2 and ^{14}C-based ΔffCO_2 from the flasks yields a RMSD of about 4 ppm for the urban site Heidelberg and of 1.5 ppm for the remote site OPE. While for OPE, this uncertainty can be explained by observational uncertainties alone, for Heidelberg about half of the uncertainty is caused by the neglected spatiotemporal variability of the ratios. We further show that modelled ratios based on the Netherlands Organization for Applied Scientific Research (TNO) emission inventory would lead to substantial biases in the ΔCO-based ΔffCO_2 estimates for Heidelberg, but also for OPE. This highlights the need for an ongoing observational calibration/validation of inventory-based ratios, if those shall be applied for large-scale ΔCO-based ΔffCO_2 estimates, e.g. from satellites.

5.1 Introduction

The observational separation of the fossil fuel CO_2 contributions (ΔffCO_2) in regional atmospheric CO_2 excess is a prerequisite for independent "top-down" evaluation of bottom-up ffCO_2 emission inventories (Ciais et al., 2016). The most direct method for estimating regional ΔffCO_2 contributions is measuring the ambient air $\Delta^{14}CO_2$ depletion compared to a clean air $\Delta^{14}CO_2$ reference, as fossil fuels are devoid of ^{14}C, which has a half-life of 5700 years (Currie, 2004; for the $\Delta^{14}CO_2$ notation see Stuiver and Polach, 1977). Many studies have successfully applied this approach to directly estimate regional ΔffCO_2 concentrations in urban regions (e.g., Levin et al., 2003; Levin and Rödenbeck, 2008; Turnbull et al., 2015; Zhou et al., 2020), which could then be used in atmospheric inverse modeling systems to compare with bottom-up ffCO_2 emission inventories (Graven et al., 2018; Wang et al., 2018). One drawback of this method is, however, that ^{14}C-based ΔffCO_2 estimates have typically only a low (i.e. weekly or monthly) temporal resolution and poor spatial coverage, due to the labor-intensive and costly process of collecting and measuring precisely air samples for $^{14}CO_2$. Up to now, $^{14}CO_2$ observations cannot be conducted continuously with the precision needed for atmospheric ΔffCO_2 determination neither can $^{14}CO_2$ observations be performed remotely, e.g. with satellites. This limits the potential of ^{14}C observations to estimate ffCO_2 emissions at the continental scale and at high spatiotemporal resolution.

Therefore, frequently measured gases like carbon monoxide (CO), which is co-emitted with ffCO_2 during incomplete combustion has been used as additional constraint for estimating ffCO_2 emissions (e.g., Palmer et al., 2006; Boschetti et al., 2018). Also, CO observations from satellites turned out to be a powerful tool for verifying and optimizing bottom-up ffCO_2 emission estimates of large industrial regions in the whole world (Konovalov et al., 2016). However, using CO observations in inverse models for estimating ffCO_2 emissions requires decent information about the spatiotemporal variability of the CO/ffCO_2 emission ratios. Typically, this information is taken from bottom-up CO and CO_2 emission inventories, which are based on national activity data and source sector specific emission factors (Kuenen et al., 2014; Janssens-Maenhout et al., 2019). However, these emission factors are associated with high uncertainties, especially for CO, since they strongly depend on the often variable combustion conditions (Dellaert et al., 2019). This urgently calls for an observation-based verification of the bottom-up emission ratios to prevent biases in top-down ffCO_2 emission estimates.

In the case of in-situ observations, continuously measured ΔCO offsets compared to a clean air reference were used in the past to construct temporally highly resolved ΔffCO$_2$ concentration records, which can provide additional spatiotemporal information for constraining fossil emissions in transport model inversions. For this, the continuous ΔCO measurements are divided by mean $\langle\Delta\text{CO}/\Delta\text{ffCO}_2\rangle$ ratios, which are representative for the observation site and the averaging period (e.g., Gamnitzer et al., 2006 ; Levin and Karstens, 2007; Van Der Laan et al., 2010; Vogel et al., 2010). At observation sites with simultaneous ^{14}CO$_2$ measurements these $\langle\Delta\text{CO}/\Delta\text{ffCO}_2\rangle$ ratios can be calculated from ^{14}C-based ΔffCO$_2$ estimates. This allows to calculate continuous ΔCO-based ΔffCO$_2$ concentration offsets, which are fully independent of bottom-up emission information. For example, Vogel et al. (2010) used weekly integrated Δ^{14}CO$_2$ observations combined with occasional hourly Δ^{14}CO$_2$ flask data from the urban site Heidelberg, located in a heavily industrialized area in the Upper Rhine Valley in Southwestern Germany, to estimate continuous ΔCO-based ΔffCO$_2$ concentrations. They show that calculating the ΔCO/ΔffCO$_2$ ratios from the weekly integrated ^{14}CO$_2$ samples leads to biases in the ΔCO-based ΔffCO$_2$ estimates, since the weekly averaged ratios are biased towards hours with high ΔffCO$_2$ concentrations. That is why they used the ^{14}CO$_2$ flask data to calculate mean diurnal cycles for the summer and winter period. By correcting the weekly averaged ratios with these diurnal profiles, they could reduce some of the bias of the ΔCO-based ΔffCO$_2$ estimates.

In the two years of 2019 and 2020, we have collected almost 350 hourly integrated ^{14}CO$_2$ flask samples during very different atmospheric conditions at the Heidelberg observation site. The purpose of this high-frequent flask sampling is to investigate if such a large flask pool allows an estimation of the urban ffCO$_2$ emissions in Heidelberg. Our aim of the present study is to investigate the potential of using these ^{14}CO$_2$ flask results directly to calculate ΔCO/ΔffCO$_2$ ratios and construct a continuous ΔCO-based ΔffCO$_2$ record for the Heidelberg observation site. We further estimate the uncertainty of this ΔCO-based ΔffCO$_2$ record therewith assessing the share of uncertainty that is caused by the spatiotemporal variability of the emission ratios in the surrounding of Heidelberg. A similar investigation was conducted at a more remote Integrated Carbon Observation System (ICOS, Heiskanen et al., 2022) atmosphere station at Observatoire pérenne de l'environnement (OPE), but here only based on about 50 hourly integrated flask samples collected between September 2020 and March 2021.

We further compare the flask-based ΔCO/ΔffCO$_2$ ratios with modelled ratios based on bottom-up estimates from the high-resolution emission inventory of the Netherlands Organization for Applied Scientific Research (TNO, Dellaert et al., 2019; Denier van der Gon et al., 2019). As mentioned above, this observation-based validation of the bottom-up emission ratios is essential when using CO concentration measurements as an additional tracer in inverse models to estimate $ffCO_2$ emissions. This comparison also allows to investigate if the modelled, inventory-based $\Delta CO/\Delta ffCO_2$ ratios could be solely used to construct a ΔCO-based $\Delta ffCO_2$ record at sites without $^{14}CO_2$ measurements. Indeed, ambient air CO concentrations are frequently measured at urban emission hot spots, as CO emissions affect air pollution and human health (Pinty et al., 2019). Thus, the ability of constructing continuous ΔCO-based $\Delta ffCO_2$ records from inventory-based $\Delta CO/\Delta ffCO_2$ ratios could play an important role in quantifying anthropogenic $ffCO_2$ emissions from hot spots. Obviously, the success of such an approach strongly relies on correct bottom-up CO and $ffCO_2$ emissions, and that the impact of natural CO sources and sinks, e.g. due to oxidation of methane and volatile organic compounds (VOCs), and sinks like the oxidation by hydroxyl (OH) radicals (Folberth et al., 2006) and soil uptake (Inman et al., 1971), is negligible.

Based on the results from this work we will investigate, in a follow-up paper by Maier et al. (2023a), which $\Delta ffCO_2$ observations – discrete ^{14}C-based or continuous ΔCO-based $\Delta ffCO_2$ – are better suited and provide more reliable estimates of the $ffCO_2$ emissions in the main footprint of our Heidelberg station in the highly polluted Rhine-Neckar metropolitan area.

5.2 Methods

5.2.1 Site and data description

We calculate representative $\Delta CO/\Delta ffCO_2$ ratios for the urban site Heidelberg (49.42°N, 8.67°E) in Southwest Germany and the rural site OPE (48.56°N, 5.50°E) in Eastern France. Heidelberg is a medium-sized city (∼160'000 inhabitants) located in the densely populated Upper Rhine Valley. As is typical for an urban site, Heidelberg is surrounded by many different anthropogenic CO_2 and CO emitters, which leads to a large spatial variability of the $CO/ffCO_2$ emission ratios in the footprint of the station. The observation site (30 m a.g.l.) is situated on the campus of the university, so that local emissions mainly originate from the traffic and heating sector. However, there is also a combined heat and power plant located to the North at 500 m distance of the site, as well as the two heavily industrialised cities Mannheim and Ludwigshafen, including a large coal-fired power plant and the BASF company at a distance of 15-20 km to the North-West. The OPE site is located in a much less populated remote rural region, about 250 km South-East of Paris, and might be mainly influenced by cropland (Storm et al., 2022). The OPE site is a so-called class-1 tower station within the ICOS atmosphere station network and is situated on an almost 400 m high hill with the air inlet at 120 m above ground.

At both stations, CO is continuously measured with a Cavity Ring-Down Spectroscopy (CRDS) gas analyser (for OPE data see Ramonet et al., 2022). Furthermore, hourly flask samples are collected at both stations with an automated ICOS flask sampler (see Levin et al., 2020). Thereby, the air flow into the flasks is regulated by mass flow controllers, so that the final air sample in the flasks approximates 1-hour average concentrations of ambient air. In Heidelberg, we sampled very different atmospheric situations, i.e. during well-mixed conditions in the afternoon, but also during the morning and evening rush-hours and at night, with almost 350 flasks during the two years 2019 and 2020. At OPE, the flask sampler was programmed to fill one flask every third noon between September 2020 and March 2021, so that there are more than 50 flasks available in this time period. The CO_2 and CO concentrations of the collected flask samples are measured at the ICOS Flask and Calibration Laboratory (FCL, `https://www.icos-cal.eu/fcl`) with a gas chromatographic analysis system (GC). Afterwards, the CO_2 in the flask samples is extracted and graphitized in the Central Radiocarbon Laboratory (CRL, `https://www.icos-cal.eu/crl`; Lux, 2018), and the ^{14}C is analysed with an accelerator mass spectrometer (AMS, Kromer et al., 2013). The $\Delta^{14}CO_2$ measurements are reported in the so-called Δ-notation introduced by Stuiver and Polach (1977), which is normalized for fractionation processes and expresses the $^{14}C/C$ deviation of the sample from a standard activity in ‰. The typical $\Delta^{14}CO_2$ and CO measurement uncertainties for the hourly flasks are better than 2.5‰ and 2 ppb, respectively.

5.2.2 Construction of a continuous ΔCO-based $\Delta ffCO_2$ record

We construct a continuous ΔCO-based $\Delta ffCO_2$ record with hourly resolution ($\Delta ffCO_2^{hrly}$) by dividing the hourly ΔCO concentrations (ΔCO^{hrly}) by an average ^{14}C flask-based $\Delta CO/\Delta ffCO_2$ ratio $\langle R_{flask} \rangle$:

$$\Delta ffCO_2^{hrly} = \frac{\Delta CO_2^{hrly}}{\langle R_{flask} \rangle} \tag{5.1}$$

To calculate the ΔCO and the ^{14}C-based $\Delta ffCO_2$ excess concentrations at the Heidelberg and OPE observation sites, we must choose an appropriate CO and $\Delta^{14}CO_2$ background. Back-trajectory analyses by Maier et al. (2023b) show a predominant westerly influence for stations in Central Europe; about 2/3 of all back-trajectories, which were calculated for nine European ICOS sites for the full year 2018 end over the Atlantic Ocean at the western boundary of the European continent. Indeed, we identified Mace Head (MHD, 53.33°N, 9.90°W, 5 m a.s.l.), which is located at the west coast of Ireland, to be an appropriate marine reference site for Central Europe. Therefore, we use smooth fit curves through weekly CO flask results (Petron et al., 2022) and two-week integrated $\Delta^{14}CO_2$ samples from MHD as our CO and $\Delta^{14}CO_2$ background, respectively. The applied curve fitting algorithm was developed by the National Oceanic and Atmospheric Administration (NOAA, Thoning et al., 1989). This algorithm yields a fit standard deviation of 13.37 ppb and 0.86‰, respectively, for the CO and $\Delta^{14}CO_2$ background curves.

Obviously, MHD is a less representative background station for situations with non-western air masses. For this, Maier et al. (2023b) estimated a representativeness bias and uncertainty for the MHD background of 0.09 ± 0.28 ppm ffCO$_2$ for hourly flask samples collected in Central Europe at the eastern ICOS site Křešín. We assume this estimate to be an upper limit for the Heidelberg and OPE sites, which are located further to the West. Therefore, we decided to neglect the representativeness bias in our calculations. However, we take into account its variability, which is the representativeness uncertainty of the MHD background. The 0.28 ppm ffCO$_2$ uncertainty would result in a representativeness uncertainty of 0.64‰ for the MHD $\Delta^{14}CO_2$ background, if one assumes that a 1 ppm ffCO$_2$ signal is caused by a 2.3‰ $\Delta^{14}CO_2$ depletion (we deduced this conversion factor from the Heidelberg flask results). Similarly, we can estimate the representativeness uncertainty for the CO background, if we assume a mean CO/ffCO$_2$ ratio to convert the estimated 0.28 ppm ffCO$_2$ uncertainty into a CO uncertainty. The TNO inventory suggests for the Eastern boundary of our model domain (within 22-23°E and 37-61°N) a mean CO/ffCO$_2$ emission ratio of roughly 18 ppb/ppm in 2020. We expect this ratio as an upper limit and get a CO background representativeness uncertainty of 0.28 ppm*18 ppb/ppm=5.04 ppb. To estimate the overall CO and $\Delta^{14}CO_2$ background uncertainty, we add the fit uncertainty and the representativeness uncertainty quadratically, which yields 14.29 ppb and 1.07‰, respectively.

Calculation of an observation-based $\langle \mathbf{R_{flask}} \rangle$ ratio

To calculate the ^{14}C-based $\langle R_{flask} \rangle$ ratio, we first estimate the ΔffCO$_2$ concentrations from the $\Delta^{14}CO_2$ difference between the flask and background observations. For this, we use the following Eq. (5.2) from Maier et al. (2023b), which also contains a correction for contaminating $^{14}CO_2$ emissions from nuclear facilities and for the potentially ^{14}C-enriched increased $\Delta^{14}CO_2$ signature of biosphere respiration (still releasing stored nuclear bomb test

$^{14}CO_2$ to the atmosphere):

$$\Delta \mathrm{ffCO_2} = \mathrm{C_{bg}} \frac{\Delta^{14}_{\mathrm{bg}} - \Delta^{14}_{\mathrm{meas}}}{\Delta^{14}_{\mathrm{meas}} + 1000‰} + \mathrm{C_{meas}} \frac{\Delta^{14}_{\mathrm{nuc}}}{\Delta^{14}_{\mathrm{meas}} + 1000‰} + \mathrm{C_{resp}} \frac{\Delta^{14}_{\mathrm{resp}} - \Delta^{14}_{\mathrm{meas}}}{\Delta^{14}_{\mathrm{meas}} + 1000‰} \quad (5.2)$$

Table 5.1 shows a compilation of all components of Eq. (5.2) with short explanations. In general, we used the same procedure as described by Maier et al. (2023b) to estimate the correction terms in Eq. (5.2). Note, that we only use the flask results with a modelled nuclear contamination below 2‰, to avoid huge nuclear corrections whose uncertainty exceeds the typical uncertainty of the $\Delta^{14}CO_2$ measurements (see Maier et al., 2023b).

Table 5.1 Description of the components in Eq. (5.2).

Component	**Description**	**Method**
$\Delta^{14}_{\mathrm{meas}}$	$\Delta^{14}CO_2$ of flasks from observation site	Measured
$\Delta^{14}_{\mathrm{bg}}$	$\Delta^{14}CO_2$ background curve	NOAA fit through integrated samples from MHD
$\Delta^{14}_{\mathrm{nuc}}$	$\Delta^{14}CO_2$ contamination from nuclear facilities	Modelled using WRF-STILT in combination with nuclear $^{14}CO_2$ emissions from the Radioactive Discharges Database RADD (see Maier et al., 2023b)
$\Delta^{14}_{\mathrm{resp}}$	$\Delta^{14}CO_2$ signature of biosphere respiration	Modelled based on Naegler and Levin (2009)
$\mathrm{C_{meas}}$	CO_2 concentration of flasks from observation site	Measured
$\mathrm{C_{bg}}$	CO_2 background curve	NOAA fit through weekly flasks from MHD
$\mathrm{C_{resp}}$	CO_2 signal from respiration	Modelled with the Vegetation Photosynthesis and Respiration Model (VPRM, Mahadevan et al., 2008) coupled to STILT

We then use the weighted total least squares algorithm from Wurm (2022) to calculate regression lines to the ΔCO and ^{14}C-based $\Delta ffCO_2$ concentrations of the 343 flasks from Heidelberg and the 52 flasks from OPE. This regression algorithm is built on the code from Krystek and Anton (2007) and considers uncertainties in both the ΔCO and $\Delta ffCO_2$ flask concentrations. In this study, we force the regression line through the origin. Thus, we assume that the very well-mixed and clean air masses at the observation sites without ΔffCO$_2$ excess also represent the background CO concentrations at MHD. The slope of the regression line gives then an estimate for the average $\langle R_{\text{flask}} \rangle$ ratio, which is representative for the respective observation site and the time period of the flask samples. In Appendix 5.6.1, we show why one should use a regression algorithm, which considers the uncertainties in the dependent and independent variables, to calculate a mean bias-free $\langle \Delta\text{CO}/\Delta\text{ffCO}_2 \rangle$ ratio instead of error-weighted means or median estimates from individual samples.

Modelling of inventory-based ΔCO/ΔffCO$_2$ ratios

To compare the ^{14}C-based ΔCO/ΔffCO$_2$ ratios with inventory-based ratios, we need to weight the bottom-up emissions with the footprints of the observation sites. For this, we use the Stochastic Time-Inverted Lagrangian Transport (STILT) model (Lin et al., 2003), which is coupled with the Weather Research and Forecast (WRF) model (Nehrkorn et al., 2010) in combination with high-resolution CO and ffCO$_2$ emission fluxes from the TNO inventories (Dellaert et al., 2019; Denier van der Gon et al., 2019) to simulate hourly ΔCO and ΔffCO$_2$ concentrations at the Heidelberg and OPE observation sites. The WRF-STILT domain expands from 37°N to 61°N and from 10°W to 23°E (see Fig. 5.1). The meteorological fields are taken from the European Centre for Medium-Range Weather Forecasts (ECMWF) and have a horizontal resolution of 0.25° (European ReAnalysis 5 data, `https://www.ecmwf.int/en/forecasts/datasets/reanalysis-datasets/era5`). These meteorological data were used as input for the WRF model to generate high-resolution meteorological fields with a horizontal resolution of 2 km in the Rhine Valley (red rectangular in Fig. 5.1) and of 10 km outside the Rhine Valley, which were finally used to calculate hourly footprints with STILT. Those footprints are then mapped with the high-resolution CO and ffCO$_2$ emissions from TNO to get CO and ffCO$_2$ concentrations for Heidelberg and OPE. As we assume zero CO and ffCO$_2$ boundaries at the edge of the STILT model domain, the modelled CO and ffCO$_2$ concentrations directly correspond to the ΔCO and ΔffCO$_2$ excesses compared to the model domain boundaries. The TNO inventory divides the total CO and ffCO$_2$ emissions into 15 emission sectors with individual monthly, weekly and diurnal temporal emission profiles. Note, that the CO emissions from TNO contain the fossil fuel and biofuel CO contributions. Since Heidelberg is surrounded by many point sources with elevated stacks, we treat the TNO point sources within the Rhine Valley separately with the STILT volume source influence (VSI) approach (see Maier et al., 2022), to model the point source contributions at the Heidelberg site. In this model study, we fully neglect natural CO sources and sinks as well as atmospheric CO chemistry.

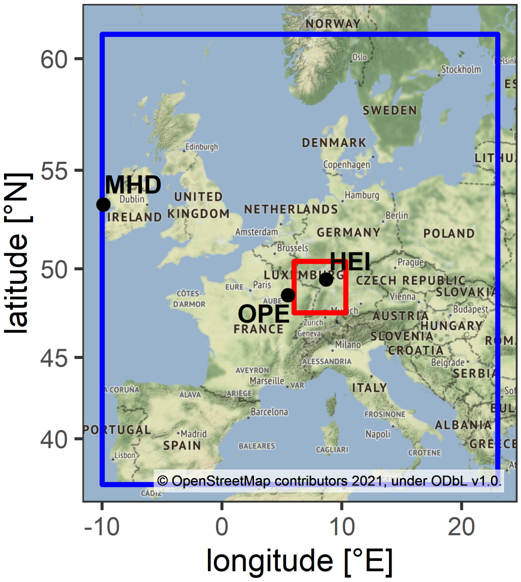

Figure 5.1 Map of the European WRF-STILT model domain (framed in blue). The Heidelberg (HEI) and OPE observation sites as well as the Mace Head (MHD) background site are indicated. The red rectangular shows the Rhine Valley domain.

5.3 Results

5.3.1 Study at the urban site Heidelberg

^{14}C-based ΔCO/ΔffCO$_2$ ratios from flask samples

Fig. 5.2 shows the ^{14}C-based ΔCO/ΔffCO$_2$ ratios of the hourly flask samples from Heidelberg, which were collected during very different atmospheric conditions (see colors in Fig. 5.2). By testing different flask sampling strategies, we sampled very different situations ranging from background conditions, nighttime CO$_2$ enhancements, morning and evening rush-hour signals and local contaminations as well as large-scale synoptic events and diurnal patterns. We observe large positive and also negative ratios with enormous error bars mainly during summer and during well-mixed atmospheric background conditions (green dots). These outliers are associated with very low (or even negative) ΔffCO$_2$ concentrations and large relative ΔffCO$_2$ uncertainties that blow up the ratio and its uncertainty. Indeed, these individual unrealistic ratios can lead to a bias in the mean or median of the (averaged) ratios, as we show with a synthetic data study in Appendix 5.6.1. However, the slope of an error weighted regression through the flask ΔCO and ΔffCO$_2$ excess concentrations represents an un-biased estimate for the average flask $\langle \mathrm{R_{flask}} \rangle$ ratio (see Fig. 5.3a).

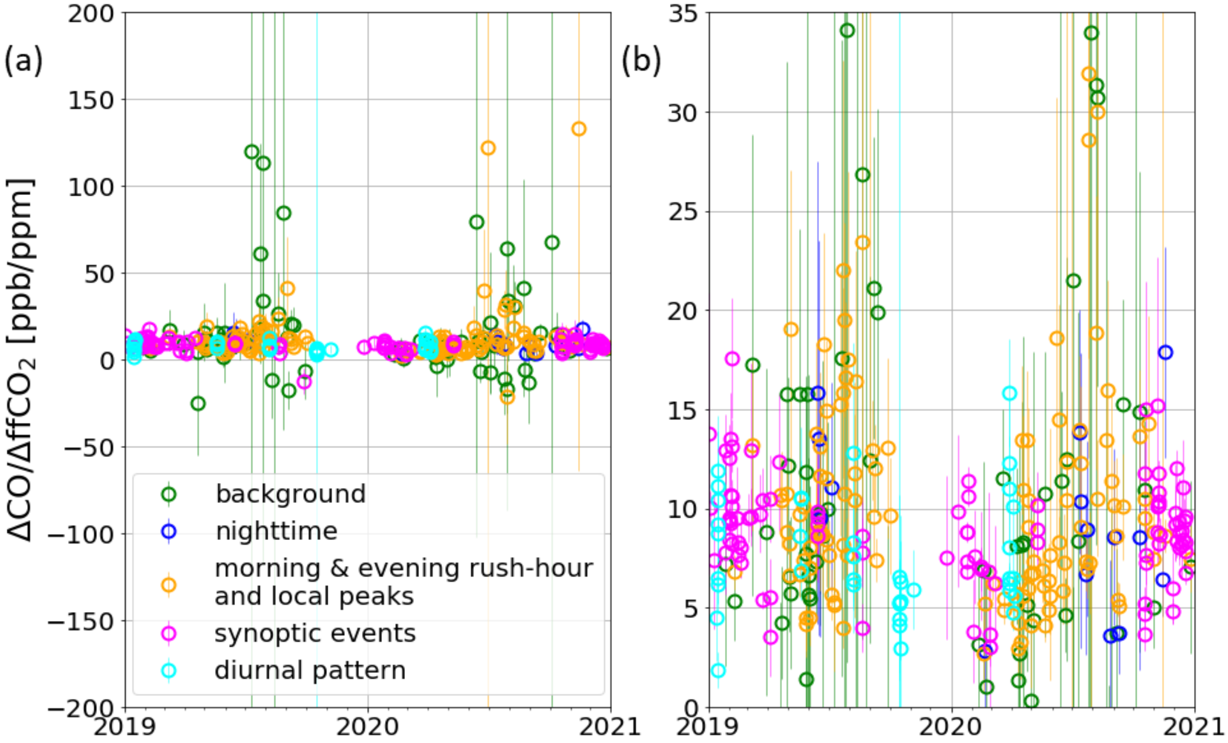

Figure 5.2 ^{14}C-based $\Delta CO/\Delta ffCO_2$ ratios from hourly flasks collected at the Heidelberg observation site between 2019 and 2020. Very different atmospheric conditions are sampled as indicated by the different colors. We sampled background conditions (green), CO_2 enhancements during night (blue), morning and evening rush-hour peaks and CO_2 spikes from most probably local sources (orange), synoptic events with a CO_2 concentration built up over several days (magenta) as well as diurnal cycles (cyan). Panel (b) shows a zoom into panel (a).

The slope of this regression yields an average ratio of 8.44 ± 0.07 ppb/ppm for all flasks collected during the two years 2019 and 2020. The good correlation indicated by an R^2 value of 0.88 is predominantly caused by the flasks with large ΔCO and $\Delta ffCO_2$ concentrations, which were mainly collected during synoptic events in the winter half-year (see Fig. 5.8). While the flasks from only the winter half-year show an average ratio of 8.52 ± 0.08 ppb/ppm with high correlation ($R^2 = 0.89$), the flasks from the summer half-year are associated with a slightly smaller average ratio of 8.08 ± 0.17 ppb/ppm but much worse correlation ($R^2 = 0.36$). Thus, there might be a small seasonal cycle in the ratios with about 5% larger ratios during winter compared to summer. The daily cycle of the ratios seems to be small, too. Afternoon flasks show an average ratio of 8.60 ± 0.19 ppb/ppm ($R^2 = 0.84$) and non-afternoon flasks have an average ratio of 8.41 ± 0.08 ppb/ppm ($R^2 = 0.88$). Furthermore, there is also a slightly decreasing trend between 2019 (8.57 ± 0.11 ppb/ppm, $R^2 = 0.87$) and 2020 (8.35 ± 0.10 ppb/ppm, $R^2 = 0.88$), which is, however, within the 2σ uncertainty range.

Uncertainty of the ΔCO-based ΔffCO$_2$ record

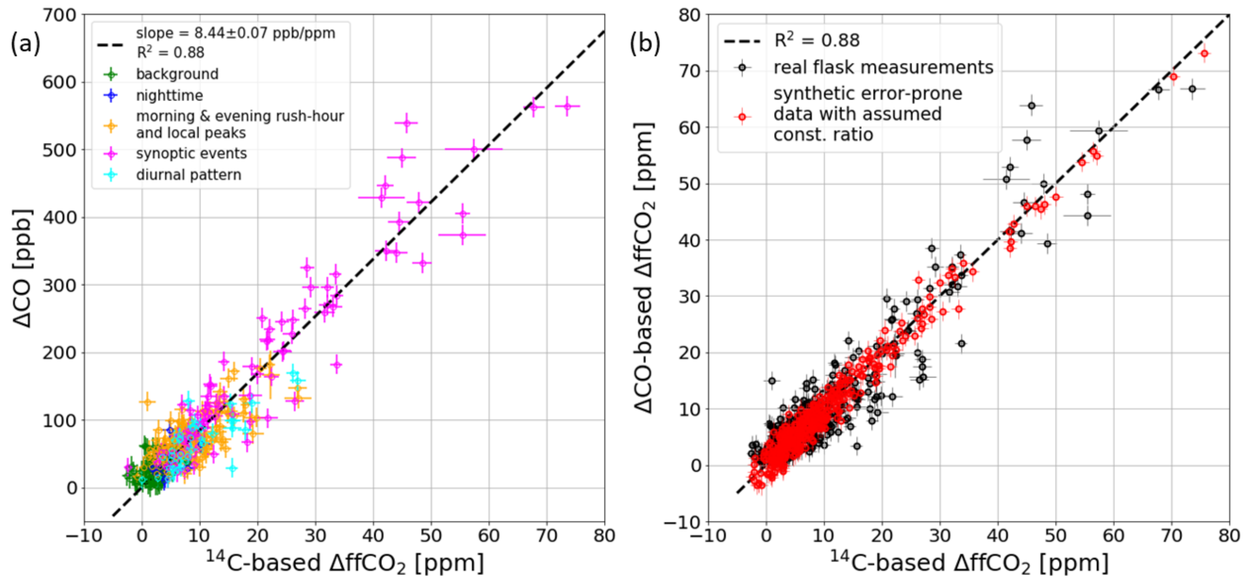

Figure 5.3 (a) Scatter plot with the measured ΔCO and the ^{14}C-based ΔffCO$_2$ concentrations of the hourly flasks collected at the Heidelberg observation site between 2019 and 2020. The colors indicate the sampling situation of the flasks (see description in the caption of Fig. 5.2). The black dashed line shows a regression line calculated with the weighted total least squares algorithm from Wurm (2022). (b) Comparison between the ΔCO-based ΔffCO$_2$ (from Eq. (5.1)) and the ^{14}C-based ΔffCO$_2$ concentrations of the Heidelberg flasks (black dots) and of the synthetic data (red dots). The synthetic data were generated by assuming a constant ΔCO/ΔffCO$_2$ ratio of 8.44 ppb/ppm, which is the average $\langle \Delta CO/\Delta ffCO_2 \rangle$ ratio from the flasks. Therefore, the scattering of the red data points is only caused by the measurement and background representativeness uncertainties of the ΔCO and ^{14}C-based ΔffCO$_2$ concentrations. This means that the increased scattering of the real data (black) compared to the synthetic data (red) is caused by the variability of the ratios.

Because of the small daily and seasonal differences in the ^{14}C-based ΔCO/ΔffCO$_2$ ratios and the difficulty to calculate average summer ratios (see Appendix 5.6.1), we decided to use the average ratio of all flasks to compute a continuous hourly ΔCO-based ΔffCO$_2$ record for the two years 2019 and 2020. However, this means that we fully neglect any spatiotemporal variability in the ratios. At times when we have collected flasks, we can then compare these ΔCO-based ΔffCO$_2$ estimates with the ^{14}C-based ΔffCO$_2$ concentrations of the flasks (see Fig. 5.3b, black dots). Obviously, a regression through this data yields a slope of 1 since we used the average ratio of all flasks to construct the ΔCO-based $\Delta ffCO_2$ record. The (vertical) scattering of the data around this 1:1 line, e.g. the root-mean-square deviation (RMSD) between ΔCO- and ^{14}C-based $\Delta ffCO_2$, can be used as an estimate for the uncertainty of the ΔCO-based $\Delta ffCO_2$ record. This RMSD is 3.95 ppm, which is almost 4 times larger than the typical uncertainty for ^{14}C-based $\Delta ffCO_2$. As the RMSD is dependent on the range of the $\Delta ffCO_2$ concentrations, we also calculate a normalized RMSD (NRMSD), by dividing the RMSD by the mean ^{14}C-based $\Delta ffCO_2$ concentration of the flasks. We get a NRMSD of 0.39, which means that the RMSD adds up to 39% of the average $\Delta ffCO_2$ excess at Heidelberg.

In the following, we want to investigate the reason for this increased uncertainty: Is it caused by the measurement and background representativeness uncertainties of the ΔCO and ^{14}C-based $\Delta ffCO_2$ concentrations, or rather by the spatiotemporal variability of the ratios that we fully neglect when using an average ratio to construct the ΔCO-based $\Delta ffCO_2$ record? To answer this, we performed a synthetic data experiment, in which we assumed a "true" constant $\Delta CO/\Delta ffCO_2$ ratio of 8.44 ppb/ppm. We used this constant ratio together with the observed $\Delta ffCO_2$ concentrations from the flasks to create synthetic "true", i.e., error-free ΔCO and $\Delta ffCO_2$ data pairs. We then drew random numbers from an unbiased Gaussian distribution with a 1σ range of 1.16 ppm (for $\Delta ffCO_2$) and 14.49 ppb (for ΔCO), which represents the mean ΔCO and $\Delta ffCO_2$ uncertainties of the real measurements (see Sect. 5.2.2). These random numbers were added to the synthetic "true" ΔCO and $\Delta ffCO_2$ data to get error-prone synthetic data. Obviously, the weighted total least squares fit through these error-prone synthetic data yields again a slope of 8.44 ± 0.06 ppb/ppm, which we used to calculate from the error-prone ΔCO data synthetic ΔCO-based $\Delta ffCO_2$ concentrations. Comparing the error-prone synthetic $\Delta ffCO_2$ concentrations with the synthetic ΔCO-based $\Delta ffCO_2$ concentrations (see Fig. 5.3b, red dots), we get a lower RMSD of only 2.07 ppm. By construction, this synthetic data experiment covers the same ΔCO and $\Delta ffCO_2$ ranges like the real flask observations but assumes a constant ratio. Therefore, the difference between the RMSD of the real $\Delta ffCO_2$ observations (3.95 ppm) and the synthetic data (2.07 ppm) must be caused by the spatiotemporal variability of the ratios. Thus, about half of the uncertainty of the ΔCO-based $\Delta ffCO_2$ record can be attributed to uncertainties of the ΔCO and $\Delta ffCO_2$ excess concentrations, and the remaining half of this uncertainty originates from the spatiotemporal variability of the ratios.

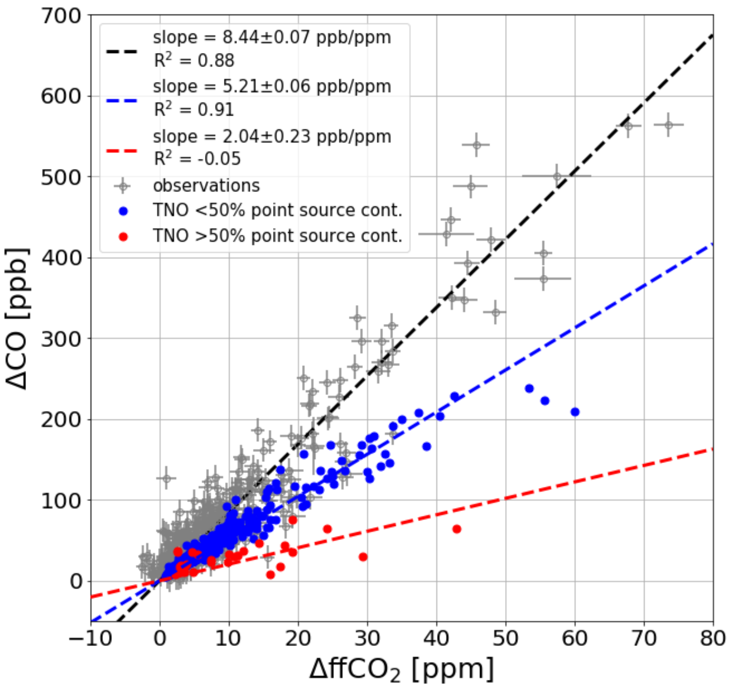

Figure 5.4 WRF-STILT simulation of the TNO ΔCO and $\Delta ffCO_2$ contributions in Heidelberg, 30 m, from emissions within the European STILT domain (see Fig. 5.1). Shown are the model results for hours with flask sampling events between 2019 and 2020. The blue and red points indicate hourly situations with a point source contribution of less and more than 50%, respectively. As a reference, the flask observations are also shown in grey. The dashed lines show linear regressions through the respective data points.

Comparison with inventory-based $\Delta CO/\Delta ffCO_2$ ratios

We also compared our ^{14}C-based $\Delta CO/\Delta ffCO_2$ ratios with the high-resolution emission inventory from TNO. For this, we modeled hourly ΔCO and $\Delta ffCO_2$ contributions in Heidelberg, by transporting the CO and $ffCO_2$ emissions from the European STILT domain (see Fig. 5.1) to the observation site. Figure 5.4 shows for the flask sampling hours in 2019 and 2020 the respective modelled ΔCO and $\Delta ffCO_2$ results (red and blue dots). In contrast to the flask observations (grey crosses), the modelled data do not scatter around a single regression line corresponding to a constant ratio. The model results rather show two branches indicating two different ratios. If the contributions from point sources in the modelled $\Delta ffCO_2$ is larger than 50% (red points in Fig. 5.4), the data scatter around a regression line with slope 2.04 ± 0.23 ppb/ppm and poor correlation (R^2=-0.05). Else, if the contributions from point sources in the modelled $\Delta ffCO_2$ is below 50% (blue points in Fig. 5.4), the data yield a ratio of 5.21 ± 0.06 ppb/ppm with high correlation (R^2=0.91).

The comparison with the flask observations provides two findings. First, the Heidelberg observation site is rarely influenced by events with strong point source contributions larger than 50% because hardly any of the observed ratio scatters around the red regression line in Fig. 5.4 and thus shows a point source dominated ratio (that lies around 2 ppb/ppm). The model results for Heidelberg thus often overestimate the contributions from point sources. Second, the area source dominated model results with point source contributions smaller than 50% show an equally high correlation as the observations. This indicates that the emission ratios for the dominating heating and traffic sectors are probably currently very similar in the main footprint of Heidelberg. However, the mean ratio of 5.2 ppb/ppm in the model results is almost 40% lower compared to the average ratio of the flask observations. Also, the contributions from the area source emissions alone lead to an average ratio of merely 6.02 ± 0.06 ppb/ppm. This might indicate that TNO underestimates the ratios of the area source emissions in the Rhine Valley. Consequently, those inventory-based ratios would lead to huge biases if they were used to calculate a ΔCO-based ΔffCO$_2$ record for Heidelberg.

5.3.2 Study at the remote ICOS site Observatoire Pérenne de l'Environnement (OPE)

We also want to investigate if the flask observations from a remote site can be used for calculating a continuous ΔCO-based ΔffCO$_2$ record. For this, Fig. 5.5a shows the ΔCO and ^{14}C-based ΔffCO$_2$ observations of 52 flasks from the OPE station, which were collected roughly every third day between September 2020 and March 2021 in the early afternoon. The flasks have an average ΔffCO$_2$ concentration of 2.19 ppm showing that OPE is much less influenced by polluted air masses compared to the urban site Heidelberg. The regression algorithm from Wurm (2022) yields an average flask ΔCO/ΔffCO$_2$ ratio of 11.49 ± 0.81 ppb/ppm ($R^2 = 0.70$), which is 3 ppb/ppm larger than the average ratio from Heidelberg during 2019 and 2020. Furthermore, the 1σ uncertainty of the slope of the regression line is 10 times larger compared to Heidelberg. This comes along with a reduced correlation between ΔCO and ΔffCO$_2$ and can at least partly be explained by the smaller range of ΔffCO$_2$ concentrations sampled at OPE (see Appendix 5.6.1). Since all flasks were collected in the winter half-year and during the afternoon, it is not possible to draw conclusions about potential seasonal or diurnal cycles in the ΔCO/ΔffCO$_2$ ratios at OPE.

Again, we want to use this average ratio from the collected flasks to calculate with Eq. (5.1) an hourly ΔCO-based ΔffCO$_2$ record for OPE. The RMSD between the ΔCO-based ΔffCO$_2$ and the ^{14}C-based ΔffCO$_2$ from the flasks is only 1.49 ppm, which is due to the much smaller

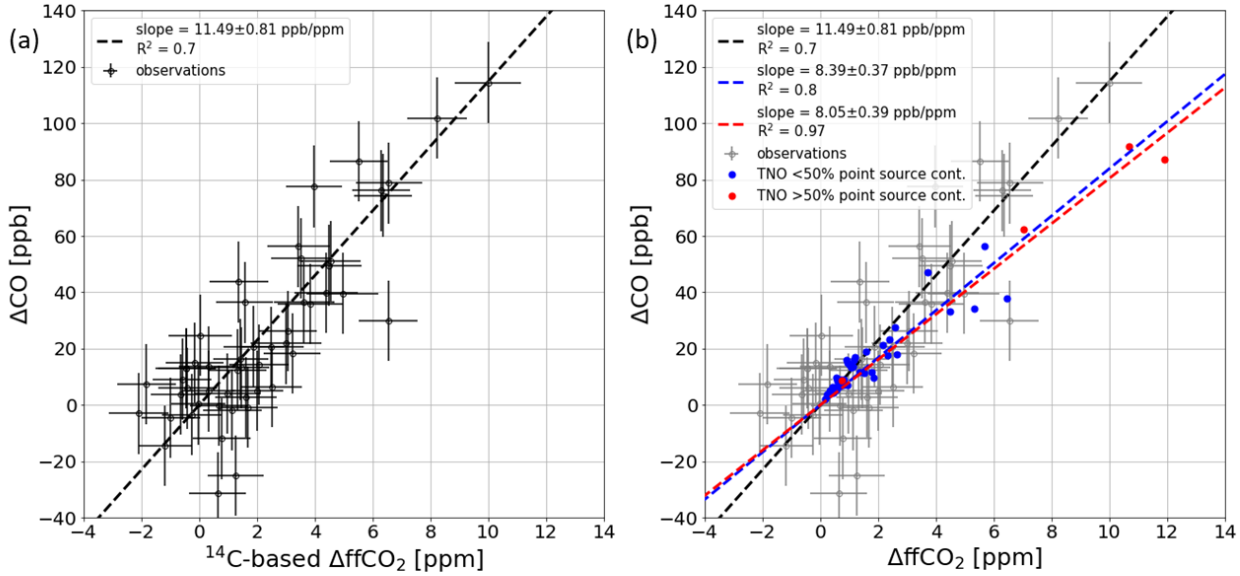

Figure 5.5 (a) ΔCO and $\Delta ffCO_2$ concentrations from hourly afternoon flasks collected at the OPE observation site between September 2020 and March 2021. The black dashed line shows a regression line performed with the weighted total least squares algorithm from Wurm (2022). (b) WRF-STILT simulation of the TNO ΔCO and $\Delta ffCO_2$ contributions at OPE from emissions within the European STILT domain (see Fig. 5.1) for the hours with flask sampling events at OPE. The blue and red points indicate hourly situations with a point source contribution of less and above 50%, respectively. As a reference, the flask observations are also shown in grey. The dashed lines show linear regressions through the respective data points.

$\Delta ffCO_2$ excess at OPE compared to Heidelberg. However, the NRMSD is 0.68, which indicates that at OPE the RMSD is almost 70% of the average $\Delta ffCO_2$ afternoon signal during Sept. 2020 and Mar. 2021. We perform a similar synthetic data experiment as for Heidelberg (see Sect. 5.3.1) to investigate, which share of the RMSD can be attributed to the uncertainty of the observations and which part is due to the (neglected) spatiotemporal variability of the ratios. It follows, that the assumption of a constant synthetic ratio of 11.49 ppb/ppm together with the consideration of the ΔCO and ^{14}C-based $\Delta ffCO_2$ excess uncertainties already leads to a RMSD of 1.61 ± 0.16 ppm between the synthetic ΔCO-based and ^{14}C-based $\Delta ffCO_2$ data. This is in the range of the observed RMSD of 1.49 ppm. Thus, the ΔCO and ^{14}C-based $\Delta ffCO_2$ excess uncertainties alone can fully explain the observed RMSD and the spatiotemporal variability of the ratios in the footprint of the OPE site seem to have minor influence.

Finally, Fig. 5.5b shows the modelled ΔCO and ΔffCO$_2$ contributions for the flask sampling hours at OPE. A linear regression through the data yields an average ratio of 8.18 ± 0.24 ppb/ppm with high correlation (R^2=0.93). There is only a very small difference <5% between the average ratio of the situations with point source contributions lower than 50% (blue points) and the very few events with point source contributions larger than 50% (red points). This indicates that the simulations do not show events with purely point source dominated contributions at OPE, which is in agreement with the observations. However, the average ratio of the model results is 29% lower compared to the average ratio of the observations. In contrast, the area source emissions alone would lead to an average ratio of 10.98 ± 0.53 ppb/ppm, which is well in the uncertainty range of the observed ratio. This could indicate that the contributions from point sources are still overestimated by STILT and/or that the emission ratio of the area sources is still underestimated by TNO. Furthermore, there could be a contribution of additional non-fossil CO sources in the vicinity of this remote site, which we ignored in STILT.

5.4 Discussion

5.4.1 How large is the uncertainty of an hourly ΔCO-based ΔffCO$_2$ record based on flask observations?

As was shown by Vogel et al. (2010) for the Heidelberg observation site, there is a bias in the ΔCO-based ΔffCO$_2$ estimates when calculating the ΔCO/ΔffCO$_2$ ratios from weekly integrated $^{14}CO_2$ samples. Since the weekly ratios are weighted by the ΔffCO$_2$ concentration, their value is biased towards hours with high ΔffCO$_2$. Therefore, Vogel et al. (2010) used flasks to sample the diurnal cycles in summer and winter, so that they can correct the weekly averaged ratios for the diurnal variations. This allowed them to reduce some of the bias in the ΔCO-based ΔffCO$_2$ estimates. In the present study we aim to investigate whether frequently collected flask samples can directly be used to estimate a continuous ΔCO-based ΔffCO$_2$ record and examine what uncertainty this would lead to. For this, we focus on the urban site Heidelberg and the remote site OPE.

Results from the urban site Heidelberg

In Heidelberg, there are almost 350 ^{14}CO2 flask samples collected during very different situations between 2019 and 2020. Their ΔCO and ΔffCO$_2$ excess concentrations compared to the marine background from MHD show a strong correlation. This indicates that the emission ratios of the traffic and heating sectors are quite similar in the main footprint of Heidelberg and the investigated period of time. Furthermore, it follows that the Heidelberg observation site with an air intake height of 30 m above ground is hardly influenced by the plumes from nearby point sources, which are associated with rather low emission ratios. Indeed, there are very small differences below 3% between the mean afternoon and non-afternoon ratios, and between the average ratios in 2019 and 2020. Moreover, there might be only a small seasonal cycle in the ratios, since the average ratio of the flasks collected in the summer half-year is ca. 5% smaller than the average ratio of the flasks from the winter half-year.

However, we must emphasize the difficulty to reliably calculate average ratios for the summer period. If for example only the flasks from the three main summer months June, July and August are considered, the correlation between ΔCO and ΔffCO_2 disappears ($R^2 = 0.06$), which prohibits calculating average summer ratios (see Appendix 5.6.1). This has also been found by other studies (Vogel et al., 2010; Miller et al., 2012; Turnbull et al., 2015; Wenger et al., 2019) and can be explained by smaller ΔffCO_2 signals with large relative uncertainties (see Appendix 5.6.1) or by the increased contribution from biospheric CO sources during summer (Vimont et al., 2019). Therefore, we calculated the average ratio from summer and winter flasks and neglect a potential seasonal cycle in the ratios. However, it is important to note that the slope of the regression line through the entire flask pool is strongly determined by the flasks with large ΔCO and ΔffCO_2 concentrations, which were predominantly collected during synoptic events in the winter half-year.

The comparison of the ΔCO-based ΔffCO_2 estimates with the ^{14}C-based ΔffCO_2 data from the flasks yields a RMSD of about 4 ppm, which we use as an estimate for the 1σ uncertainty of the ΔCO-based ΔffCO_2 concentrations. One half of this uncertainty could be attributed to the measurement uncertainty and the representativeness uncertainty of the CO and $\Delta^{14}CO_2$ background from the marine site MHD. The other half of this uncertainty is caused by the spatiotemporal variability of the ratios in the main footprint of Heidelberg, which has been ignored by applying a constant ratio to calculate the ΔCO-based ΔffCO_2 concentrations. Overall, this uncertainty is almost 4 times larger than the typical uncertainty of ^{14}C-based ΔffCO_2 estimates and corresponds to ca. 40% of the mean ΔffCO_2 signal of the flasks collected in Heidelberg. However, by using the average ratio from the flasks we got a bias-free ΔCO-based ΔffCO_2 record with hourly resolution. In the companion paper by Maier et al. (2023a) we investigate which observation is better suited to estimate the ffCO_2 emissions in the main footprint of Heidelberg – discrete ^{14}C-based ΔffCO_2 from flasks with a small uncertainty or continuous ΔCO-based ΔffCO_2 with hourly coverage but a 4 times larger uncertainty.

Results from the remote site OPE

At OPE there are only afternoon ^{14}C flasks collected roughly every 3rd day between September 2020 and March 2021. Thus, we cannot investigate any potential diurnal or seasonal cycle in the ratios. Hence, we again use a constant ratio for calculating the ΔCO-based $\Delta ffCO_2$ record. The flask ΔCO and ^{14}C-based $\Delta ffCO_2$ concentrations show a lower correlation ($R^2=0.7$) compared to the flasks from the urban site Heidelberg ($R^2=0.87$), which might predominantly be explained by the almost 80% lower mean signal of the flasks collected at OPE and the smaller number of flask samples. This affects the uncertainty of the slope of the regression line, which is at OPE with 0.81 ppb/ppm more than 10 times larger compared to Heidelberg. The RMSD between the ΔCO-based $\Delta ffCO_2$ and the ^{14}C-based $\Delta ffCO_2$ from the flasks is 1.5 ppm, which accounts for almost 70% of the mean $\Delta ffCO_2$ signal from the flasks. Compared to the typical ^{14}C-based $\Delta ffCO_2$ uncertainty, the uncertainty of the ΔCO-based $\Delta ffCO_2$ is only about 30% higher. Therefore, the remote site might be less influenced by the spatiotemporal variability of the ratios. Indeed, we determined that the whole RMSD of 1.5 ppm can entirely be explained by the measurement uncertainties and the representativeness uncertainty of the background concentrations. This is indeed expected for remote sites like OPE and shows that atmospheric mixing has smoothed out the different $CO/ffCO_2$ emission ratios before the air masses arrive at OPE. Therefore, this ΔCO-based $\Delta ffCO_2$ record with continuous data coverage, if well calibrated with $^{14}CO_2$ measurements, could be a valuable alternative compared to discrete ^{14}C-based $\Delta ffCO_2$ estimates for constraining $ffCO_2$ emissions – at least for afternoon situations during the winter half-year.

5.4.2 How many $^{14}CO_2$ flask measurements are needed to estimate a reliable continuous ΔCO-based $\Delta ffCO_2$ record?

We can use the STILT forward runs to examine how representative the collected flask samples are for the entire period covered by the ΔCO-based $\Delta ffCO_2$ record. For this, we determine the average STILT $\Delta CO/\Delta ffCO_2$ ratios by calculating a linear regression through the modelled ΔCO and $\Delta ffCO_2$ data for (1) the hours with flask samples only and for (2) all hours covered by the ΔCO-based $\Delta ffCO_2$ record. For Heidelberg, this yields a difference of less than 3% between the average modelled ratio of the hours with flask sampling events and the average modelled ratio of all hours between 2019 and 2020. As the STILT results suggest unrealistic situations with more than 50% point source influence in Heidelberg, we have only used those hours where STILT predicts a point source influence below 50% for this analysis. This result suggests that the Heidelberg flasks are indeed quite representative for these two years. In the case of OPE, the STILT average ratio of the hours with flask samplings differs by less than 1% from the average ratio of all afternoon hours between Sept. 2020 and Mar. 2021, indicating that the flask samples are very representative for the afternoons during this period. Interestingly, the difference to the average ratio of all, i.e. afternoon and non-afternoon, hours during these 7 months is about 8%, which indicates that the model suggests a small diurnal cycle in the OPE ratios.

After having shown that the flask pools from both observation sites seem to be quite representative, we want to investigate how many flasks are needed to determine a robust average ratio for constructing the ΔCO-based $\Delta \mathrm{ffCO}_2$ record. For this, we perform a small bootstrapping experiment. We select from the Heidelberg (and OPE) flask pool randomly i flasks, with i ranging from 3 to the total number of flasks $\mathrm{N}_{\mathrm{tot}}$ ($\mathrm{N}_{\mathrm{tot}} = 343$ flasks in Heidelberg and $\mathrm{N}_{\mathrm{tot}} = 52$ flasks at OPE). Then we calculate from the ΔCO and $\Delta \mathrm{ffCO}_2$ data of the i flasks an average ratio $\langle \mathrm{R}_{i,j} \rangle$ by using the regression algorithm from Wurm (2022). We repeat this experiment j=100 times for each i. After that, we can calculate for each i the standard deviation $\sigma(\langle \mathrm{R}_i \rangle)$ over the 100 realizations of $\{\langle \mathrm{R}_{i,1} \rangle, \ldots, \langle \mathrm{R}_{i,100} \rangle\}$. Obviously, we get for i=$\mathrm{N}_{\mathrm{tot}}$ the average flask ratio $\langle \mathrm{R}_{\mathrm{flask}} \rangle$ and $\sigma(\langle \mathrm{R}_{i=\mathrm{N}_{\mathrm{tot}}} \rangle) = 0$, as we used all available flasks. Figure 5.6 shows the relative standard deviation $\sigma(\langle \mathrm{R}_i \rangle)/\langle \mathrm{R}_{\mathrm{flask}} \rangle$ for different shares $i/\mathrm{N}_{\mathrm{tot}}$ of flasks used to calculate the ratio. Apparently, this relative standard deviation of the ratio increases for a decreasing number of flasks used to calculate the ratio. At the urban site Heidelberg, we would need 15 flasks, which are less than 5% of our flask pool, to keep the standard deviation of the ratio below 10%. At the remote site OPE, we would need 20 flasks, i.e. almost 40% of the collected OPE flasks, to reduce the standard deviation of the ratio to 10%.

Overall, this experiment shows that the number of flasks needed to determine a robust average $\Delta \mathrm{CO}/\Delta \mathrm{ffCO}_2$ ratio with an uncertainty below 10% depends on the correlation between the ΔCO and $\Delta \mathrm{ffCO}_2$ data. For R^2 values between 0.7 and 0.9 it takes about 15 to 20 flasks to determine the average $\Delta \mathrm{CO}/\Delta \mathrm{ffCO}_2$ ratio with an uncertainty of less than 10%. For this, however, these flasks must cover a wide range of the observed ΔCO and $\Delta \mathrm{ffCO}_2$ concentrations. As mentioned above, the determination of an average ratio is associated with much larger uncertainties during summer with typically lower R^2 values. Thus, in order to investigate a potential seasonal cycle in the ratios, it is important to also collect flasks during summer situations with large ΔCO concentrations. This might increase the chance of getting better correlations and thus lower uncertainties in the summer ratios.

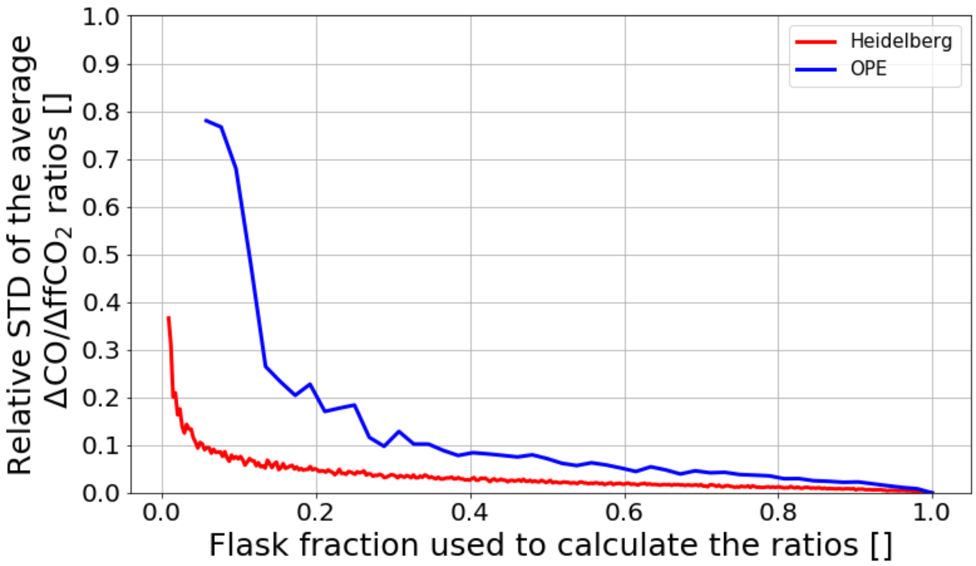

Figure 5.6 Results of the bootstrapping experiment. We used an increasing number of random flasks from the Heidelberg (in red) and OPE (in blue) flask pools to deduce an average $\Delta CO/\Delta ffCO_2$ ratio. For each number of flasks, we repeat this experiment 100 times. Finally, we calculate the standard deviation of the average ratios over the 100 repetitions for each number of flasks. Here, we show the relative standard deviation (STD) of the average ratios for an increasing flask fraction used to calculate the ratios. A flask fraction of 1 means that all available flask samples from Heidelberg and OPE, respectively, were used to calculate the average ratios. Obviously, this leads to a standard deviation of 0. See the text for a detailed description of the bootstrapping experiment.

5.4.3 Can inventory-based $\Delta CO/\Delta ffCO_2$ ratios be used to construct the ΔCO-based $\Delta ffCO_2$ record?

The big advantage of flask-based $\Delta CO/\Delta ffCO_2$ ratios is that they are independent of the correctness of the sector specific inventory emission ratios and the transport model uncertainties. Moreover, they intrinsically include all potential CO contributions from natural sources and sinks. However, for many observation sites with continuous CO measurements but without ^{14}C measurements, the usage of inventory-based $\Delta CO/\Delta ffCO_2$ ratios could possibly be an option to calculate hourly ΔCO-based $\Delta ffCO_2$ estimates. Therefore, we also compared the flask-based ratios from Heidelberg and OPE with $\Delta CO/\Delta ffCO_2$ ratios from TNO, which are transported with STILT to those observational stations.

At the urban site Heidelberg, there are two issues: First, the model predicts events with pure point source emissions which have very low $\Delta CO/\Delta ffCO_2$ ratios of about 2 ppb/ppm, but are hardly observed at the observation site. This illustrates the deficits of STILT to correctly simulate point source emissions. Thus, even the improved STILT-VSI approach, which considers the effective emission heights of the point sources seems to overestimate the contributions from point sources for individual hours. Second, the contributions from the area source emissions alone would lead to an average ratio that is almost 30% lower compared to the average flask ratio. Indeed, Rosendahl (2022) found during a field campaign next to a highway in Heidelberg, that the measured traffic ratios are about 80% higher compared to the TNO emission ratio for the highway traffic sector. If we assume that the overall TNO traffic ratio is underestimated throughout the Rhine Valley and would increase it by 80% in this domain, the modelled ratio of the total area source emissions would increase by more than 20%.

Also, the ratios of the heating sector come along with large uncertainties. In particular, the share of biomass burning has a major impact on the ΔCO/ΔffCO$_2$ ratios of the total heating sector since it releases no ffCO$_2$ emissions. In TNO, the proximity to forested areas is used as a proxy to determine the share of biomass burning within a grid cell (as cited by Rosendahl, 2022). During two measurement campaigns in two villages around Heidelberg, Rosendahl (2022) showed that this also can lead to biases between the measured and inventory-based heating ratios. Overall, it seems that the TNO emission inventory underestimates the ΔCO/ΔffCO$_2$ ratios in the Rhine Valley during the two years 2019 and 2020. Thus, using those inventory-based (area source) emission ratios would result in strong biases on the order of 40% in the ΔCO-based ΔffCO$_2$ estimates.

At the remote site OPE, the model results show no distinct point source events. This is expected, too, since the ICOS atmosphere stations are typically located at distances larger than 40 km from large point sources (ICOS RI, 2020). The average modelled ΔCO/ΔffCO$_2$ ratio at OPE turned out to be 30% smaller compared to the average flask ratio. However, if only the contributions from area sources were considered, the modelled ratio would agree with the flask ratio within their 1σ uncertainty ranges. Thus, there are three possibilities that could explain the 30% difference between the modelled and observed average ratio: (1) the STILT model might also at the OPE site overestimate the contributions from the point sources, (2) the TNO inventory still underestimates the emission ratios of the area sources, and/or (3) there is an additional CO contribution from natural sources, which we ignored in STILT as we only transport the TNO emissions to the observation site.

To investigate the potential contribution from non-fossil CO sources, we calculate the linear regression through the flask ΔCO and ΔffCO_2 concentrations by not forcing the regression line through the origin. This yields a slightly larger slope of 11.72 ± 1.09 ppb/ppm with an almost vanishing ΔCO-offset of -1 ± 3 ppb. In principle, this ΔCO-offset could be explained by a representativeness bias of the MHD CO background or by non-fossil CO contributions between the MHD background site and the OPE observation site. Thus, from this small (and even slightly negative) ΔCO-offset there is no observational evidence for significant non-fossil CO sources or an inappropriate CO background. The former can be confirmed by the top-down inversion results from Worden et al. (2019), who used the Measurements Of Pollution In The Troposphere (MOPITT) CO satellite retrievals in combination with the global chemical transport model GEOS-Chem to calculate monthly gridded (5° x 4°) a-posteriori CO fluxes for the years 2001 until 2015. The CO fluxes are separated into the three primary source sectors: anthropogenic fossil fuel and biofuel, biomass burning, and oxidation from biogenic non-methane VOCs (NMVOCs). When averaging their results over the 15 years from 2001 until 2015 for the 7 months between September and March, one gets a mean top-down biogenic CO flux of 1.38 nmol/(m^2s) in the 4° x 5° grid cell around the OPE site. If we apply this biogenic CO source for the whole European STILT domain, the modelled average ΔCO/ΔffCO_2 ratio would only slightly increase from 7.6 ± 0.3 ppb/ppm with ΔCO-offset of 3 ± 1 ppb to 7.8 ± 0.4 ppb/ppm with ΔCO-offset of 9 ± 1 ppb. Thus, this non-fossil CO source would mainly affect the ΔCO-offset and might be neglectable during winter. Indeed, the 2001-2015 mean top-down biogenic CO flux in the grid cell around OPE is for the period September to March almost 10 times smaller than the respective anthropogenic CO flux from Worden et al. (2019).

Therefore, we expect that the differences between the modelled and observed average ratio at OPE are rather caused by inconsistencies in the TNO emission ratios or deficits in the transport model. However, for the period April to August, the mean biogenic and mean anthropogenic CO fluxes from Worden et al. (2019) are of the same magnitude, which indicates that the biogenic influence on the ΔCO/ΔffCO_2 ratios is much more important during summer than during winter. Overall, these results show that the ratios from emission inventories should be validated by observations before they are used to construct a ΔCO-based ΔffCO_2 record. Otherwise, there could be large biases in the ΔCO-based ΔffCO_2 estimates. While the contribution of natural CO sources and sinks in winter seems negligible even at remote stations, additional modeling of the natural CO contributions in summer may be needed, especially for remote sites.

5.5 Conclusions

In the present study, we investigated if ^{14}C-based ΔCO/ΔffCO$_2$ ratios from flasks collected at the urban site Heidelberg and at the remote site OPE can be used to construct a continuous ΔCO-based ΔffCO$_2$ record for these sites. The almost 350 Heidelberg flasks were sampled during very different meteorological conditions between 2019 and 2020 but show a strong correlation, suggesting for this period similar heating and traffic emission ratios in the Upper Rhine Valley. Therefore, we could use the average flask ΔCO/ΔffCO$_2$ ratio to construct an hourly ΔCO-based ΔffCO$_2$ record. The comparison between ΔCO-based and ^{14}C-based ΔffCO$_2$ from flasks yields a RMSD of about 4 ppm, which is almost 4 times higher than the typical uncertainty for ^{14}C-based ΔffCO$_2$ estimates. We showed that about one half of this RMSD is due to observational uncertainties and the other half is caused by the variability of the ratios, which we ignored by applying a constant flask ratio. In a companion paper (Maier et al., 2023a) we therefore compare the information content of less but precise ^{14}C-based ΔffCO$_2$ observations in contrast to hourly ΔCO-based ΔffCO$_2$ estimates with a 4 times larger uncertainty. For this, we perform a ΔffCO$_2$ model inversion within the urban Rhine Valley around Heidelberg.

At the remote site OPE, about 50 afternoon flasks were collected from September 2020 to March 2021. Compared to Heidelberg, these flasks show a slightly smaller correlation, but still allowed the determination of a (constant) ratio to construct the ΔCO-based ΔffCO$_2$ record for the afternoon hours. The RMSD between ΔCO-based and ^{14}C-based ΔffCO$_2$ from flasks is about 1.5 ppm, which is about 70% of the mean ΔffCO$_2$ signal of the flasks but only about 30% higher than the uncertainty of the ^{14}C-based ΔffCO$_2$ estimates. Here, the RMSD can fully be explained by the observational uncertainties alone, which indicates that atmospheric mixing has smoothed out the spatiotemporal variability in the ratios. Therefore, it is interesting to investigate if the continuous ΔCO-based ΔffCO$_2$ record could provide additional spatiotemporal information to constrain the ffCO$_2$ emissions around a remote site.

Overall, this study highlights a number of challenges in estimating ΔCO-based ΔffCO$_2$ concentrations for an urban and a remote site. Urban sites like Heidelberg with large CO and ffCO$_2$ signals allow the estimation of ΔCO/ΔffCO$_2$ ratios with typically smaller uncertainties. However, the spatiotemporal variability of the ratios from nearby emissions has a strong impact on the overall ΔCO-based ΔffCO$_2$ uncertainty. In contrast, the heterogeneity in the fossil emission ratios seems to be smoothed out when the air masses arrive at remote sites like OPE. However, at these sites it is more difficult to calculate average ratios due to the lower correlations between ΔCO and ^{14}C-based ΔffCO$_2$, which might be caused by the smaller signals and a potentially larger influence from natural CO sources and sinks, especially during summer.

Finally, we also compared the flask-based ratios with ΔCO/ΔffCO$_2$ ratios from TNO, which we modelled with STILT. At both sites there are substantial differences between the observed and the modelled ratios, which might mainly be caused by inconsistencies in the TNO emission ratios and deficits in the STILT transport model. Consequently, there are systematic biases in the ΔCO-based ΔffCO$_2$ record if those inventory-based estimates are used. This illustrates the importance of an ongoing observation-based validation of the sector-specific bottom-up CO/ffCO$_2$ emission ratios, so that also the frequent CO measurements from many urban and remote sites without ^{14}C measurements could be used as additional constraint for estimating ffCO$_2$ emissions.

5.6 Appendix

5.6.1 A1. How to estimate the average $\langle \Delta$CO/ΔffCO$_2\rangle$ ratio from error-prone ΔCO and ΔffCO$_2$ observations

Here, we want to show why one should use a weighted total least squares regression to calculate average $\langle \Delta$CO/ΔffCO$_2\rangle$ ratios from error-prone ΔCO and ΔffCO$_2$ observations. For this, we perform a synthetic data experiment. We use the positive ^{14}C-based ΔffCO$_2$ concentrations from the Heidelberg flasks as the synthetic "true", i.e., error-free ΔffCO$_2$ observations and multiply them with a constant "true" ΔCO/ΔffCO$_2$ ratio of 8.44 ppb/ppm to get synthetic "true" ΔCO observations (see 5.7a). We then draw random numbers from an unbiased Gaussian distribution with 1σ range of 1.16 ppm (for ΔffCO$_2$) and 14.49 ppb (for ΔCO), which corresponds to the mean uncertainties of the real flask observations. We add those random numbers to the "true" ΔffCO$_2$ and ΔCO concentrations, respectively, to get synthetic error-prone data (see 5.7b). If we plot the synthetic error-prone ΔCO/ΔffCO$_2$ ratios against the synthetic error-prone ΔffCO$_2$ concentrations, we get a large scattering for low ΔffCO$_2$ concentrations (see 5.7c). This scattering is only caused by the uncertainties as we have assumed a constant ratio in this synthetic data experiment.

For a comparison, we now can calculate the arithmetic mean, the error-weighted mean, and the median of the synthetic error-prone ratios, as well as the slope of a weighted total least squares regression line from Wurm (2022) through the synthetic error-prone ΔCO and

ΔffCO$_2$ data. To get better statistics we repeat this experiment 10'000 times. On average, we get the following results (average ± standard deviation over 10'000 repetitions):

— Arithmetic mean of the ratios: 9.42 ± 77.84 ppb/ppm

— Error-weighted mean of the ratios: 8.24 ± 0.08 ppb/ppm

— Median of the ratios: 8.39 ± 0.11 ppb/ppm

— Slope of regression line: 8.44 ± 0.06 ppb/ppm

This indicates that only the slope of a regression line, which takes into account the uncertainty of the ΔCO and ΔffCO$_2$ data yields the initial "true" constant ratio of 8.44 ppb/ppm. The arithmetic mean of the ratios shows the largest deviation to the "true" ratio with a very large variability within the 10'000 repetitions. This can be explained by the widely scattering ratios during situations with low ΔffCO$_2$ concentrations but huge relative ΔffCO$_2$ uncertainties. The error-weighted mean ratio and the median ratio is on average 2.4% and 0.6%, respectively, too low. This bias might be introduced by negative ratios, which are caused by very small synthetic "true" ΔCO or ΔffCO$_2$ data that became negative after adding the random uncertainty contribution. Therefore, we recommend to use a weighted total least squares algorithm to calculate the average $\langle\Delta\text{CO}/\Delta\text{ffCO}_2\rangle$ ratio.

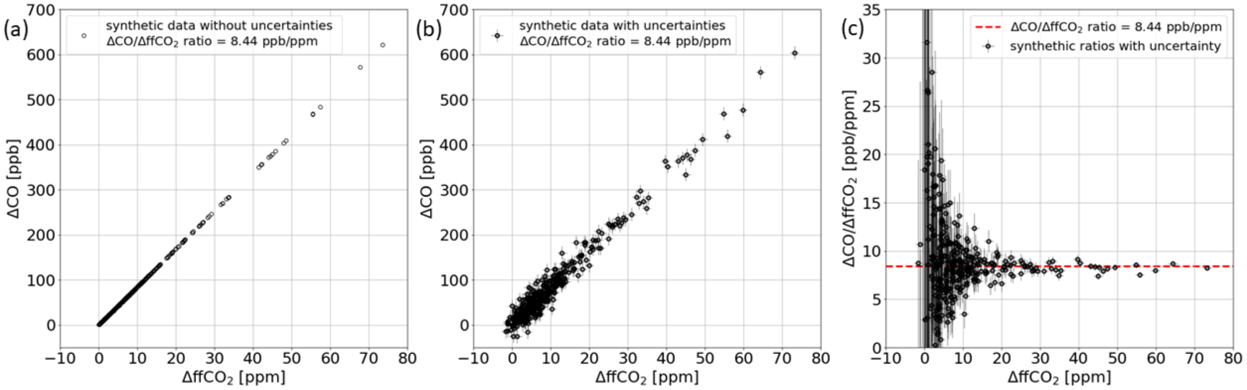

Figure 5.7 (a) synthetic "true" ΔCO and ΔffCO$_2$ data with a constant ratio of 8.44 ppb/ppm. (b) synthetic error-prone ΔCO and ΔffCO$_2$ data under the assumption of a constant ratio of 8.44 ppb/ppm. (c) synthetic error-prone ΔCO/ΔffCO$_2$ ratios.

This synthetic data experiment simulates the situation at an urban site like Heidelberg with a large range of ΔCO and ΔffCO$_2$ concentrations. In this case, we have a very good correlation between the ΔCO and ΔffCO$_2$ data. Indeed, the R^2-value from the applied regression is on average 0.968 ± 0.003 and the uncertainty of the slope is on average 0.06 ppb/ppm. But what happens if we have a smaller range of ΔCO and ΔffCO$_2$ data, for example at a remote site or during summer? To answer this, we perform the synthetic data experiment again, but only with synthetic "true" ΔffCO$_2$ concentrations that are smaller than 5 ppm.

This increases the uncertainty of the slope to 0.55 ppb/ppm, which is almost a factor of 10. Moreover, the R^2-value dramatically decreases to 0.08 ± 0.12. This shows the difficulty of calculating average ratios during summer or at very remote sites with low ΔffCO$_2$ signals (even in the absence of natural CO sources).

In Fig. 5.3b we want to estimate the contribution of the observational uncertainties (i.e., the measurement and background representativeness uncertainty) to the RMSD between the ΔCO- and ^{14}C-based ΔffCO$_2$ concentrations of the Heidelberg flasks. For this, we used the average ratio of 8.44 ± 0.06 ppb/ppm to calculate from the error-prone ΔCO data (see 5.7b) synthetic ΔCO-based ΔffCO$_2$ concentrations. In Fig. 5.3b (red dots), we plot these synthetic ΔCO-based ΔffCO$_2$ data against the error-prone synthetic ΔffCO$_2$ concentrations from 5.7b.

5.6.2 A2. Summer vs. winter ratios

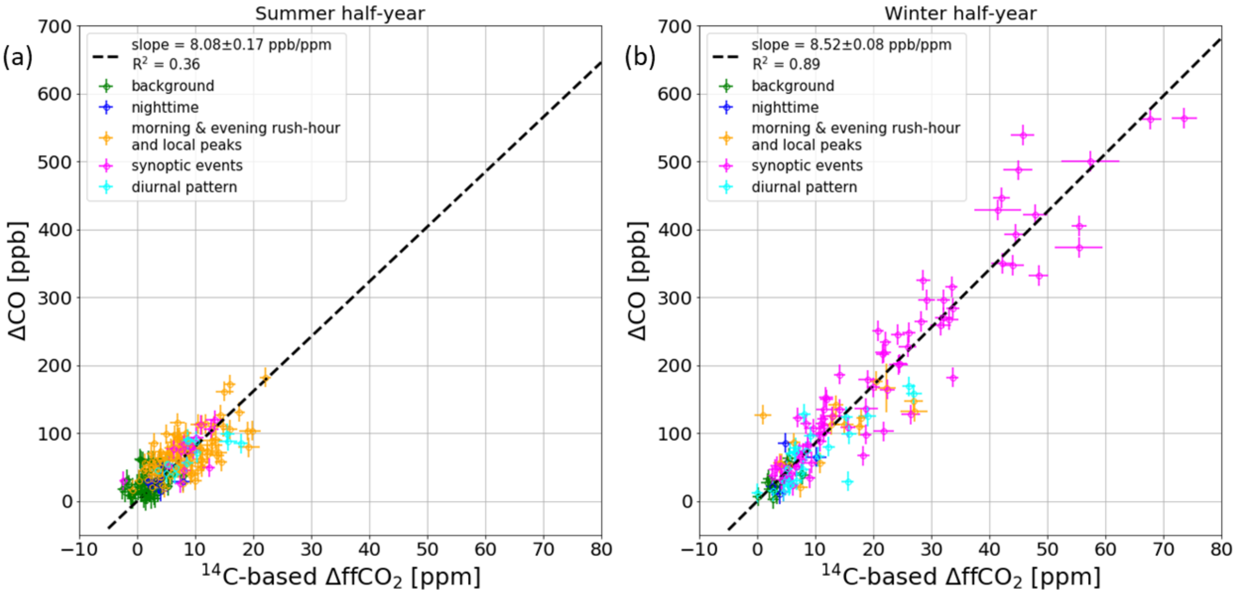

Figure 5.8 Scatter plot with the measured ΔCO and the ^{14}C-based ΔffCO$_2$ concentrations of the hourly flasks collected at the Heidelberg observation site between 2019 and 2020 during (a) the summer half-year and (b) the winter half-year. The colors indicate the sampling situation of the flasks (see description in the caption of Fig. 5.2). The black dashed line shows a regression line performed with the weighted total least squares algorithm from Wurm (2022).

5.7 References

Boschetti, F., Thouret, V., Maenhout, G. J., Totsche, K. U., Marshall, J., and Gerbig, C.: Multi-species inversion and IAGOS airborne data for a better constraint of continental-scale fluxes, Atmos. Chem. Phys., 18, 9225–9241, `https://doi.org/10.5194/acp-18-9225-2018`, 2018.

Ciais, P., Crisp, D., Denier Van Der Gon, H., Engelen, R., Heimann, M., Janssens-Maenhout, G., Rayner, P., and Scholze, M.: Towards a European operational observing system to monitor fossil CO_2 emissions. Final report from the expert group, European Commission, Joint Research Centre, Publications Office, `https://data.europa.eu/doi/10.2788/52148`, 2016.

Currie, L. A.: The remarkable metrological history of radiocarbon dating [II], J. Res. Natl. Inst. Stand. Technol., 109(2), 185-217, `https://doi.org/10.6028/jres.109.013`, 2004.

Dellaert, S., Super, I., Visschedijk, A., and Denier van der Gon, H.: High resolution scenarios of CO_2 and CO emissions, CHE deliverable D4.2, 2019. Available at `https://www.che-project.eu/sites/default/files/2019-05/CHE-D4-2-V1-0.pdf`, Last access: March 28, 2023.

Denier van der Gon, H., Kuenen, J., Boleti, E., Maenhout, G., Crippa, M., Guizzardi, D., Marshall, J., and Haussaire, J.: Emissions and natural fluxes Dataset, CHE deliverable D2.3, 2019. Available at `https://www.che-project.eu/sites/default/files/2019-02/CHE-D2-3-V1-1.pdf`, Last access: March 28, 2023.

Folberth, G. A., Hauglustaine, D. A., Lathière, J., and Brocheton, F.: Interactive chemistry in the Laboratoire de Météorologie Dynamique general circulation model: model description and impact analysis of biogenic hydrocarbons on tropospheric chemistry, Atmos. Chem. Phys., 6, 2273–2319, `https://doi.org/10.5194/acp-6-2273-2006`, 2006.

Gamnitzer, U., Karstens, U., Kromer, B., Neubert, R. E. M., Meijer, H. A. J., Schroeder, H., and Levin, I.: Carbon monoxide: A quantitative tracer for fossil fuel CO_2?, J. Geophys. Res., 111, D22302, `https://doi.org/10.1029/2005JD006966`, 2006.

Graven, H., Fischer, M. L., Lueker, T., Jeong, S., Guilderson, T. P., Keeling, R. F., Bambha, R., Brophy, K., Callahan, W., Cui, X., Frankenberg, C., Gurney, K. R., LaFranchi, B. W., Lehman, S. J., Michelsen, H., Miller, J. B., Newman, S., Paplawsky, W., Parazoo, N. C., Sloop, C., and Walker, S. J.: Assessing fossil fuel CO_2 emissions in California using atmospheric observations and models, Environ. Res. Lett., 13, 065007, `https://dx.doi.org/10.1088/1748-9326/aabd43`, 2018.

Heiskanen, J., Brümmer, C., Buchmann, N., Calfapietra, C., Chen, H., Gielen, B., Gkritzalis, T., Hammer, S., Hartman, S., Herbst, M., Janssens, I. A., Jordan, A., Juurola, E., Karstens, U., Kasurinen, V., Kruijt, B., Lankreijer, H., Levin, I., Linderson, M., Loustau, D., Merbold, L., Myhre, C. L., Papale, D., Pavelka, M., Pilegaard, K., Ramonet, M., Rebmann, C., Rinne, J., Rivier, L., Saltikoff, E., Sanders, R., Steinbacher, M., Steinhoff, T., Watson, A., Vermeulen, A. T., Vesala, T., Vítková, G., and Kutsch, W.: The Integrated Carbon Observation System in Europe, Bulletin of the American Meteorological Society, 103(3), E855-E872, `https://doi.org/10.1175/BAMS-D-19-0364.1`, 2022.

ICOS RI: ICOS Atmosphere Station Specifications V2.0, edited by: Laurent, O., ICOS ERIC, `https://doi.org/10.18160/GK28-2188`, 2020.

Inman, R. E., Ingersoll, R. B., Levy, E. A.: Soil: A Natural Sink for Carbon Monoxide, Science, 172, 1229-1231, `htpps://doi.org/10.1126/science.172.3989.1229`, 1971.

Janssens-Maenhout, G., Crippa, M., Guizzardi, D., Muntean, M., Schaaf, E., Dentener, F., Bergamaschi, P., Pagliari, V., Olivier, J. G. J., Peters, J. A. H. W., van Aardenne, J. A., Monni, S., Doering, U., Petrescu, A. M. R., Solazzo, E., and Oreggioni, G. D.: EDGAR v4.3.2 Global Atlas of the three major greenhouse gas emissions for the period 1970–2012, Earth Syst. Sci. Data, 11, 959–1002, `https://doi.org/10.5194/essd-11-959-2019`, 2019.

Konovalov, I. B., Berezin, E. V., Ciais, P., Broquet, G., Zhuravlev, R. V., and Janssens-Maenhout, G.: Estimation of fossil-fuel CO_2 emissions using satellite measurements of "proxy" species, Atmos. Chem. Phys., 16, 13509–13540, `https://doi.org/10.5194/acp-16-13509-2016`, 2016.

Kuenen, J. J. P., Visschedijk, A. J. H., Jozwicka, M., and Denier van der Gon, H. A. C.: TNO-MACC_II emission inventory; a multi-year (2003–2009) consistent high-resolution European emission inventory for air quality modelling, Atmos. Chem. Phys., 14, 10963–10976, `https://doi.org/10.5194/acp-14-10963-2014`, 2014.

Kromer, B., Lindauer, S., Synal, H.-A., and Wacker, L.: MAMS – A new AMS facility at the Curt-Engelhorn-Centre for Achaeometry, Mannheim, Germany, Nucl. Instrum. Methods Phys. Res. B, 294, 11-13, `https://doi.org/10.1016/j.nimb.2012.01.015`, 2013.

Krystek M. and Anton M.: A weighted total least-squares algorithm for fitting a straight line, Meas. Sci. Technol., 18, 3438, `https://doi.org/10.1088/0957-0233/18/11/025`, 2007

Levin, I., Kromer, B., Schmidt, M., and Sartorius, H.: A novel approach for independent budgeting of fossil fuel CO_2 over Europe by $^{14}CO_2$ observations, Geophys. Res. Lett., 30 (23), 2194, `https://doi.org/10.1029/2003GL018477`, 2003.

Levin, I. and Karstens, U.: Inferring high-resolution fossil fuel CO_2 records at continental sites from combined $^{14}CO_2$ and CO observations, Tellus B, 59, 245-250. `https://doi.org/10.1111/j.1600-0889.2006.00244.x`, 2007.

Levin, I. and Rödenbeck, C.: Can the envisaged reductions of fossil fuel CO_2 emissions be detected by atmospheric observations?, Naturwissenschaften, 95(3), 203-208, `https://doi.org/10.1007/s00114-007-0313-4`, 2008.

Levin, I., Karstens, U., Eritt, M., Maier, F., Arnold, S., Rzesanke, D., Hammer, S., Ramonet, M., Vítková, G., Conil, S., Heliasz, M., Kubistin, D., and Lindauer, M.: A dedicated flask sampling strategy developed for Integrated Carbon Observation System (ICOS) stations based on CO_2 and CO measurements and Stochastic Time-Inverted Lagrangian Transport (STILT) footprint modelling, Atmos. Chem. Phys., 20, 11161–11180, `https://doi.org/10.5194/acp-20-11161-2020`, 2020.

Lin, J. C., Gerbig, C., Wofsy, S. C., Andrews, A. E., Daube, B. C., Davis, K. J., and Grainger, C. A.: A near-field tool for simulating the upstream influence of atmospheric observations: The Stochastic Time-Inverted Lagrangian Transport (STILT) model, J. Geophys. Res., 108, 4493, `https://doi.org/10.1029/2002JD003161`, 2003.

Lux, J. T.: A new target preparation facility for high precision AMS measurements and strategies for efficient $^{14}CO_2$ sampling, Doctoral dissertation, `https://doi.org/10.11588/heidok.00024767`, 2018.

Mahadevan, P., Wofsy, S. C., Matross, D. M., Xiao, X., Dunn, A. L., Lin, J. C., Gerbig, C., Munger, J. W., Chow, V. Y., and Gottlieb, E. W.: A satellite-based biosphere parameterization for net ecosystem CO_2 exchange: Vegetation Photosynthesis and Respiration Model (VPRM), Global Biogeochem. Cycles, 22, GB2005, `https://doi.org/10.1029/2006GB002735`, 2008.

Maier, F., Gerbig, C., Levin, I., Super, I., Marshall, J., and Hammer, S.: Effects of point source emission heights in WRF–STILT: a step towards exploiting nocturnal observations in models, Geosci. Model Dev., 15, 5391–5406, https://doi.org/10.5194/gmd-15-5391-2022, 2022.

Maier, F., and co-authors: Potential of ^{14}C-based versus ΔCO-based ΔffCO$_2$ observations to estimate urban fossil fuel CO$_2$ (ffCO$_2$) emissions, 2023a [to be submitted, see Ch. 6].

Maier, F., Levin, I., Gachkivskyi, M., Rödenbeck, C., and Hammer, S.: Estimating regional fossil-fuel CO$_2$ concentrations from ^{14}CO$_2$ observations: Challenges and uncertainties, Phil. Trans. R. Soc. A, https://doi.org/10.1098/rsta.2022.0203 [link not yet available], 2023b [approved for publication].

Miller, J. B., Lehman, S. J., Montzka, S. A., Sweeney, C., Miller, B. R., Karion, A., Wolak, C., Dlugokencky, E. J., Southon, J., Turnbull, J. C., Tans, P. P.: Linking emissions of fossil fuel CO$_2$ and other anthropogenic trace gases using atmospheric ^{14}CO$_2$, J. Geophys. Res., 117, D08302, https://doi.org/10.1029/2011JD017048, 2012.

Naegler, T. and Levin, I.: Biosphere-atmosphere gross carbon exchange flux and the δ^{13}CO$_2$ and Δ^{14}CO$_2$ disequilibria constrained by the biospheric excess radiocarbon inventory, J. Geophys. Res., 114, D17303, https://doi.org/10.1029/2008JD011116, 2009.

Nehrkorn, T., Eluszkiewicz, J., Wofsy, S. C., Lin, J. C., Gerbig, C., Longo, M., Freitas, S.: Coupled weather research and forecasting–stochastic time-inverted lagrangian transport (WRF–STILT) model. Meteorol. Atmos. Phys. 107, 51–64, https://doi.org/10.1007/s00703-010-0068-x, 2010.

Palmer, P. I., Suntharalingam, P., Jones, D. B. A., Jacob, D. J., Streets, D. G., Fu, Q., Vay, S. A., and Sachse, G. W.: Using CO$_2$:CO correlations to improve inverse analyses of carbon fluxes, J. Geophys. Res., 111, D12318, https://doi.org/10.1029/2005JD006697, 2006.

Petron, G., Crotwell, A. M., Crotwell, M. J., Dlugokencky, E., Madronich, M., Moglia, E., Neff, D., Thoning, K., Wolter, S., and Mund, J. W.: Atmospheric Carbon Monoxide Dry Air Mole Fractions from the NOAA GML Carbon Cycle Cooperative Global Air Sampling Network, 1988-2021, Version: 2022-07-28, https://doi.org/10.15138/33bv-s284, 2022.

Pinty, B., Ciais, P., Dee, D., Dolman, H., Dowell, M., Engelen, R., Holmlund, K., Janssens-Maenhout, G., Meijer, Y., Palmer, P., Scholze, M., Denier van der Gon, H., Heimann, M., Juvyns, O., Kentarchos, A., and Zunker, H.: An Operational Anthropogenic CO$_2$ Emissions Monitoring & Verification Support Capacity – Needs and high level requirements for in situ measurements, European Commission, Joint Research Centre, Publications Office, `https://data.europa.eu/doi/10.2760/182790`, 2019.

Ramonet, M., Conil, S., Delmotte, M., Laurent, O.: ICOS Atmosphere Level 2 data, Observatoire pérenne de l'environnement, release 2022-1, ICOS RI, `https://doi.org/10.18160/ARMY-T852`, 2022.

Rosendahl C.: Proxy to fossil-fuel CO_2 emission ratios: in-situ versus inventory data, PhD-Thesis, University of Heidelberg, `https://doi.org/10.11588/heidok.00031909`, 2022.

Storm, I., Karstens, U., D'Onofrio, C., Vermeulen, A., and Peters, W.: A view of the European carbon flux landscape through the lens of the ICOS atmospheric observation network, Atmos. Chem. Phys. Discuss. [preprint], `https://doi.org/10.5194/acp-2022-756`, in review, 2022.

Stuiver, M. and Polach, H.: Discussion Reporting of 14C Data, Radiocarbon, 19(3), 355-363, `https://doi.org/10.1017/S0033822200003672`, 1977.

Thoning, K. W., Tans, P. P., and Komhyr, W. D.: Atmospheric carbon dioxide at Mauna Loa Observatory: 2. Analysis of the NOAA GMCC data, 1974–1985, J. Geophys. Res., 94(D6), 8549–8565, `https://doi.org/10.1029/JD094iD06p08549`, 1989.

Turnbull, J., Sweeney, C., Karion, A., Newberger, T., Lehman, S., Tans, P., Davis, K., Lauvaux, T., Miles, N., Richardson, S., Cambaliza, M., Shepson, P., Gurney, K., Patarasuk, R., and Razlivanov, I.: Toward quantification and source sector identification of fossil fuel CO_2 emissions from an urban area: Results from the INFLUX experiment, J. Geophys. Res. Atmos., 120, 292– 312, `https://doi.org/10.1002/2014JD022555`, 2015.

Van Der Laan, S., Karstens, U., Neubert, R. E. M., Van Der Laan-Luijkx, I. T., and Meijer, H. A. J.: Observation-based estimates of fossil fuel-derived CO_2 emissions in the Netherlands using $\Delta^{14}C$, CO and ^{222}Radon, Tellus B: Chemical and Physical Meteorology, 62,5, 389-402, `https://doi.org/10.1111/j.1600-0889.2010.00493.x`, 2010.

Vimont, I. J., Turnbull, J. C., Petrenko, V. V., Place, P. F., Sweeney, C., Miles, N., Richardson, S., Vaughn, B. H., and White, J. W. C.: An improved estimate for the $\delta^{13}C$ and $\delta^{18}O$ signatures of carbon monoxide produced from atmospheric oxidation of volatile organic compounds, Atmos. Chem. Phys., 19, 8547–8562, `https://doi.org/10.5194/acp-19-8547-2019`, 2019.

Vogel, F., Hammer, S., Steinhof, A., Kromer, B., and Levin, I.: Implication of weekly and diurnal ^{14}C calibration on hourly estimates of CO-based fossil fuel CO_2 at a moderately polluted site in southwestern Germany, Tellus B: Chemical and Physical Meteorology, 62, 5, 512-520, `https://doi.org/10.1111/j.1600-0889.2010.00477.x`, 2010.

Wang, Y., Broquet, G., Ciais, P., Chevallier, F., Vogel, F., Wu, L., Yin, Y., Wang, R., and Tao, S.: Potential of European $^{14}CO_2$ observation network to estimate the fossil fuel CO_2 emissions via atmospheric inversions, Atmos. Chem. Phys., 18, 4229–4250, `https://doi.org/10.5194/acp-18-4229-2018`, 2018.

Wenger, A., Pugsley, K., O'Doherty, S., Rigby, M., Manning, A. J., Lunt, M. F., and White, E. D.: Atmospheric radiocarbon measurements to quantify CO_2 emissions in the UK from 2014 to 2015, Atmos. Chem. Phys., 19, 14057–14070, `https://doi.org/10.5194/acp-19-14057-2019`, 2019.

Worden, H. M., Bloom, A. A., Worden, J. R., Jiang, Z., Marais, E. A., Stavrakou, T., Gaubert, B., and Lacey, F.: New constraints on biogenic emissions using satellite-based estimates of carbon monoxide fluxes, Atmos. Chem. Phys., 19, 13569–13579, `https://doi.org/10.5194/acp-19-13569-2019`, 2019.

Wurm, M.: A universal and fast method to solve linear systems with correlated coefficients using weighted total least squares, Meas. Sci. Technol., 33, `htpps://doi.org/10.1088/1361-6501/ac32ec`, 2022.

Zhou, W., Niu, Z., Wu, S., Xiong, X., Hou, Y., Wang, P., Feng, T., Cheng, P., Du, H., Lu, X., An, Z., Burr, G. S., Zhu, Y.: Fossil fuel CO_2 traced by radiocarbon in fifteen Chinese cities, Science of The Total Environment, 729, `https://doi.org/10.1016/j.scitotenv.2020.138639`, 2020.

CHAPTER 6

Potential of ^{14}C-based versus ΔCO-based ΔffCO$_2$ observations to estimate urban fossil fuel CO$_2$ (ffCO$_2$) emissions

This chapter will be submitted to *Atmospheric Chemistry and Physics*: Maier, F., and co-authors: Potential of ^{14}C-based versus ΔCO-based ΔffCO$_2$ observations to estimate urban fossil fuel CO$_2$ (ffCO$_2$) emissions, 2023.

Abstract

Atmospheric transport inversions are a powerful tool for independently estimating surface CO_2 fluxes from atmospheric CO_2 concentration measurements. However, additional tracers are needed to separate the fossil fuel CO_2 ($ffCO_2$) emissions from natural CO_2 fluxes. In this study we focus on radiocarbon (^{14}C), the most direct tracer for $ffCO_2$, and the continuously measured surrogate tracer carbon monoxide (CO), which is co-emitted with $ffCO_2$ during incomplete combustion. In the companion paper by Maier et al. (2023a) we determined for the urban Heidelberg observation site in Southwestern Germany discrete ^{14}C-based and continuous ΔCO-based estimates of the $ffCO_2$ excess concentration ($\Delta ffCO_2$) compared to a clean-air reference. Here, we use the CarboScope inversion framework adapted for the urban domain around Heidelberg to assess the potential of both types of $\Delta ffCO_2$ observations to investigate $ffCO_2$ emissions and their seasonal cycle. We find that discrete ^{14}C-based $\Delta ffCO_2$ observations from almost 100 afternoon flask samples collected in the two years 2019 and 2020 are not well suited for estimating robust $ffCO_2$ emissions in the main footprint of this urban area with a very heterogeneous distribution of sources including several point sources. The benefit of the continuous ΔCO-based $\Delta ffCO_2$ estimates is that they can be averaged to reduce the impact of individual hours with an inadequate model performance. We show that the weekly averaged ΔCO-based $\Delta ffCO_2$ observations allow for a robust reconstruction of the seasonal cycle of the area source $ffCO_2$ emissions from temporally flat a-priori emissions. In particular, the distinct COVID-19 signal with a steep drop in emissions in spring 2020 is clearly present in these data-driven a-posteriori results. Moreover, our top-down results show a shift in the seasonality of the area source $ffCO_2$ emissions around Heidelberg in 2019 compared to the bottom-up estimates from TNO. This highlights the huge potential of ΔCO-based $\Delta ffCO_2$ to verify bottom-up $ffCO_2$ emissions at urban stations if the $\Delta CO/\Delta ffCO_2$ ratios can be determined without biases.

6.1 Introduction

The combustion of fossil fuels (ff) like coal, oil and gas is the major reason for the steep increase in the atmospheric CO_2 concentration, which causes current global warming. About 70% of the global $ffCO_2$ emissions are released from urban hotspot regions (Duren and Miller, 2012). However, the atmospheric CO_2 increase is fortunately strongly weakened, since about half of the human-induced CO_2 emissions are currently taken up by the terrestrial biosphere and the oceans in roughly equal shares (Friedlingstein et al., 2022). Indeed, there are large seasonal and inter-annual variations in the natural CO_2 sinks and sources that need to be better understood in order to make predictions about future changes in the carbon cycle owing to increased atmospheric CO_2 levels.

The “atmospheric transport inversion” (Newsam and Enting, 1988) is a powerful tool for deducing surface CO_2 fluxes from atmospheric CO_2 observations. Hence, many studies have applied this top-down approach to constrain natural CO_2 fluxes (e.g., Rödenbeck et al., 2003; Peylin et al., 2013; Jiang et al., 2016; Rödenbeck et al., 2018; Monteil et al., 2020; Liu et al., 2021). In these calculations, $ffCO_2$ emissions are typically prescribed using bottom-up information from emission inventories. These bottom-up $ffCO_2$ emission estimates are typically based on national annual activity data that describe the fuel consumption and sector-specific emission factors (Janssens-Maenhout et al., 2019). While annual national total $ffCO_2$ emissions are associated with low uncertainties of typically a few percent for developed countries (Andres et al., 2012), their proxy-based distribution on individual spatial grid cells and individual months, days or hours can dramatically increase the uncertainties (Super et al., 2020). Therefore, it is essential to have an independent verification of the bottom-up statistics, especially on the relevant urban scales. In particular, the seasonal cycle of bottom-up $ffCO_2$ emissions needs to be validated, if they are used in CO_2 inversions to deduce biogenic CO_2 fluxes that are dominated by a large seasonal cycle.

Atmospheric transport inversions can be used to validate these bottom-up $ffCO_2$ emissions (e.g., Lauvaux et al., 2016; Basu et al., 2020). However, their success relies on the ability of the used observational tracers to separate fossil fuel from natural CO_2 contributions (Ciais et al., 2015; Bergamaschi et al., 2018). The most direct tracer for $ffCO_2$ is radiocarbon (^{14}C) in CO_2. Radiocarbon has a half-life of 5700 years and is therefore no longer present in fossil fuels (Currie, 2004). Thus, the ^{14}C depletion in ambient air CO_2 compared to a clean-air reference site can directly be used to estimate the recently added $ffCO_2$ excess ($\Delta ffCO_2$) at the observation site (Levin et al., 2003; Turnbull et al., 2006). These $\Delta ffCO_2$ estimates can then be implemented in regional inversions to evaluate bottom-up $ffCO_2$ emissions in the footprints of the observation sites (Graven et al., 2018; Wang et al., 2018). However, a drawback of ^{14}C-based $\Delta ffCO_2$ estimates is that they have poor temporal and spatial coverage due to the labor-intensive and expensive ^{14}C sampling and analysis. Therefore, continuously measured atmospheric excess concentrations of trace gases like CO, which is co-emitted with $ffCO_2$, have been used as alternative proxies for $\Delta ffCO_2$ (e.g., Gamnitzer et al., 2006; Turnbull et al., 2006; Levin and Karstens, 2007; Van Der Laan et al., 2010; Vogel et al., 2010). However, to construct a high-resolution ΔCO-based $\Delta ffCO_2$ record requires to correctly determine the $\Delta CO/\Delta ffCO_2$ ratio in the footprint of the observation site. This can indeed be a big challenge: As the $CO/ffCO_2$ emission ratio depends on the combustion efficiency and applied end-of-pipe measures, it is very variable for different emission processes and changes with time due to technological progress (Dellaert et al., 2019).

In the companion paper by Maier et al. (2023a) we calculated a ΔCO-based $\Delta ffCO_2$ record for the urban Heidelberg observation site from the $\Delta CO/\Delta ffCO_2$ ratios of almost 350 $^{14}CO_2$ flask samples collected between 2019 and 2020. By comparing the ΔCO-based $\Delta ffCO_2$ with the ^{14}C-based $\Delta ffCO_2$ from the flasks we estimated for the hourly ΔCO-based $\Delta ffCO_2$ record an uncertainty of about 4 ppm, which is almost 4 times larger than typical ^{14}C-based $\Delta ffCO_2$ uncertainties. About half of this uncertainty could be attributed to the spatiotemporal variability of the $\Delta CO/\Delta ffCO_2$ ratios.

The goal of this study is to investigate which type of $\Delta ffCO_2$ observations provides the greater benefit in an atmospheric transport inversion to verify bottom-up $ffCO_2$ emission estimates in an urban region: (1) sparse ^{14}C-based $\Delta ffCO_2$ observations from flasks with a small uncertainty or (2) ΔCO-based $\Delta ffCO_2$ estimates at high temporal resolution but with an increased uncertainty? For this, we adapt the CarboScope inversion framework (Rödenbeck, 2005) for the highly populated and industrialized Rhine Valley in Southwestern Germany around the Heidelberg observation site. We perform separate inversion runs with the ^{14}C- and ΔCO-based $\Delta ffCO_2$ observations from Heidelberg. Thereby, we mainly focus on the seasonal cycle in the $ffCO_2$ emissions and investigate which $\Delta ffCO_2$ information is best suited to verify the seasonal cycle of the bottom-up emissions in the main footprint of Heidelberg.

6.2 Methods

6.2.1 Heidelberg observation site

Heidelberg is a medium-sized city with about 160'000 inhabitants, which is part of the Rhine-Neckar metropolitan area with over 2 million people. The Heidelberg observation site is located on the university campus in the northern part of the city. The sampling inlet line is 30 m above ground on the roof of the institute's building. Local ffCO_2 emissions originate mainly from traffic and residential heating but there is also a nearby combined heat and power station as well as a large coal-fired power plant and the giant industrial complex from BASF at 15-20 km to the North-West. Due to its location in the Upper Rhine Valley, Heidelberg is frequently influenced by south-westerly air masses, which carry the signals from heterogeneous sources in the Rhine Valley. A more detailed description of the Heidelberg observation site can be found in Hammer (2008). The ^{14}C-based and ΔCO-based ΔffCO_2 observations from Heidelberg are presented in Sect. 6.2.2.

6.2.2 Inversion setup

The CarboScope inversion algorithm was initially introduced by Rödenbeck et al. (2003) to estimate inter-annual and spatial variability in global CO_2 surface-atmosphere fluxes. The algorithm can also be applied to regional inversions (Rödenbeck et al., 2009). In the present study we adapt this inversion modelling framework to estimate ffCO_2 surface fluxes in the regional Rhine Valley domain (see Fig. 6.1) with ΔffCO_2 observations from the Heidelberg observation site (see Fig. 6.2). This requires a high-resolution atmospheric transport model and a careful estimation of the lateral ΔffCO_2 boundary conditions.

The CarboScope inversion system uses Bayesian inference to minimize the deviations between observed and modelled ΔffCO_2 concentrations by finding the (global) minimum of the cost function (for technical details see Rödenbeck, 2005). This cost function consists of a data constraint and an a-priori constraint, which is needed to regularize the underdetermined problem and to prevent large and unrealistic spatiotemporal ffCO_2 flux variabilities (Rödenbeck et al., 2018). The data constraint is weighted by the uncertainties of the transport model and the ΔffCO_2 observations. Furthermore, the uncertainty applied for the a-priori ffCO_2 emissions determines the impact of the a-priori constraint. Overall, the ratio between the model-data uncertainty and the a-priori flux uncertainty controls the strength of the a-priori constraint over the observational constraint (Rödenbeck, 2005).

Atmospheric transport model

We use the Stochastic Time-Inverted Lagrangian Transport (STILT, Lin et al., 2003; Nehrkorn et al., 2010) model, driven by meteorological fields from the high-resolution Weather Research and Forecasting (WRF) model, to simulate the atmospheric transport in the Rhine Valley domain (see red rectangular in Fig. 6.1). The WRF meteorological fields have a horizontal resolution of 2 km and are based on hourly 0.25°-resolved European ReAnalysis 5 (ERA5, Hersbach et al., 2020) data from the European Centre for Medium-Range Weather Forecasts (ECMWF). As there are many point source emissions within the Rhine Valley, we apply the STILT volume source influence (VSI) approach introduced by Maier et al. (2022) to model them. This model approach takes into account the effective heights of the point source emissions, which are typically released from elevated chimney stacks. For the area source emissions, we apply the standard approach in STILT, which assumes that all emissions are released from the surface.

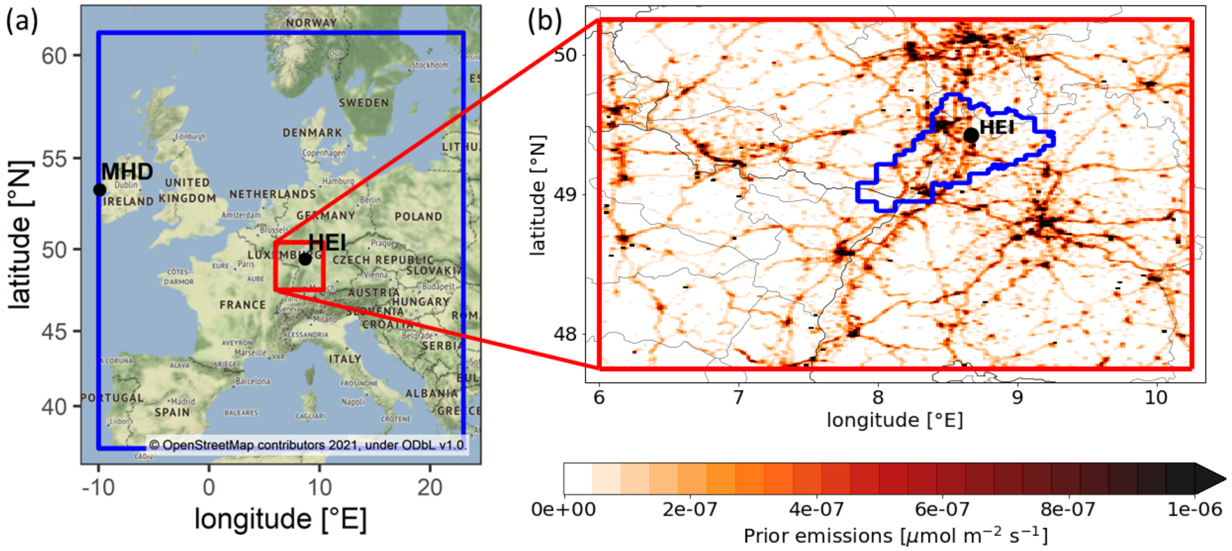

Figure 6.1 (a) Map with the entire Central European STILT model domain (blue) and the Rhine Valley domain (red). The observation site Heidelberg (HEI) and the marine background site Mace Head (MHD) are indicated. (b) Zoom into the Rhine Valley domain with the mean prior ffCO$_2$ emissions from the TNO inventory. The blue surrounded region in the zoom shows the "50%-footprint" range, i.e., the area accounting for 50% of the Heidelberg average footprint within the Rhine Valley.

A-priori information

We use the ffCO$_2$ emissions from TNO (Dellaert et al., 2019; Denier van der Gon et al., 2019) with a horizontal resolution of about 1 km (1/60° lon, 1/120° lat) as a-priori estimates for our Rhine Valley inversion. The TNO emission inventory provides annual total ffCO$_2$ emissions for 15 different source sectors as well as sector-specific temporal profiles. In this study, we treat the ffCO$_2$ emissions from the point source dominated "energy production" and "industry" TNO sectors separately due to the following reasons: (1) While the VSI approach (see above) strongly improves the vertical representation of point source emissions in STILT, it still remains difficult to correctly describe the mixing and transport of narrow point source plumes with a 2 km resolved meteorology. (2) Due to the elevated release of point source emissions from high stacks, the Heidelberg observation site with an air intake height of only 30 m above ground is rarely influenced by distinct emission plumes from nearby point sources (see Maier et al., 2023a). This makes it difficult to evaluate those point source emissions with ΔffCO$_2$ observations from the Heidelberg observation site alone. (3) We expect that the energy and industry emissions in the Rhine Valley are better known in TNO than the more diffuse area source emissions. We thus focus on how well our observations are able to constrain area source emissions in the footprint of the Heidelberg site.

For these reasons, we prescribe the energy and industry emissions in our inversion setup and adjust only the area source emissions in the Rhine Valley, which mainly originate from the heating and traffic sector. We use the sector-specific monthly profiles provided by TNO to calculate from the annual total emissions monthly ffCO$_2$ emissions for the energy and industry sectors and treat them as fixed fluxes in our inversion system. As we aim to investigate the information of the ΔffCO$_2$ observations regarding the seasonal cycle of the area source ffCO$_2$ emissions, we apply temporally constant ("flat") a-priori ffCO$_2$ emissions for the area sources. For this, we use the (spatially highly resolved) 2-year average TNO area source emissions of the years 2019 and 2020.

Observations

In separate inversion runs, we use either the discrete ^{14}C-based ΔffCO$_2$ estimates from flasks, collected as integrals over one hour, or the hourly ΔCO-based ΔffCO$_2$ record from the Heidelberg observation site (see Fig. 6.2). The companion paper (Maier et al., 2023a) describes in detail the construction of this continuous ΔCO-based ΔffCO$_2$ record and gives an estimation of its uncertainty. In short, the ΔCO-based ΔffCO$_2$ record has been constructed by dividing the observed hourly ΔCO offsets compared to the marine reference site Mace Head

(MHD) by an average ΔCO/ΔffCO$_2$ ratio, which was determined by the ΔCO and ^{14}C-based ΔffCO$_2$ observations of almost 350 day- and night-time flask samples collected in 2019 and 2020. In the inversion, however, we only use the afternoon ^{14}C-based and ΔCO-based ΔffCO$_2$ observations between 11 and 16 UTC, as night-time situations are related with a poorer transport model performance.

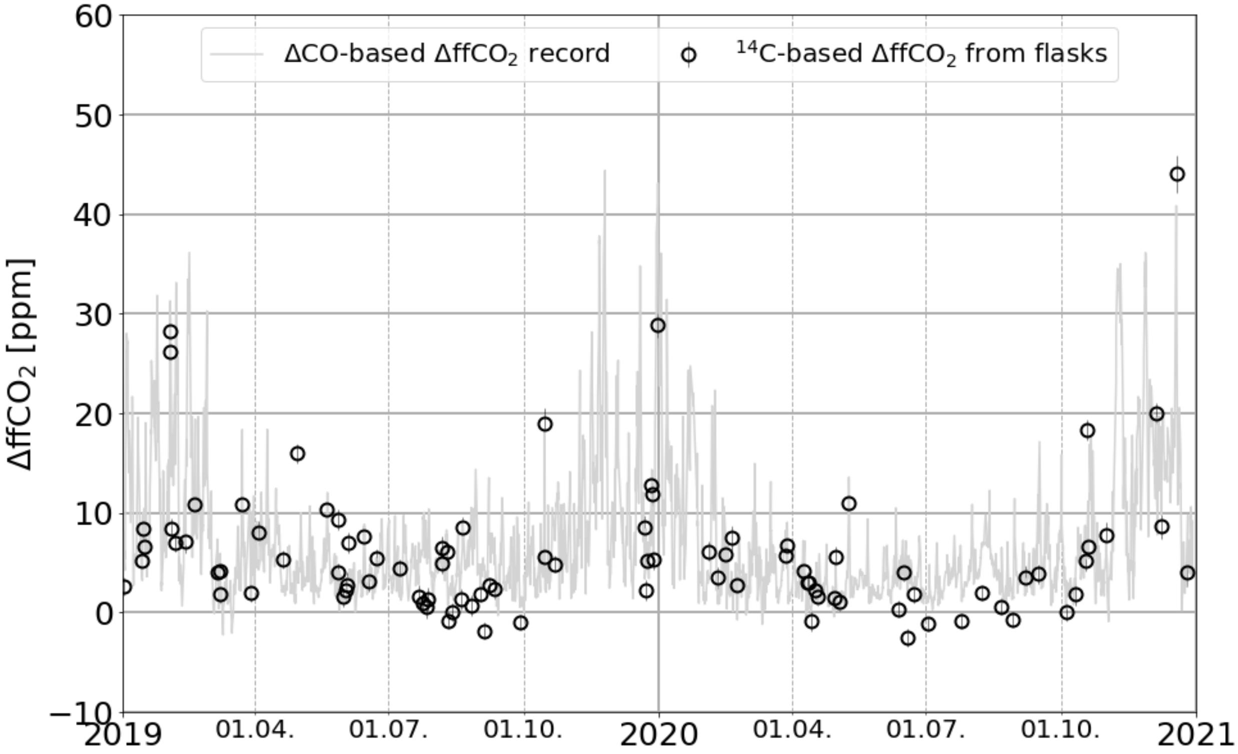

Figure 6.2 Afternoon ΔffCO$_2$ observations from the Heidelberg observation site. The grey curve indicates the ΔCO-based ΔffCO$_2$ record and the black circles the ^{14}C-based ΔffCO$_2$ estimates from flasks. Both, the ^{14}C-based and ΔCO-based ΔffCO$_2$ observations are 2σ-selected.

Furthermore, we apply a 2σ-selection criterion to the ΔffCO$_2$ observations as introduced by Rödenbeck et al. (2018). For this, we take the high-resolution annual total ffCO$_2$ emissions from TNO and apply the hourly sector-specific temporal profiles. These hourly resolved ffCO$_2$ emissions are then transported with the WRF-STILT model to simulate hourly ΔffCO$_2$ concentrations. The mean difference between the simulated and the ΔCO-based ΔffCO$_2$ observations is only -0.04 ppm during afternoon hours with a standard deviation of 6.76 ppm, which indicates that the model is able to reproduce, on average, the afternoon ΔCO-based ΔffCO$_2$ observations without a significant mean bias. This directly allows the application of the 2σ-selection criterion, which means that we only use those ΔffCO$_2$ observations, whose deviation to the modelled ΔffCO$_2$ is smaller than 2 times the standard deviation between observed and modelled ΔffCO$_2$, i.e. which is within the 2σ-range of 2*6.76 = 13.52 ppm. Therewith, we exclude the data outside the 2σ-range, which obviously cannot be represented with our transport model. Examples of such data are observations during very strong synoptic events in winter, which are underestimated in the model, or vice versa, situations when the model overestimates the point source influence at the observation site. Since the inversion system assumes a Gaussian distribution for the model-data mismatch, these extreme outlier events would have a strong impact on the inversion results (Rödenbeck et al., 2018). Thus, this 2σ-selection can be seen as an additional regularization for the inversion to avoid overfitting of individual situations with unrealistic model simulations. We apply the 2σ-selection criterion to both the ^{14}C-based ΔffCO$_2$ observations from the afternoon flask samples and the afternoon hours of the ΔCO-based ΔffCO$_2$ record.

Lateral boundary conditions

We set up the inversion system for the Rhine Valley domain (6.00°E – 10.25°E, 47.75°N – 50.25°N, red rectangular in Fig. 6.1a) around the Heidelberg observation site and run the inversion for the full two years 2019 and 2020 within this domain. As we calculated the ^{14}C- and ΔCO-based ΔffCO$_2$ excess compared to MHD (see Maier et al., 2023a), however, we need to define a suitable ΔffCO$_2$ background representative for the boundary of the Rhine Valley domain. In the following, we call this the "Rhine Valley ΔffCO$_2$ background". By definition, we assume that the Δ^{14}CO$_2$ observations from MHD correspond to ΔffCO$_2$ = 0 ppm, which might be reasonable since the MHD ^{14}CO$_2$ samples were only collected during situations with clean westerly air masses from the Atlantic. Therefore, it seems to be suitable to apply the MHD (ΔffCO$_2$ = 0 ppm) background to the entire western boundary of the Central European STILT domain (blue rectangular in 6.1a). But how representative is this background for the other boundaries of the Central European domain? Maier et al. (2023b) estimated the representativeness bias of the MHD background for the probably most polluted eastern boundary of the Central European domain. They could show that the representativeness bias is on average smaller than 0.1 ppm for an observation site in Central Europe. Therefore, we neglect this bias and assume ΔffCO$_2$ = 0 ppm also at the non-western boundaries of the Central European domain. To estimate the Rhine Valley ΔffCO$_2$ background we model for the Heidelberg site for each hour during 2019 and 2020 the ΔffCO$_2$ contributions from the Central European domain *outside* the Rhine Valley (ΔffCO$_{2,\mathrm{CE-RV}}$). For this, we use the WRF-STILT model and hourly ffCO$_2$ emissions from TNO (Dellaert et al., 2019; Denier van der Gon et al., 2019). Note that the WRF meteorology outside the Rhine Valley has a reduced horizontal resolution of 10 km. We then subtract the modelled Rhine

Valley ΔffCO_2 background ($\Delta\text{ffCO}_{2,\text{CE}-\text{RV}}$) from the estimated ΔffCO_2 excess compared to MHD ($\Delta\text{ffCO}_{2,\text{MHD}}$), to obtain the ΔffCO_2 excess compared to the Rhine Valley boundary ($\Delta\text{ffCO}_{2,\text{RV}}$):

$$\Delta\text{ffCO}_{2,\text{RV}} = \Delta\text{ffCO}_{2,\text{MHD}} - \Delta\text{ffCO}_{2,\text{CE}-\text{RV}} \tag{6.1}$$

The $\Delta\text{ffCO}_{2,\text{RV}}$ excess concentrations compared to the Rhine Valley boundary are then introduced into the inversion system to constrain the ffCO_2 emissions within the Rhine Valley.

Model-data mismatch

The model-data mismatch is calculated by subtracting the modelled from the observed $\Delta\text{ffCO}_{2,\text{RV}}$ concentrations. The uncertainties of the ΔCO-based and ^{14}C-based ΔffCO_2 observations are estimated to be 3.9 ppm and 1.1 ppm, respectively (see Maier et al., 2023a). The transport model uncertainty of urban, continental sites like Heidelberg with complex local circulations was assumed to be 5 ppm. The quadratically added observational and transport model uncertainties yield the total uncertainty of the model-data mismatch. To account for the temporal correlations of observations that are close together in time, we apply a data density weighting as described in Rödenbeck (2005). It artificially increases the uncertainty of the model-data mismatch, so that all observations within one week lead to the same constraint as a single observation per week. The weighting interval was set to one week because this is a typical length scale of large-scale weather patterns.

Degrees of freedom

Since we only use ΔffCO_2 observations from a single station in the Rhine Valley, we must restrict the number of degrees of freedom in our inversion system so that the inverse problem is not too strongly underdetermined. Therefore, we only investigate the area source emissions in the Rhine Valley and prescribe the energy and industry emissions, as mentioned above. Moreover, the inversion system adjusts only one spatial scaling factor, which increases or decreases the area source emissions in the whole Rhine Valley domain equally. Hence, we expect that the high-resolution TNO inventory is much better at describing the large spatial heterogeneity in the ffCO_2 emissions within the Rhine Valley than our top-down approach. As we want to investigate the seasonal cycle of the ffCO_2 emissions, additional temporal degrees of freedom are needed. For this, we choose a temporal correlation length of about 4 months (“Filt3T” in CarboScope notation), which should be appropriate to explore seasonal cycles. Finally, since the Heidelberg observations cannot be used to constrain the emissions in the whole Rhine Valley domain, we only analyze the a-posteriori area source emissions in the (most constrained) nearfield of the observation site. We define the nearfield of Heidelberg as the area which accounts for 50% of the temporally accumulated footprint in the Rhine Valley domain for the two years 2019 and 2020 (blue surrounded region in Fig. 6.1b).

6.3 Results

6.3.1 Potential of flask-based ΔffCO$_2$ estimates to investigate the seasonal cycle in ffCO$_2$ emissions

First, we investigate the potential of flask-based ΔffCO$_2$ estimates to explore the seasonal cycle of the area source ffCO$_2$ emissions around the urban Heidelberg observation site. For this we use the average of the TNO area source ffCO$_2$ emissions of the two years 2019 and 2020 as a temporally constant prior estimate (see Sect. 6.2.2). To analyze the impact of the observational constraint on the a-posteriori results, we apply different prior uncertainties, which effectively lead to different ratios between a-priori and data constraint (see Fig. 6.3). In a first inversion run (Fig. 6.3a), we use the ^{14}C-based ΔffCO$_2$ observations from the 94 afternoon flasks collected in the two years 2019 and 2020 in Heidelberg. The distribution of the flask samplings over the two years can be seen in Fig. 6.2. Due to various reasons (e.g. testing of the flask sampler associated with frequent changes of the flask sampling strategy) the flasks were not evenly collected and especially the winter 2019/2020 has only thin flask coverage. The ^{14}C-based a-posteriori ffCO$_2$ emissions show a clear seasonal cycle for the larger prior uncertainties, which is fully data-driven. However, large and unrealistic a-posteriori flux variabilities emerge for prior uncertainties larger than 50% of the flat a-priori emissions. For example, the low flask coverage during the winter period 2019/2020 leads to a huge maximum in the area source ffCO$_2$ emissions in November 2019 when the inversion algorithm tries to minimize the model-data mismatches of individual flasks. Similarly, the flask samples with vanishing or even negative ΔffCO$_2$ estimates in summer 2020 (cf. Fig. 6.2) cause a strong reduction of the a-posteriori emissions. Therefore, this urban inversion setup obviously needs a very strong regularization through low prior uncertainties to prevent the fitting of individual flask observations.

We further investigate whether these overfitting patterns can be attributed to the uneven distribution of the flask samples. For this, we subsample the continuous ΔCO-based ΔffCO$_2$ record. In a first step, we use the ΔCO-based ΔffCO$_2$ observations from those 94 afternoon hours with flask samplings as observational constraint (Fig. 6.3b). For the most part, the subsampled ΔCO-based ΔffCO$_2$ observations reproduce the a-posteriori results of the ^{14}C-based

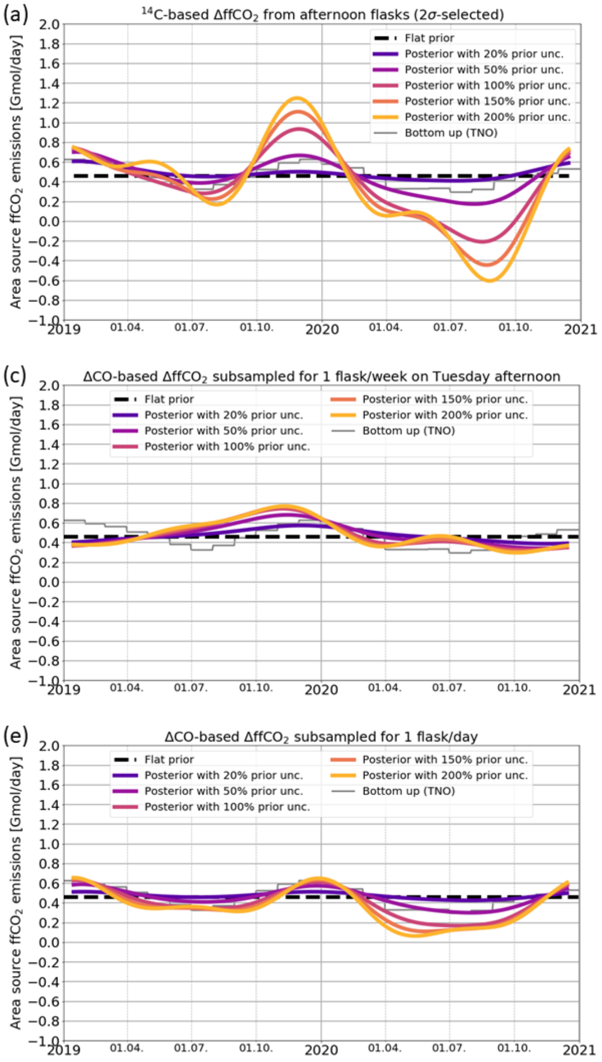

(a) ^{14}C-based ΔffCO$_2$ from afternoon flasks (2σ-selected)

(b) ΔCO-based ΔffCO$_2$ subsampled for real flask times

(c) ΔCO-based ΔffCO$_2$ subsampled for 1 flask/week on Tuesday afternoon

(d) ΔCO-based ΔffCO$_2$ subsampled for 1 flask/week on Friday afternoon

(e) ΔCO-based ΔffCO$_2$ subsampled for 1 flask/day

(f) ΔCO-based ΔffCO$_2$ subsampled for 1 flask/day and weekly averaged

Figure 6.3 Area source ffCO$_2$ emissions in the nearfield (blue surrounded area in Fig. 6.1b) of Heidelberg. Shown are the flat prior emissions (black dashed line), the a-posteriori emissions for different prior uncertainties between 20% and 200% of the flat a-priori emissions (colored solid lines) as well as the bottom-up estimates from TNO (grey line). In panel (a) ^{14}C-based ΔffCO$_2$ estimates from 94 2σ-selected afternoon flasks from Heidelberg were used as observational input (cf. Fig. 6.2). Panel (b) shows the inversion results if the ΔCO-based ΔffCO$_2$ observations subsampled during the 94 flask sampling hours were used. In the panels (c) and (d) the inversion was constrained with one hourly afternoon (at 13 UTC) ΔCO-based ΔffCO$_2$ observation every week collected on Tuesday (c) or Friday (d). Panel (e) shows the results if each day at 13 UTC one hypothetical flask is collected. In panel (f), the 7 afternoon flask observations within one week are averaged.

ΔffCO$_2$ estimates. However, there are differences like the shifted summer minimum in 2019. These differences can be explained by the variability of the ΔCO/ΔffCO$_2$ ratios that we fully neglected by using a constant mean ratio for constructing the ΔCO-based ΔffCO$_2$ record. Thus, when comparing the results with the TNO seasonality of emissions (grey histogram) it seems obvious that the ^{14}C-based ΔffCO$_2$ estimates provide the more accurate data than the subsampled ΔCO-based ΔffCO$_2$ record. However, the general similarity between both results means that we can use the continuous ΔCO-based ΔffCO$_2$ record to investigate an even data coverage with hypothetical flask samples collected in Heidelberg.

The middle panels in Fig. 6.3 show the inversion results if the ΔCO-based ΔffCO$_2$ record is subsampled for one flask every week on Tuesday (c) or on Friday afternoon (d), respectively. The increased number of evenly distributed weekly flasks strongly dampens the variability of the a-posteriori results. However, they show large differences depending on which day of the week the hypothetical afternoon flask was collected. Whereas the Tuesday flasks for example lead to a quite unrealistic gradual increase in the ffCO$_2$ emissions between January and November 2019, the Friday flasks show a more realistic seasonal cycle in this year. In contrast, both Tuesday and Friday flasks lead to an unexpected maximum in summer 2020. This implies that the a-posteriori results are still dependent on the selection of the individual hypothetical flasks. Therefore, it seems that even a uniform data coverage with a realistic flask sampling frequency of one flask per week is not sufficient to determine a plausible seasonal cycle of the area source ffCO$_2$ emissions around Heidelberg, as suggested by the TNO inventory. However, the situation should be better in the case of real, weekly ^{14}C flasks, as the average ΔCO/ΔffCO$_2$ ratio used to construct the ΔCO-based ΔffCO$_2$ record might be inappropriate for individual hours.

Finally, we investigated the benefit of an extremely high flask sampling frequency with one flask per afternoon (see Fig. 6.3e). Here, the a-posteriori results seem to approach towards the TNO bottom-up emissions in 2019. However, there are still unexpectedly strong deviations between the top-down and bottom-up estimates in the summer half-year 2020 for increased prior uncertainties. These differences might be caused by individual afternoon hours with a negative model-data mismatch in summer 2020. To reduce the impact of such hours, we perform a separate inversion run where we average the modelled and observational data of all 7 hypothetical afternoon flasks within each week (Fig. 6.3f). This further reduces the spread of a-posteriori results, particularly in summer 2020, further approaching towards the seasonal amplitude of the bottom-up TNO emissions. Thus, several afternoon flasks per week would be needed so that the influence of individual flasks on the inversion results can be averaged out and a plausible seasonal cycle amplitude in the area source ffCO$_2$ emissions around Heidelberg can be obtained.

Overall, these results show that the a-posteriori estimates are very sensitive to individual flask observations in this target region with very heterogeneously distributed ffCO$_2$ sources. Obviously, the transport model fails to appropriately simulate the ΔffCO$_2$ concentrations for individual afternoon hours. This can be explained by remaining shortcomings in the transport model but also by the enormous heterogeneity of the ffCO$_2$ emissions in the footprint of the Heidelberg observation site. As already mentioned in Sect. 6.2.2, modelling individual plumes from point source emissions is a particular challenge in this urban region, and e.g. the forward model estimates of point source signals, even with the improved VSI approach seem often incorrect, at least at a temporal resolution of one hour. Therefore, we decided to average the model results – and thus the observations – over multiple hours and therewith minimize the impact of individual hours with poor model performance (e.g. when an exhaust plume hits the observational station at a slightly displaced time).

6.3.2 Potential of continuous ΔCO-based ΔffCO$_2$ estimates to investigate the seasonal cycle in ffCO$_2$ emissions

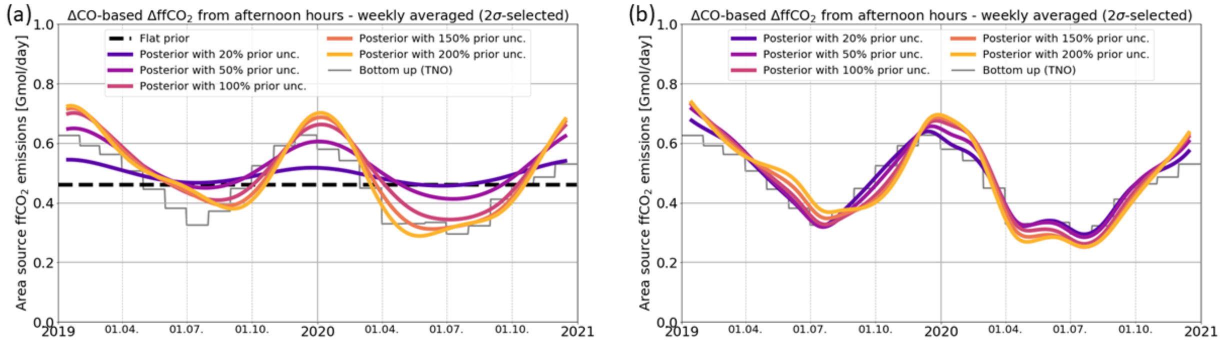

Figure 6.4 Area source ffCO$_2$ emissions in the nearfield (blue surrounded area in Fig. 6.1b) of Heidelberg. In (a) a flat prior (black dashed line) was used for the area source emissions and in (b) the monthly bottom-up estimates from TNO (grey line) were used as a-priori estimate. Shown are the a-posteriori emissions for different prior uncertainties between 20 and 200% (colored solid lines). The inversion was constrained with weekly averages of hourly, 2σ-selected afternoon ΔCO-based ΔffCO$_2$ observations from Heidelberg.

The big advantage of the continuous ΔCO-based ΔffCO$_2$ record is that it provides a full temporal coverage of the inversion period and can, thus, also be averaged such that the sensitivity of the a-posteriori results on individual (hourly) model-data mismatches is strongly reduced. In Appendix 6.6.1, we investigate if the averaging over the five (11 – 16 UTC) afternoon hours of the ΔCO-based ΔffCO_2 record is enough to sufficiently reduce the impact of the point source emissions on the a-posteriori area source emissions (see magenta curves in Fig. 6.6). For this, we perform in addition to the standard inversion runs with fixed point source emissions further sensitivity runs with adjustable point source emissions. Ideally, the a-posteriori area source emissions are identical for both inversion runs, meaning that the modelling of the well-known point source emissions has no impact on the area source emissions. However, depending on whether the point source emissions are being adjusted in the inversion framework or not, the a-posteriori area source ffCO_2 emissions can differ by more than 100% for individual seasons. Thus, an averaging interval of one afternoon only seems to be too short.

The averaging interval of one week strongly reduces the impact of the point sources on the a-posteriori area source emissions (see blue curves in Fig. 6.6). It limits the differences between the a-posteriori area source emissions of the inversion runs with fixed and adjustable point source emissions to below 30% for individual seasons. Averaged over the two years 2019 and 2020, these differences are below 10%. We also tested an extreme averaging interval of one month, which further reduces the difference between the respective a-posteriori area source emissions to below 20% for individual seasons (see pink curves in Fig. 6.6). However, such a long interval would lead to an averaging of very different meteorological situations, which reduces the temporal information of the observations. Therefore, we decided to apply in the following an averaging interval of one week, which is the typical length scale of synoptic weather patterns. The difference between the a-posteriori area source emissions of the inversion runs with fixed and adjustable point source emissions can be seen as an uncertainty estimate for the area source emissions due to imperfect point source modelling.

In the following, we use the weekly averaged afternoon ΔCO-based ΔffCO_2 observations to investigate the seasonal cycle of the area source ffCO_2 emissions around Heidelberg (see Fig. 6.4a). If the prior uncertainty is chosen large enough, the a-posteriori estimates agree the seasonal cycle amplitude of the TNO inventory reasonably well. Moreover, the data-driven inversion results distinctly show the effect of the COVID-19 restrictions with lower emissions in 2020 compared to 2019. In Southwestern Germany, the first COVID-19 lockdown started in mid-March 2020. Indeed, the inversion results show at that time a strong decrease in the area source ffCO_2 emissions. In particular, the decline in the a-posteriori ffCO_2 emissions is much steeper in spring 2020 compared to spring 2019 and the minimum of the seasonal cycle is flatter in 2020 as it extends over several summer months.

The agreement with the phasing of the seasonal cycle of the TNO inventory seems to be better in 2020 than in 2019. In 2020, TNO provides country-specific "COVID-19" seasonal cycles, which take into account the timing and the strength of the respective national restrictions. In Fig. 6.4 an average over the German and French seasonal cycle is shown, which seems to be confirmed by our observations. The shown TNO seasonal cycle for 2019 is a general European average estimate that is not specific for 2019. It assumes minimum emissions in July, whereas our observations show minimal emissions in August and September. Indeed, this shifted minimum of the seasonal cycle coincides with the summer holidays in Southwestern Germany, which are from August to mid-September.

We want to further investigate the consistency of the seasonal cycles from the bottom-up and the top-down estimates. For this, we explore the effect of applying the monthly TNO bottom-up seasonal cycle to the a-priori emissions (see Fig. 6.4b). As expected, the phase of the a-posteriori seasonal cycle is in agreement with the TNO inventory in 2020. However, in 2019 the a-priori information pulls the summer emission minimum to July. With weakening regularization of the prior the inversion algorithm tries to shift the minimum of the a-posteriori seasonal cycle from July towards August and September. Due to the limited temporal degrees of freedom of the inversion this shifting results in artificially increasing the emissions in May 2019 and lowering them in October. Hence, these results point to some inconsistencies in the seasonality of the TNO emissions in the main footprint of the Heidelberg observation site. In fact, a correct phasing of the fossil emissions is essential when prescribed ffCO_2 emissions are used in CO_2 model inversions to separate the fossil from the biogenic contribution in atmospheric CO_2 observations to constrain CO_2 fluxes from the biosphere.

Overall, the (weekly averaged) ΔCO-based ΔffCO_2 record seems to be well suited to estimate (and verify) the seasonal cycle of bottom-up ffCO_2 emissions in the nearfield of the Heidelberg observation site. This is a very promising result, especially considering how simple the ΔCO-based ΔffCO_2 record was constructed. It is based on the average ΔCO/ΔffCO_2 ratio estimated from ^{14}C measurements on flask samples where a potential seasonal cycle in the ΔCO/ΔffCO_2 ratios was fully neglected. In the following we investigate, among other possible error influences, the effect of a hypothetical seasonal cycle in the ΔCO/ΔffCO_2 ratios on the inversion results.

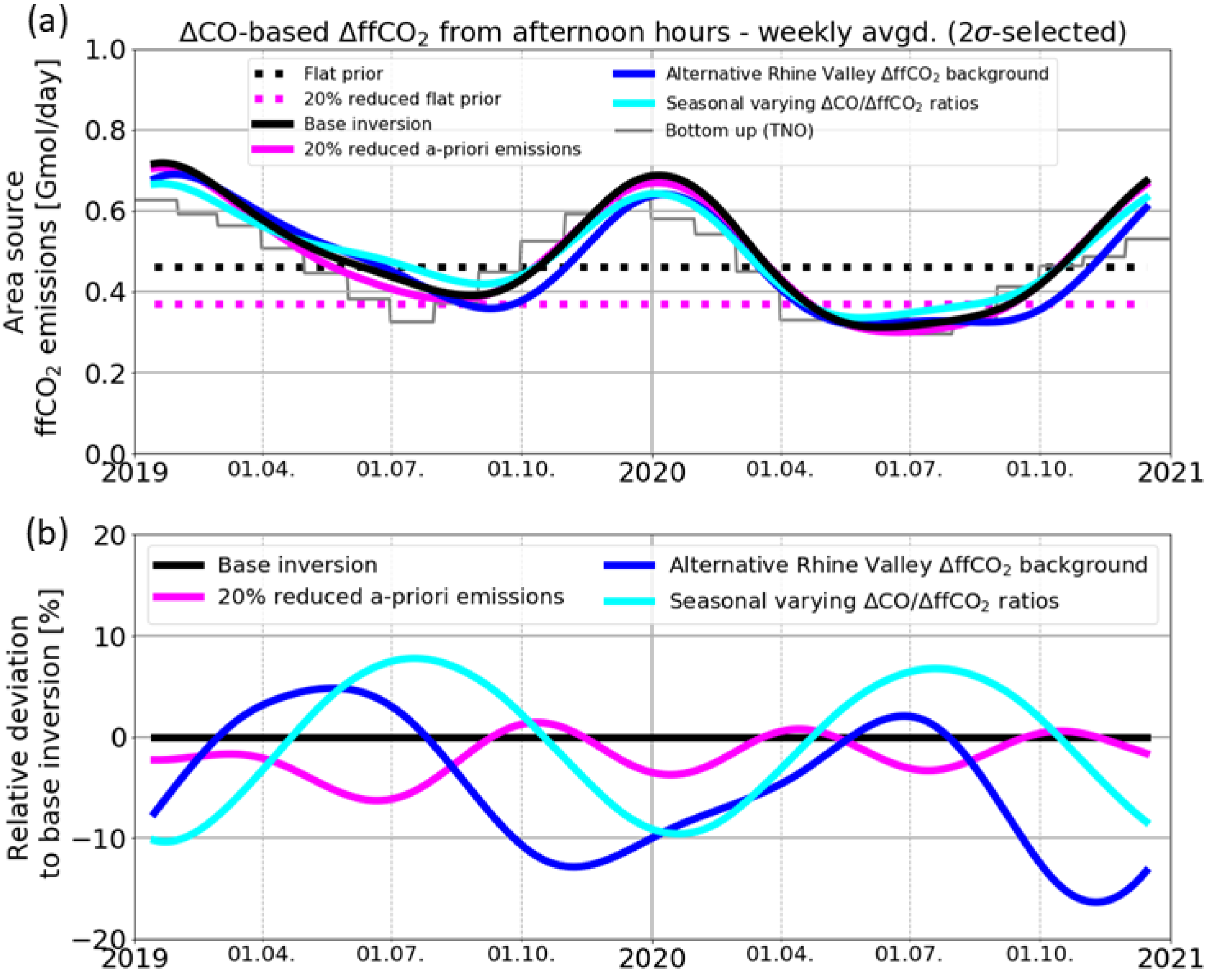

Figure 6.5 (a): Area source ffCO$_2$ emissions in the nearfield (blue surrounded area in Fig. 6.1b) of Heidelberg for different sensitivity runs. Shown are the a-posteriori results for 20% reduced flat a-priori emissions (solid magenta line), for an alternative Rhine Valley ΔffCO$_2$ background modelled with EDGAR emissions (blue) and for an assumed seasonal cycle in the ΔCO/ΔffCO$_2$ ratios (cyan, see Fig. 6.7). As a reference, the a-posteriori result of the base inversion from Fig. 6.4a is shown in black. All a-posteriori results correspond to a 150% prior uncertainty. The dotted lines indicate the flat prior emissions (black) and the by 20% reduced prior emissions (magenta). (b): Relative deviations between the different a-posteriori area source emissions of the sensitivity runs and the base inversion in %.

6.3.3 Robustness of the ΔCO-based ΔffCO_2 inversion results

In the following we want to investigate the robustness of the (weekly averaged) ΔCO-based ΔffCO_2 inversion results. For this, we (1) reduce the flat prior emissions by 20%, (2) assume a seasonal cycle in the ΔCO/ΔffCO_2 ratios, and (3) apply an alternative Rhine Valley ΔffCO_2 background. Figure 6.5 shows the respective a-posteriori results for a 150% prior uncertainty, which constitutes enough weighting on the (weekly averaged) ΔCO-based ΔffCO_2 observations to reconstruct the seasonal cycle from the flat a-priori area source ffCO_2 emissions (see Fig. 6.4a).

First, if the a-priori area source ffCO_2 emissions in the Rhine Valley domain are equally reduced by 20% (see dotted magenta curve in Fig. 6.5a), the ΔCO-based ΔffCO_2 inversion manages to compensate for almost all of this bias (compare the magenta curves with the black curves in Fig. 6.5). The deviations between the a-posteriori emissions of the inversion runs with perturbed and unperturbed flat prior emissions is typically below 5% for all seasons. Accordingly, the a-posteriori seasonal cycle of the ffCO_2 emissions is hardly affected by a potential bias in the flat prior emissions. The deviations between the annual totals of the a-posteriori estimates of the perturbed and unperturbed prior inversion runs is only 2% for both years. This means that on an annual scale about 90% of this 20%-bias in the perturbed flat prior could be corrected for.

With the second sensitivity test, we want to investigate the effect of the ΔCO/ΔffCO_2 ratios used to construct the ΔCO-based ΔffCO_2 record. For our base inversion, the ΔCO-based ΔffCO_2 record was constructed by using the average ΔCO/ΔffCO_2 ratio of 8.44 ppb/ppm, which was calculated from all flask samples collected in 2019 and 2020. However, as discussed in Maier et al. (2023a), the ratio during summer with lower signals is hard to determine and thus less constrained. The question is thus: How would our inversion results change if the ΔCO/ΔffCO_2 ratios would have a (small) seasonal cycle? For this, we assume a seasonal cycle in the ratios for the two years with 5% lower ratios in summer and correspondingly 5% larger ratios in winter, so that the two-year mean is still 8.44 ppb/ppm (see Fig. 6.7). Notice, that we use the ratios to calculate the Δff$CO_{2,\mathrm{MHD}}$ excess compared to the MHD background site and then subtract the modelled Rhine Valley Δff$CO_{2,\mathrm{CE-RV}}$ background to get the Δff$CO_{2,\mathrm{RV}}$ observations for our Rhine Valley inversion (see Eq. (6.1)). This effectively results in summer and winter ΔffCO_2 concentrations being more than 5% larger and lower, respectively, than the ΔffCO_2 concentrations based on the average ratio. Obviously, this leads to larger a-posteriori emissions (cyan curve in Fig. 6.5) during summer and lower emissions in winter compared to the base inversion results. The largest seasonal deviations to the base inversion a-posteriori emissions are 10%. Since by construction the mean of the seasonally varying ratios corresponds to the average ratio used for the base inversion, the effect on the annual totals of the a-posteriori $ffCO_2$ emissions is neglectable.

Finally, we investigate the impact of the lateral $\Delta ffCO_2$ boundaries on the area source $ffCO_2$ emissions estimates. For our base inversion, we used the high-resolution TNO emission inventory and WRF-STILT to model for the Heidelberg observation site the $\Delta ffCO_2$ contributions from the European STILT domain outside the Rhine Valley (see Sect. 6.2.2). For the following sensitivity run (blue curve in Fig. 6.5), we model the Rhine Valley $\Delta ffCO_2$ background with $ffCO_2$ emissions based on the Emissions Database for Global Atmospheric Research (EDGAR, Janssens-Maenhout et al., 2019) and use the coarser ECMWF meteorology in STILT. The application of this alternative Rhine Valley $\Delta ffCO_2$ background leads to more than 10% lower emissions in the autumn of both years, which can be explained by strong deviations between the weekly averages of the two modelled background concentrations during these periods (see Fig. 6.8). Thus, the Rhine Valley background affects the seasonal cycle of the area source $ffCO_2$ emissions. During summer, the deviations to the base inversion results are below 5%. The annual totals of the area source $ffCO_2$ emissions around Heidelberg are 3% and 7% lower in the years 2019 and 2020, respectively, if the alternative Rhine Valley $\Delta ffCO_2$ background is used.

6.4 Discussion

In the present study we investigate the potential of ^{14}C-based and ΔCO-based $\Delta ffCO_2$ observations to evaluate the $ffCO_2$ emissions and their seasonal cycle in an urban region around the Heidelberg observation site. This urban area is characterized by a complex topography and a large spatial heterogeneity in the $ffCO_2$ sources, including several nearby point sources. Thus, deficits in the transport model and inaccuracies in the driving meteorology strongly impact the model-data mismatch at the observation site, which will be minimized by the inversion algorithm. We focus on the estimation of the $ffCO_2$ emissions from area sources, since the observations from the Heidelberg site with an air intake height of 30 m above the ground are not suitable to constrain the emissions of nearby point sources with elevated stack heights. Indeed, the analysis of the $\Delta CO/\Delta ffCO_2$ ratios in Maier et al. (2023a) showed that the Heidelberg observation site is hardly influenced by pure point source emission plumes. Thus, we prescribe the well-known point source $ffCO_2$ emissions in the inversion setup and only adjust the area source emissions in the Rhine Valley domain.

6.4.1 Can flask-based ΔffCO$_2$ observations be used to predict the seasonal cycle of ffCO$_2$ emissions at an urban site?

To investigate the potential of ΔffCO$_2$ observations to predict the seasonal cycle of the area source ffCO$_2$ emissions around Heidelberg, we applied temporally constant (flat) a-priori ffCO$_2$ emissions in our inversion system, such that all seasonal information comes from the atmospheric data. We could show that ^{14}C-based ΔffCO$_2$ observations from almost 100 hourly flask samples collected in the two years 2019 and 2020 are not sufficient to reconstruct a robust seasonal cycle from the flat a-priori estimate. As the Bayesian inversion setup assumes a Gaussian distribution for the model-data mismatch, the inversion algorithm tries to primarily reduce the largest model-data differences. Therefore, we applied a 2σ selection to exclude the flask events with the largest model-data mismatches and thus worse model performances. However, the a-posteriori ffCO$_2$ emissions are still very sensitive to individual flask observations. Therefore, a strong regularization through small a-priori uncertainties (i.e. $< 50\%$ prior uncertainty, Fig. 6.3a) is needed to avoid large overfitting patterns in the inversion results.

By subsampling the ΔCO-based ΔffCO$_2$ record, we further investigate the potential of a uniform data coverage with one hypothetical afternoon flask per week to reliably estimate the seasonal cycle in the area source emissions. Indeed, several afternoon flask samples per week are needed, as well as an averaging of the flask observations within one week so that the overfitting of individual flask data is reduced. However, the situation should be better for real, e.g. sub-weekly, ^{14}C flasks compared to the subsampled ΔCO-based ΔffCO$_2$ record; as the applied average ΔCO/ΔffCO$_2$ ratio may be inappropriate for individual hours, this could amplify the overfitting of the individual hypothetical flasks. For the Heidelberg observation site where the flask sampling during our study period was rather irregularly, we used the ΔCO/ΔffCO$_2$ flask ratios to construct a continuous ΔCO-based ΔffCO$_2$ record (see Maier et al., 2023a) that, due to its high frequency could then be averaged in the inversion framework to explore the seasonal cycle of the ffCO$_2$ emissions.

6.4.2 What is an appropriate averaging interval for urban observations?

The main advantage of the ΔCO-based ΔffCO$_2$ record is its continuous data coverage that allows an averaging so that the influence of individual hours with poor model performance on the inversion results is strongly reduced. In this urban region, this is especially necessary because of the shortcomings in the STILT model and its driving meteorology to describe the transport and mixing of nearby point source emissions. Imagine that the plume of a point source arrives a few hours earlier or later at the observation site than simulated by STILT. In such cases, the averaging is inevitable to prevent a wrong adjustment of the $ffCO_2$ emissions. Moreover, the STILT-VSI approach itself has its deficits as it assumes mean effective emission height profiles for all meteorological situations and ignores the stack heights of individual power plants. Furthermore, the VSI approach still relies on a correct mixing in STILT. Whereas in Maier et al. (2022) we could show that the VSI approach strongly improves the agreement between modelled and observed $\Delta ffCO_2$ concentrations from two-week integrated samples, it thus still may overestimate the point source contributions for individual hours. Therefore, an averaging of the observations is very helpful when a transport model like STILT is used to describe the transport and mixing of nearby point source emissions.

In Appendix 6.6.1, we investigate how to appropriately average the observational data. Ideally, the a-posteriori area source $ffCO_2$ emissions are independent of a wrong modelling of the point source emissions. Thus, they should not be affected by whether the a-priori point source emissions are fixed or adjustable in the inversion framework. We showed that an averaging interval of one week limits the differences between the a-posteriori area source $ffCO_2$ emissions of the inversion runs with fixed and adjustable point source emissions, respectively, to below 30% for all seasons. This deviation can be used as a measure for the uncertainty of the a-posteriori area source $ffCO_2$ emissions that is induced by an inadequate modelling of the point source emissions.

A longer, e.g. monthly, averaging interval further reduces this difference, but comes along with an averaging over very different meteorological situations and thus reduces the spatiotemporal information comprised in the observations. This might be especially important if there are several observation sites, and the inversion system optimizes the $\Delta ffCO_2$ gradients between these different stations. The averaging interval of a week corresponds to the typical length scale of synoptic weather patterns. Therefore, a certain correlation between the observations within one week has anyhow to be considered in the inversion and the weekly averaging should, thus, not destroy too much information. In this study, we thus applied an averaging interval of one week as a compromise between reducing the impact of hours with an inadequate model performance and using as much observational information as possible.

6.4.3 What is the potential of ΔCO-based ΔffCO$_2$ to estimate the seasonal cycle in urban ffCO$_2$ emissions?

The potential of weekly averaged ΔCO-based ΔffCO$_2$ observations to explore the seasonal cycle of the ffCO$_2$ emissions in an urban region is very promising. In Heidelberg, we could reliably reconstruct the seasonal cycle from flat a-priori area source ffCO$_2$ emissions with the ΔCO-based ΔffCO$_2$ observations for increased prior uncertainties. We further could detect the COVID-19 signal in 2020, which is characterized by lower emissions compared to 2019 and a very steep decline in the emissions in spring 2020. In this latter year, the a-posteriori seasonal cycle agrees very well with the bottom-up seasonal cycle from TNO, where the timing of the COVID-19 restrictions has explicitly been considered. For 2019, TNO only provides a non-year-specific European average seasonal cycle, which has its annual minimum in July. In contrast, our ΔCO-based ΔffCO$_2$ observations suggest the 2019 minimum of the (restricted) Rhine Valley area source ffCO$_2$ emissions to be in August and September, when local summer holidays take place in that part of Germany. Even when we apply the bottom-up seasonal cycles from TNO to the flat a-priori ffCO$_2$ emissions the inversion system still tries to shift the minimum in 2019 from July into September. However, due to the limited temporal degrees of freedom in our inversion system, this comes along with artificially increased or decreased emissions in May and October 2019, respectively. Thus, this result of the Heidelberg inversion points to some inconsistencies in the seasonality of TNO emissions in the footprint of the station. A correct phasing of the fossil emissions is essential when prescribed ffCO$_2$ emissions and associated forward modelling results are used in atmospheric transport inversions to constrain the CO$_2$ fluxes from the biosphere.

In contrast to the inversion with flask-^{14}C-based ΔffCO$_2$ observations, the ΔCO-based ΔffCO$_2$ inversion allows a weakening of the regularization strength without generating unrealistic variabilities in the seasonal cycle of the ffCO$_2$ emissions. This implies that the a-posteriori results are less dependent on a potential bias in the a-priori emissions. Indeed, a sensitivity run with a 20% reduced flat prior estimate for the area source ffCO$_2$ emissions leads for sufficiently large prior uncertainties to similar results as the base inversion run with unperturbed prior estimate. Thus, the ΔCO-based ΔffCO$_2$ inversion is able to simultaneously reconstruct the seasonal cycle from a flat prior and correct a potential bias in the a-priori emissions.

However, the ΔCO-based ΔffCO$_2$ inversion results strongly depend on a potential bias in the ΔCO/ΔffCO$_2$ ratios that are applied to calculate the ΔffCO$_2$ estimates. Since there is no evidence for a strong seasonal cycle in the ΔCO/ΔffCO$_2$ ratios at the Heidelberg observation site, we used a constant average ΔCO/ΔffCO$_2$ ratio to calculate the ΔCO-based ΔffCO$_2$ record for the two years 2019 and 2020 (see Maier et al., 2023a). But due to the low signals and the weak correlation between ΔCO and ΔffCO$_2$ during summer, it is hard to determine separate summer ratios. Nevertheless, our results indicate that there might be a small seasonal cycle on the order of 5% in the ratio. In this study, we could show that a hypothetical seasonal cycle with 5% lower and 5% larger ratios in summer and winter, respectively, would lead to changes in the area source ffCO$_2$ emissions of up to 10% for individual seasons. This emphasizes the importance of a thorough determination of the ΔCO/ΔffCO$_2$ ratios to prevent biases in estimates of total fluxes and the seasonal cycle of the ffCO$_2$ emissions.

Indeed, we are currently in a kind of a fortunate situation in Heidelberg, since the emission ratios of the traffic and heating sectors seem to be quite similar in the main footprint of the station (see Maier et al., 2023a). Hence, despite the varying share of traffic and heating over the course of a year, this simply allowed the usage of a constant average flask-based ΔCO/ΔffCO$_2$ ratio for constructing the ΔCO-based ΔffCO$_2$ record. Of course, it is much more challenging to determine continuous ΔCO-based ΔffCO$_2$ estimates for stations where the ΔCO/ΔffCO$_2$ ratios show large seasonal or even diurnal variabilities.

A common challenge in regional inversions is the determination of the lateral boundary conditions (Munassar et al., 2023). In this study, we used two different emission inventories and meteorological fields to estimate the ΔffCO$_2$ background for the Rhine Valley domain by modelling the contributions from the Central European ffCO$_2$ emissions outside the Rhine Valley. For individual seasons the a-posteriori area source ffCO$_2$ emissions around Heidelberg can differ by more than 10%. This highlights the strong need for appropriate boundary conditions. In Europe, the Integrated Carbon Observation System (ICOS, Heiskanen et al., 2022) provides high-quality atmospheric in-situ data from a network of tall-tower stations that cover a large part of the European continent. These observations may help to verify the ffCO$_2$ emissions in Europe. Then, the optimized European ffCO$_2$ emissions could be used to estimate more reliably the ΔffCO$_2$ background for the Rhine Valley domain.

Overall, our results demonstrate that the weekly averaged ΔCO-based ΔffCO$_2$ observations are currently well suited to investigate the amplitude and the phasing of the seasonal cycle of the area source ffCO$_2$ emissions in the main footprint of the Heidelberg observation site. The different sensitivity runs suggest that ΔCO-based ΔffCO$_2$ allows a reconstruction of this seasonal cycle from temporally constant a-priori estimates with an uncertainty of below ca.

30% for all seasons. Thus, one may recommend applying this ΔCO-based ΔffCO$_2$ inversion at further urban sites with a strong heterogeneity in the local ffCO$_2$ sources if the ΔCO/ΔffCO$_2$ ratios can be determined accurately.

6.5 Conclusions

This study illustrates the strong potential of continuous ΔCO-based ΔffCO$_2$ observations to determine the seasonal cycle of ffCO$_2$ emissions in an urban region with highly heterogeneous ffCO$_2$ sources in its vicinity. The ability of averaging and thus reducing the influence of individual hours with an inadequate model performance makes ΔCO-based ΔffCO$_2$, despite its larger uncertainty, currently a better tracer than discrete ^{14}C-based ΔffCO$_2$ from weekly flasks for estimating the seasonal cycle of the area source ffCO$_2$ emissions in the Upper Rhine Valley around the urban Heidelberg observation site.

For our study, we set up the CarboScope inversion system in the Rhine Valley. It is based on the high-resolution WRF-STILT model and uses the STILT volume source influence (VSI) approach developed in Maier et al. (2022) to represent the emission heights of point sources. However, despite the high-resolution WRF meteorology and the improved STILT-VSI approach, almost 100 ^{14}C-based ΔffCO$_2$ estimates from flasks collected in Heidelberg during the two years 2019 and 2020 are insufficient to robustly estimate seasonal cycles of the area source ffCO$_2$ emissions in the main footprint of the site. Indeed, it seems that several flasks per week would be needed, so that the flask observations within one week could be averaged and overfitting of individual flask observations be prevented.

Due to the fortunate circumstance of currently having similar heating and traffic emission ratios in the main footprint of Heidelberg, we could use the average ^{14}C-based ΔCO/ΔffCO$_2$ ratio from the flasks to construct a continuous ΔCO-based ΔffCO$_2$ record (see Maier et al., 2023a). The weekly averaging of this ΔCO-based ΔffCO$_2$ record strongly reduces the impact of hours with an inadequate modelling on the a-posteriori ffCO$_2$ emissions. In fact, the weekly averaged ΔCO-based ΔffCO$_2$ observations can robustly reconstruct the amplitude and the phasing of the seasonal cycle of the ffCO$_2$ area source emissions even from temporally constant a-priori emissions. In particular, the observational data clearly contain the distinct COVID-19 signal in 2020, which is characterized by overall lower emissions compared to 2019 and a steep drop in emissions in spring 2020 with the onset of the restrictions. Moreover, the comparison with the bottom-up emissions from TNO points to some inconsistencies in the TNO seasonality of the area source ffCO$_2$ emissions in the footprint of Heidelberg in 2019.

Overall, our sensitivity runs suggest that we can reconstruct the seasonal cycle of the ffCO_2 area source emissions around Heidelberg with an uncertainty of below ca. 30%. Therefore, one may recommend applying the ΔCO-based ΔffCO_2 inversion at further urban sites with heterogeneous ffCO_2 sources, if the ΔCO/ΔffCO_2 ratios can be estimated accurately. If ratios from bottom-up inventories are not trusted or the urban region is influenced by CO emissions from the biosphere, the ratios are most reliably calculated from ^{14}C flasks. Then, at least some of the summer ^{14}C flasks should be collected during situations with significant CO and ffCO_2 signals, so that a possible seasonal cycle in the ΔCO/ΔffCO_2 ratios could be identified. At remote sites, such as at several ICOS atmosphere stations, with low ffCO_2 signals and predominant biosphere influence the calculation of ΔCO/ΔffCO_2 ratios and the construction of a bias-free ΔCO-based ΔffCO_2 record might be more challenging than at an urban site. However, the model performance is expected to be better at remote sites with a typically higher air intake above the ground and a much lower heterogeneity in the surrounding ffCO_2 sources with minor influences from nearby point sources. Consequently, the outcome of our urban study cannot directly be transferred to remote sites; further studies are needed to investigate the potential of ^{14}C-based versus ΔCO-based ΔffCO_2 to estimate ffCO_2 emissions at such sites.

6.6 Appendix

6.6.1 A1. Impact of point sources on the a-posteriori area source ffCO_2 emissions

To investigate the influence of inadequate point source modelling on the a-posteriori area source ffCO_2 emissions, we use two different ΔCO-based ΔffCO_2 inversion setups: (1) an inversion with fixed point source emissions (“INV_fix”) and (2) an inversion with adjustable point source emissions (“INV_adj”). The first inversion setup corresponds to the inversion described in Sect. 6.2.2. It optimizes the flat a-priori area source emissions by using fixed monthly point source emissions. The second inversion setup optimizes both, the flat a-priori area source emissions, and the monthly a-priori point source emissions. Thereby, the point source emissions from the energy production and the industry sector, respectively, get the same temporal (i.e. “Filt3T” in CarboScope notation, see Sect. 6.2.2) and spatial (i.e. one spatial scaling factor) degrees of freedom like the area source emissions.

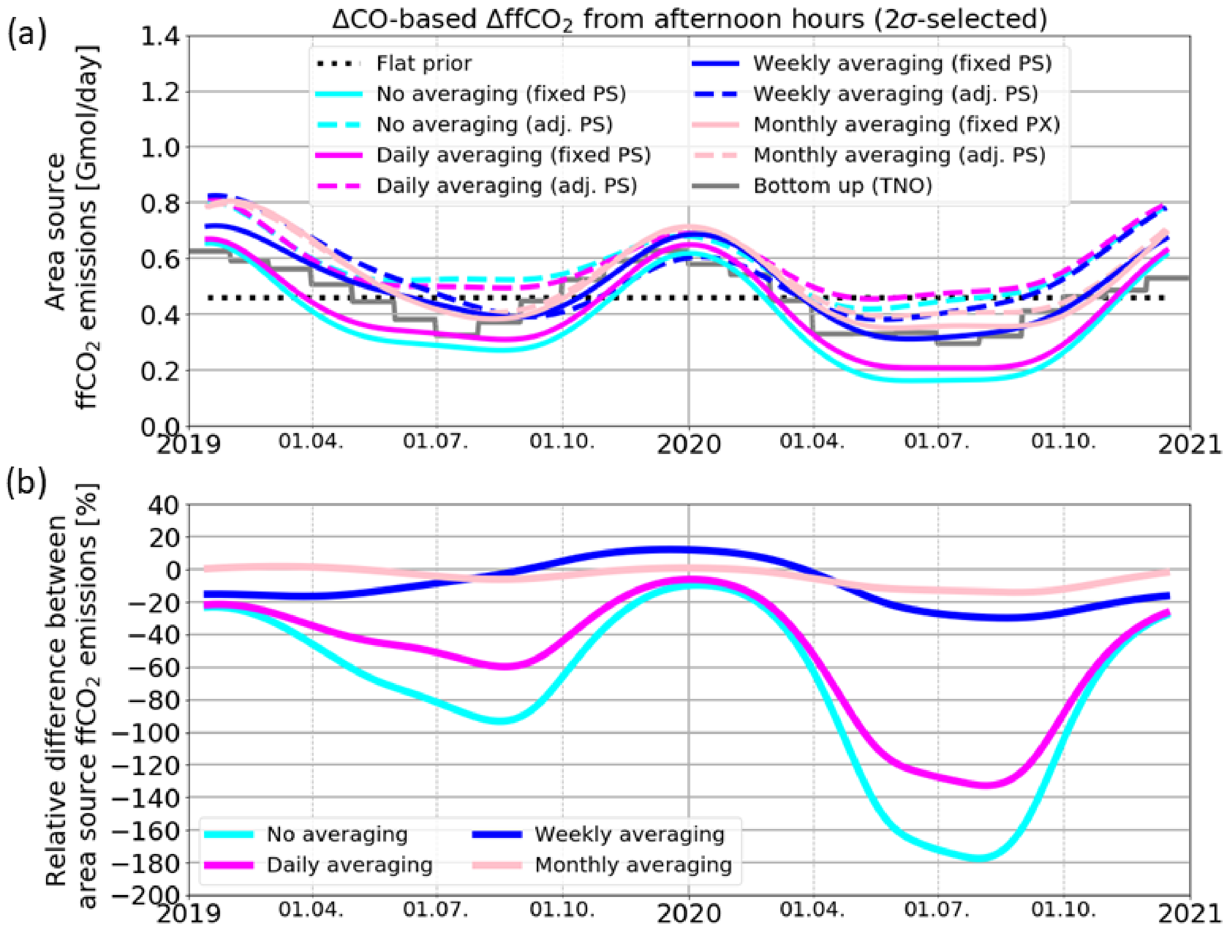

Figure 6.6 (a): Area source ffCO_2 emissions in the nearfield (blue surrounded area in Fig. 1b) of Heidelberg. Shown are the results of the ΔCO-based ΔffCO_2 inversion with fixed point sources (solid lines, "fixed PS") and adjustable point sources (dashed lines, "adj. PS") for different averaging intervals ranging from no averaging at all (cyan) to daily averaging of the five hours of each afternoon (magenta) and weekly (blue) and monthly (pink) averaging. All a-posteriori results correspond to a 150% prior uncertainty. The flat a-priori emissions and the bottom-up emissions are shown as a reference in black and grey, respectively. (b): Relative differences (fixed PS minus adj. PS) between the a-posteriori area source ffCO_2 emissions of the inversion runs with adjustable and fixed point source emissions in %.

Ideally, both inversion setups should lead to the same a-posteriori area source emissions, meaning that the modelling of the well-known point source emissions has no influence on the area source emission estimates. Obviously, this is not the case. If the model-data mismatches of the individual afternoon hours of the ΔCO-based ΔffCO_2 record are not averaged, the INV_fix inversion leads to much lower area source emissions estimates than the INV_adj inversion (see cyan curves in Fig. 6.6). For individual seasons, e.g. in summer 2020, the differences are larger than 150%. Thus, the INV_fix inversion tends to decrease the area source emissions to compensate for an inadequate modelling of the (fixed) point source emissions. This shows that even with the VSI approach the model seems to overestimate the contributions from point sources at the Heidelberg observation site for individual hours.

The averaging over one afternoon (magenta curve in Fig. 6.6) leads only to minor improvements; there are still deviations larger than 100% in summer 2020. In contrast, the averaging interval of one week (blue curve) limits the largest deviations in summer 2020 to below 30%. Averaged over the two years 2019 and 2020, these deviations between the INV_fix and INV_adj a-posteriori area source emissions are even less than 10%. A monthly averaging interval (pink curve) further reduces the deviations to below 20% in summer 2020.

6.6.2 A2. Hypothetical seasonal cycle in the ΔCO/ΔffCO_2 ratios

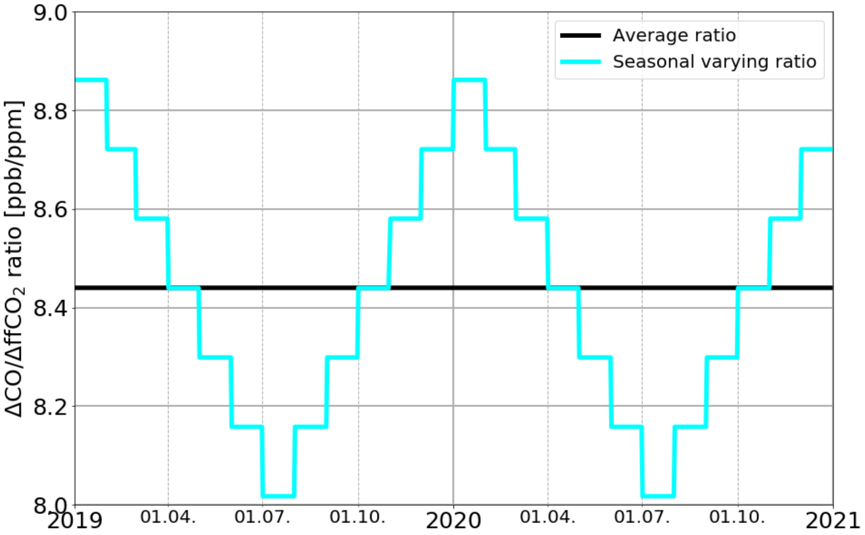

Figure 6.7 Average ΔCO/ΔffCO_2 ratio (black) and hypothetical seasonal varying ratio (cyan) used to construct the ΔCO-based ΔffCO_2 record for the base inversion (Fig. 6.4) and the sensitivity inversion run (cyan curve in Fig. 6.5), respectively.

6.6.3 A3. Comparison between two modelled Rhine Valley ΔffCO$_2$ backgrounds

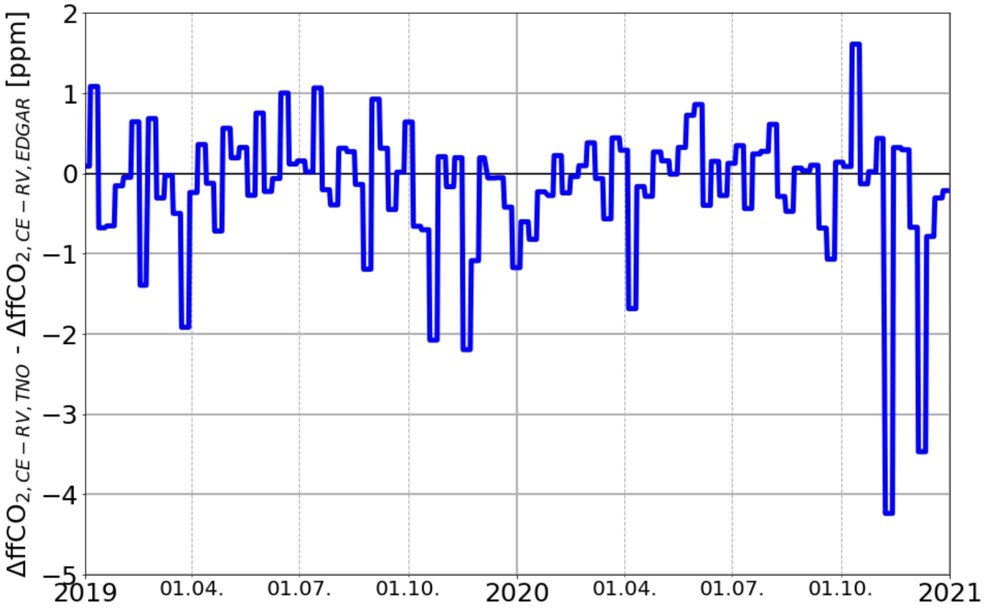

Figure 6.8 Difference between the Rhine Valley background modelled with TNO emissions (ΔffCO$_{2,\mathrm{CE-RV,TNO}}$) and the Rhine Valley background modelled with EDGAR emissions (ΔffCO$_{2,\mathrm{CE-RV,EDGAR}}$). Shown are weekly averages for afternoon situations.

6.7 References

Andres, R. J., Boden, T. A., Bréon, F.-M., Ciais, P., Davis, S., Erickson, D., Gregg, J. S., Jacobson, A., Marland, G., Miller, J., Oda, T., Olivier, J. G. J., Raupach, M. R., Rayner, P., and Treanton, K.: A synthesis of carbon dioxide emissions from fossil-fuel combustion, Biogeosciences, 9, 1845–1871, `https://doi.org/10.5194/bg-9-1845-2012`, 2012.

Basu, S., Lehman, S. J., Miller, J. B., Andrews, A. E., Sweeney, C., Gurney, K. R., Xue, X., Southon, J., and Tans, P. P.: Estimating US fossil fuel CO$_2$ emissions from measurements of ^{14}C in atmospheric CO$_2$, PNAS 117(24): 13300–13307, `https://doi.org/10.1073/pnas.1919032117`, 2020.

Bergamaschi, P., Danila, A., Weiss, R. F., Ciais, P., Thompson, R. L., Brunner, D., Levin, I., Meijer, Y., Chevallier, F., Janssens-Maenhout, G., Bovensmann, H., Crisp, D., Basu, S., Dlugokencky, E., Engelen, R., Gerbig, C., Günther, D., Hammer, S., Henne, S., Houweling, S., Karstens, U., Kort, E., Maione, M., Manning, A. J., Miller, J., Montzka, S., Pandey, S., Peters, W., Peylin, P., Pinty, B., Ramonet, M., Reimann, S., Röckmann, T., Schmidt, M., Strogies, M., Sussams, J., Tarasova, O., van Aardenne, J., Vermeulen, A. T., and Vogel, F.: Atmospheric monitoring and inverse modelling for verification of greenhouse gas inventories, EUR 29276 EN, Publications Office of the European Union, Luxembourg, ISBN 978-92-79-88938-7, JRC111789, `https://doi.org/10.2760/759928`, 2018.

Ciais, P., D. Crisp, H. Denier Van Der Gon, R. Engelen, M. Heimann, G. Janssens-Maenhout, P. Rayner, and M. Scholze: Towards a European Operational Observing System to Monitor Fossil CO_2 Emissions. Final Report from the Expert Group, European Commission, October 2015, ISBN 978-92-79- 53482-9, doi:10.2788/350433, 2015. Available at `https://www.copernicus.eu/sites/default/files/2019-09/CO2_Blue_report_2015.pdf`, Last access: December 01, 2022.

Currie, L. A.: The remarkable metrological history of radiocarbon dating [II], J. Res. Natl. Inst. Stand. Technol., 109(2), 185-217, `https://doi.org/10.6028/jres.109.013`, 2004.

Dellaert, S., Super, I., Visschedijk, A., and Denier van der Gon, H.: High resolution scenarios of CO_2 and CO emissions, CHE deliverable D4.2, 2019. Available at `https://www.che-project.eu/sites/default/files/2019-05/CHE-D4-2-V1-0.pdf`, Last access: March 28, 2023.

Denier van der Gon, H., Kuenen, J., Boleti, E., Maenhout, G., Crippa, M., Guizzardi, D., Marshall, J., and Haussaire, J.: Emissions and natural fluxes Dataset, CHE deliverable D2.3, 2019. Available at `https://www.che-project.eu/sites/default/files/2019-02/CHE-D2-3-V1-1.pdf`, Last access: March 28, 2023.

Duren, R., and Miller, C.: Measuring the carbon emissions of megacities, Nature Clim Change 2, 560–562, `https://doi.org/10.1038/nclimate1629`, 2012.

Friedlingstein, P., O'Sullivan, M., Jones, M. W., Andrew, R. M., Gregor, L., Hauck, J., Le Quéré, C., Luijkx, I. T., Olsen, A., Peters, G. P., Peters, W., Pongratz, J., Schwingshackl, C., Sitch, S., Canadell, J. G., Ciais, P., Jackson, R. B., Alin, S. R., Alkama, R., Arneth, A., Arora, V. K., Bates, N. R., Becker, M., Bellouin, N., Bittig, H. C., Bopp, L., Chevallier, F., Chini, L. P., Cronin, M., Evans, W., Falk, S., Feely, R. A., Gasser, T., Gehlen, M., Gkritzalis, T., Gloege, L., Grassi, G., Gruber, N., Gürses, Ö., Harris, I., Hefner, M., Houghton, R. A., Hurtt, G. C., Iida, Y., Ilyina, T., Jain, A. K., Jersild, A., Kadono, K., Kato, E., Kennedy, D., Klein Goldewijk, K., Knauer, J., Korsbakken, J. I., Landschützer, P., Lefèvre, N., Lindsay, K., Liu, J., Liu, Z., Marland, G., Mayot, N., McGrath, M. J., Metzl, N., Monacci, N. M., Munro, D. R., Nakaoka, S.-I., Niwa, Y., O'Brien, K., Ono, T., Palmer, P. I., Pan, N., Pierrot, D., Pocock, K., Poulter, B., Resplandy, L., Robertson, E., Rödenbeck, C., Rodriguez, C., Rosan, T. M., Schwinger, J., Séférian, R., Shutler, J. D., Skjelvan, I., Steinhoff, T., Sun, Q., Sutton, A. J., Sweeney, C., Takao, S., Tanhua, T., Tans, P. P., Tian, X., Tian, H., Tilbrook, B., Tsujino, H., Tubiello, F., van der Werf, G. R., Walker, A. P., Wanninkhof, R., Whitehead, C., Willstrand Wranne, A., Wright, R., Yuan, W., Yue, C., Yue, X., Zaehle, S., Zeng, J., and Zheng, B.: Global Carbon Budget 2022, Earth Syst. Sci. Data, 14, 4811–4900, `https://doi.org/10.5194/essd-14-4811-2022`, 2022.

Gamnitzer, U., Karstens, U., Kromer, B., Neubert, R. E. M., Meijer, H. A. J., Schroeder, H., and Levin, I.: Carbon monoxide: A quantitative tracer for fossil fuel CO_2?, J. Geophys. Res., 111, D22302, `https://doi.org/10.1029/2005JD006966`, 2006.

Graven, H., Fischer, M. L., Lueker, T., Jeong, S., Guilderson, T. P., Keeling, R. F., Bambha, R., Brophy, K., Callahan, W., Cui, X., Frankenberg, C., Gurney, K. R., LaFranchi, B. W., Lehman, S. J., Michelsen, H., Miller, J. B., Newman, S., Paplawsky, W., Parazoo, N. C., Sloop, C., and Walker, S. J.: Assessing fossil fuel CO_2 emissions in California using atmospheric observations and models, Environ. Res. Lett., 13, 065007, `https://dx.doi.org/10.1088/1748-9326/aabd43`, 2018.

Hammer, S.: Quantification of the regional H_2 sources and sinks inferred from atmospheric trace gas variability, PhD Thesis, University of Heidelberg, 2008.

Heiskanen, J., Brümmer, C., Buchmann, N., Calfapietra, C., Chen, H., Gielen, B., Gkritzalis, T., Hammer, S., Hartman, S., Herbst, M., Janssens, I. A., Jordan, A., Juurola, E., Karstens, U., Kasurinen, V., Kruijt, B., Lankreijer, H., Levin, I., Linderson, M., Loustau, D., Merbold, L., Myhre, C. L., Papale, D., Pavelka, M., Pilegaard, K., Ramonet, M., Rebmann, C., Rinne, J., Rivier, L., Saltikoff, E., Sanders, R., Steinbacher, M., Steinhoff, T., Watson, A., Vermeulen, A. T., Vesala, T., Vítková, G., and Kutsch, W.: The Integrated Carbon Observation System in Europe, Bulletin of the American Meteorological Society, 103(3), E855-E872, `https://doi.org/10.1175/BAMS-D-19-0364.1`, 2022.

Hersbach, H., Bell, B., Berrisford, P., Hirahara, S., Horányi, A., Muñoz-Sabater, J., Nicolas, J., Peubey, C., Radu, R., Schepers, D., Simmons, A., Soci, C., Abdalla, S., Abellan, X., Balsamo, G., Bechtold, P., Biavati, G., Bidlot, J., Bonavita, M., De Chiara, G., Dahlgren, P., Dee, D., Diamantakis, M., Dragani, R., Flemming, J., Forbes, R., Fuentes, M., Geer, A., Haimberger, L., Healy, S., Hogan, R. J., Hólm, E., Janisková, M., Keeley, S., Laloyaux, P., Lopez, P., Lupu, C., Radnoti, G., de Rosnay, P., Rozum, I., Vamborg, F., Villaume, S., and Thépaut, J.-N.: The ERA5 global reanalysis, Q J R Meteorol Soc., 146, 1999–2049, `https://doi.org/10.1002/qj.3803`, 2020.

Janssens-Maenhout, G., Crippa, M., Guizzardi, D., Muntean, M., Schaaf, E., Dentener, F., Bergamaschi, P., Pagliari, V., Olivier, J. G. J., Peters, J. A. H. W., van Aardenne, J. A., Monni, S., Doering, U., Petrescu, A. M. R., Solazzo, E., and Oreggioni, G. D.: EDGAR v4.3.2 Global Atlas of the three major greenhouse gas emissions for the period 1970–2012, Earth Syst. Sci. Data, 11, 959–1002, `https://doi.org/10.5194/essd-11-959-2019`, 2019.

Jiang, F., Chen, J. M., Zhou, L., Ju, W., Zhang, H., Machida, T., Ciais, P., Peters, W., Wang, H., Chen, B., Liu, L., Zhang, C., Matsueda, H., and Sawa, Y.: A comprehensive estimate of recent carbon sinks in China using both top-down and bottom-up approaches, Sci. Rep. 6, 22130, `https://doi.org/10.1038/srep22130`, 2016.

Lauvaux, T., Miles, N. L., Deng, A., Richardson, S. J., Cambaliza, M. O., Davis, K. J., Gaudet, B., Gurney, K. R., Huang, J., O'Keefe, D., Song, Y., Karion, A., Oda, T., Patarasuk, R., Razlivanov, I., Sarmiento, D., Shepson, P., Sweeney, C., Turnbull, J., and Wu, K.: High-resolution atmospheric inversion of urban CO_2 emissions during the dormant season of the Indianapolis Flux Experiment (INFLUX), J. Geophys. Res. Atmos., 121, 5213– 5236, `https://doi.org/10.1002/2015JD024473`, 2016.

Levin, I., Kromer, B., Schmidt, M., and Sartorius, H.: A novel approach for independent budgeting of fossil fuel CO_2 over Europe by $^{14}CO_2$ observations, Geophys. Res. Lett., 30 (23), 2194, `https://doi.org/10.1029/2003GL018477`, 2003.

Levin, I. and Karstens, U.: Inferring high-resolution fossil fuel CO_2 records at continental sites from combined $^{14}CO_2$ and CO observations, Tellus B, 59, 245-250. `https://doi.org/10.1111/j.1600-0889.2006.00244.x`, 2007.

Lin, J. C., Gerbig, C., Wofsy, S. C., Andrews, A. E., Daube, B. C., Davis, K. J., and Grainger, C. A.: A near-field tool for simulating the upstream influence of atmospheric observations: The Stochastic Time-Inverted Lagrangian Transport (STILT) model, J. Geophys. Res., 108, 4493, `https://doi.org/10.1029/2002JD003161`, 2003.

Liu, J., Baskaran, L., Bowman, K., Schimel, D., Bloom, A. A., Parazoo, N. C., Oda, T., Carroll, D., Menemenlis, D., Joiner, J., Commane, R., Daube, B., Gatti, L. V., McKain, K., Miller, J., Stephens, B. B., Sweeney, C., and Wofsy, S.: Carbon Monitoring System Flux Net Biosphere Exchange 2020 (CMS-Flux NBE 2020), Earth Syst. Sci. Data, 13, 299–330, `https://doi.org/10.5194/essd-13-299-2021`, 2021.

Maier, F., Gerbig, C., Levin, I., Super, I., Marshall, J., and Hammer, S.: Effects of point source emission heights in WRF–STILT: a step towards exploiting nocturnal observations in models, Geosci. Model Dev., 15, 5391–5406, `https://doi.org/10.5194/gmd-15-5391-2022`, 2022.

Maier, F., and co-authors: Uncertainty of continuous ΔCO-based ΔffCO_2 estimates derived from ^{14}C flask and bottom-up ΔCO/ΔffCO_2 ratios, 2023a [to be submitted, see Ch. 5].

Maier, F., Levin, I., Gachkivskyi, M., Rödenbeck, C., and Hammer, S.: Estimating regional fossil-fuel CO_2 concentrations from $^{14}CO_2$ observations: Challenges and uncertainties, Phil. Trans. R. Soc. A, `https://doi.org/10.1098/rsta.2022.0203` [link not yet available], 2023b [approved for publication].

Monteil, G., Broquet, G., Scholze, M., Lang, M., Karstens, U., Gerbig, C., Koch, F.-T., Smith, N. E., Thompson, R. L., Luijkx, I. T., White, E., Meesters, A., Ciais, P., Ganesan, A. L., Manning, A., Mischurow, M., Peters, W., Peylin, P., Tarniewicz, J., Rigby, M., Rödenbeck, C., Vermeulen, A., and Walton, E. M.: The regional European atmospheric transport inversion comparison, EUROCOM: first results on European-wide terrestrial carbon fluxes for the period 2006–2015, Atmos. Chem. Phys., 20, 12063–12091, `https://doi.org/10.5194/acp-20-12063-2020`, 2020.

Munassar, S., Monteil, G., Scholze, M., Karstens, U., Rödenbeck, C., Koch, F.-T., Totsche, K. U., and Gerbig, C.: Why do inverse models disagree? A case study with two European CO_2 inversions, Atmos. Chem. Phys., 23, 2813–2828, `https://doi.org/10.5194/acp-23-2813-2023`, 2023.

Nehrkorn, T., Eluszkiewicz, J., Wofsy, S. C., Lin, J. C., Gerbig, C., Longo, M., Freitas, S.: Coupled weather research and forecasting–stochastic time-inverted lagrangian transport (WRF–STILT) model. Meteorol. Atmos. Phys. 107, 51–64, `https://doi.org/10.1007/s00703-010-0068-x`, 2010.

Newsam, G. N. and Enting, I. G.: Inverse problems in atmospheric constituent studies: I. Determination of surface sources under a diffusive transport approximation, Inverse Problems, 4, 1037–1054, 1988.

Peylin, P., Law, R. M., Gurney, K. R., Chevallier, F., Jacobson, A. R., Maki, T., Niwa, Y., Patra, P. K., Peters, W., Rayner, P. J., Rödenbeck, C., van der Laan-Luijkx, I. T., and Zhang, X.: Global atmospheric carbon budget: results from an ensemble of atmospheric CO_2 inversions, Biogeosciences, 10, 6699–6720, `https://doi.org/10.5194/bg-10-6699-2013`, 2013.

Rödenbeck, C., Houweling, S., Gloor, M., and Heimann, M.: CO_2 flux history 1982–2001 inferred from atmospheric data using a global inversion of atmospheric transport, Atmos. Chem. Phys., 3, 1919–1964, `https://doi.org/10.5194/acp-3-1919-2003`, 2003.

Rödenbeck, C.: Estimating CO_2 sources and sinks from atmospheric mixing ratio measurements using a global inversion of atmospheric transport, Tech. Rep. 6, Max Planck Institute for Biogeochemistry, Jena, Germany, 2005.

Rödenbeck, C., Gerbig, C., Trusilova, K., and Heimann, M.: A two-step scheme for high-resolution regional atmospheric trace gas inversions based on independent models, Atmos. Chem. Phys., 9, 5331–5342, `https://doi.org/10.5194/acp-9-5331-2009`, 2009.

Rödenbeck, C., Zaehle, S., Keeling, R., and Heimann, M.: How does the terrestrial carbon exchange respond to interannual climatic variations? A quantification based on atmospheric CO_2 data, Biogeosciences, 15, 1–18, `https://doi.org/10.5194/bg-15-1-2018`, 2018.

Super, I., Dellaert, S. N. C., Visschedijk, A. J. H., and Denier van der Gon, H. A. C.: Uncertainty analysis of a European high-resolution emission inventory of CO_2 and CO to support inverse modelling and network design, Atmos. Chem. Phys., 20, 1795–1816, `https://doi.org/10.5194/acp-20-1795-2020`, 2020.

Turnbull, J. C., Miller, J. B., Lehman, S. J., Tans, P. P., Sparks, R. J., and Southon, J.: Comparison of $^{14}CO_2$, CO, and SF_6 as tracers for recently added fossil fuel CO_2 in the atmosphere and implications for biological CO_2 exchange, Geophys. Res. Lett., 33, L01817, `https://doi.org/10.1029/2005GL024213`, 2006.

Van Der Laan, S., Karstens, U., Neubert, R. E. M., Van Der Laan-Luijkx, I. T., and Meijer, H. A. J.: Observation-based estimates of fossil fuel-derived CO_2 emissions in the Netherlands using Δ14C, CO and ^{222}Radon, Tellus B: Chemical and Physical Meteorology, 62,5, 389-402, `https://doi.org/10.1111/j.1600-0889.2010.00493.x`, 2010.

Vogel, F., Hammer, S., Steinhof, A., Kromer, B., and Levin, I.: Implication of weekly and diurnal ^{14}C calibration on hourly estimates of CO-based fossil fuel CO_2 at a moderately polluted site in southwestern Germany, Tellus B: Chemical and Physical Meteorology, 62, 5, 512-520, `https://doi.org/10.1111/j.1600-0889.2010.00477.x`, 2010.

Wang, Y., Broquet, G., Ciais, P., Chevallier, F., Vogel, F., Wu, L., Yin, Y., Wang, R., and Tao, S.: Potential of European $^{14}CO_2$ observation network to estimate the fossil fuel CO_2 emissions via atmospheric inversions, Atmos. Chem. Phys., 18, 4229–4250, `https://doi.org/10.5194/acp-18-4229-2018`, 2018.

CHAPTER 7

Discussion

7.1 Context of this thesis

Bottom-up $ffCO_2$ emissions are often prescribed in atmospheric transport inversions to deduce from atmospheric CO_2 observations the potentially less known natural CO_2 fluxes from the biosphere or the oceans (e.g., Rödenbeck et al., 2003; Peylin et al., 2013; Jiang et al., 2016; Rödenbeck et al., 2018; Monteil et al., 2020, Liu et al., 2021). In particular, the estimation of the seasonal (or diurnal) cycle of the biospheric CO_2 emissions relies on accurate temporal profiles in the bottom-up $ffCO_2$ emissions. With the ongoing reduction of the measurement uncertainties and a growing spatiotemporal availability, $^{14}CO_2$ observations have been used to estimate $ffCO_2$ emissions directly and to verify bottom-up $ffCO_2$ emissions (Basu et al., 2020). Accordingly, several observation system simulation experiments (OSSEs) have been performed to assess the potential of $^{14}CO_2$ in constraining monthly $ffCO_2$ emissions from national scale to urban regions (Basu et al., 2016; Kunik et al., 2019), and to investigate the benefit of different $^{14}CO_2$ observation networks and sampling strategies (Wang et al., 2018).

So far, inversions with real $^{14}CO_2$ observations have mainly been conducted on continental or national scales. Basu et al. (2020) used $^{14}CO_2$ and CO_2 flask observations from the North American part of the NOAA station network to estimate the annual and monthly $ffCO_2$ emissions of the US in 2010 with a $^{14}CO_2$-CO_2 dual-tracer inversion framework. Graven et al. (2018) implemented ^{14}C-based $\Delta ffCO_2$ estimates from nine sites in a $\Delta ffCO_2$ model inversion system to deduce the $ffCO_2$ emissions in California for three months between 2014 and 2015. Due to the lack of $^{14}CO_2$ observations at urban sites, city-scale $ffCO_2$ emissions have commonly been verified by using total CO_2 observations during the dormant season when the contribution of the biosphere is expected to be small (Lauvaux et al., 2016; Pisso et al., 2019; Lopez-Coto et al., 2020). For example, Turnbull et al. (2019) utilizes in-situ CO_2 observations from 13 towers within the Indianapolis urban area to estimate its total CO_2 emissions in winter. Furthermore, they calculated $\Delta CO_2/\Delta ffCO_2$ ratios from $^{14}CO_2$ and CO_2 flasks collected up- and downwind of the city with which they scale their top-down CO_2 emissions estimates to finally derive $ffCO_2$ emissions, which could be compared with bottom-up data. For comparison, they also calculated flask-based $\Delta CO/\Delta ffCO_2$ ratios to scale the CO emissions, which they deduced from an aircraft mass balance approach (Heimburger et al., 2017).

In my thesis, I aimed to estimate the seasonal cycle of $ffCO_2$ emissions in an urban area using in-situ $\Delta ffCO_2$ observations and inverse modelling. To the best of my knowledge, this is the first time that ^{14}C- and ΔCO-based $\Delta ffCO_2$ observations have been used in a high-resolution

ΔffCO$_2$ model inversion system for this purpose. The study area is the Upper Rhine Valley around the Heidelberg observation site, which is a highly populated and industrialized region with complex emissions patterns, including several point sources. The Heidelberg observation site has an air intake height of only 30 m above ground, resulting in small-scale representativity of the measurements. Overall, this places high demands on the atmospheric transport model and makes it challenging to estimate ffCO$_2$ emissions accurately. Therefore, appropriate model approaches and a careful estimation of the ΔffCO$_2$ concentrations are essential in this urban inversion framework.

The main goal of this thesis was to develop these methods and to finally investigate the potential of ^{14}C-based vs. ΔCO-based ΔffCO$_2$ observations to evaluate the seasonal cycle of the ffCO$_2$ emissions in the Upper Rhine Valley. Below is a discussion of my main findings in which I also elaborate on what needs to be considered when estimating ffCO$_2$ emissions in other urban regions. Since Heidelberg was chosen as a pilot site for the ICOS atmosphere station network, I will also analyze which conclusions can be drawn from my thesis work for an application at remote stations.

7.2 How to represent elevated point source emissions in STILT?

A challenging part in modelling ΔffCO$_2$ concentrations at the Heidelberg observation site is the large heterogeneity of the surrounding ffCO$_2$ emissions, and in particular the nearby point sources. This requires the usage of an appropriate transport model and a high-resolution emission inventory, which accurately describes the spatial heterogeneity in the emissions. In this thesis, I used the WRF-STILT (Lin et al., 2003; Nehrkorn et al., 2010) model, which is driven by highly resolved meteorological fields with a horizontal resolution of 2 km. Furthermore, I applied the high-resolution ffCO$_2$ emission inventory from TNO (Dellaert et al., 2019; Denier van der Gon et al., 2019), which distinguishes between area and point source emissions and thus allows a separate treatment of the area and point source emissions in the inversion system.

7.2.1 Performance of the STILT volume source influence (VSI) approach

The difficulty of modelling point source emissions is based on the small spatial extent of the point sources and their emission release from elevated stacks. However, point source emissions are commonly released from the surface in most Lagrangian and Eulerian atmospheric transport modelling studies (Brunner et al., 2019). This can lead to large overestimations of near-surface CO_2 concentrations (Brunner et al., 2019) and may thus impact the inversion results (Kunik et al., 2019). Therefore, I developed in my thesis a novel model approach in STILT, the so-called volume source influence (VSI) approach, which takes into account the effective emission heights of point sources (see Ch. 2).

In the case of the Heidelberg observation site with an air intake height of 30 m above ground and several large power plants in its vicinity, the VSI approach improves the root-mean-square deviation (RMSD) between modelled and ^{14}C-based two-week integrated $\Delta ffCO_2$ by almost a factor of 2 at night. As a result, the VSI approach leads to a similar RMSD at night as during the afternoon. In the afternoon with typically well-mixed conditions, the RMSD between modelled and observed $\Delta ffCO_2$ is on average quite similar for the VSI and the standard STILT surface source influence (SSI) approach, which releases all point source emissions at the surface. However, there are individual synoptic events in winter when also afternoon situations show suppressed atmospheric mixing and low PBL heights. For such situations, the SSI approach yields up to a few ppm larger $\Delta ffCO_2$ concentrations than the VSI approach even during the afternoon. Therefore, the VSI approach should not only be used at night, but also for afternoon situations with low PBL heights.

Overall, these results clearly illustrate that the improved representation of point source emissions with the VSI approach leads to a much more reliable modelling of their $\Delta ffCO_2$ contributions at the Heidelberg observation site. Therefore, this VSI approach could be a first step towards exploiting nighttime situations in models. However, also the VSI approach depends on accurate meteorological fields and a reliable simulation of the atmospheric transport and mixing processes, which includes, e.g., a realistic representation of stable boundary layers during night and their erosion in the morning hours.

7.2.2 Application of the STILT-VSI approach

As already mentioned, the application of the VSI approach is especially important during stable conditions with low PBL heights. In order to estimate up to which distance from the observation site the point source emission heights should be represented in STILT, I conducted a model experiment with artificial power plants (see Ch. 2). In fact, this distance depends on whether the observation site is above or within the PBL during stable conditions, and thus on the air intake height of the observation site. For this analysis I assumed an air intake height of 30 m above the ground and considered typical power plants with an annual CO_2 emission of 1 million tons. It turned out that such power plants should be treated with the VSI approach if they have a distance of less than roughly 50 km to the observation site. Thus, the VSI approach is particularly important for urban sites. For observation sites with their air intake above the PBL during stable conditions, the differences between the VSI and the SSI approach are less pronounced. For tower sites with an air intake height of e.g. 200 m above the ground, the VSI approach should be applied to all power plants within a ca. 10 km radius.

To consider the point source emissions heights in the Rhine Valley inversion, I implemented – with technical support from Christian Rödenbeck at the Max Planck Institute for Biogeochemistry – the STILT-VSI model approach in the CarboScope inversion system. Thus, the CarboScope framework now allows a more reliably representation of the point source emissions, which is particularly beneficial for CO_2 inversions in urban regions.

7.3 Estimation of ΔffCO$_2$ concentrations from ^{14}CO$_2$ observations

After having provided the modelling basis for estimating ffCO$_2$ emissions in the Rhine Valley, accurate estimates of the ΔffCO$_2$ concentrations and their uncertainties are needed. For this, I described and revisited the challenges and assumptions in estimating ΔffCO$_2$ from ^{14}CO$_2$ observations (see Ch. 3).

7.3.1 How to calculate bias-free ^{14}C-based ΔffCO$_2$ estimates in Central Europe?

The most important challenge in estimating ^{14}C-based ΔffCO$_2$ concentrations is the selection of an appropriate Δ^{14}CO$_2$ background. For observation sites in Central Europe with prevailing westerly winds, the Δ^{14}CO$_2$ observations from the marine site Mace Head (MHD), located at the western coast of Ireland, turned out to be a suitable background. In Ch. 3 a study with the coarse resolution TM3 model (Heimann and Körner, 2003) was conducted to assess the representativeness of this marine background site for non-western air masses. This study yields an average representativeness bias and uncertainty of 0.1 ± 0.3 ppm for observation sites in Central Europe.

In Europe, the high density of nuclear facilities is a severe problem for estimating ^{14}C-based ΔffCO$_2$ concentrations. For example, the two-week integrated ^{14}CO$_2$ samples collected at the ICOS sites show a median nuclear contamination, which accounts for about 30% of the median Δ^{14}CO$_2$ depletion compared to MHD. This would lead to a ΔffCO$_2$ masking of 25%

if the $^{14}CO_2$ samples are not corrected. However, the modelling of the nuclear contamination at the observation sites is associated with huge uncertainties on the order of 100%. These uncertainties are mainly induced by the uncertainties of the nuclear $^{14}CO_2$ emissions, which can show large variabilities (Kuderer et al., 2018; Lehmuskoski et al., 2021) but are typically only available annually.

^{14}C-enriched heterotrophic CO_2 respiration can lead to similar $\Delta ffCO_2$ masking effects like nuclear contaminations, especially during summer and for remote observation sites with low $\Delta ffCO_2$ signals and strong biosphere influence. Therefore, the $^{14}CO_2$ samples should also be corrected for biosphere respiration. However, this requires an estimation for the respired CO_2 signal and its $\Delta^{14}CO_2$ signature, which further increases the uncertainty of the ^{14}C-based $\Delta ffCO_2$ observations.

Overall, the $\Delta^{14}CO_2$ measurement uncertainties together with the background representativeness uncertainty are with 0.9-1.0 ppm the dominant contributions to the overall $\Delta ffCO_2$ uncertainty if the biases due to nuclear contamination and heterotrophic respiration are corrected. However, those corrections can increase the overall $\Delta ffCO_2$ uncertainty by several tenths of ppm. This study showed that almost the half of the two-week integrated $^{14}CO_2$ samples collected at the remote ICOS sites have an uncertainty larger than 50%.

7.3.2 How to collect flask samples for ^{14}C analysis?

The methodological study on how to estimate accurate ^{14}C-based $\Delta ffCO_2$ illustrated that $^{14}CO_2$ flask samples should be collected during situations with pronounced $\Delta ffCO_2$ signals. Such a flask sampling strategy would decrease the relative uncertainty of the ^{14}C-based $\Delta ffCO_2$ estimates and further reduces the impact of an inappropriate background or of masking effects due to nuclear contaminations and biosphere respiration. Therefore, the ICOS flask sampling strategy suggests collecting ^{14}C flasks during situations with elevated CO excess concentrations, which are indicative of $ffCO_2$ influence at the observation site (see Ch. 4).

Furthermore, significant nuclear contaminations of the ^{14}C flask samples should be avoided whenever possible as its correction is associated with large uncertainties. Therefore, ^{14}C flasks should only be collected during situations with less nuclear $^{14}CO_2$ influence at the observation site. For this, near-real time or forecasted footprints could be used to estimate the potential nuclear contamination at the observation site. Then, ^{14}C flasks should only be collected if the predicted nuclear contamination is below a set threshold, which may depend on the expected ΔffCO$_2$ signals at the observation sites. In case of the urban Heidelberg observation site, this threshold was set to 2‰, which corresponds to roughly 10% of the mean ΔffCO$_2$ signal of the flask samples.

Finally, the transport model must be able to represent the signals sampled with the ^{14}C flasks, so that these observations can be used in inverse models to estimate ffCO$_2$ emissions. For this, the ICOS flask sampler is programmed to collect hourly integrated flasks, whose final concentration corresponds to the mean ambient air concentration during the sampling hour (see Ch. 4). Hereby, the hourly integration time leads to a smoothing of high-frequent ambient air variabilities, which cannot be represented by models.

7.4 Estimation of ΔffCO$_2$ concentrations from ΔCO observations

In the two years 2019 and 2020 I have collected almost 350 ^{14}CO$_2$ flask samples with the ICOS flasks sampler at the Heidelberg observation site. These flasks were taken during very different atmospheric conditions to characterize the observation site and to test different flask sampling strategies. Examples are the sampling of background conditions, local signals like from the rush-hour, nighttime situations, synoptic events, or diurnal cycles. In Ch. 5, I investigated if this large ^{14}C flask pool can be used to construct a continuous ΔCO-based ΔffCO$_2$ record, which could then also be exploited in the Rhine Valley inversion.

7.4.1 How to determine continuous ΔCO-based ΔffCO$_2$ estimates and their uncertainties?

The ΔCO/ΔffCO$_2$ ratios of the flask samples showed only small diurnal, seasonal and inter-annual differences below ca. 5%. Obviously, we are currently in a quite fortunate situation in Heidelberg of having similar emission ratios from the traffic and heating sectors. Furthermore, the Heidelberg observation site seems to be less influenced by distinct point source emissions, which are associated with low ΔCO/ΔffCO$_2$ ratios. Therefore, the average ΔCO/ΔffCO$_2$ ratio of the whole flask pool could be used to construct an hourly ΔCO-based ΔffCO$_2$ record for 2019 and 2020.

By comparing the ΔCO-based ΔffCO$_2$ with the ^{14}C-based ΔffCO$_2$ concentrations of the flask samples the uncertainty of the ΔCO-based ΔffCO$_2$ record could be estimated. It turned out that the RMSD between ^{14}C- and ΔCO-based ΔffCO$_2$ is about 4 ppm, which is almost 4 times larger than the typical uncertainty of ^{14}C-based ΔffCO$_2$ observations. At this urban observation site, about one half of the uncertainty can be explained by the measurement and background representativeness uncertainties and the other half can be attributed to the spatiotemporal variabilities of the CO/ffCO$_2$ emission ratios in the footprint of the observation site.

7.4.2 Can inventory-based ΔCO/ΔffCO$_2$ ratios be used to estimate the continuous ΔCO-based ΔffCO$_2$ record?

I further investigated if inventory-based emission ratios could be used instead of the ^{14}C-based ΔCO/ΔffCO$_2$ ratios to estimate the continuous ΔCO-based ΔffCO$_2$ record. This would allow the construction of ΔCO-based ΔffCO$_2$ records at many sites with CO but without ^{14}CO$_2$ observations. For this, I used STILT to calculate footprint weighted ΔCO/ΔffCO$_2$ ratios from TNO. This analysis showed that the modelled ratios are about 40% lower than the flask ratios from Heidelberg. Consequently, this would lead to a direct bias in the ΔCO-based ΔffCO$_2$ record, and thus in the top-down ffCO$_2$ emission estimates if those modelled ratios would have been used to construct the ΔCO-based ΔffCO$_2$ record. Thus, this illustrates the need for an independent validation of the bottom-up ffCO$_2$ (and CO) emissions.

7.5 What is the potential of ^{14}C-based vs. ΔCO-based ΔffCO$_2$ observations to estimate the seasonal cycle of the ffCO$_2$ emissions in the Rhine Valley metropolitan region?

After having calculated the ^{14}C-based and ΔCO-based ΔffCO$_2$ concentrations and their uncertainties, these observations were used in the Rhine Valley inversion system to investigate their potential to estimate robust ffCO$_2$ emissions. For this study, only afternoon observations were used, so that the inversion results are not influenced by the typically poorer model performance at night.

7.5.1 How to deal with point source emissions in the Rhine Valley inversion?

As mentioned above, I used the STILT-VSI approach to represent nearby point source emissions more reliably, which is especially important for winter afternoons with low PBL heights. However, while on average the difference between modelled and observed ΔffCO$_2$ is quite small (the median difference is below 0.4 ppm for both ^{14}C- and ΔCO-based ΔffCO$_2$ observations), there are still some large model-data ΔffCO$_2$ differences with several tens of ppm for individual hours. These large deviations could be attributed to a wrong simulation of the low-level PBL heights during synoptic weather patterns in winter and an occasionally inadequate modelling of the contributions from point sources for individual hours. Indeed, the study in Ch. 5 shows that the STILT-VSI approach predicts for the Heidelberg observation site events with strong point source influences that are associated with low ΔCO/ΔffCO$_2$ ratios, but are hardly observed at the Heidelberg observation site at 30 m above ground. Obviously, such situations cannot be represented appropriately with the transport model. Thus, a 2σ-selection was applied, to exclude the observations with the largest model-data mismatches.

The inadequate modelling of the contributions from point source emissions for individual hours with the STILT-VSI approach can be explained by inconsistencies in the driving WRF meteorology and deficits in the VSI approach, which is still dependent on accurate mixing in STILT. To appropriately simulate the mixing of narrow plumes from nearby power plant stacks, the 2 km resolution of the WRF meteorology is still too coarse. Moreover, small errors in the wind fields would lead to slight changes in the arrival time of the point source plumes at the observation site. The shortcomings of the VSI approach are that it assumes default effective emission height profiles for all meteorological situations and for all point sources in a specific emission sector. This means that, e.g., the different chimney heights of individual power plants are not taken into account.

For these reasons, and the fact that the observations from Heidelberg are not strongly influenced by point sources anyway, I decided to use the monthly energy production and industrial point source ffCO$_2$ emissions from TNO as fixed a-priori estimates that are not adjusted in the inversion system. Furthermore, the fixing of the a-priori point source emissions can be motivated by the fact that they are typically much better known than the more diffuse area source emissions.

7.5.2 Potential of flask-based ΔffCO$_2$ observations to estimate ffCO$_2$ emissions in the Rhine Valley

The goal of the Rhine Valley inversion is to investigate the potential of ^{14}C-based vs. ΔCO-based ΔffCO$_2$ observations to evaluate the seasonal cycle of the area source ffCO$_2$ emissions in the main footprint of the Heidelberg observation site. For this, I used the 2019-2020 bi-annual mean area source ffCO$_2$ emissions from TNO as a temporally constant, i.e. flat, a-priori estimate and evaluated if the observational data can reconstruct the seasonal cycle in the a-posteriori estimates. The discrete ^{14}C-based ΔffCO$_2$ estimates from almost 100 afternoon flasks collected during 2019 and 2020 lead to a distinct seasonal cycle in the a-posteriori area source ffCO$_2$ emissions with larger emissions during winter and lower emissions in summer. Thus, the ^{14}C flask data intrinsically contain the information about the seasonal cycle of the ffCO$_2$ emissions. However, there are huge overfitting patterns, i.e. unexpected large variabilities in the a-posteriori seasonal cycles, for increased prior uncertainties larger than ca. 50%. These variabilities occur predominantly during times with a low flask coverage when the inversion tries to minimize the model-data mismatch of individual flask samples. Thus, a strong prior constraint is needed to avoid this overfitting. However, this means that the a-posteriori results are less data driven. Overall, the strong dependence of the a-posteriori seasonal cycle on the prior uncertainty prevents the determination of a robust inversion result when using the ^{14}C-based ΔffCO$_2$ flask observations from Heidelberg.

To investigate if a higher and more uniform flask coverage would help to reduce the overfitting patterns in the inversion results, I subsampled the continuous ΔCO-based ΔffCO$_2$ record for, e.g., one hypothetical afternoon flask per week or per day, respectively. Such a high-frequent flask sampling reduces the spread in the a-posteriori results for different prior uncertainties and leads to more robust signals. However, the a-posteriori seasonal cycles differ strongly, if the weekly hypothetical flask samples are collected, e.g., every Tuesday, or every Friday afternoon, respectively. This illustrates that the a-posteriori seasonal cycles still depend on the model-data mismatches of individual (hypothetical) flask samples.

To investigate the impact of the point source modelling on the a-posteriori area source ffCO$_2$ emissions, I performed additional inversion runs with adjustable (instead of fixed) a-priori point source emissions. Indeed, even if all (2σ-selected) afternoon hours of the ΔCO-based ΔffCO$_2$ record are used in the inversion, there are huge deviations larger than 100% between the a-posteriori area source ffCO$_2$ emissions of the inversion runs with fixed and adjustable point source emissions. This illustrates that – despite the applied 2σ-selection – there are still individual hours, which are not well represented by the transport model.

Therefore, the model results must be averaged over multiple hours – and thus also the observations – to reduce the impact of individual hours with poor transport model performance on the area source ffCO$_2$ emission estimates. I showed that the averaging interval of one week strongly reduces the differences between the a-posteriori area source emissions of the inversion runs with fixed and adjustable a-priori point source emissions, respectively, to below

30% for all seasons. A longer, i.e. monthly, averaging would further reduce this difference to below 20%, but would result in an averaging over very different meteorological situations and thus less temporal information. Therefore, I decided to use an averaging interval of one week, which is a compromise between reducing the impact of individual hours with inadequate model performance and using as much individual information as possible.

Overall, this work showed that even the STILT-VSI approach combined with a high-resolution WRF meteorology as well as the 2σ-selection, applied to exclude the potentially poorest simulated hours with the largest model-data mismatches, is not enough for ^{14}C-based ΔffCO$_2$ observations from flasks to be used to estimate robust seasonal cycles of the ffCO$_2$ emissions in the Upper Rhine Valley. Although ^{14}C-based ΔffCO$_2$ observations provide the more accurate information than the ΔCO-based ΔffCO$_2$ data for individual hours, the results of the subsampled ΔCO-based ΔffCO$_2$ inversion suggest that several flasks per week are needed to prevent unrealistic variabilities in the urban ffCO$_2$ emission estimates.

7.5.3 Potential of ΔCO-based ΔffCO$_2$ observations to estimate ffCO$_2$ emissions in the Rhine Valley

The big advantage of the continuous ΔCO-based ΔffCO$_2$ record is that it can be averaged, so that the impact of individual hours with a poor transport model performance is reduced. The weekly averaged (2σ-selected) afternoon ΔCO-based ΔffCO$_2$ observations from Heidelberg allow a reliable and robust reconstruction of the seasonal cycle of the area source ffCO$_2$ emissions for increased uncertainties of the flat a-priori emissions. In particular, these observations show the distinct COVID-19 signal in 2020 with lower emissions compared to 2019 and steeply declining emissions in spring 2020. In the COVID-19-year 2020, the a-posteriori seasonal cycle of the area source ffCO$_2$ emissions agrees very well with the bottom-up seasonal cycle from TNO, which has been adapted for the national COVID-19 restrictions in 2020. For 2019 TNO provides a non-year-specific European average seasonal cycle with the summer minimum in July. However, for this year (2019) the inversion leads to a summer minimum in August and September, when summer holidays take place in our region.

When using the seasonal cycles of 2019 and 2020 from TNO as a-priori estimate for the area source ffCO$_2$ emissions, the inversion tries to shift the summer minimum from July into September in 2019 but hardly changes the seasonal cycle in 2020. Thus, for 2019, this might point to some inconsistencies in the phasing of the (European average) seasonal cycle of the TNO area source ffCO$_2$ emissions in the main footprint of Heidelberg. As mentioned before, an accurate phasing of the seasonal cycle of the ffCO$_2$ emissions is essential when these estimates are used in atmospheric transport inversions to separate the fossil from the biogenic contribution in atmospheric CO$_2$ observations and therewith constrain the seasonal cycle of the CO$_2$ exchange with the biosphere.

In contrast to the ^{14}C-based ΔffCO$_2$ inversion, the ΔCO-based ΔffCO$_2$ inversion allows for a weakening of the regularization strength, i.e. the prior constraint, without causing unrealistic variability in the a-posteriori seasonal cycles. Consequently, the a-posteriori results are less dependent on potential biases in the a-priori emission estimates. In Ch. 6, I showed that the ΔCO-based ΔffCO$_2$ inversion is able to simultaneously reconstruct the seasonal cycle from flat a-priori area source ffCO$_2$ emissions and to compensate for a potential bias in the a-priori area source ffCO$_2$ emissions of the order of 20%. This illustrates the very promising potential of weekly averaged ΔCO-based ΔffCO$_2$ observations to explore the ffCO$_2$ emissions in an urban region with very heterogeneously distributed fossil emissions.

However, it must be emphasized that the ΔCO-based ΔffCO$_2$ inversion results rely on an accurate determination of the ΔCO/ΔffCO$_2$ ratios, which are used to construct the ΔCO-based ΔffCO$_2$ record. This also includes the investigation of a potential seasonal cycle in the ΔCO/ΔffCO$_2$ ratios. As mentioned before, the flask samples from Heidelberg showed only small summer-winter differences. However, a sensitivity inversion run, which assumes a hypothetical seasonal cycle in the ΔCO/ΔffCO$_2$ ratios with 5% larger and 5% lower ratios during winter and summer, respectively, showed that the a-posteriori area source ffCO$_2$ emissions can change by 10% for individual seasons. This highlights the importance of carefully determining the ΔCO/ΔffCO$_2$ ratios by investigating their potential seasonal cycles, so that the amplitude and the phasing of the seasonal cycle of the ffCO$_2$ emissions can be estimated without biases.

7.6 Application of the ^{14}C- and ΔCO-based ΔffCO$_2$ inversion in other urban regions

After having discussed the potential of ^{14}C- and ΔCO-based ΔffCO$_2$ observations to estimate the ffCO$_2$ emissions in the urban Rhine Valley, I want to elaborate on what needs to be considered when ΔffCO$_2$ observations are used to estimate ffCO$_2$ emissions in other urban regions. This thesis showed that urban areas with very heterogeneously distributed ffCO$_2$ emissions and a complex local circulation are hard to represent with atmospheric transport models like STILT, even if they are driven with high-resolution meteorological fields and coupled with a highly resolved emission inventory. In particular, the contributions from nearby point sources in the footprint of the observation site are difficult to predict for individual hours. For such sites, an averaging of the modelled ΔffCO_2 concentrations, and thus the observational data, is needed to reduce the impact of individual hours with an inadequate model performance on the inversion results. Therefore, the continuous data coverage of the ΔCO-based ΔffCO_2 observations is the clear benefit compared to discrete ^{14}C-based ΔffCO_2 data from hourly flasks when ffCO_2 emissions are to be estimated in such urban regions.

Overall, the very promising potential of ΔCO-based ΔffCO_2 observations to estimate ffCO_2 emissions in the main footprint of Heidelberg motivates the application of ΔCO-based ΔffCO_2 model inversions in other urban regions. However, the $\Delta CO/\Delta$ffCO_2 ratios used to construct the ΔCO-based ΔffCO_2 record must be determined thoroughly to prevent biases in the ffCO_2 emission estimates. As inventory-based $\Delta CO/\Delta$ffCO_2 ratios can lead to strong biases in the ΔCO-based ΔffCO_2 observations (see Ch. 5), ^{14}C flasks should be used to derive observation-based $\Delta CO/\Delta$ffCO_2 ratios, which also include all natural CO contributions from the terrestrial biosphere and CO losses e.g. due to atmospheric chemistry. To be as representative as possible, the flasks should be collected during very different meteorological situations. As was shown in Ch. 6, a potential seasonal cycle in the $\Delta CO/\Delta$ffCO_2 ratios can influence both, the amplitude and the phasing of the seasonal cycle of the a-posteriori ffCO_2 emissions. Therefore, it is important to collect ^{14}C flasks during all seasons (at least during summer and winter) to investigate a potential seasonal cycle in the ratios. If there is a significant seasonal cycle in the ratios, this must be incorporated when calculating the ΔCO-based ΔffCO_2 record. However, in particular for the summer period with typically lower ffCO_2 signals it is difficult to determine average $\Delta CO/\Delta$ffCO_2 ratios. Therefore, some flasks should also be collected during situations with elevated ΔCO signals, so that the correlation between ΔCO and ΔffCO_2 can be increased. In Ch. 5, I showed that one needs roughly 15-20 flasks at sites with a good correlation, i.e. a R^2 value between 0.7 and 0.9, to determine the average $\Delta CO/\Delta$ffCO_2 ratio with an uncertainty of below 10%. This implies that at least 30 flasks per year are needed to determine an average summer and winter $\Delta CO/\Delta$ffCO_2 ratio.

Another challenge is the selection of an appropriate $\Delta^{14}CO_2$ and CO background. For the Heidelberg observation site, I used smoothly fitted curves through the $\Delta^{14}CO_2$ and CO observations from Mace Head (MHD) as a marine background for the boundary of the European STILT domain. However, to apply the ΔffCO_2 observations in the regional Rhine Valley, the ΔffCO_2 contributions from the European continent outside the Rhine Valley have to be subtracted from the ^{14}C- and ΔCO-based $\Delta ffCO_2$ excesses compared to MHD. These European $\Delta ffCO_2$ contributions (called the Rhine Valley $\Delta ffCO_2$ background) were modelled with STILT by using two different emission inventories (TNO and EDGAR (Janssens-Maenhout et al., 2019), see Ch. 6). Indeed, the top-down $ffCO_2$ emission estimates can show pronounced deviations of more than 10% depending on the chosen emission inventory used to model the Rhine Valley $\Delta ffCO_2$ background. This calls for a thorough determination of the $\Delta ffCO_2$ background. Depending on the availability of suitable background sites, it may be beneficial to use a more regional $\Delta^{14}CO_2$ and CO background, which is representative for the boundaries of the regional model domain. In Indianapolis, e.g., Turnbull et al. (2015) used an observation station upwind of the city as local background site for downwind stations, which measure the signal of the city. Then, a model study similar to what has been done in Ch. 3 could be conducted to assess the representativeness of the local background site for all boundaries of the targeted model domain. A further advantage of this upwind-downwind sampling approach is that the $\Delta^{14}CO_2$ measurements at both sites are similarly influenced by nuclear contaminations if there is no nuclear $^{14}CO_2$ source between the two sites. This means that the $\Delta^{14}CO_2$ differences between the two sites, and thus the $\Delta ffCO_2$ concentrations, are less influenced by nuclear $^{14}CO_2$ contaminations.

7.7 Which conclusions can be drawn for remote observation sites?

From this study at the ICOS pilot site Heidelberg, it is difficult to draw detailed conclusions about the potential of remote site ^{14}C- and ΔCO-based $\Delta ffCO_2$ observations to estimate $ffCO_2$ emissions with inverse modelling. In contrast to the urban observation site Heidelberg, remote sites are more distant from point sources and heterogeneous $ffCO_2$ emissions. In fact, the ICOS station specifications (ICOS RI, 2020) recommend for ICOS atmosphere stations a distance of at least 40 km from point sources so that their emissions are well mixed when they arrive at the ICOS site and can be better represented in models. Furthermore, in case of tower stations, the observation sites have a higher air intake of typically well above 100 m, which leads to a larger scale representativity of the observations. This facilitates the modelling of $\Delta ffCO_2$ concentrations at remote sites and might result in a better model performance. Moreover, in the case of remote stations an entire observational network is typically used to constrain $ffCO_2$ emissions at continental or national scales (Graven et al., 2018; Basu et al., 2020) instead of at urban scales. Indeed, such a large-scale inversion setup would be quite different from that used in this work. Therefore, ^{14}C-based $\Delta ffCO_2$ gradients between remote sites could be well suited for estimating national $ffCO_2$ emissions (see Graven et al., 2018).

However, remote sites are also characterized by less signals and a stronger influence from the biosphere. Consequently, the background selection and the correction for nuclear contaminations and biospheric CO_2 respiration have a stronger impact on the $\Delta ffCO_2$ estimates and their uncertainties than at urban sites. Therefore, the ICOS flask sampling strategy suggests collecting ^{14}C flasks during situations with pronounced ΔCO concentrations. However, to avoid sampling biases, also some randomly collected flasks should be analyzed for ^{14}C. Currently, the ICOS sampling strategy developed in Ch. 4 is therefore adapted so that one half of the ^{14}C flasks is collected randomly, e.g. every first flask sampling of the month, and the other half of the flasks is taken during situations with elevated ΔCO concentrations. Overall, many small but persistent ^{14}C-based $\Delta ffCO_2$ gradients between the remote observation sites might still provide valuable information for the inversion system to estimate large scale $ffCO_2$ fluxes. Therefore, it will be interesting to explore the performance of the ^{14}C-based $\Delta ffCO_2$ observations from the ICOS sites in estimating the $ffCO_2$ emissions in Europe.

The distance to heterogeneously distributed $ffCO_2$ emissions seems to lead to less variable $\Delta CO/\Delta ffCO_2$ ratios at remote observation sites. In Ch. 5, I showed that at the remote ICOS site OPE a constant $\Delta CO/\Delta ffCO_2$ ratio could be used to construct a ΔCO-based $\Delta ffCO_2$ record with an uncertainty of 1.5 ppm, which is entirely explainable by the measurement and background representativeness uncertainties alone. This ΔCO-based $\Delta ffCO_2$ uncertainty is only about 30% larger than the typical uncertainty of ^{14}C-based $\Delta ffCO_2$ observations. Thus, it will be interesting to investigate the potential of this record to estimate $ffCO_2$ emissions in the footprint of the OPE site and to analyze if such a ΔCO-based $\Delta ffCO_2$ record could also be constructed for other remote (ICOS) sites. Thereby, the ^{14}C flasks collected during situations with elevated ΔCO offsets could help to improve the correlation between the ΔCO and $\Delta ffCO_2$ flask data and to determine average $\Delta CO/\Delta ffCO_2$ ratios. However, the study at OPE is based on flasks collected between September and March when biospheric CO contributions are expected to be small (Worden et al., 2019). Thus, it will be exciting to see if an average $\Delta CO/\Delta ffCO_2$ ratio can also be calculated for the summertime with lower signals and more biosphere influence.

Finally, an advantage of the ΔCO-based $\Delta ffCO_2$ compared to the ^{14}C-based $\Delta ffCO_2$ observations is that they might be less influenced from the nuclear contaminations of individual flasks, as the average $\Delta CO/\Delta ffCO_2$ ratios are calculated from several (nuclear corrected) ^{14}C flasks. This could be a benefit for nuclear-influenced sites, e.g. in Europe. However, the feasibility of calculating ΔCO-based ΔffCO$_2$ records at other remote sites and their potential to estimate large-scale ffCO$_2$ emissions must first be investigated.

CHAPTER 8

Conclusions

Conclusions

The main goal of this thesis was to investigate the potential of ^{14}C- and ΔCO-based ΔffCO$_2$ observations from Heidelberg to evaluate the seasonal cycle of the urban ffCO$_2$ emissions in the Upper Rhine Valley. For this, the CarboScope inversion framework was used in combination with the high-resolution WRF-STILT model to account for the large heterogeneity in the surrounding fossil emissions. Furthermore, a STILT model approach was developed to represent the effective emission heights of the several nearby point sources. The ^{14}C-based ΔffCO$_2$ observations from almost 100 hourly afternoon flasks collected in 2019 and 2020 allow the reconstruction of a clear seasonal cycle from flat a-priori ffCO$_2$ emissions, which implies that these data contain the seasonality of the ffCO$_2$ emissions. However, these observations cannot be used to derive robust ffCO$_2$ emissions estimates, which is due to the fact that the transport model is not able to adequately represent individual hours. This, combined with a strong heterogeneity of the fossil CO$_2$ sources, leads to a model-data mismatch, which the inversion algorithm tries to compensate for by unrealistic changes in the emissions.

The benefit of the continuous ΔCO-based ΔffCO$_2$ record is that it can be averaged to reduce the impact of hours with an inadequate modelling performance on the inversion results. Indeed, the weekly averaged ΔCO-based ΔffCO$_2$ observations allow to explore the distinct COVID-19 signal in 2020 and to validate the seasonal cycle of the bottom-up ffCO$_2$ emissions in the main footprint of Heidelberg. Therefore, ΔCO-based ΔffCO$_2$ observations might be a valuable alternative for estimating ffCO$_2$ emissions in urban areas, if the ΔCO/ΔffCO$_2$ ratios can be determined without biases. Overall, this work provides expedient tools and approaches for treating point source emissions in urban model inversions and reliably estimating ^{14}C- and ΔCO-based ΔffCO$_2$ concentrations and their uncertainties.

References

Andres, R. J., Boden, T. A., and Higdon, D. M.: Gridded uncertainty in fossil fuel carbon dioxide emission maps, a CDIAC example, Atmos. Chem. Phys., 16, 14979–14995, `https://doi.org/10.5194/acp-16-14979-2016`, 2016.

Arrhenius, S.: On the influence of carbonic acid in the air upon the temperature of the ground, The London, Edinburgh and Dublin Philosophical Magazine and Journal of Science, 41, 237-276, `https://doi.org/10.1080/14786449608620846`, 1896.

Basu, S., Miller, J. B., and Lehman, S.: Separation of biospheric and fossil fuel fluxes of CO_2 by atmospheric inversion of CO_2 and $^{14}CO_2$ measurements: Observation System Simulations, Atmos. Chem. Phys., 16, 5665–5683, `https://doi.org/10.5194/acp-16-5665-2016`, 2016.

Basu, S., Lehman, S. J., Miller, J. B., Andrews, A. E., Sweeney, C., Gurney, K. R., Xue, X., Southon, J., and Tans, P. P.: Estimating US fossil fuel CO_2 emissions from measurements of ^{14}C in atmospheric CO_2, PNAS 117(24): 13300–13307, `https://doi.org/10.1073/pnas.1919032117`, 2020.

Bergamaschi, P., Danila, A., Weiss, R. F., Ciais, P., Thompson, R. L., Brunner, D., Levin, I., Meijer, Y., Chevallier, F., Janssens-Maenhout, G., Bovensmann, H., Crisp, D., Basu, S., Dlugokencky, E., Engelen, R., Gerbig, C., Günther, D., Hammer, S., Henne, S., Houweling, S., Karstens, U., Kort, E., Maione, M., Manning, A. J., Miller, J., Montzka, S., Pandey, S., Peters, W., Peylin, P., Pinty, B., Ramonet, M., Reimann, S., Röckmann, T., Schmidt, M., Strogies, M., Sussams, J., Tarasova, O., van Aardenne, J., Vermeulen, A. T., and Vogel, F.: Atmospheric monitoring and inverse modelling for verification of greenhouse gas inventories, EUR 29276 EN, Publications Office of the European Union, Luxembourg, ISBN 978-92-79-88938-7, JRC111789, `https://doi.org/doi:10.2760/759928`, 2018.

Brunner, D., Kuhlmann, G., Marshall, J., Clément, V., Fuhrer, O., Broquet, G., Löscher, A., and Meijer, Y.: Accounting for the vertical distribution of emissions in atmospheric CO_2 simulations, Atmos. Chem. Phys., 19, 4541–4559, `https://doi.org/10.5194/acp-19-4541-2019`, 2019.

Chandra, N., Patra, P. K., Niwa, Y., Ito, A., Iida, Y., Goto, D., Morimoto, S., Kondo, M., Takigawa, M., Hajima, T., and Watanabe, M.: Estimated regional CO_2 flux and uncertainty based on an ensemble of atmospheric CO_2 inversions, Atmos. Chem. Phys., 22, 9215–9243, `https://doi.org/10.5194/acp-22-9215-2022`, 2022.

Chevallier, F., Broquet, G., Zheng, B., Ciais, P., and Eldering, A.: Large CO_2 emitters as seen from satellite: Comparison to a gridded global emission inventory, Geophys. Res. Lett., 49, `https://doi.org/10.1029/2021GL097540`, 2022.

Ciais, P., D. Crisp, H. Denier Van Der Gon, R. Engelen, M. Heimann, G. Janssens-Maenhout, P. Rayner, and M. Scholze: Towards a European Operational Observing System to Monitor Fossil CO_2 Emissions. Final Report from the Expert Group, European Commission, October 2015, ISBN 978-92-79- 53482-9, doi:10.2788/350433, 2015. Available at `https://www.copernicus.eu/sites/default/files/2019-09/CO2_Blue_report_2015.pdf`, Last access: December 01, 2022.

Currie, L. A.: The remarkable metrological history of radiocarbon dating [II], J. Res. Natl. Inst. Stand. Technol., 109(2), 185-217, `https://doi.org/10.6028/jres.109.013`, 2004.

Dellaert, S., Super, I., Visschedijk, A., and Denier van der Gon, H.: High resolution scenarios of CO_2 and CO emissions, CHE deliverable D4.2, 2019. Available at `https://www.che-project.eu/sites/default/files/2019-05/CHE-D4-2-V1-0.pdf`, Last access: March 28, 2023.

Denier van der Gon, H., Kuenen, J., Boleti, E., Maenhout, G., Crippa, M., Guizzardi, D., Marshall, J., and Haussaire, J.: Emissions and natural fluxes Dataset, CHE deliverable D2.3, 2019. Available at `https://www.che-project.eu/sites/default/files/2019-02/CHE-D2-3-V1-1.pdf`, Last access: March 28, 2023.

Duren, R., and Miller, C.: Measuring the carbon emissions of megacities, Nature Clim Change 2, 560–562, `https://doi.org/10.1038/nclimate1629`, 2012.

Enting, I.: Inverse Problems in Atmospheric Constituent Transport, Cambridge Univ. Press, `https://doi.org/10.1017/CBO9780511535741`, 2002.

Folberth, G. A., Hauglustaine, D. A., Lathière, J., and Brocheton, F.: Interactive chemistry in the Laboratoire de Météorologie Dynamique general circulation model: model description and impact analysis of biogenic hydrocarbons on tropospheric chemistry, Atmos. Chem. Phys., 6, 2273–2319, `https://doi.org/10.5194/acp-6-2273-2006`, 2006.

Friedlingstein, P., O'Sullivan, M., Jones, M. W., Andrew, R. M., Gregor, L., Hauck, J., Le Quéré, C., Luijkx, I. T., Olsen, A., Peters, G. P., Peters, W., Pongratz, J., Schwingshackl, C., Sitch, S., Canadell, J. G., Ciais, P., Jackson, R. B., Alin, S. R., Alkama, R., Arneth, A., Arora, V. K., Bates, N. R., Becker, M., Bellouin, N., Bittig, H. C., Bopp, L., Chevallier, F., Chini, L. P., Cronin, M., Evans, W., Falk, S., Feely, R. A., Gasser, T., Gehlen, M., Gkritzalis, T., Gloege, L., Grassi, G., Gruber, N., Gürses, Ö., Harris, I., Hefner, M., Houghton, R. A., Hurtt, G. C., Iida, Y., Ilyina, T., Jain, A. K., Jersild, A., Kadono, K., Kato, E., Kennedy, D., Klein Goldewijk, K., Knauer, J., Korsbakken, J. I., Landschützer, P., Lefèvre, N., Lindsay, K., Liu, J., Liu, Z., Marland, G., Mayot, N., McGrath, M. J., Metzl, N., Monacci, N. M., Munro, D. R., Nakaoka, S.-I., Niwa, Y., O'Brien, K., Ono, T., Palmer, P. I., Pan, N., Pierrot, D., Pocock, K., Poulter, B., Resplandy, L., Robertson, E., Rödenbeck, C., Rodriguez, C., Rosan, T. M., Schwinger, J., Séférian, R., Shutler, J. D., Skjelvan, I., Steinhoff, T., Sun, Q., Sutton, A. J., Sweeney, C., Takao, S., Tanhua, T., Tans, P. P., Tian, X., Tian, H., Tilbrook, B., Tsujino, H., Tubiello, F., van der Werf, G. R., Walker, A. P., Wanninkhof, R., Whitehead, C., Willstrand Wranne, A., Wright, R., Yuan, W., Yue, C., Yue, X., Zaehle, S., Zeng, J., and Zheng, B.: Global Carbon Budget 2022, Earth Syst. Sci. Data, 14, 4811–4900, `https://doi.org/10.5194/essd-14-4811-2022`, 2022.

Gamnitzer, U., Karstens, U., Kromer, B., Neubert, R. E. M., Meijer, H. A. J., Schroeder, H., and Levin, I.: Carbon monoxide: A quantitative tracer for fossil fuel CO_2?, J. Geophys. Res., 111, D22302, `https://doi.org/10.1029/2005JD006966`, 2006.

Graven, H., Fischer, M. L., Lueker, T., Jeong, S., Guilderson, T. P., Keeling, R. F., Bambha, R., Brophy, K., Callahan, W., Cui, X., Frankenberg, C., Gurney, K. R., LaFranchi, B. W., Lehman, S. J., Michelsen, H., Miller, J. B., Newman, S., Paplawsky, W., Parazoo, N. C., Sloop, C., and Walker, S. J.: Assessing fossil fuel CO_2 emissions in California using atmospheric observations and models, Environ. Res. Lett., 13, 065007, `https://doi.org/10.1088/1748-9326/aabd43`, 2018.

Heimann, M. and Körner, S.: The Global Atmospheric Tracer Model TM3, Model Description and User's Manual Release 3.8a, Tech. Rep. 5, Max Planck Institute for Biogeochemistry (MPI-BGC), Jena, Germany, 2003.

Heimburger, A. M., Harvey, R. M., Shepson, P. B., Stirm, B. H., Gore, C., Turnbull, J. C., Cambaliza, M. O. L., Salmon, O. E., Kerlo, A.-E., Lavoie, T. N., Davis, K. J., Lauvaux, T., Karion, A., Sweeney, C., Brewer, W. A., Hardesty, R. M., and Gurney, K. R.: Assessing the optimized precision of the aircraft mass balance method for measurement of urban greenhouse gas emission rates through averaging, Elem. Sci. Anth., 5(26), `https://doi.org/10.1525/elementa.134`, 2017.

Heiskanen, J., Brümmer, C., Buchmann, N., Calfapietra, C., Chen, H., Gielen, B., Gkritzalis, T., Hammer, S., Hartman, S., Herbst, M., Janssens, I. A., Jordan, A., Juurola, E., Karstens, U., Kasurinen, V., Kruijt, B., Lankreijer, H., Levin, I., Linderson, M., Loustau, D., Merbold, L., Myhre, C. L., Papale, D., Pavelka, M., Pilegaard, K., Ramonet, M., Rebmann, C., Rinne, J., Rivier, L., Saltikoff, E., Sanders, R., Steinbacher, M., Steinhoff, T., Watson, A., Vermeulen, A. T., Vesala, T., Vítková, G., and Kutsch, W.: The Integrated Carbon Observation System in Europe, Bulletin of the American Meteorological Society, 103(3), E855-E872, `https://doi.org/10.1175/BAMS-D-19-0364.1`, 2022.

ICOS RI: ICOS Atmosphere Station Specifications V2.0, edited by: Laurent, O., ICOS ERIC, `https://doi.org/10.18160/GK28-2188`, 2020.

IPCC, 2021: Climate Change 2021: The Physical Science Basis. Contribution of Working Group I to the Sixth Assessment Report of the Intergovernmental Panel on Climate Change, edited by: Masson-Delmotte, V., Zhai, P., Pirani, A., Connors, S. L., Péan, C., Berger, S., Caud, N., Chen, Y., Goldfarb, L., Gomis, M. I., Huang, M., Leitzell, K., Lonnoy, E., Matthews, J. B. R., Maycock, T. K., Waterfield, T., Yelekçi, O., Yu, R., and Zhou, B., Cambridge University Press, Cambridge, United Kingdom and New York, NY, USA, 2391 pp., https://doi.org/10.1017/9781009157896.

IPCC, 2023: Synthesis report of the IPCC sixth assessment report (AR6) - Longer report, available at: `https://www.ipcc.ch/report/ar6/syr/downloads/report/IPCC_AR6_SYR_LongerReport.pdf`, last access: April 27, 2023.

Janssens-Maenhout, G., Crippa, M., Guizzardi, D., Muntean, M., Schaaf, E., Dentener, F., Bergamaschi, P., Pagliari, V., Olivier, J. G. J., Peters, J. A. H. W., van Aardenne, J. A., Monni, S., Doering, U., Petrescu, A. M. R., Solazzo, E., and Oreggioni, G. D.: EDGAR v4.3.2 Global Atlas of the three major greenhouse gas emissions for the period 1970–2012, Earth Syst. Sci. Data, 11, 959–1002, `https://doi.org/10.5194/essd-11-959-2019`, 2019.

Jiang, F., Chen, J. M., Zhou, L., Ju, W., Zhang, H., Machida, T., Ciais, P., Peters, W., Wang, H., Chen, B., Liu, L., Zhang, C., Matsueda, H., and Sawa, Y.: A comprehensive estimate of recent carbon sinks in China using both top-down and bottom-up approaches, Sci. Rep. 6, 22130, `https://doi.org/10.1038/srep22130`, 2016.

Keeling, C. D., Bacastow, R. B., Bainbridge, A. E., Ekdahl, C. A., Guenther, P. R., Waterman, L. S., and Chin, J. F. S.: Atmospheric carbon dioxide variations at Mauna Loa Observatory, Hawaii, Tellus A., 28, 538–551, `https://doi.org/10.1111/j.2153-3490.1976.tb00701.x`, 1976.

Konovalov, I. B., Berezin, E. V., Ciais, P., Broquet, G., Zhuravlev, R. V., and Janssens-Maenhout, G.: Estimation of fossil-fuel CO_2 emissions using satellite measurements of "proxy" species, Atmos. Chem. Phys., 16, 13509–13540, `https://doi.org/10.5194/acp-16-13509-2016`, 2016.

Kromer, B., Lindauer, S., Synal, H.-A., and Wacker, L.: MAMS – A new AMS facility at the Curt-Engelhorn-Centre for Achaeometry, Mannheim, Germany, Nucl. Instrum. Methods Phys. Res. B, 294, 11-13, `https://doi.org/10.1016/j.nimb.2012.01.015`, 2013.

Kromer, B., Levin, I., Lindauer, S., Jähne, B., Münnich, M., Platt, U., and Schlosser, P.: Karl Otto Münnich (1925–2003): In Memoriam, Radiocarbon, 64(3), 445-449, `htpps://www.doi.org/10.1017/RDC.2021.38`, 2022.

Kuderer, M., Hammer, S., and Levin, I.: The influence of $^{14}CO_2$ releases from regional nuclear facilities at the Heidelberg $^{14}CO_2$ sampling site (1986–2014), Atmos. Chem. Phys., 18, 7951–7959, `https://doi.org/10.5194/acp-18-7951-2018`, 2018.

Kuenen, J. J. P., Visschedijk, A. J. H., Jozwicka, M., and Denier van der Gon, H. A. C.: TNO-MACC_II emission inventory; a multi-year (2003–2009) consistent high-resolution European emission inventory for air quality modelling, Atmos. Chem. Phys., 14, 10963–10976, `https://doi.org/10.5194/acp-14-10963-2014`, 2014.

Kunik, L., Mallia, D. V., Gurney, K. R., Mendoza, D. L., Oda, T., and Lin, J. C.: Bayesian inverse estimation of urban CO_2 emissions: Results from a synthetic data simulation over Salt Lake City, UT, Elem. Sci. Anth., 7(36), `https://doi.org/10.1525/elementa.375`, 2019.

Kutsch, W., Ciais, P., Becker, M., Cantoni, C., Cristofanelli, P., Delmotte, M., Denier van der Gon, H., Droste, A., Gerosa, G., Gkritzalis, T., Gielen, B., Holst, J., Kubistin, D., Luchetta, A., Ramonet, M., Rehder, G., Rutgersson, A., Steinbacher, M., and Super, I.: Are Carbon Sinks at Risk? FLUXES - The European Greenhouse Gas Bulletin, Volume 1, ICOS ERIC, `https://doi.org/10.18160/8NKQ-65S1`, 2022.

Lan, X., Tans, P. and K.W. Thoning: Trends in globally-averaged CO_2 determined from NOAA Global Monitoring Laboratory measurements, Version 2023-04, `https://doi.org/10.15138/9N0H-ZH07`, 2023.

Lauvaux, T., Miles, N. L., Deng, A., Richardson, S. J., Cambaliza, M. O., Davis, K. J., Gaudet, B., Gurney, K. R., Huang, J., O'Keefe, D., Song, Y., Karion, A., Oda, T., Patarasuk, R., Razlivanov, I., Sarmiento, D., Shepson, P., Sweeney, C., Turnbull, J., and Wu, K.: High-resolution atmospheric inversion of urban CO_2 emissions during the dormant season of the Indianapolis Flux Experiment (INFLUX), J. Geophys. Res. Atmos., 121, 5213– 5236, `https://doi.org/10.1002/2015JD024473`, 2016.

Lehmuskoski, J., Vasama, H., Hämäläinen, J., Hokkinen, J., Kärkelä, T., Heiskanen, K., Reinikainen, M., Rautio, S., Hirvelä, M., and Genoud, G.: On-Line Monitoring of Radiocarbon Emissions in a Nuclear Facility with Cavity Ring-Down Spectroscopy, Anal. Chem., 93, 16096-16104, `https://doi.org/10.1021/acs.analchem.1c03814`, 2021.

Levin, I., Kromer, B., Schmidt, M., and Sartorius, H.: A novel approach for independent budgeting of fossil fuel CO_2 over Europe by $^{14}CO_2$ observations, Geophys. Res. Lett., 30 (23), 2194, `https://doi.org/10.1029/2003GL018477`, 2003.

Levin, I. and Karstens, U.: Inferring high-resolution fossil fuel CO_2 records at continental sites from combined $^{14}CO_2$ and CO observations, Tellus B, 59, 245-250. `https://doi.org/10.1111/j.1600-0889.2006.00244.x`, 2007.

Levin, I. and Rödenbeck, C.: Can the envisaged reductions of fossil fuel CO_2 emissions be detected by atmospheric observations?, Naturwissenschaften, 95(3), 203-208, `https://doi.org/10.1007/s00114-007-0313-4`, 2008.

Levin, I., Hammer, S., Kromer, B., Preunkert, S., Weller, R., and Worthy, D.: Radiocarbon in global tropospheric carbon dioxide, Radiocarbon, 64(4), 781-791, `https://doi.org/10.1017/RDC.2021.102`, 2022.

Lin, J. C., Gerbig, C., Wofsy, S. C., Andrews, A. E., Daube, B. C., Davis, K. J., and Grainger, C. A.: A near-field tool for simulating the upstream influence of atmospheric observations: The Stochastic Time-Inverted Lagrangian Transport (STILT) model, J. Geophys. Res., 108, 4493, `https://doi.org/10.1029/2002JD003161`, 2003.

Liu, J., Baskaran, L., Bowman, K., Schimel, D., Bloom, A. A., Parazoo, N. C., Oda, T., Carroll, D., Menemenlis, D., Joiner, J., Commane, R., Daube, B., Gatti, L. V., McKain, K., Miller, J., Stephens, B. B., Sweeney, C., and Wofsy, S.: Carbon Monitoring System Flux Net Biosphere Exchange 2020 (CMS-Flux NBE 2020), Earth Syst. Sci. Data, 13, 299–330, `https://doi.org/10.5194/essd-13-299-2021`, 2021.

Lopez-Coto, I., Ren, X., Salmon, O. E., Karion, A., Shepson, P. B., Dickerson, R. R., Stein, A., Prasad, K., and Whetstone, J. R.: Wintertime CO_2, CH_4, and CO Emissions Estimation for the Washington, DC-Baltimore Metropolitan Area Using an Inverse Modeling Technique, Environ. Sci. Technol., 54, 2606–2614, `https://doi.org/10.1021/acs.est.9b06619`, 2020.

Lux, J. T.: A new target preparation facility for high precision AMS measurements and strategies for efficient $^{14}CO_2$ sampling, Doctoral dissertation, `https://doi.org/10.11588/heidok.00024767`, 2018.

Monteil, G., Broquet, G., Scholze, M., Lang, M., Karstens, U., Gerbig, C., Koch, F.-T., Smith, N. E., Thompson, R. L., Luijkx, I. T., White, E., Meesters, A., Ciais, P., Ganesan, A. L., Manning, A., Mischurow, M., Peters, W., Peylin, P., Tarniewicz, J., Rigby, M., Rödenbeck, C., Vermeulen, A., and Walton, E. M.: The regional European atmospheric transport inversion comparison, EUROCOM: first results on European-wide terrestrial carbon fluxes for the period 2006–2015, Atmos. Chem. Phys., 20, 12063–12091, `https://doi.org/10.5194/acp-20-12063-2020`, 2020.

Nehrkorn, T., Eluszkiewicz, J., Wofsy, S. C., Lin, J. C., Gerbig, C., Longo, M., Freitas, S.: Coupled weather research and forecasting–stochastic time-inverted lagrangian transport (WRF–STILT) model. Meteorol. Atmos. Phys. 107, 51–64, `https://doi.org/10.1007/s00703-010-0068-x`, 2010.

Newsam, G. N. and Enting, I. G.: Inverse problems in atmospheric constituent studies: I. Determination of surface sources under a diffusive transport approximation, Inverse Problems, 4, 1037–1054, 1988.

Peylin, P., Law, R. M., Gurney, K. R., Chevallier, F., Jacobson, A. R., Maki, T., Niwa, Y., Patra, P. K., Peters, W., Rayner, P. J., Rödenbeck, C., van der Laan-Luijkx, I. T., and Zhang, X.: Global atmospheric carbon budget: results from an ensemble of atmospheric CO_2 inversions, Biogeosciences, 10, 6699–6720, `https://doi.org/10.5194/bg-10-6699-2013`, 2013.

Pinty, B., Ciais, P., Dee, D., Dolman, H., Dowell, M., Engelen, R., Holmlund, K., Janssens-Maenhout, G., Meijer, Y., Palmer, P., Scholze, M., Denier van der Gon, H., Heimann, M., Juvyns, O., Kentarchos, A., and Zunker, H.: An Operational Anthropogenic CO_2 Emissions Monitoring & Verification Support Capacity – Needs and high level requirements for in situ measurements, European Commission, Joint Research Centre, Publications Office, `https://data.europa.eu/doi/10.2760/182790`, 2019.

Pisso, I., Patra, P., Takigawa, M., Machida, T., Matsueda, H., and Sawa, Y.: Assessing Lagrangian inverse modelling of urban anthropogenic CO_2 fluxes using in situ aircraft and ground-based measurements in the Tokyo area, Carbon Balance Manage, 14(6), `https://doi.org/10.1186/s13021-019-0118-8`, 2019.

Reuter, M., Buchwitz, M., Schneising, O., Krautwurst, S., O'Dell, C. W., Richter, A., Bovensmann, H., and Burrows, J. P.: Towards monitoring localized CO_2 emissions from space: co-located regional CO_2 and NO_2 enhancements observed by the OCO-2 and S5P satellites, Atmos. Chem. Phys., 19, 9371–9383, `https://doi.org/10.5194/acp-19-9371-2019`, 2019.

Rodhe, H., Charlson, R., and Crawford, E.: Svante Arrhenius and the Greenhouse Effect, Ambio, 26(1), 2–5, `http://www.jstor.org/stable/4314542`, 1997.

Rödenbeck, C., Houweling, S., Gloor, M., and Heimann, M.: CO_2 flux history 1982–2001 inferred from atmospheric data using a global inversion of atmospheric transport, Atmos. Chem. Phys., 3, 1919–1964, `https://doi.org/10.5194/acp-3-1919-2003`, 2003.

Rödenbeck, C.: Estimating CO_2 sources and sinks from atmospheric mixing ratio measurements using a global inversion of atmospheric transport, Tech. Rep. 6, Max Planck Institute for Biogeochemistry, Jena, Germany, 2005.

Rödenbeck, C., Zaehle, S., Keeling, R., and Heimann, M.: How does the terrestrial carbon exchange respond to interannual climatic variations? A quantification based on atmospheric CO_2 data, Biogeosciences, 15, 1–18, `https://doi.org/10.5194/bg-15-1-2018`, 2018.

Rosendahl C.: Proxy to fossil-fuel CO_2 emission ratios: in-situ versus inventory data, PhD-Thesis, University of Heidelberg, `https://doi.org/10.11588/heidok.00031909`, 2022.

Stuiver, M. and Polach, H.: Discussion Reporting of ^{14}C Data, Radiocarbon, 19(3), 355-363, `https://doi.org/10.1017/S0033822200003672`, 1977.

Suess, H. E.: Radiocarbon Concentration in Modern Wood, Science, 122, 415-417, `https://doi.org/10.1126/science.122.3166.415.b`, 1955.

Super, I., Dellaert, S. N. C., Visschedijk, A. J. H., and Denier van der Gon, H. A. C.: Uncertainty analysis of a European high-resolution emission inventory of CO_2 and CO to support inverse modelling and network design, Atmos. Chem. Phys., 20, 1795–1816, `https://doi.org/10.5194/acp-20-1795-2020`, 2020.

Turnbull, J. C., Miller, J. B., Lehman, S. J., Tans, P. P., Sparks, R. J., and Southon, J.: Comparison of $^{14}CO_2$, CO, and SF_6 as tracers for recently added fossil fuel CO_2 in the atmosphere and implications for biological CO_2 exchange, Geophys. Res. Lett., 33, L01817, `https://doi.org/10.1029/2005GL024213`, 2006.

Turnbull, J., Sweeney, C., Karion, A., Newberger, T., Lehman, S., Tans, P., Davis, K., Lauvaux, T., Miles, N., Richardson, S., Cambaliza, M., Shepson, P., Gurney, K., Patarasuk, R., and Razlivanov, I.: Toward quantification and source sector identification of fossil fuel CO_2 emissions from an urban area: Results from the INFLUX experiment, J. Geophys. Res. Atmos., 120, 292– 312, `https://doi.org/10.1002/2014JD022555`, 2015.

Turnbull, J., Karion, A., Davis, K. J., Lauvaux, T., Miles, N. L., Richardson, S. J., Sweeney, C., McKain, K., Lehman, S. J., Gurney, K. R., Patarasuk, R., Liang, J., Shepson, P. B., Heimburger, A., Harvey, R., and Whetstone, J.: Synthesis of Urban CO_2 Emission Estimates from Multiple Methods from the Indianapolis Flux Project (INFLUX), Environ. Sci. Technol., 53, 287–295, `https://doi.org/10.1021/acs.est.8b05552` 2019.

Van Der Laan, S., Karstens, U., Neubert, R. E. M., Van Der Laan-Luijkx, I. T., and Meijer, H. A. J.: Observation-based estimates of fossil fuel-derived CO_2 emissions in the Netherlands using $\Delta^{14}C$, CO and ^{222}Radon, Tellus B: Chemical and Physical Meteorology, 62,5, 389-402, `https://doi.org/10.1111/j.1600-0889.2010.00493.x`, 2010.

Vogel, F., Hammer, S., Steinhof, A., Kromer, B., and Levin, I.: Implication of weekly and diurnal ^{14}C calibration on hourly estimates of CO-based fossil fuel CO_2 at a moderately polluted site in southwestern Germany, Tellus B: Chemical and Physical Meteorology, 62, 5, 512-520, `https://doi.org/10.1111/j.1600-0889.2010.00477.x`, 2010.

Walker, A.P., De Kauwe, M.G., Bastos, A., Belmecheri, S., Georgiou, K., Keeling, R.F., McMahon, S.M., Medlyn, B.E., Moore, D.J.P., Norby, R.J., Zaehle, S., Anderson-Teixeira, K.J., Battipaglia, G., Brienen, R.J.W., Cabugao, K.G., Cailleret, M., Campbell, E., Canadell, J.G., Ciais, P., Craig, M.E., Ellsworth, D.S., Farquhar, G.D., Fatichi, S., Fisher, J.B., Frank, D.C., Graven, H., Gu, L., Haverd, V., Heilman, K., Heimann, M., Hungate, B.A., Iversen, C.M., Joos, F., Jiang, M., Keenan, T.F., Knauer, J., Körner, C., Leshyk, V.O., Leuzinger, S., Liu, Y., MacBean, N., Malhi, Y., McVicar, T.R., Penuelas, J., Pongratz, J., Powell, A.S., Riutta, T., Sabot, M.E.B., Schleucher, J., Sitch, S., Smith, W.K., Sulman, B., Taylor, B., Terrer, C., Torn, M.S., Treseder, K.K., Trugman, A.T., Trumbore, S.E., van Mantgem, P.J., Voelker, S.L., Whelan, M.E. and Zuidema, P.A.: Integrating the evidence for a terrestrial carbon sink caused by increasing atmospheric CO_2, New Phytol, 229, 2413-2445, `https://doi.org/10.1111/nph.16866`, 2021.

Wang, Y., Broquet, G., Ciais, P., Chevallier, F., Vogel, F., Wu, L., Yin, Y., Wang, R., and Tao, S.: Potential of European $^{14}CO_2$ observation network to estimate the fossil fuel CO_2 emissions via atmospheric inversions, Atmos. Chem. Phys., 18, 4229–4250, `https://doi.org/10.5194/acp-18-4229-2018`, 2018.

Worden, H. M., Bloom, A. A., Worden, J. R., Jiang, Z., Marais, E. A., Stavrakou, T., Gaubert, B., and Lacey, F.: New constraints on biogenic emissions using satellite-based estimates of carbon monoxide fluxes, Atmos. Chem. Phys., 19, 13569–13579, `https://doi.org/10.5194/acp-19-13569-2019`, 2019.

Zheng, B., Chevallier, F., Ciais, P., Broquet, G., Wang, Y., Lian, J., and Zhao, Y.: Observing carbon dioxide emissions over China's cities and industrial areas with the Orbiting Carbon Observatory-2, Atmos. Chem. Phys., 20, 8501–8510, `https://doi.org/10.5194/acp-20-8501-2020`, 2020.

Zhou, W., Niu, Z., Wu, S., Xiong, X., Hou, Y., Wang, P., Feng, T., Cheng, P., Du, H., Lu, X., An, Z., Burr, G. S., Zhu, Y.: Fossil fuel CO_2 traced by radiocarbon in fifteen Chinese cities, Science of The Total Environment, Volume 729, 138639, ISSN 0048-9697, `https://doi.org/10.1016/j.scitotenv.2020.138639`, 2020.

My contribution to the manuscripts

Chapter 2: I designed this study together with Ingeborg Levin, Christoph Gerbig und Samuel Hammer. I developed the STILT-VSI approach and conducted all model simulations, as well as the comparison with the observations. I wrote the manuscript with help from all co-authors.

Chapter 3: I designed this study together with all co-authors. I estimated and discussed the biases and uncertainties of the ΔffCO$_2$ calculation (see Fig. 1, 2, 4, 5, and 7) and calculated the trajectories for Fig. 2. I wrote this manuscript togehter with Ingeborg Levin.

Chapter 4: I intensively tested the ICOS flask sampler in Heidelberg by testing various sampling methods. I collected and analyzed the flask samples shown in Fig. 3 (top panel). Furthermore, I helped Sabrina Arnold analyzing the flask samples from Hohenpeißenberg (see Fig. 3, bottom panel). By analyzing the integrated ^{14}C samples from 4 ICOS sites (see Fig. 6), I estimated which ΔffCO$_2$ signal can be expected at ICOS sites.

Chapter 5: I designed this study togehter with Ingeborg Levin, Samuel Hammer and Makysm Gachkivskyi. I calculated the flask and inventory-based ΔCO/ΔffCO$_2$ ratios for Heidelberg and OPE and estimated and discussed the biases and uncertainties of the continuous ΔCO-based ΔffCO$_2$ records. I wrote this manuscript with help from all co-authors.

Chapter 6: I designed this study togehter with Ingeborg Levin, Chrisitan Rödenbeck, Samuel Hammer and Makysm Gachkivskyi. Christian Rödenbeck helped me adapting the CarboScope inversion system for the Rhine Valley. I performed all inversion runs and evaluated the results. I wrote the manuscript with help from all co-authors.

Acknowledgements

Als erstes möchte ich mich ganz herzlich bei Ingeborg Levin und Samuel Hammer bedanken, die mein Doktorstudium und diese Arbeit innerhalb der Kohlenstoffkreislauf-Gruppe überhaupt erst möglich gemacht haben. Die langjährige Erfahrung von Ingeborg ist ein großer Schatz, von dem ich – sowohl für diese Arbeit als auch menschlich – sehr profitieren konnte. Ich danke Euch sehr für Eure Unterstützung und Betreuung während meinem gesamten Doktorstudium und Euren vielen guten Ideen, die uns immer ein Stück weitergebracht haben.

Des Weiteren möchte ich Ingeborg Levin und André Butz danken für das Begutachten dieser Dissertation.

Ein großes Dankeschön geht an die gesamte Carbon Cycle Arbeitsgruppe; es hat mir sehr viel Spaß gemacht mit Euch zusammen zu arbeiten. Die Diskussion von neuen Ergebnissen in der wöchentlichen Gruppensitzung hat mir nicht nur bei meiner eigenen Arbeit sehr geholfen, sondern ermöglichte mir auch einen spannenden Einblick in die anderen Arbeitsbereiche der Gruppe. Besonders danken möchte ich meinen PhD Kollegen Makysm Gachkivskyi und Claudius Rosendahl für die gegenseitige Unterstützung bei unseren Arbeiten und auch die Gemeinschaft neben der Wissenschaft.

Ich möchte dem gesamten technischen Team unserer Arbeitsgruppe danken, allen voran Julian Della Coletta, Sabine Kühr, Eva Gier, Michael Sabasch und Zoe Gatt. Ihr habt das Labor am Laufen gehalten und meine ganzen Luftproben aufbereitet. Außerdem möchte ich mich bei Ronny Friedrich für die Messung der Luftproben am AMS und bei Suzanne Preunkert für das Pflegen der Datenbank bedanken. Eure sorgfältigen Messungen sind das Herzstück dieser Arbeit, deshalb vielen Dank! Ein Dankeschön auch an Caterina Keller, die mir bei verwaltungstechnischen Fragen stets geholfen hat.

Besonders danken möchte ich Christoph Gerbig und Christian Rödenbeck vom Max-Planck-Insitut für Biogeochemie. Ihr habt mir die Modellierung beigebracht und gabt mir viele gute Anregungen für diese Arbeit. Ich danke Euch beiden für Eure Unterstützung und Hilfe mit STILT und CarboScope. Es ist wirklich toll, diese für mich anfangs komplett neue Welt der Modellierung durch Euch kennengelernt zu haben! Bedanken möchte ich mich auch bei Julia Marshall und Michał Gałkowski für das Prozessieren der hochaufgelösten meteorologischen WRF-Felder und Thomas Koch für die Hilfe bei technischen Fragen zur Modellierung.

Ein Dankeschön auch an Armin Jordan und das gesamte Team vom ICOS FCL für die Konzentrationsmessungen meiner Luftproben. Insbesondere danke ich Markus Eritt, Richard Kneißl und Lars Borchard, die den ICOS Flasksammler in Heidelberg aufgebaut haben und mir bei technischen Problemen immer weitergeholfen haben.

Vielen Dank auch an Ida Storm, Ute Karstens und dem ICOS Carbon Portal für die Entwicklung von sehr hilfreichen jupyter Notebooks, insbesondere für die Berechnung der nuklearen Kontamination.

Abschließend möchte ich allen meinen Freunden und meiner Familie danken, die mich auf meinem gesamten Lebensweg unterstützt haben. Ich bin sehr glücklich so tolle Eltern zu haben, die immer für mich da sind. Sophia, danke, dass du so eine liebe Schwester bist. Valentin, durch dich habe ich gelernt, was im Leben wirklich wichtig ist.

Mein liebster Dank geht an die wichtigste Person in meinem Leben, Samira.